Modeling the intragranular ductile fracture of irradiated steels. Effects of crystal anisotropy and strain gradient

Chao Ling

THÈSE DE DOCTORAT

de l'Universitè de recherche Paris Sciences et Lettres
PSL Research University

Préparée à MINES ParisTech

Simulation de la rupture ductile intragranulaire des aciers irradiés. Effets de l'anisotropie cristalline et du gradient de déformations

Modeling the intragranular ductile fracture of irradiated steels. Effects of crystal anisotropy and strain gradient

Ecole doctorale n°432

SCIENCE ET MÉTIERS DE L'INGÉNIEUR

Spécialité SCIENCE ET GÉNIE DES MATÉRIAUX

JURY :

M. Christian Frithiof NIORDSON
Technical University of Denmark, Président

M. Renald BRENNER
Université Pierre et Marie Curie, Rapporteur

M. Jeffrey KYSAR
Columbia University, Rapporteur

M. Kostas DANAS
École Polytechnique, Examinateur

M. Benoît TANGUY
CEA Saclay, Examinateur

M. Félix LATOURTE
EDF R&D, Examinateur

M. Samuel FOREST
Mines ParisTech, Examinateur

M. Jacques BESSON
Mines ParisTech, Examinateur

Soutenue par **Chao LING**
le 24 janvier 2017

Dirigée par **Jacques BESSON**
Samuel FOREST

MINES ParisTech | PSL RESEARCH UNIVERSITY PARIS

This thesis is dedicated to my family!

Acknowledgements

Après un peu plus de 3 ans de travail, je arrive finalement à la dernière étape de cette aventure scientifique. C'est une aventure pour moi, parce que je découvre le monde de la mécanique en rencontrant des difficultés et proposant des solutions. Cette aventure est inoubliable grâce aux laboratoires qui m'ont accueilli et grâce aux gens avec qui j'ai travaillé. Mes premiers remerciements sont donc dédiés à mes directeurs de thèse : Jacques Besson et Samuel Forest de l'École des Mines, et Benoît Tanguy du laboratoire du comportement mécanique des matériaux irradiés du CEA, et aussi à mon encadrant EDF Félix Latourte. C'est leur professionnalisme, leurs connaissances, leur exigence, leur patience, leur encouragement et leur soutien qui me permettent d'aller jusqu'au bout de cette aventure. Je remercie aussi Elodie Bosso d'EDF, qui m'a appris les études expérimentales sur le monocristal.

Je veux également remercier Renald Brenner, Kostas Danas, Jeffrey Kysar et Christian Niordson, qui ont examiné soigneusement ma thèse et participé à ma soutenance malgré leurs emplois du temps chargés.

Je tiens à remercier tous mes collègues du laboratoire du comportement mécanique des matériaux irradiés du CEA. En particulier merci à Thomas Helfer, Jérémy Hure et Pierre-Olivier Barrioz avec qui j'ai beaucoup discuté sur la mécanique et l'implémentation numérique des modèles. Merci également à mon stagiaire Pushpander Rathore pour sa contribution à l'implementation des modèles dans MFront.

Je souhaite remercier tous mes collègues du Centre des matériaux pour leurs aides durant ces trois ans. Merci aux doctorants de mon bureau : Nicloas Gueninchault, Quentin Roirand, Juan-Manuel Garcia et Sicong Ren. Grâce à eux, je peux avoir un bureau très agréable pour travailler.

Merci aussi à mes amis chinois au Centre des matériaux: Yi Zhang, Yang Zhang, Tang Gu, Fang Lu, Qi Huang et Youbin Chen, pour les échanges que nous avons par rapport à la science et à la vie en France.

Finalement, je voudrais remercier toute ma famille, en particulier ma femme et mes parents pour leur encouragement et support.

Abstract

Irradiation causes drastic modifications of mechanical properties of austenitic stainless steels and a decrease in the fracture toughness with irradiation has been observed. Ductile fracture due to void growth and coalescence remains one dominant fracture mechanism for doses in the range of 0–10 dpa. Voids may have different origins: nucleated at inclusions or irradiation-induced precipitates during mechanical loading, or produced directly by irradiation. The present work is to investigate ductile fracture of irradiated steels due to growth and coalescence of intragranulaire voids. Based on continuum crystal plasticity theory, FE simulations are performed on unit cells for studying effects of lattice orientation and stress triaxiality on void growth and coalescence. The influence of post-irradiation hardening/softening on void growth and coalescence is evaluated with a physically based crystal plasticity model. Besides, an elastoviscoplastic model at finite strains is proposed to describe void growth up to coalescence in single crystals, and is assessed based unit cell simulations. The model is then applied to simulate ductile damage in single crystals and polycrystals. As voids in irradiated steels may have different origins, they may have different sizes, which potentially have an influence on ductile fracture process and fracture toughness of irradiated steels. In order to assess the size effect, a micromorphic crystal plasticity model is proposed and applied to simulate growth and coalescence of intragranular voids of different sizes.

Keywords: ductile fracture, FCC steels, irradiation, intragranular voids, crystal plasticity, strain gradient plasticity

Contents

x

1 Introduction

Résumé

Les aciers austénitiques inoxydables sont largement utilisés dans les réacteurs nucléaires. L'irradiation peut créer des défauts microstructuraux dans les aciers et ainsi modifier leurs propriétés mécaniques. Une diminution de la ténacité à la rupture des aciers en fonction de la dose est observée. La rupture ductile due à la croissance et la coalescence des cavités est un mécanisme dominant dans les aciers irradiés jusqu'à 10 dpa. Des cavités peuvent être créées de manière différente : nucléées à partir des inclusions ou des précipités d'irradiation, ou créées directement par irradiation. Ces cavités se trouvent souvent au sein des grains et elles sont plus petites que les grains. Cette thèse a pour objectif d'étudier la rupture ductile des aciers irradiés due à ces cavités intragranulaires. Dans ce chapitre, une approche multi-échelle est proposée pour la modélisation de la rupture ductile intragranulaire des aciers irradiés. La thèse se décompose en 4 parties. La première partie présente une recherche bibliographique sur les propriétés mécaniques des aciers irradiés et les modèles existant dans la littérature. Dans la deuxième partie, on montre des simulations par éléments finis effectuées sur des cellules unitaires pour étudier la cinétique de la croissance et la coalescence des cavités dans le monocristal. Dans la troisième partie, un modèle élastoviscoplastique en grandes transformations est proposé pour le monocristal poreux. Le modèle est appliqué à la simulation de l'endommagement ductile dans le monocristal et le polycristal. Dans la dernière partie, un modèle micromorphe de plasticité cristalline est proposé et appliqué à la simulation de la croissance et la coalescence des cavités intragranulaires de différentes tailles ainsi qu'aux phénomènes de localisation dans les monocristaux.

Industrial context

Austenitic stainless steels of 300 series are widely used as structural materials in nuclear power plants (see fig. 1.1), especially for reactor vessel internals, due to their good mechanical properties and resistance to corrosion (Zinkle and Was, 2013). These steels are exposed to complex operating conditions such as high temperature (over 300 °C), mechanical loadings, radiation damage and corrosion. Under such conditions, properties of the steels evolve over time. Austenitic stainless steels undergo continual microstructure evolution during neutron irradiation, which leads to drastic modifications of mechanical properties: increase in yield stress, decrease in ductility (uniform elongation) and strain hardening capacity, and decrease of fracture toughness (Pokor et al., 2004a; Pokor et al., 2004b; Zinkle and Was, 2013). All the modifications in the materials certainly have an influence on the operation of reactors and cause challenges for designing reactors compatible with the changes. Thus it is very important to understand why these changes occur and what are the consequences on fracture properties of austenitic stainless steels.

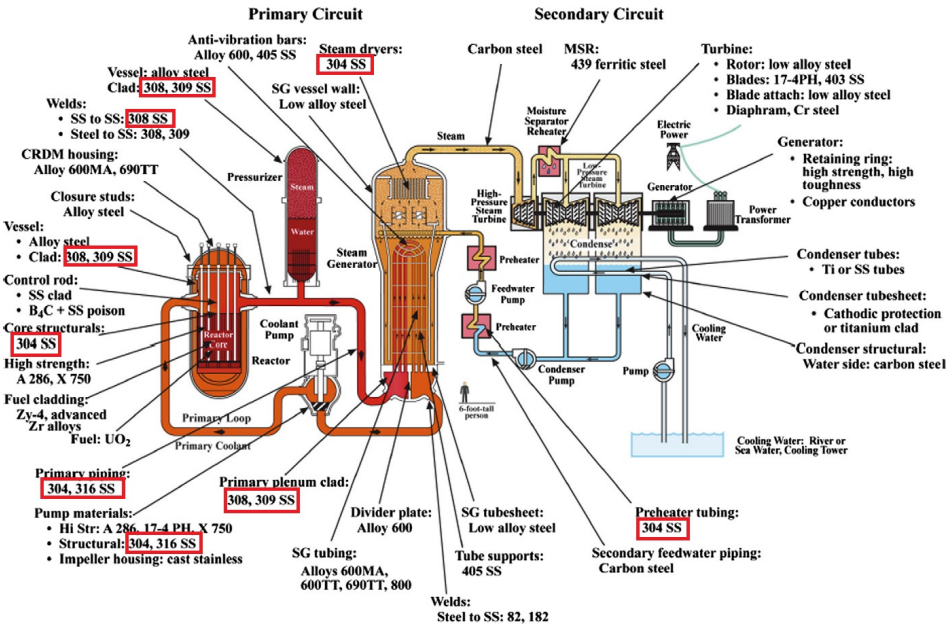

Figure 1.1: Schematic of the circuits of a pressurized water reactor and materials of construction (Zinkle and Was, 2013). Stainless steels of 300 series are indicated by red rectangles.

The modification of mechanical properties are usually related to irradiation-induced microstructural defects, such as Frank loops (a type of dislocation loops) which are often observed in austenitic stainless steels (Pokor et al., 2004c). These defects can interact with dislocations, leading to a change of plastic deformation

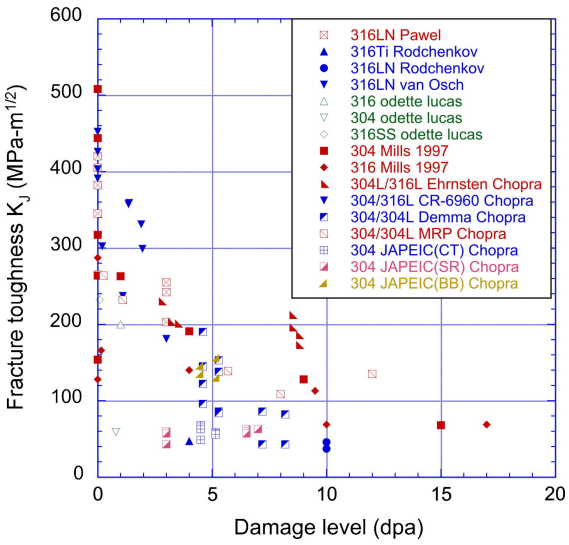

Figure 1.2: Fracture toughness of 304 and 316 stainless steels irradiated in light water reactor (LWR) conditions at 250–350 °C. (Zinkle and Was, 2013)

mechanism. Besides, voids and bubbles can form in the materials during irradiation, which has been shown to be correlated with the change of mechanical properties (Neustroev and Garner, 2008; Neustroev and Garner, 2009; Margolin et al., 2016).

Fracture toughness, an important parameter for the integrity assessment, displays a decreasing trend with radiation, as reported in the literature (see fig. 1.2 from Zinkle and Was (2013)). Ductile fracture is found to be a dominant fracture mode of austenitic stainless steels after irradiation (Little, 1986; Fukuya et al., 2008; Margolin et al., 2016), especially at low irradiation dose, while some non-ductile modes, e.g., intragranular and channel fracture, are also reported for doses in the range of 30–80 dpa. However, there is no commonly accepted physical mechanism explaining the reduction in the fracture toughness after irradiation, because of the complexity of the phenomena. It is probably related to a kind of localized plastic deformation mode existing in irradiated materials, to a modification of kinetics of plastic deformation driven void growth and coalescence, or to formation of new voids. The present work will concern the latter two phenomena. To better understand the role of different irradiation-induced microstructural defects in decreasing the fracture toughness of steels, a multi-scale approach is needed to study fracture mechanisms in irradiated austenitic stainless steels.

Objectives

As explained above, fracture toughness of austenitic stainless steels decreases with irradiation, accompanied with change of fracture mechanism. **A demand**

of the nuclear industry is to develop theoretical and numerical tools able to predict the evolution of fracture toughness of austenitic stainless steels with irradiation.

For this purpose, **the objective of the present work is to investigate one dominant fracture mechanism in irradiated austenitic stainless steels—ductile fracture due to void growth and coalescence**. As well known, void is an important notion in the mechanics of ductile fracture. In unirradiated steels, voids can nucleate at inclusions or second phase particles during mechanical loading (Pineau and Pardoen, 2007; Besson, 2010; Benzerga and Leblond, 2010; Pineau et al., 2016). Voids can then grow and coalesce in stress fields leading to final failure. These are known as very important fracture mechanisms. In irradiated steels, voids may have different origins. Besides the same nucleation sources in unirradiated steels, voids can also nucleate from irradiation-induced precipitates (Little, 1986). In addition, irradiation-induced nano-voids may be another origin of voids leading to fracture (Margolin et al., 2016). In another word, the size of voids varies according to their origins: micro-sized for those nucleated from irradiation-induced precipitates and nano-sized for irradiation-induced voids. However, whatever their origins are, voids are very often located inside grains, i.e, intragranular voids, and thus of a size smaller than that of the grains. In addition, growth and coalescence of voids are proved to be controlled by plastic strains. Compared with unirradiated steels, plastic deformation is influenced by irradiation-induced defects in irradiated steels, which may in turn change the evolution of voids.

With consideration of the characteristics mentioned above, **the ductile fracture due to void growth and coalescence of unirradiated and irradiated austenitic stainless steels is investigated in the present work at the scale of the grain, i.e., single crystal. and voids are regarded as embedded in a single crystal.**

Methodology

For studying void growth and coalescence in single crystals, two approaches are adopted in the present work, as presented in fig. 1.3. The first approach corresponds to finite element simulations on unit cells with periodic boundary conditions, i.e., **unit cell simulations**, which will be performed using classical continuum theory of crystal plasticity to study the effects of

- crystal orientations,
- post-irradiation strain hardening/softening behavior

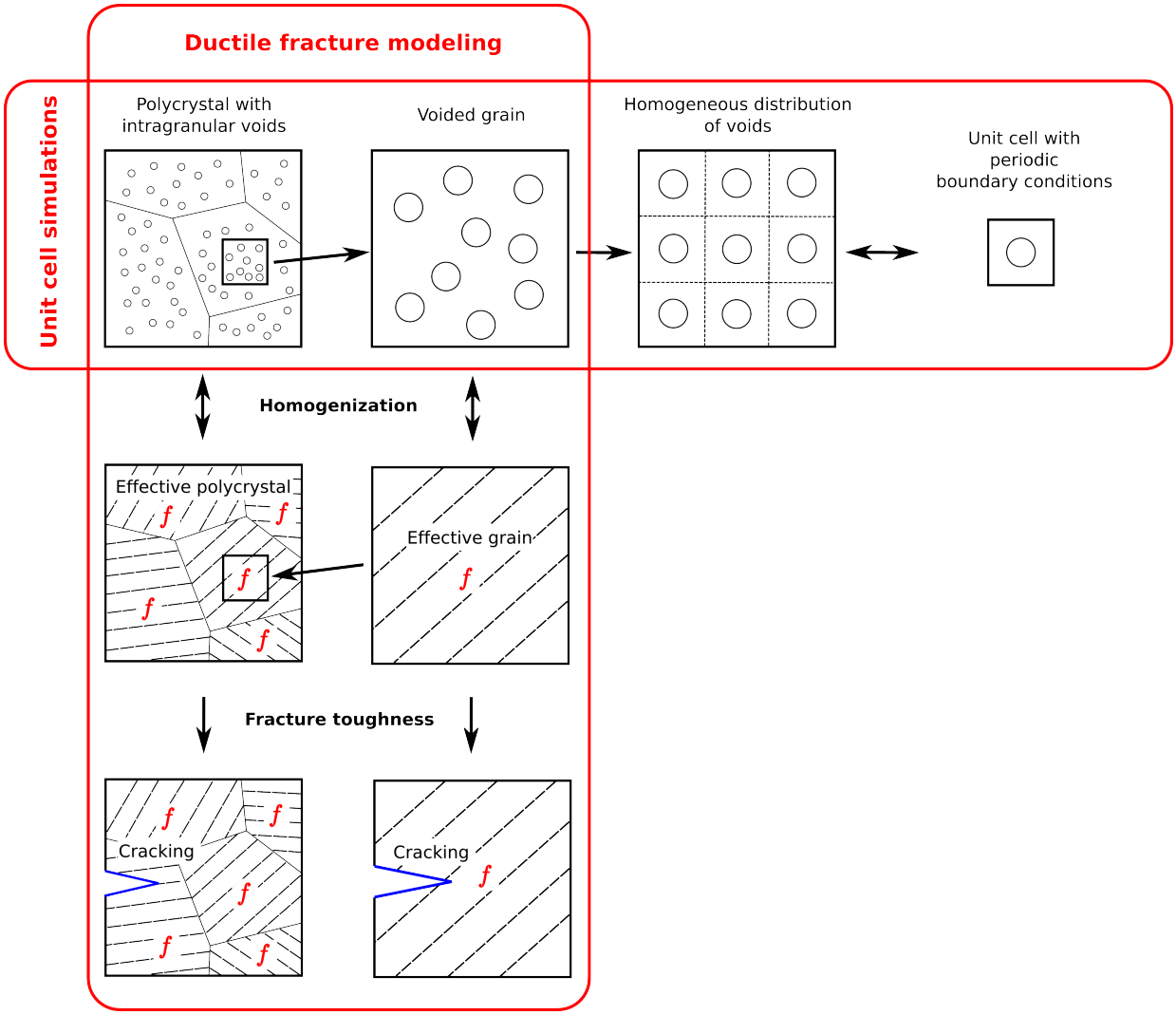

Figure 1.3: Multi-scale approach for investigating ductile fracture of irradiated stainless steels due to void growth and coalescence.

on void growth and coalescence. As the size of voids in irradiated stainless steels varies from nano to micro-scale,

- effects of void size

will be investigated in a second step. For this purpose, a strain gradient crystal plasticity model will be derived following the micromorphic approach (Germain, 1973; Forest, 2009; Aslan et al., 2011).

The second approach is to propose **an elastoviscoplastic model at finite strains** for porous single crystals, which incorporates effects of strain hardening of single crystal matrix and is able to describe void growth to coalescence. This model will be applied to simulate ductile damage evolution in a specimen of single crystal in the presence of a defect representation of a crack. The model can be further applied

to the scale of polycrystals. This approach can finally be used to assess effects of post-irradiation strain hardening/softening on fracture toughness on stainless steels.

Organization of the thesis

According to the approaches proposed for studying ductile fracture of irradiated austenitic stainless steels, the present work is organized as follows:

- chapter 2: A literature review is given for experimental observations on mechanical behavior of irradiated stainless steels and modeling tools existing in the literature. Based on this review, a further explanation will be given for the multi-scale approach proposed for this study.
- chapter 3: Void growth and coalescence in single crystals are studied with unit cell simulations based on crystal plasticity finite element method. 1) Some parameters influencing the void evolution are investigated, such as crystal orientation, stress triaxiality and initial void volume fracture. 2) Effects of post-irradiation strain hardening/softening behavior are outlined.
- chapter 4: An elastoviscoplastic model for porous single crystals at finite strains is formulated based on the work of Han (2012) and assessed numerically with the results of unit cell simulations. The model will be applied to simulate ductile damage in a polycrystalline aggregate under triaxial loadings and a single-edge-notch-tension test on a single crystal specimen of 316L stainless steels.
- chapter 5: Size effects on void growth and coalescence are studied. To this end, an enhanced single crystal plasticity model at finite strains is proposed and implemented in finite element code. Size dependent void growth and coalescence are investigated by unit simulations with the enhanced model for verifying if it is important to consider size effects in the multi-scale modeling of ductile fracture of irradiated austenitic stainless steels.

2
Literature review

Résumé

Ce chapitre présente brièvement les propriétés mécaniques des aciers irradiés et les approches de modélisation associées. On s'intéresse d'abord aux défauts microstructuraux induits par l'irradiation dans les aciers et à leur influence sur le comportement mécanique macroscopique. On montre que la rupture ductile intragranulaire est un mécanisme de rupture dominant pour les aciers irradiés, en particulier à faible dose. Les modèles classiques de rupture ductile sont présentés. En outre, l'effet de la taille des cavités sur la cinétique de la rupture ductile est discuté.

Contents

A literature review is performed in this chapter to first discuss effects of radiation on stainless steels. Irradiation-induced microstructure changes in stainless steels will be first considered, followed by a discuss on modifications of mechanical properties associated with the microstructure evolution. In particular, radiation effects on fracture behaviors of stainless steels will be outlined. It will be shown in the following that ductile fracture is one of the fracture mechanisms in irradiated steels. Hence, classical methods used to study ductile fracture in metallic materials will be reviewed. In addition, plastic size effects can play a role in ductile fracture and may also an influence on fracture behaviors of irradiated steels due to void growth and coalescence. Thus, a review about size effects on void growth will be performed. Based on the review, the objectives of the thesis will be outlined and the approaches used to study ductile fracture of irradiated steels will be presented as the conclusions of the chapter.

2.1 Microstructural effects of radiation damage on stainless steels

Irradiation produces microstructural defects in materials, mainly Frank loops in stainless steels, as a result of particles–matter interaction. The defects interact under irradiation, even without mechanical loading, with grown-in dislocations (already present before irradiation) resulting in dramatic changes of dislocation densities. Cavities are also produced during irradiation, which can play a role in fracture process. Under mechanical loading, dislocations interact with irradiation-induced defects, which can lead to a particular mode of deformation, where deformation is localized in channels sometimes called “cleared band”. These points are outlined in the following.

2.1.1 Frank loops and dislocations

Frank loops correspond to dislocation loops with pure edge character for every segments, which are often nucleated in a displacement cascade. A displacement cascade is a collection of point defects, including vacancies and interstitials, resulting from the interaction of energetic incident particles (irradiation) and lattice atoms. When the point defects collapse/condense onto a close-packed plane, a Frank loop may be produced. Two types of Frank loops exist: interstitial and vacancy loops. They correspond respectively to intrinsic and extrinsic stacking fault as shown in fig. 2.1. Interstitial Frank loops are often observed in stainless steels and they can be

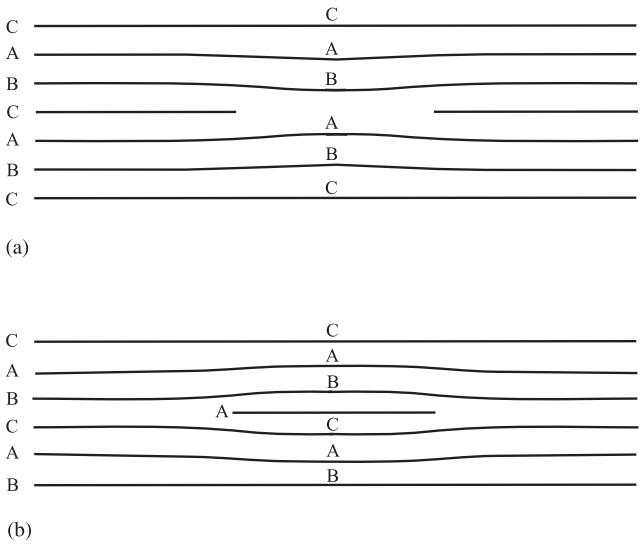

Figure 2.1: (a) Vacancy Frank loops; (b) interstitial Frank loops. (Was, 2007)

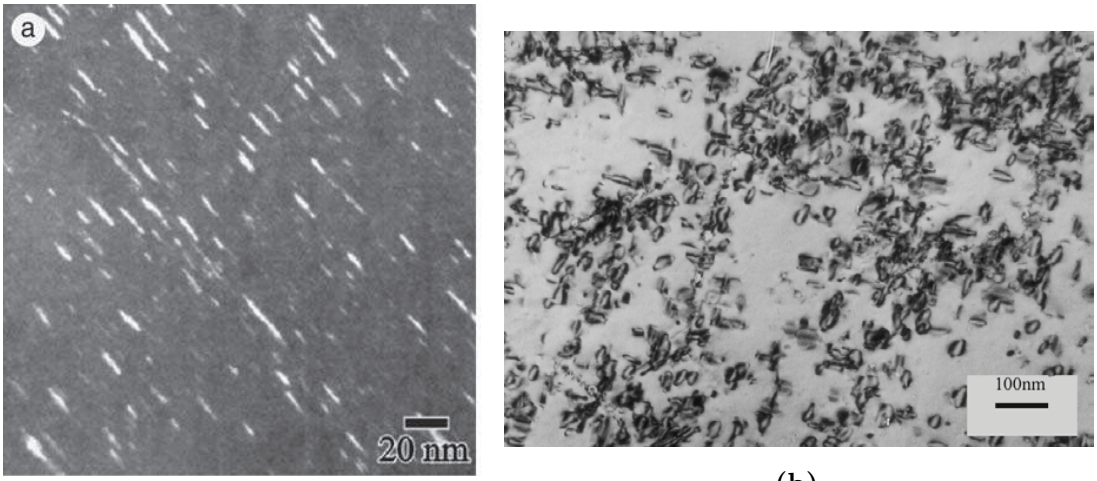

Figure 2.2: (a) TEM image showing Frank loops in a baffle bolt made from CW 316 stainless steels extracted from Tihange PWR (Edwards et al., 2003); (b) TEM image showing Frank loops in 12X18H9T stainless steels irradiated in BR-10 fast reactor to 0.6 dpa at 350 °C (Garner et al., 2005).

imaged under TEM as shown in fig. 2.2. During irradiation, the Frank loop density increases as a result of nucleation and growth and reaches a saturation value (fig. 2.3).

Dislocation evolution in metals during irradiation is closely related to interactions with irradiation-induced defects and is found to depend on their microstructural state before irradiation. Typical evolutions of dislocation density with irradiation dose are presented in fig. 2.4 for cold worked (CW) and solution annealed (SA) 300-series austenitic stainless steels irradiated in a fast breeder reactor at 510 °C.

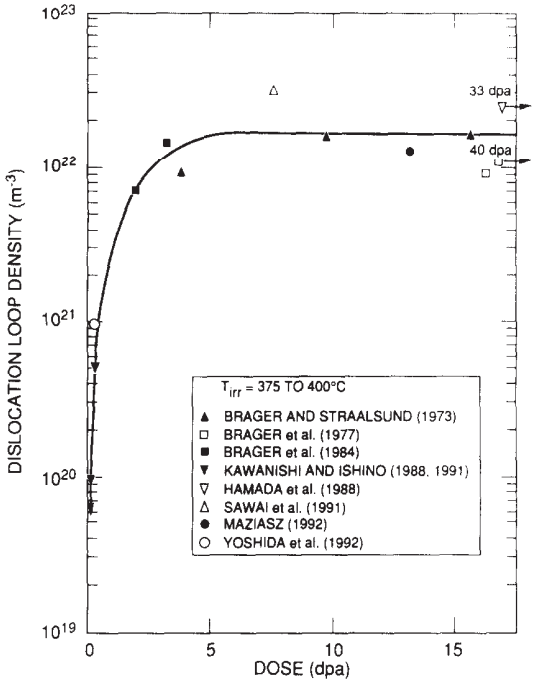

Figure 2.3: Evolution of Frank loop density in austenitic stainless steels irradiated with fission neutrons at 375 to 400 °C (Zinkle et al., 1993).

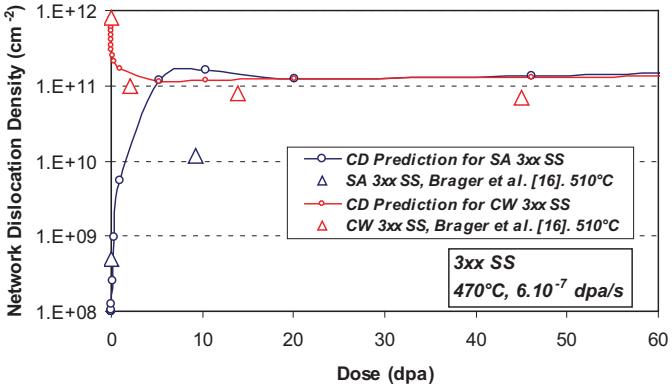

Figure 2.4: Evolution of dislocation density as a function of irradiation dose in SA and CW 300-series austenitic stainless steels irradiated in a fast breeder reactor at 510 °C. Note that triangle points are for experimental data at 510 °C at and that solid lines with circle points are for simulation results at 470 °C. (Zouari et al., 2012)

In annealed metals, dislocation density increases sharply with irradiation dose and eventually approaches a saturation value. In cold-worked metals, however, the dislocation density drops and approaches a saturation value. It is often observed that the saturation values in annealed and cold worked steels are nearly the same.

Inspired by these observations, investigations have been performed for modeling the dislocation evolution during irradiation. Generation and elimination are two competitive mechanisms (Wolfer and Glasgow, 1985; Stoller, 1990; Zouari et al.,

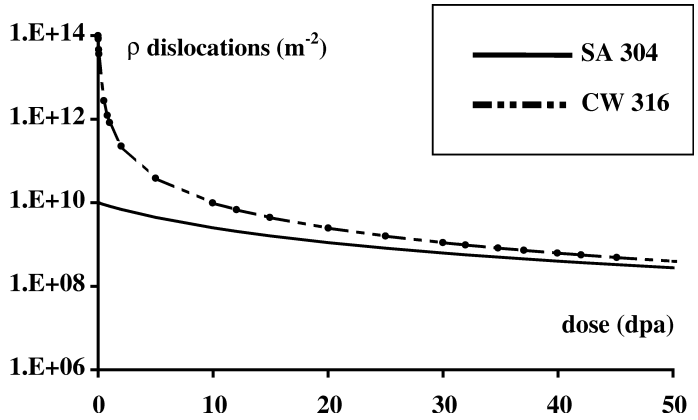

Figure 2.5: Evolution of dislocation density for stainless steels irradiated in BOR-60 at 375 °C. (Pokor et al., 2004c)

2012). Two generation mechanisms are often encountered in the literature: the thermal activation of Bardeen–Herring sources and unfaulting of Frank loops by mobile dislocations. Bardeen–Herring sources are similar to Frank–Read sources except that the former are driven by climb while the latter are by glide. Under irradiation, dislocations move and interact with Frank loops resulting in their unfaulting. The elimination mechanism corresponds to the annihilation of dislocation segments with opposite Burgers vectors.

The dose dependent dislocation densities to be used for simulations in the present thesis is taken from the work of Pokor et al., 2004a (see fig. 2.5). The results for SA 304 are considered. Notice that the dislocation density measured for unirradiated SA 304 steels seems lower than usual cases ($10^{12}\,\mathrm{m}^{-2}$ usually reported in the literature, such as in Zinkle et al. (1993) and Lucas (1993)) and that the dislocation density decreases with irradiation dose, which is different from the dislocation density evolution trend reported by Zouari et al. (2012).

Frank loops generated by irradiation modify plastic deformation mechanisms of the steels. Under mechanical loading, Frank loops interact with dislocations and cause a change in the yielding and hardening process. This is usually believed to lead to the mechanical effects of radiation damage presented in section 2.2. Numerous studies have being performed for understanding details about their interactions and also for modeling the irradiation dose dependent mechanical properties. A detailed literature review has already been performed in the thesis work of Han (2012). The author has proposed a single crystal plasticity model for irradiated austenitic stainless steels based on physical mechanism of Frank loop-dislocation interactions. This model will be used in the present work and presented later in section 3.1.

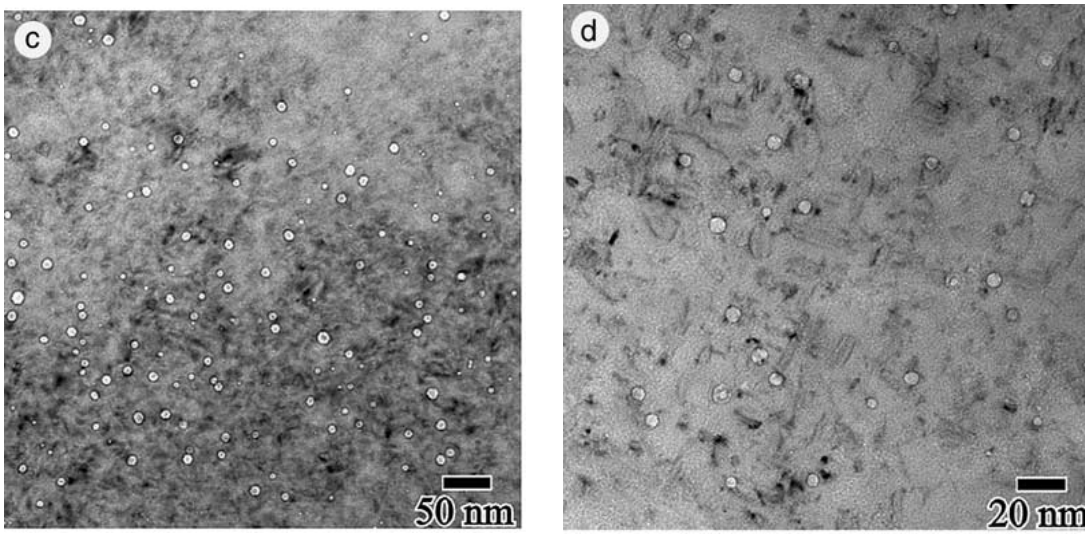

Figure 2.6: Cavities observed in the baffle-former bolts, made of CW 316SS stainless steels, of Tihange 1 PWR reactor. The material is irradiated at $T_{\mathrm{irr}} = 343\,^{\circ}\mathrm{C}$ to 12.2 dpa. The swelling level is about 0.2%. (Edwards et al., 2003)

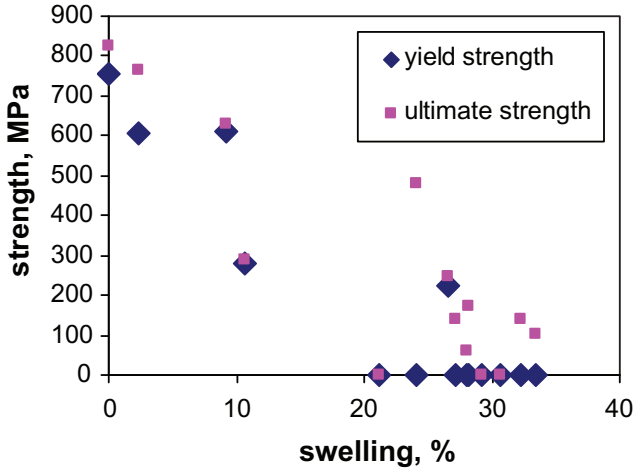

Figure 2.7: Decrease of yield stress and ultimate strength with swelling level in in Fe-18Cr-10Ni-0.5Ti stainless steels (Neustroev and Garner, 2008).

2.1.2 Voids and bubbles

Voids (empty cavities) and bubbles (cavities with gas) are generated by irradiation, whose densities depend on dose and irradiation temperature. The formation of voids is associated with clusters of vacancies absorbing more vacancies than interstitials. Insoluble gases are formed by transmutation when certain metals are irradiated, which finally leads to the formation of bubbles. Typical cavities observed in stainless steels are shown in fig. 2.6. Voids and bubbles could cause a change in dimensions of materials (called “swelling”) and have profound influences on mechanical properties

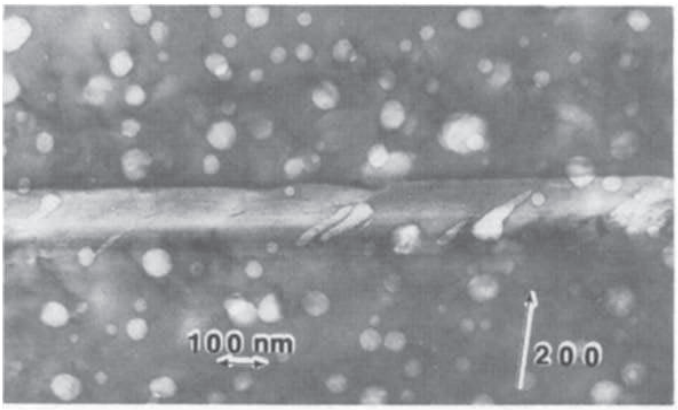

(a)

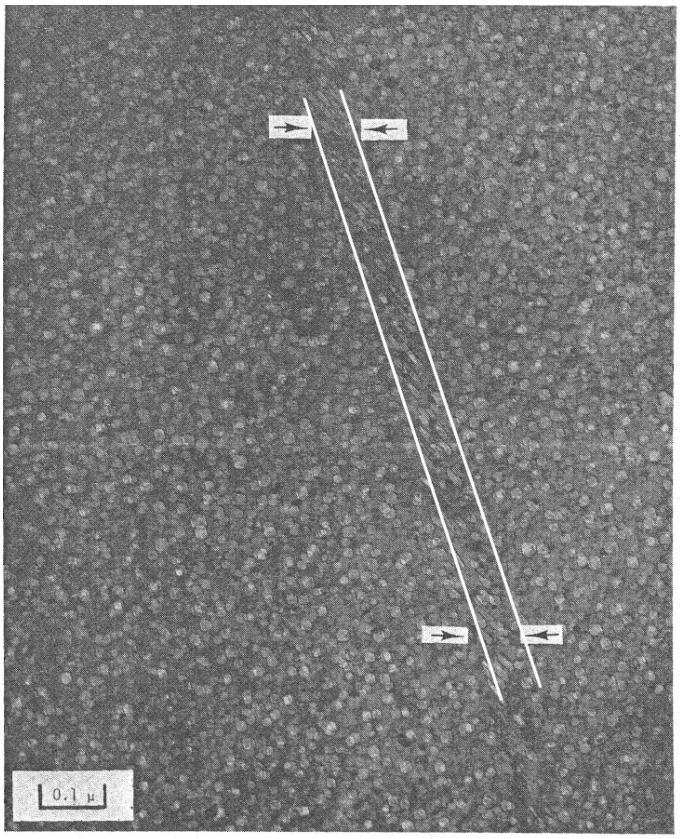

(b)

Figure 2.8: Deformed cavities in irradiated stainless steels: (a) elongated cavities in front of a crack tip of an ion-irradiated 316 stainless steel (Horton et al., 1981); (b) cavities deformed by dislocation channeling observed in a 304 stainless steels irradiated in EBR-II at 370 to 470 °C after a tensile test at 370 °C (Fish et al., 1973).

of materials. The irradiation swelling causes a great challenge for designing a reactor to accommodate dimension changes.

It has also been shown that the swelling level is correlated with the modification

of mechanical properties of stainless steels. Neustroev and Garner (2008) showed an almost linear reduction of yield stress and ultimate strength with swelling level in Fe-18Cr-10Ni-0.5Ti stainless steels irradiated in BOR-60 fast neutron reactor (fig. 2.7). Margolin et al. (2016) showed a decrease of the fracture toughness, evaluated by J-integral, with swelling level in Fe-18Cr-10Ni-Ti stainless steels irradiated in BOR-60 (fig. 2.14). Furthermore, cavities can lead to nano-dimple fracture in relatively high swelling level (see section 2.2.2). Some experimental observations have reported deformed (elongated) cavities located in plastic deformation channels in front of a crack tip (fig. 2.8a) and in a tension specimen (fig. 2.8b). These elongated cavities can probably participate in the process of cracking and final fracture of the steels.

As these cavities are potential crack sources, it is important to understand their behaviors in stress fields. Hence, one of the subjects of the present thesis work is to study the mechanical effects of cavities at the grain scale.

2.1.3 Cleared bands

It is well known that plastic strain localization occurs at the grain scale as a result of heterogeneous nature of plastic deformation. A specific plastic strain localization in defect-free channels has been widely observed in irradiated metallic single and polycrystals (see, e.g., Sharp, 1967; Tucker et al., 1969; Sharp, 1974; Singh et al., 1999; Hashimoto et al., 2005; Hashimoto et al., 2006) since a pioneering work of Greenfield and Wilsdorf (1961) on irradiated copper single crystals. The channel width is smaller than a few hundred nanometers where irradiation-induced defects (Frank loops in the case of stainless steels) are partially or fully removed by gliding dislocations. Since the number of defects are highly reduced within the channels, they are often called “cleared band” or “clear band” in the literature.

Cleared bands have also been observed in stainless steels (Bailat et al., 2000; Lee et al., 2001; Byun et al., 2006) even with relatively low irradiation damage (0.78 dpa in the study of Byun et al. (2006), shown in fig. 2.9). In Ni-ion irradiated 304L stainless steels, it was reported that cleared bands are the dominant plastic instability mode at high test temperature (about 280 °C) and slow strain rate conditions (Bruemmer et al., 1997; Cole and Bruemmer, 1995). However, Lee et al. (2001) reported that the channeling process in ion irradiated and deformed 316LN is not test temperature dependent. In addition, the observation of Edwards et al. (2005) suggested that cleared bands are initiated at places with high stress concentration such as grain boundaries, inclusions and even previously formed bands. The authors also observed that some channels can even penetrate through grain boundaries. Recently, discrete dislocation dynamics simulations were performed to

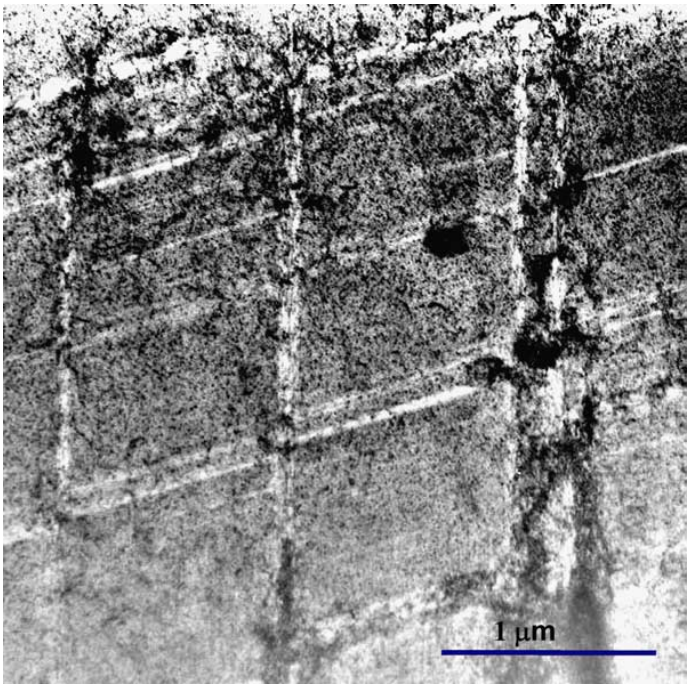

Figure 2.9: Dislocation channel structure of a 316 stainless steel irradiated by fast neutrons at low temperature to 0.78 dpa and tensile strained to 32%. (Byun et al., 2006)

simulate the formation of cleared bands based on interactions between dislocations lines and Frank loops (Gururaj et al., 2015). According to Sauzay et al. (2010), cleared bands can promote grain boundary crack initiation and propagation because of the interactions with grain boundaries. Even though the cleared bands have being widely studied, their fundamental mechanism is not well understood.

2.2 Mechanical effects of radiation damage on stainless steels

Neutron irradiation of stainless steels can lead to drastic modifications of mechanical properties, e.g., increase in yield stress, decrease in ductility (uniform elongation), decrease of strain hardening capacity and decrease of fracture toughness (Pawel et al., 1996; Pokor et al., 2004a; Pokor et al., 2004b). In this section, some effects relevant to ductile fracture of stainless steels are outlined.

2.2.1 Stress–strain relation in tension

Typical stress–strain curves are shown in fig. 2.10 for a solution annealed 304L stainless steels irradiated by neutrons up to 3.4 displacements per atom (dpa) (Pokor et al., 2004a). The behavior is dose dependent. For the unirradiated case (0 dpa),

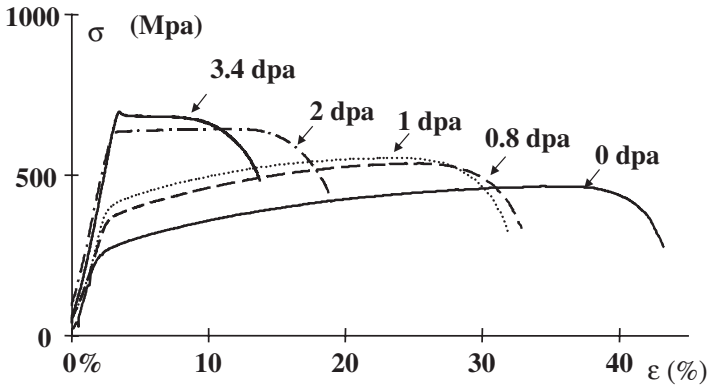

Figure 2.10: Stress-strain curves at $T_{\text{test}} = 330\,^{\circ}\text{C}$ for a solution annealed 304L stainless steels irradiated by neutrons up to 3.4 dpa. The irradiation was preformed in the OSIRIS reactor at about $T_{\text{irr}} = 330\,^{\circ}\text{C}$. (Pokor et al., 2004a)

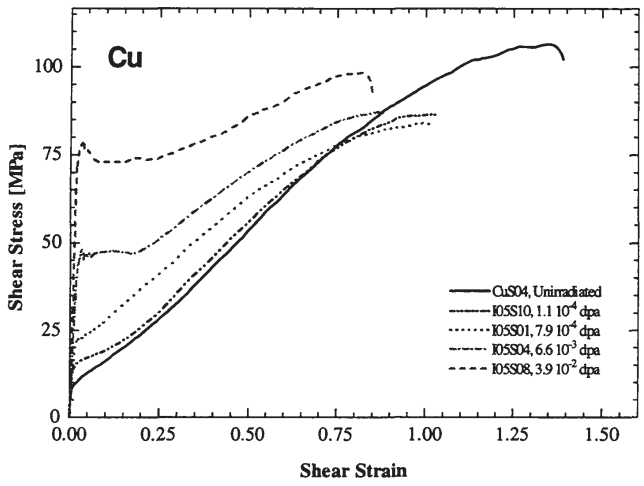

Figure 2.11: Tensile test of copper single crystals irradiated with 600 MeV protons to different doses: resolved shear stress vs. plastic slip. The tests are performed at about 22 °C and loading direction is [011]. (Dai, 1995)

a smooth elastic-plastic transition is observed followed by a plastic regime with small hardening rate before failure. After irradiation, a marked increase of the yield stress and a reduction of uniform elongation is observed. It is also important to notice that the hardening rate is also dose dependent. In addition, a sudden stress drop is observed after yield point at 3.4 dpa. This kind of stress drop, according to Trinkaus and his co-workers (Trinkaus et al., 1997a; Trinkaus et al., 1997b; Singh et al., 1997), is related to unpinning process of dislocations from radiation cascade induced Frank loops. After irradiation, a "cloud" of Frank loops decorating grown-in dislocations (which present already before irradiation) is often observed. The Frank loops play a role of trapping the dislocations and make them immobile.

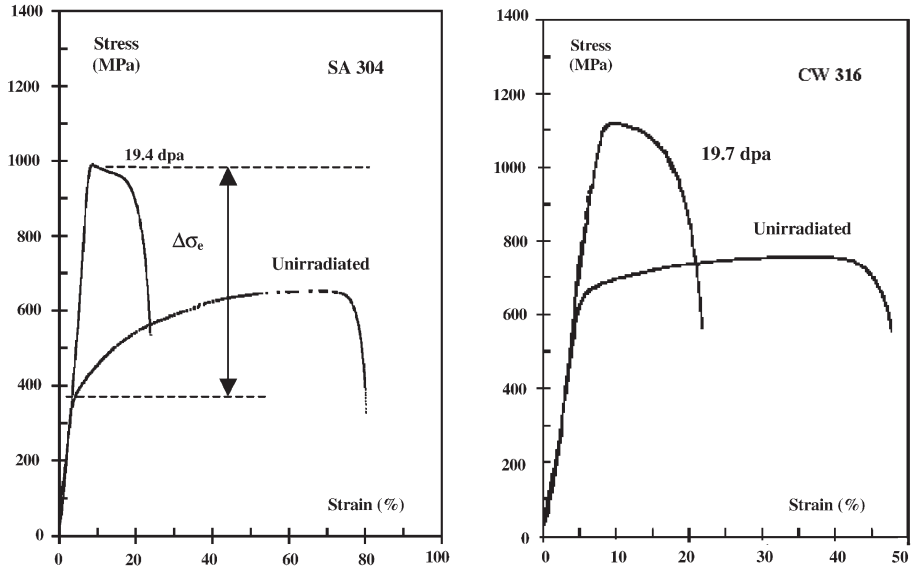

Figure 2.12: Engineering stress–strain curves for SA 304 and CW 316 steels irradiated at about 330 °C in the BOR-60 reactor. (Pokor et al., 2004b)

Frank loops and immobile dislocations cannot act as dislocation sources. The yield stress corresponds to the stress needed for unpinning grown-in dislocations from the Frank loops decorating them. Once the dislocations are unpinned, smaller stress is required for the plastic flow. It is worth noticing that the stress drop has also been observed in irradiated single crystals (Blewitt et al., 1960; Dai, 1995; Dai et al., 1994). An example is shown in fig. 2.11 for copper single crystals irradiated to 3.9×10^{-2} dpa. Compared with polycrystalline materials, a marked hardening regime was observed before final failure of single crystals.

The mechanical behavior of irradiated steels under tensile loading depends on many parameters, such as the properties of original materials, irradiation conditions, test conditions, etc. As an example, engineering stress–strain curves are presented in fig. 2.12 for solution annealed 304L stainless steels (SA 304) and cold worked 316 stainless steels (CW 316) irradiated to about 20 dpa (Pokor et al., 2004b). A marked difference between the two types of steels is that a stress drop is observed in SA 304 and not in CW 316.

2.2.2 Fracture mechanisms

Neutron irradiation generally causes a reduction in fracture toughness of stainless steels. The fracture toughness of irradiated stainless steels has been shown to be irradiation dose dependent (figs. 1.2 and 2.13) and swelling dependent (fig. 2.14). The decrease of fracture toughness in steels after irradiation is associated with a

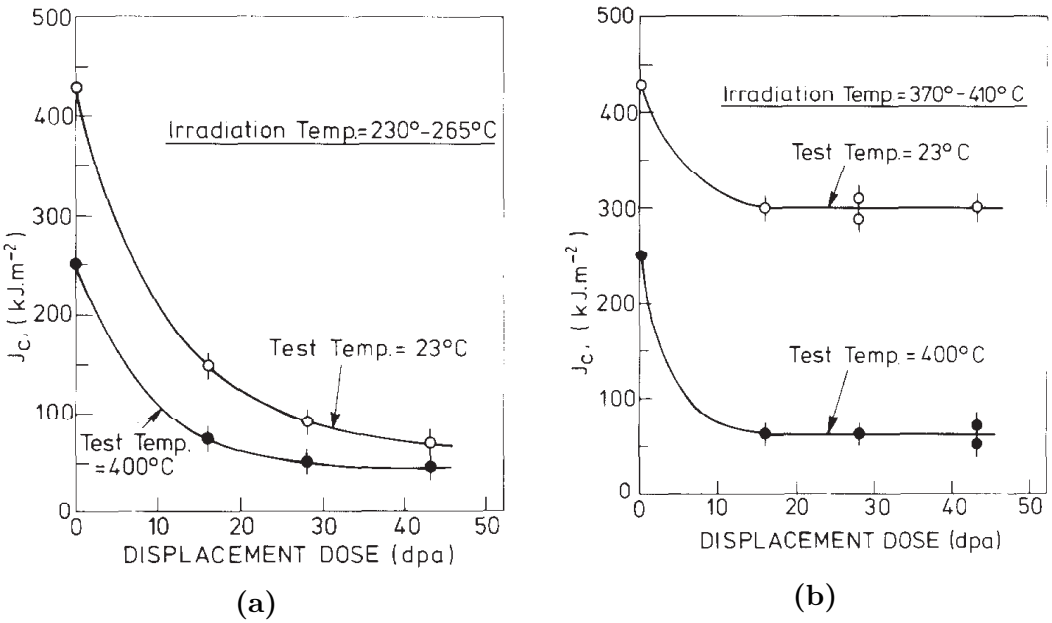

Figure 2.13: Dose dependence of dynamic J-integral calculated for impact tests on 321 austenitic stainless steels irradiated at (a) ~230 and (b) ~400 °C. (Little, 1986)

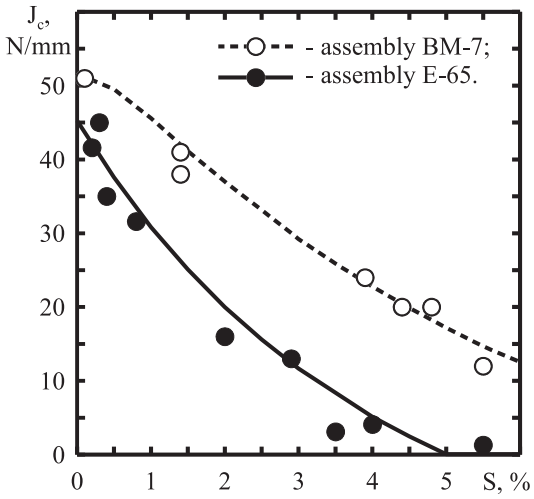

Figure 2.14: Decrease of fracture toughness measured in uniaxial tension tests for Fe-18Cr-10Ni-Ti stainless steels with irradiation swelling levels. DM-7: irradiation damage from 35 to 46 dpa; E-65: irradiation damage from 100 to 150 dpa. (Margolin et al., 2016)

change of fracture mechanism, depending on various parameters: original properties of steels, irradiation conditions, test conditions, etc. A transition from ductile to brittle fracture with increasing irradiation damage is usually observed in irradiated stainless steels.

Fukuya et al. (2008) have conducted a systematic study on fracture modes in CW 316 stainless steels (cut from flux thimble tubes) irradiated up to 73 dpa in a

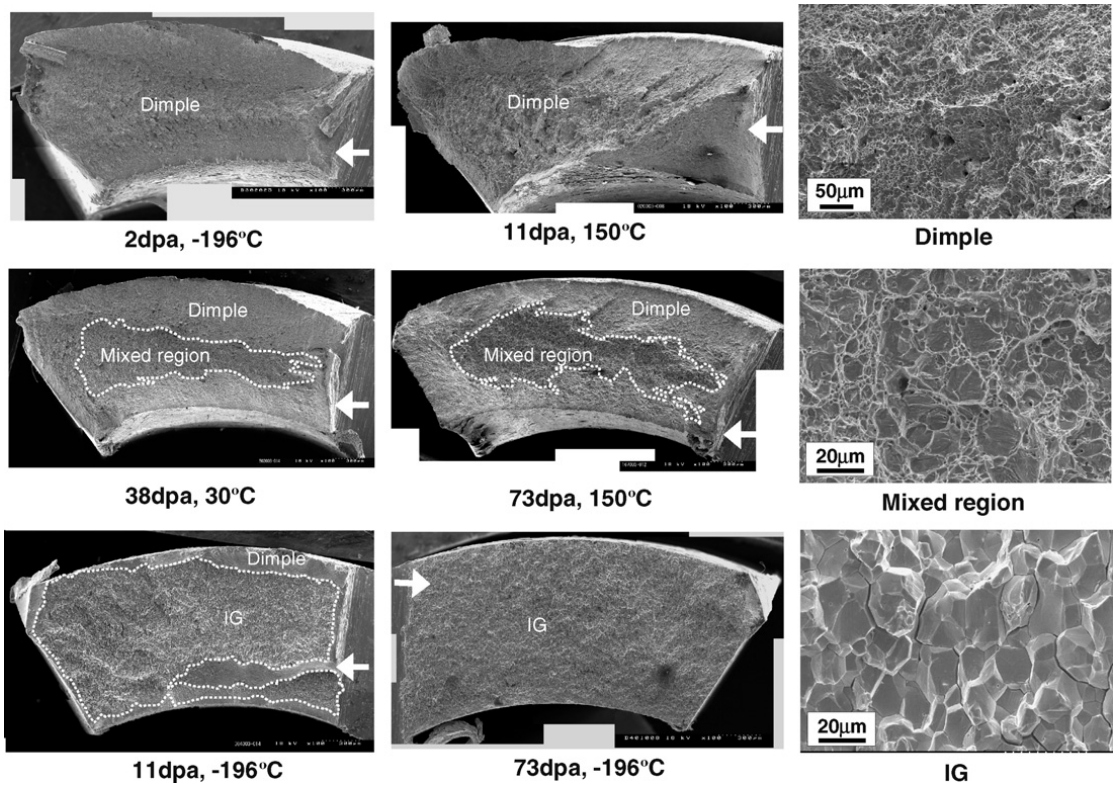

Figure 2.15: Typical fracture surface of CW 316 steels irradiated to different doses after impact tests at different at different test temperature. (Fukuya et al., 2008)

pressurized water reactor ($T_{\text{irr}} = 293$–$323\,^{\circ}\text{C}$). They showed by means of impact tests that intergranular fracture and dimple fracture occur according to irradiation dose and test temperature. Some typical fracture surfaces are presented in fig. 2.15. A transition from intergranular to dimple fracture is observed with temperature increasing from -196 to 150 °C and irradiation dose decreasing from 73 to 2 dpa (see fig. 2.16). The authors also conducted tensile tests with two strain rates (conventional: $1.1 \times 10^{-4}\,\text{s}^{-1}$ and slow: $6.7 \times 10^{-8}\,\text{s}^{-1}$). According to the tensile tests results combined with other results in the literature, the authors concluded that intergranular fracture is promoted under low-temperature high-strain-rate and high-temperature low-strain-rate conditions. However, it is important to note that dimple (ductile) fracture remains one dominant fracture mechanism at high temperature in these steels irradiated up to 38 dpa, i.e., $T_{\text{test}} = 150\,^{\circ}\text{C}$ in impact tests and $T_{\text{test}} = 320\,^{\circ}\text{C}$ in tensile tests.

Dimple fracture has been observed in other studies on stainless steels, especially those irradiated in fast neutron reactors. Solution treated Type 321 austenitic stainless steels irradiated in Dounreay Fast Reactor at about 230 and 400 °C up to 43 dpa were investigated by Little (1986) through impact tests. Fracture toughness evaluated by the dynamic J-integral was found to decrease with irradiation dose

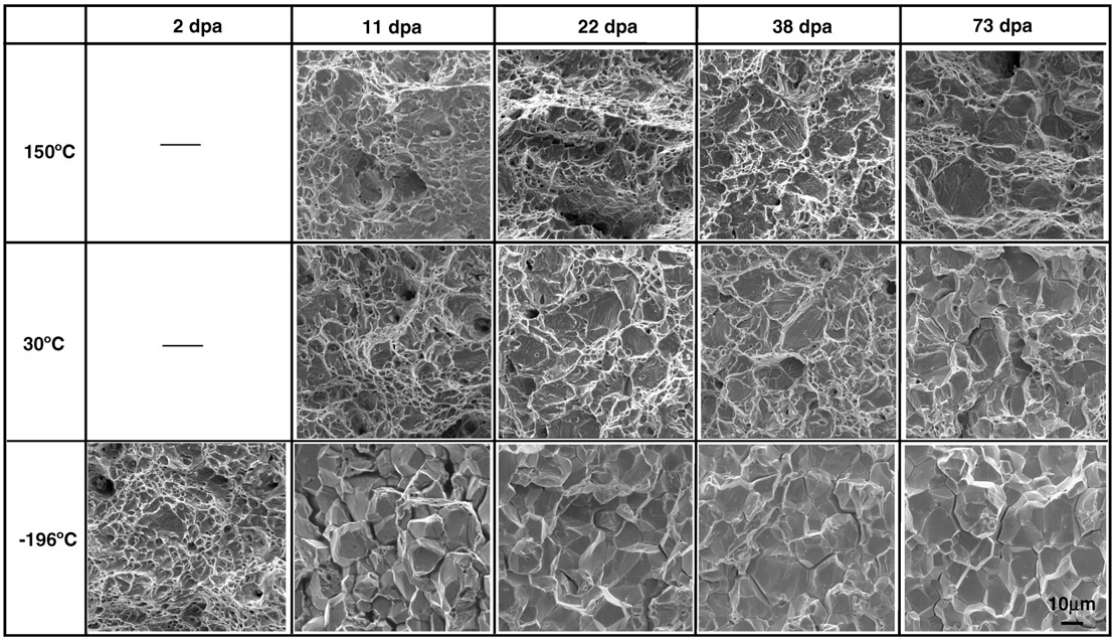

Figure 2.16: SEM micrographs showing the center of fracture surfaces of CW 316 steels irradiated to different doses after impact tests at different test temperature. (Fukuya et al., 2008)

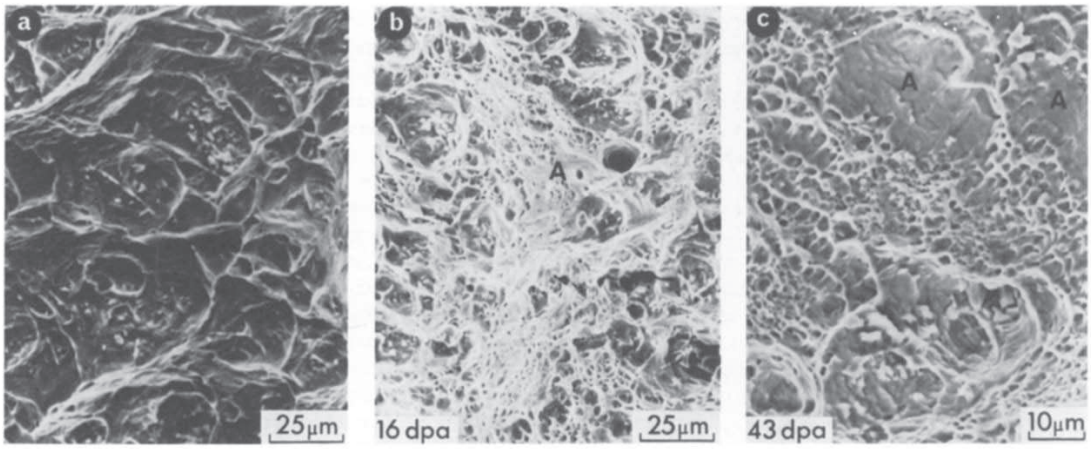

Figure 2.17: SEM micrographs of fracture surfaces after impact tests at 400 °C: (a) unirradiated; (b) irradiated to 16 dpa at 400 °C ; (c) irradiated to 43 dpa at 230 °C. (Little, 1986)

and finally reach a stabilized value (see fig. 2.13). The author found that the ductile fracture due to void growth and coalescence was the primary fracture mechanism after irradiation and that the ductile dimples were much finer (see fig. 2.17), initiating from irradiation-induced micro-sized TiC precipitates. Neustroev and Garner (2009) investigated fracture behavior of a titanium-stabilized stainless steel cut from fuel pin claddings and fuel assembly wrappers of the fast reactor BOR-60. The authors reported a transgranular cup-cone fracture morphology for tensile specimens

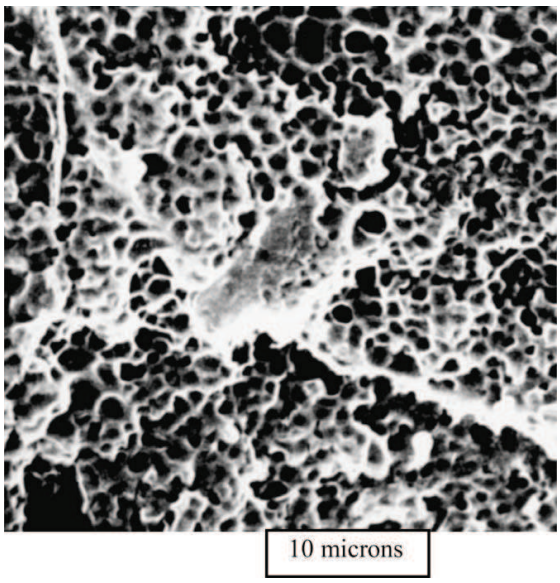

Figure 2.18: Fracture surface with micro-sized dimples of Fe-18Cr-10Ni-Ti stainless steels with a swelling level of 30%. (Neustroev and Garner, 2009)

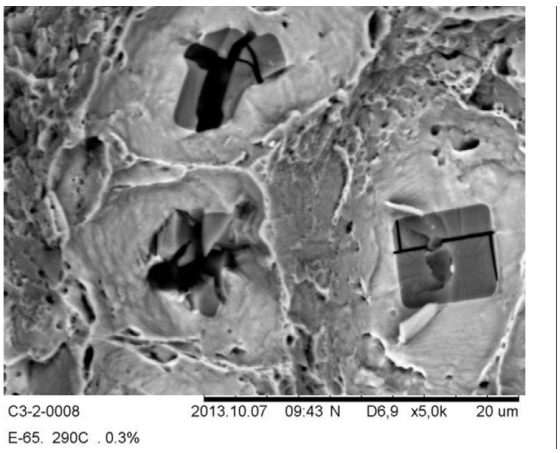

Figure 2.19: Classical dimple fracture surface with voids nucleated on Ti carbonitrides of stainless steels irradiated to 90 dpa with 0.3% swelling. (Margolin et al., 2016)

extracted from assembly wrappers with high swelling (30%). The fracture surface exhibited fine dimples which imply that failure proceeded by micropore coalescence (see fig. 2.18). They emphasized the large amount of local deformation at the failure site, despite the highly reduced elongation at the macroscopic level. Margolin et al. (2016) studied fracture mechanisms under uniaxial tension in titanium-stabilized austenitic steels taken from shield assemblies of BOR-60 reactor. The authors observed dimple fracture with voids of size 2–10 µm (fig. 2.19) nucleated from Ti carbonitrides for limited swelling cases (swelling $< 2\%$ and irradiation damage up to 80–150 dpa). For relatively high swelling level (5–6%), flat facets (zone 2 in fig. 2.20a) together with unstructured zones (zone 1 in fig. 2.20a) were observed

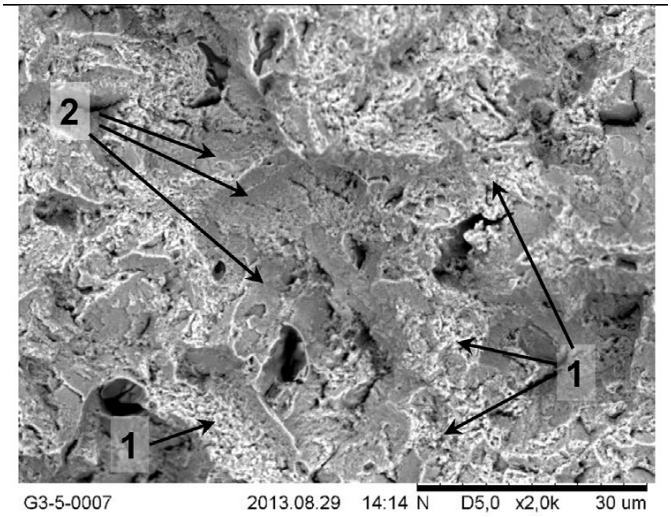

(a)

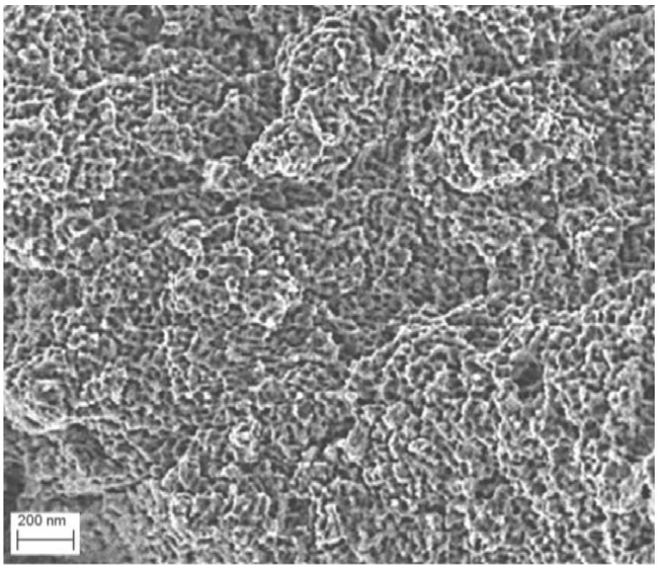

(b)

Figure 2.20: (a) Fracture surface with unstructured zones (Zone 1) and flat facets (Zone 2) of stainless steels irradiated to 130 dpa with 3% swelling; (b) enlarged micrograph showing nano-dimples on the unstructured zone. (Margolin et al., 2016)

on fracture surfaces. The fracture mode leading to flat facets is called channel fracture, which is believed to be associated with cleared bands (see more details in section 2.1.3). On the so-called unstructured zones, nano-sized voids (about 20 nm) were found, which grow, coalesce and lead to final failure (fig. 2.20b). The authors reported a specific fracture mode transition with increasing swelling level: classical dimple fracture → flat facets → nano-dimple fracture.

Ductile fracture due to void growth and coalescence (see section 2.3) is a dominant fracture mechanism in unirradiated stainless steels. According to the

experimental studies presented above, this type of fracture mechanism has been also observed in irradiated stainless steels, however, with a decrease in dimple size with irradiation. These observations motivate the present thesis work.

2.3 Ductile fracture in metallic materials

Ductile fracture refers to fracture modes involving extensive plastic deformation before final failure and is widely observed in failure of metallic materials (Pineau and Pardoen, 2007; Besson, 2010; Benzerga and Leblond, 2010; Pineau et al., 2016). Ductile fracture is also exhibited by irradiated stainless steels, as presented in section 2.2.2. Since cavities are extensively involved in the fracture processes of irradiated stainless steels, some classical mechanisms in metals and alloys associated with cavities are to be presented in the following.

2.3.1 Experimental observations and micromechanisms

Void nucleation, growth and coalescence are important mechanisms of ductile fracture in metals and alloys. An example of the observations in the literature is presented in fig. 2.21 showing the failure process from void formation to final cracking. Some dimple characteristics are often observed on fracture surface, as shown in

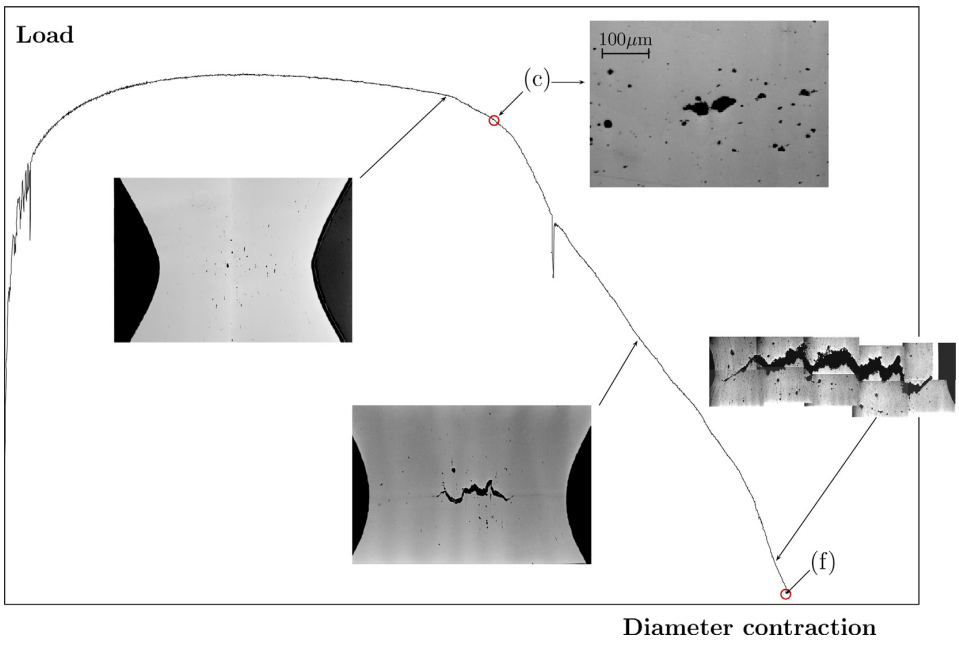

Figure 2.21: Ductile fracture process: transition from void formation to cracking in a notched bar of steel. (see Benzerga (2000) and Benzerga et al. (2004), also Pineau et al. (2016))

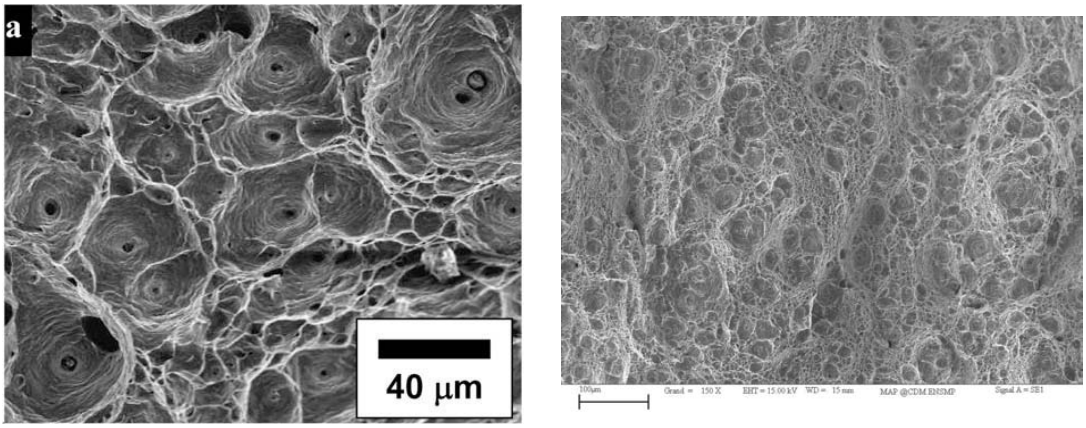

Figure 2.22: Typical dimple fracture surface: (a) tensile test at 285 °C on 304LN stainless steels (Das and Tarafder, 2009); (b) tensile test on a pipeline steel X100 (Luu, 2006).

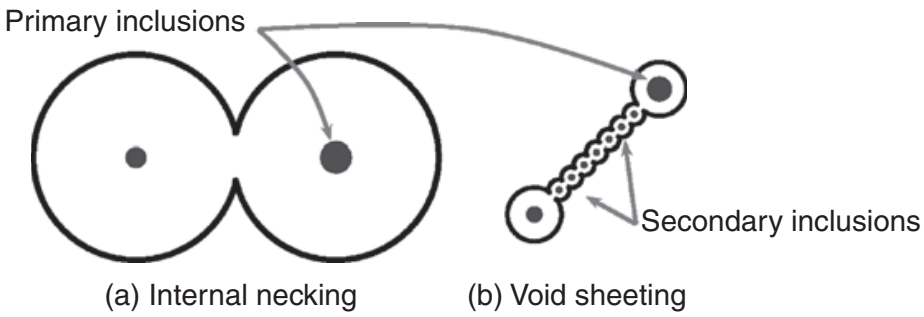

Figure 2.23: Ductile fracture micromechanisms: (a) internal necking; (b) void sheeting. (Besson, 2010)

fig. 2.22a. The presence of dimples is usually used to rationalize fracture induced by void growth and coalescence. Dimples are usually formed by void nucleation at second-phase particles or inclusions, followed by subsequent growth and coalescence. According to experimental observations, different micromechanisms are proposed (Besson, 2010). A first micromechanism is called "internal necking" (fig. 2.23). It corresponds to formation of large primary voids at high stress triaxiality, growth of voids, and necking of inter-void ligaments of neighbouring voids. In this case, failure occurs with little or no smaller secondary voids nucleation. An example of this mechanism is shown in fig. 2.22a. Recently, this mechanism was visualized by X-ray tomography in high-purity copper with artificial holes (fig. 2.24). A second micromechanism, named "void sheeting", refers to failure with secondary voids (smaller than primary ones) nucleated in strain localization bands as shown in fig. 2.23. An example of this mechanism involving two populations of voids are shown in fig. 2.22b. In this case, primary voids remain small due to low stress triaxiality.

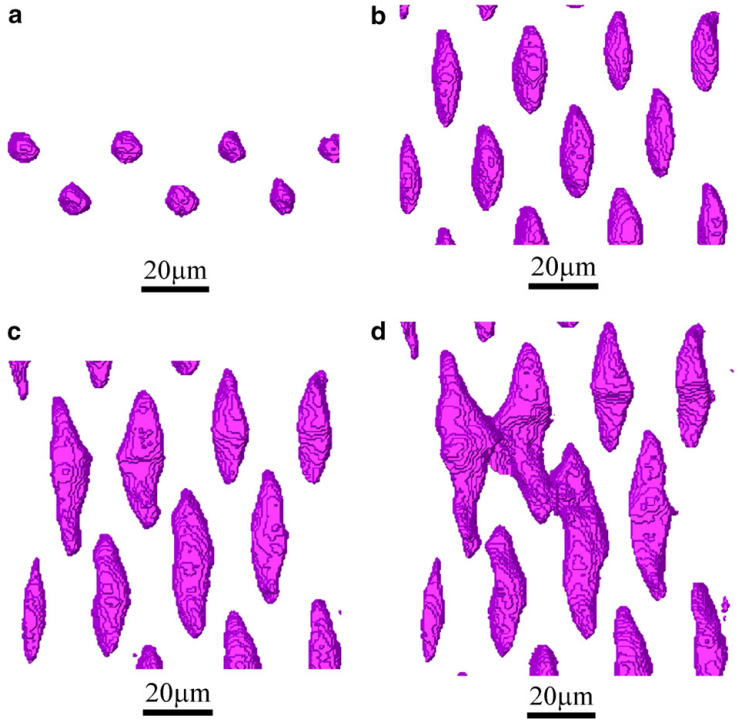

Figure 2.24: X-ray tomography showing internal necking in high-purity copper with artificial holes. (Weck et al., 2008)

2.3.2 Models for porous isotropic materials and single crystals

Numerous studies have being devoted to the modeling of mechanical behavior of elasto-(visco-)plastic media containing voids. After a pioneering work of McClintock (1968), Rice and Tracey (1969) treated the enlargement of a spherical void under remotely uniform stress in a rigid perfectly plastic von Mises material. For high stress triaxiality case, the increase rate of void radius R under a simple tension remote field writes:

$$\frac{\dot{R}}{R} = 0.283 \exp\left(\frac{3}{2}\frac{\sigma_m^\infty}{\sigma_{eq}^\infty}\right)\dot{p}^\infty, \tag{2.1}$$

with the remote von Mises equivalent stress σ_{eq}^∞, the remote mean stress σ_m^∞, the remote accumulated strain rate $\dot{p}^\infty = \sqrt{\frac{2}{3}\underset{\sim}{\dot{\varepsilon}}^\infty : \underset{\sim}{\dot{\varepsilon}}^\infty}$. The result reveals the influence of stress triaxiality, i.e., $T = \frac{\sigma_m^\infty}{\sigma_{eq}^\infty}$, on void growth rate.

Another seminal work concerning voided isotropic material was conducted by Gurson (1977). The author performed limit analysis on a rigid perfectly plastic von Mises matrix containing a void and an effective yield function accounting for void volume fraction f was derived:

$$\frac{\sigma_{eq}^2}{\sigma_0^2} + 2f\cosh\left(\frac{3}{2}\frac{\sigma_m}{\sigma_0}\right) - 1 - f^2 = 0, \tag{2.2}$$

where σ_0 is the tensile yield stress of the von Mises matrix and f is the void volume fraction. One can further formulate a porous plasticity framework combining the yield function with the normality rule and the evolution law of void volume fraction f based on mass conservation $\dot{f} = (1-f)\,\mathrm{tr}\,\dot{\underset{\sim}{\varepsilon}}^p$, where $\dot{\underset{\sim}{\varepsilon}}^p$ is plastic strain rate. This model was then extended by Tvergaard and Needleman (Tvergaard, 1982; Tvergaard and Needleman, 1984), called GTN model in the literature, to better represent unit cell simulations and experimental results. The Gurson model has also been extended for introducing void shape effects (Gologanu et al., 1993; Gologanu et al., 1994) and matrix anisotropy (Benzerga and Besson, 2001). The same approach has also been used for a matrix obeying other yield criteria such as Tresca criterion (Cazacu et al., 2014) and Mohr–Coulomb criterion (Anoukou et al., 2016) among others. Besides, other extensions of the Gurson model and other approaches for porous materials can be found in recent reviews of Besson (2010), Benzerga and Leblond (2010), Pineau et al. (2016), and Benzerga et al. (2016).

In the past few years, an increasing number of studies have been devoted to the development of models accounting for void growth in a single crystal matrix. A first yield function derived by Han et al. (2013) based on the variational homogenisation approach of DeBotton and Castaneda (1995) is written as:

$$\left(\frac{\tau^{s2}}{{\tau_0}^2} + \alpha\frac{2}{45}f\frac{\sigma_{eq}^2}{{\tau_0}^2}\right) + 2q_1 f\cosh\left\{q_2\sqrt{\frac{3}{20}}\frac{\sigma_m}{\tau_0}\right\} - 1 - q_1^2 f^2 = 0,\ s = 1, 2, \cdots, N \quad (2.3)$$

where N is the number of slip systems, τ^s is the resolved shear stress for slip system s, τ_0 is the critical resolved shear stress, and α, q_1 and q_2 are heuristic parameters (as in the GTN model for q_1 and q_2). The three parameters were identified by comparison with yield surfaces predicted by unit cell simulations for different crystal orientations and void volume fractions: $\alpha = 6.456$, $q_1 = 1.471$ and $q_2 = 1.325$. Note that the obtained value of q_1 close to 1.5 is in good agreement with the value for GTN model obtained in the literature (see Faleskog et al., 1998; Gao et al., 1998). The model is able to accurately represent the numerical limit analysis results.

Then, another model was developed by Paux et al., 2015 based on the approach of limit analysis using a regularised form of the Schmid law (Arminjon, 1991; Gambin, 1992). The yield function writes

$$\left(\frac{\left(\sum_{s=1}^{N}|\tau^s|^n\right)^{1/n}}{\tau_0}\right) + 2qf\cosh\left(\kappa'\frac{\sigma_m}{\tau_0}\right) - 1 - (qf)^2 = 0, \quad (2.4)$$

where q is a heuristic parameter and $\kappa' = 0.506$ is derived semi-analytically. Notice that $\kappa' = q_2\sqrt{\frac{3}{20}} \approx 0.513$ is obtained in Eq. (2.3) with $q_2 = 1.325$. The two yield

functions Eqs. (2.3) and (2.4) share some similarities. However, Eq. (2.3) is a multi-criterion yield function, while Eq. (2.4) is a single criterion yield function.

More recently, a more complex model accounting for void shape effects was developed by Mbiakop and his co-workers (Mbiakop et al., 2015a; Mbiakop et al., 2015b) following the variational method of Danas and Aravas (2012). The model was first derived for elliptical voids in two-dimensional case and it was then extended to three-dimensional case for ellipsoidal voids. The proposed model is expressed in the form of the effective stress potential $\widetilde{U}$ which is related to the effective strain rate tensor $\overline{\underset{\sim}{\boldsymbol{D}}}$ by

$$\overline{\underset{\sim}{\boldsymbol{D}}} = \frac{\partial \widetilde{U}}{\partial \overline{\underset{\sim}{\boldsymbol{\sigma}}}}, \tag{2.5}$$

where $\overline{\underset{\sim}{\boldsymbol{\sigma}}}$ is the average Cauchy stress of the porous medium. With n denoting the parameter of power law and $\dot{\gamma}_0^s$ the reference slip rate, $\widetilde{U}$ for single crystals with ellipsoidal voids is given by

$$\widetilde{U} = (1-f)\sum_{s=1}^{N} \frac{\dot{\gamma}_0^s (\tau_0^s)^{-n}}{n+1} \left(\overline{\underset{\sim}{\boldsymbol{\sigma}}} : \hat{\underset{\approx}{\boldsymbol{S}}}^{(\mathrm{mvar}),s} : \overline{\underset{\sim}{\boldsymbol{\sigma}}} \right)^{(n+1)/2}, \tag{2.6}$$

where

$$\hat{\underset{\approx}{\boldsymbol{S}}}^{(\mathrm{mvar}),s} = \hat{\underset{\approx}{\boldsymbol{S}}}^{(\mathrm{var}),s} + (q_J^2 - 1)\underset{\approx}{\boldsymbol{J}} : \hat{\underset{\approx}{\boldsymbol{S}}}^{(\mathrm{var}),s} : \underset{\approx}{\boldsymbol{J}}, \tag{2.7}$$

and

$$q_J = \sqrt{\frac{15}{f}} \left\{ \frac{(1-f)(\beta_n)^{1/n}}{n(f^{-1/n}-1)} \right\}^{n/(n+1)} \text{ with } \beta_n = \frac{4}{25} 6^{-n/2}. \tag{2.8}$$

Here,

$$\hat{\underset{\approx}{\boldsymbol{S}}}^{(\mathrm{var}),s} = \frac{1}{2}\underset{\approx}{\boldsymbol{E}}^s + \frac{f}{N}\hat{\underset{\approx}{\boldsymbol{S}}}^*, \ \underset{\approx}{\boldsymbol{E}}^s = 2\underset{\sim}{\boldsymbol{N}}^s_{\mathrm{sym}} \otimes \underset{\sim}{\boldsymbol{N}}^s_{\mathrm{sym}}, \ J_{ijkl} = \frac{1}{3}\delta_{ij}\delta_{kl}, \tag{2.9}$$

where $\underset{\sim}{\boldsymbol{N}}^s_{\mathrm{sym}}$ is the symmetric Schmid tensor for slip system s, δ_{ij} is the Kronecker delta, and $\hat{\underset{\approx}{\boldsymbol{S}}}^*$ is a fourth order microstructural tensor given by

$$\hat{\underset{\approx}{\boldsymbol{S}}}^* = \hat{\underset{\approx}{\boldsymbol{Q}}}^{-1} - \sum_{s=1}^{N} \frac{1}{2}\underset{\sim}{\boldsymbol{E}}^s, \ \hat{\underset{\approx}{\boldsymbol{Q}}} = \lim_{\hat{\rho}\to\infty} \lim_{\hat{\kappa}\to\infty} [\underset{\approx}{\boldsymbol{S}}_0{}^{-1} - \underset{\approx}{\boldsymbol{S}}_0{}^{-1} \hat{\underset{\sim}{\boldsymbol{P}}} \underset{\approx}{\boldsymbol{S}}_0{}^{-1}] \tag{2.10}$$

with

$$\underset{\approx}{\boldsymbol{S}}_0 = \sum_{s=1}^{N} \frac{1}{2}\underset{\approx}{\boldsymbol{E}}^s + \frac{1}{2\hat{\rho}} \sum \underset{\approx}{\boldsymbol{F}}^s + \frac{1}{3\hat{\kappa}}\underset{\approx}{\boldsymbol{J}}, \ \underset{\approx}{\boldsymbol{F}}^s = \underset{\approx}{\boldsymbol{K}} - \underset{\approx}{\boldsymbol{E}}^s, \tag{2.11}$$

where $\underset{\approx}{\boldsymbol{K}}$ and $\underset{\approx}{\boldsymbol{J}}$ are the fourth order shear and hydrostatic projection tensors. $\hat{\underset{\sim}{\boldsymbol{P}}}$ is given by

$$\hat{\underset{\sim}{\boldsymbol{P}}} = \frac{1}{4\pi \det\left(\underset{\approx}{\boldsymbol{Z}}\right)} \int_{|\underline{\boldsymbol{\xi}}|=1} \frac{(S^{-1}_{iakb}\xi_a\xi_b)^{-1}\xi_j\xi_l|_{(ij)(kl)}}{\underset{\approx}{\boldsymbol{Z}}^{-1}.\underline{\boldsymbol{\xi}}}\, dS. \tag{2.12}$$

The brackets $(ij)(kl)$ denote symmetrization with respect to the corresponding indices, $\underline{\boldsymbol{\xi}}$ is a unit three-dimensional vector and $\underset{\approx}{\boldsymbol{Z}}$ is a second order tensor describing the shape and orientation of the voids, i.e.,

$$\underset{\approx}{\boldsymbol{Z}} = w_1 \underline{\boldsymbol{n}}^1 \otimes \underline{\boldsymbol{n}}^1 + w_2 \underline{\boldsymbol{n}}^2 \otimes \underline{\boldsymbol{n}}^2 + \underline{\boldsymbol{n}}^3 \otimes \underline{\boldsymbol{n}}^3, \tag{2.13}$$

where w_1 and w_2 are two aspect ratios of the ellipsoidal void and the vectors $\underline{\boldsymbol{n}}^i$ $(i = 1, 2, 3)$ define an orthonormal basis set, which coincides with the principal axes of the ellipsoidal void.

However, to the authors' knowledge, there is currently no model for porous single crystals at finite strains, which is able to describe the void evolution up to coalescence and which is simple enough for finite element implementation in order to carry out structural computations.

2.4 Plasticity size effects in metallic materials

2.4.1 Experimental observations

Size effects in plasticity have attracted intensive attention since the 1990s. Size dependent plastic behaviors of metals and alloys were observed in various experiments. Fleck et al. (1994) performed torsion tests on commercially pure, cold drawn copper wires of diameter in the range 12 to 170 µm. The authors reported a strong dependence of torsional response on diameter. Size effect was also observed in indentation tests (see Stelmashenko et al., 1993; Poole et al., 1996; McElhaney et al., 1998; Suresh et al., 1999). For example, McElhaney et al. (1998) (see also Nix and Gao, 1998) reported an indentation depth dependence of the hardness measured by nanoindentation test for polycrystalline and single crystal copper shown in fig. 2.25. Stölken and Evans (1998) performed microbending tests on high-purity nickel foils of thickness in the range 12.5 to 50 µm. The authors showed a size dependent bending response on foil thickness (fig. 2.26).

Those size effects are usually explained by strengthening of materials by strain gradient (Fleck et al., 1994). Strong strain gradient is also expected in the plastic zone at the tip of a crack and in the plastic deformation of polycrystals at the grain boundary because of the mismatch of slip between grains. Therefore, size effects are also observed in these cases (see, e.g., Wei and Hutchinson, 1997; Smyshlyaev and Fleck, 1996, and references therein). Strain gradients result in the storage of geometrically necessary dislocations (GND) (Ashby, 1970), which is regarded as the physical foundation of the size effect. This will be presented in the next section.

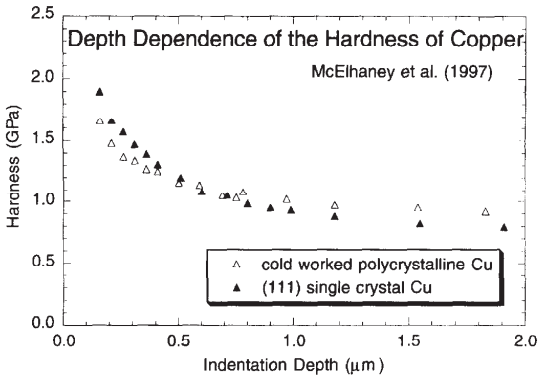

Figure 2.25: Indentation depth dependence of the hardness measured by nanoindentation of single crystal copper and cold worked polycrystalline copper. (McElhaney et al., 1998)

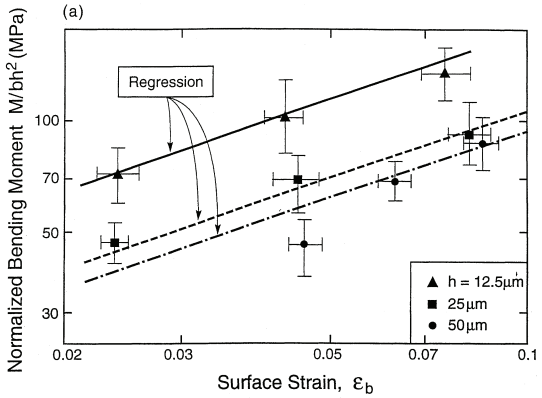

Figure 2.26: Plot of the normalized bend moment against the surface strain for different thickness of foils of nickel. (Stölken and Evans, 1998)

More recently, size effects were also reported in the absence of strain gradients (see, e.g., Uchic et al. (2004), Dimiduk et al. (2005), and Greer et al. (2005)), such as in uniaxial compression of micro/nano-pillar specimens. Some other candidate mechanisms for plasticity size effects were proposed such as dislocation starvation (Greer et al., 2005), stochastics of dislocation source lengths (Parthasarathy et al., 2007), etc. These mechanisms are not considered in the present work.

2.4.2 Geometrically necessary dislocations and strain gradient plasticity

Size effects in plasticity are often associated with strain gradients which physically require the storage of GNDs for compatibility reasons (Ashby, 1970). In contrast to GND, statistically-stored dislocations are responsible for uniform plastic deformation. A well-known illustration of GND, proposed by Fleck et al. (1994), concerns non-uniform shear of a single crystal beam (fig. 2.27). For a single crystal with a single

slip system with normal to the slip plane aligned with the x_2 and slip direction aligned with the x_1 direction, it is shown that a gradient of plastic slip along the x_1 direction causes a density ρ_G of GNDs to be stored.

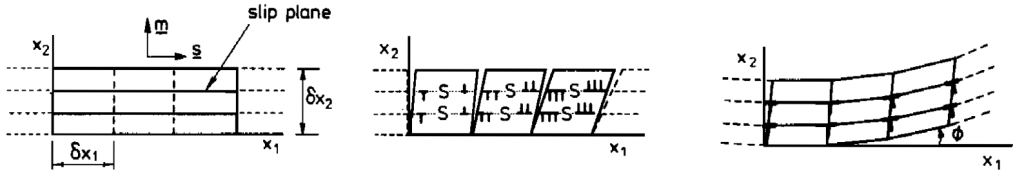

Figure 2.27: Sketch for non-uniform shear of a single crystal beam showing a gradient of plastic slip along the x_1 direction causes a density ρ_G of GNDs to be stored. (Fleck et al., 1994)

However, classical continuum mechanics fails to predict the size effect for lack of length scale in the theory. Thus, tremendous efforts have been devoted to enhance the theory by different approaches. A well-known approach to do so is to include strain gradient hardening. By this way, the so-called "strain gradient plasticity" models were first proposed for isotropic materials.

One candidate idea of modeling (Fleck and Hutchinson, 2001; Gudmundson, 2004; Gurtin and Anand, 2009) is assuming that the plastic internal work increment δw^p in a volume V follows the form:

$$\delta w^p = \int_V s\delta p + \underline{\boldsymbol{m}} \,.\delta \boldsymbol{\nabla} p \, dV, \tag{2.14}$$

where p is the effective plastic strain (also called "accumulated plastic strain") with its rate $\dot{p} = \sqrt{\frac{2}{3}\dot{\underset{\sim}{\varepsilon}}^p : \dot{\underset{\sim}{\varepsilon}}^p}$, and $\boldsymbol{\nabla} p$ is the gradient of p, s and $\underline{\boldsymbol{m}}$ are generalized stresses which are work-conjugate respectively to p and $\boldsymbol{\nabla} p$. Another important point of the models is assuming a constitutive dependence on the generalized effective plastic strain rate $\dot{E}_p$ (Fleck and Hutchinson, 2001) which is defined as

$$\dot{E}_p^2 = \dot{p}^2 + l_*^2 \boldsymbol{\nabla}\dot{p}.\boldsymbol{\nabla}\dot{p} \tag{2.15}$$

with the length parameter l_*^2.

Another candidate way to include strain gradient hardening is to account for the gradient of the total plastic strain tensor $\underset{\sim}{\boldsymbol{\varepsilon}}^p$. Thus, the plastic internal work increment in a volume V writes

$$\delta w^p = \int_V \underset{\sim}{\boldsymbol{s}} : \delta \underset{\sim}{\boldsymbol{\varepsilon}}^p + \underset{\approx}{\boldsymbol{m}} \vdots \delta \boldsymbol{\nabla} \underset{\sim}{\boldsymbol{\varepsilon}}^p \, dV, \tag{2.16}$$

where the generalized stresses $\underset{\sim}{\boldsymbol{s}}$ and $\underset{\approx}{\boldsymbol{m}}$ are respectively a second order and third order tensor. Note that, up to now, there is no common agreement on the formulation

of the theories. Detailed discussions on the formulation of strain gradient plasticity can be found in the works of Forest and Sievert (2003), Gudmundson (2004), Forest (2009), and Gurtin and Anand (2009).

In addition to the models for isotropic plastic materials, strain gradient plasticity models were also proposed for single crystals. They can be classified into three categories. The first category is based on the notion of dislocation density tensor $\underset{\sim}{\boldsymbol{\alpha}}$ (Nye, 1953) which is defined as

$$\underset{\sim}{\boldsymbol{\alpha}} = -\mathrm{curl}\,\underset{\sim}{\boldsymbol{E}}^{-1} = -\frac{1}{J}(\mathrm{Curl}\,\underset{\sim}{\boldsymbol{P}}).\underset{\sim}{\boldsymbol{F}}^{T}, \tag{2.17}$$

where $\underset{\sim}{\boldsymbol{F}}$ is the deformation gradient, $\underset{\sim}{\boldsymbol{E}}$ and $\underset{\sim}{\boldsymbol{P}}$ are its elastic and plastic part resulting from the multiplicative decomposition $\underset{\sim}{\boldsymbol{F}} = \underset{\sim}{\boldsymbol{E}}.\underset{\sim}{\boldsymbol{P}}$ (Lee, 1969; Mandel, 1973), J is the determinant of $\underset{\sim}{\boldsymbol{F}}$.[1] The microcurl model introduced by Cordero and his co-workers (Cordero et al., 2010) and that proposed by Gurtin and his co-workers (Gurtin, 2002) belong to this category. Both of them assume a free energy dependence on $\underset{\sim}{\boldsymbol{\alpha}}$. However, the microcurl model involves directly $\underset{\sim}{\boldsymbol{\alpha}}$ in the power of internal forces, while the Gurtin model relates $\underset{\sim}{\boldsymbol{\alpha}}$ to the scalar dislocation densities and thus $\underset{\sim}{\boldsymbol{\alpha}}$ does not appear explicitly in the derivation of balance equations. The second category is based on the scalar dislocation densities defined on crystallographic slip systems. Statistically stored dislocations (SSD) and geometrically necessary dislocations (GND) are often taken into account in the models of the second category. Various models of this category can be found in the literature, such as Evers et al. (2004), Bayley et al. (2006), Bayley et al. (2007), Ekh et al. (2007), Kuroda and Tvergaard (2008), Ertürk et al. (2009), and Bargmann et al. (2010), among others. An unified formulation of the models is proposed by Svendsen and Bargmann (2010). A third category corresponds to the enhancement of classical crystal plasticity model with the gradient of a single scalar plastic slip variable, which was firstly proposed in the work of Wulfinghoff and Böhlke (2012).

Numerical implementation of the models for single crystal plasticity is of great challenge especially for finite strain formulation, partly due to the complexity of the models. The number of additional degrees of freedom (DOF) besides displacement for finite element implementation is shown in table 2.1 for some models. Note that, for the model of Evers et al. (2004), 12 edge and 6 screw dislocations are taken into account for the densities GND. Thus, 18 additional DOFs are needed. It can be seen that many additional DOFs are needed for FE implementation. This usually leads to bad computational convergence or high computation time. Therefore, the numerical

[1] The curl operator is also denoted by $\nabla\times$ or rot .

Models	Additional DOFs	Number of additional DOFs
(Gurtin, 2002)	γ^s	12
(Cordero et al., 2010)	curl $\underset{\sim}{\boldsymbol{P}}$	9
(Evers et al., 2004)	ρ_{GND}	18
(Wulfinghoff and Böhlke, 2012)	γ_{cum} or γ_{eq}	1

Table 2.1: Degrees of freedom needed for FE implementation of some strain gradient crystal plasticity in the case of FCC single crystals (12 slip systems). Additional DOFs besides displacements are pointed out.

implementation is usually restricted to small strain formulation or finite strain formulation with planar double slip. However, the numerical efficiency of the model with a single additional DOF has been shown by Wulfinghoff and Böhlke (2012).

In addition, it is worth noticing that Miehe and his co-workers (Miehe, 2014; Miehe et al., 2014b; Miehe et al., 2014a) proposed a variational formulation for strain gradient plasticity models at finite strains and showed its numerical efficiency through 3D simulations.

2.5 Size effects on void growth

2.5.1 Experimental observations

Size effects are expected in the plastically driven void growth, when void dimensions are of the same order as the spacing between mobile dislocations and dislocations sources. Even though it lacks of direct evidence, some indications have been shown by recent experiments that the growth of voids is size dependent. Khraishi et al. (2001) studied the growth of a machined cylindrical hole in a thin plate made of a superplastically deforming metal. For the hole diameters considered (203, 243 and 635 μm), it was shown that void growth rate was higher for a bigger hole. In these experiments, the size of the plates was kept unchanged. Thus, the porosity, which is generally believed to affect void growth, changed with increasing hole diameter. However, as the diameter of the hole was far smaller than the width of the plate (6.35 mm), the influence of the porosity was negligible.

Even though few experimental investigations have been devoted to size effects on void growth and coalescence, discrete dislocations dynamics (DDD) and molecular dynamics (MD) have offered a great deal of details about void growth at micro- and nano-scale. However, in these studies, high strain rate loading conditions are often considered.

2.5.2 MD and DDD simulations

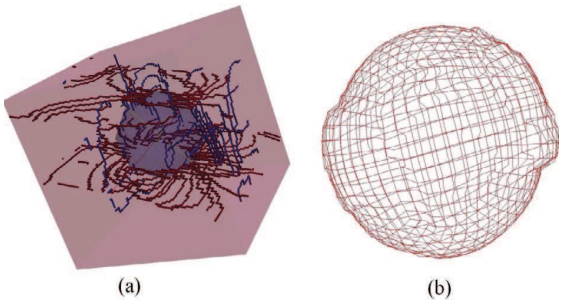

Figure 2.28: (a) Dislocation loops after shearing the void in the crystal of 2 μm at an applied strain of 0.15%. (b) Void shape after multiple shearing by dislocations. (Chang et al., 2015)

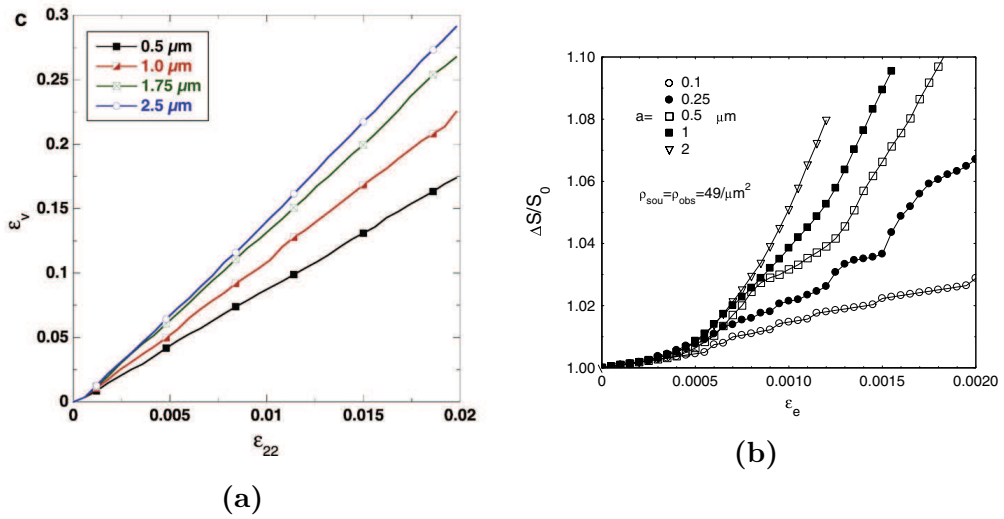

Figure 2.29: DDD simulations showing: (a) void area change as a function of applied strain under biaxial deformation for different void radii (Segurado and Llorca, 2009); (b) normalized void area fraction as a function of the remote strain for different void radii (Huang et al., 2007).

Size effects have been observed in a wide range of DDD and MD simulations, and it has been found that the mechanism responsible for the size effect is different at micro- and nano-scale. DDD simulations were usually carried out for voids with radius of several microns. At this scale, voids grow due to dislocations nucleating from sources, such as Frank-Read sources, in the matrix near the void (Huang et al., 2007; Segurado and Llorca, 2009; Chang et al., 2015). It was shown that the generated dislocation loops expand and shear successively the void surface resulting in the growth of the void (see fig. 2.28). Under this circumstance, **increasing void**

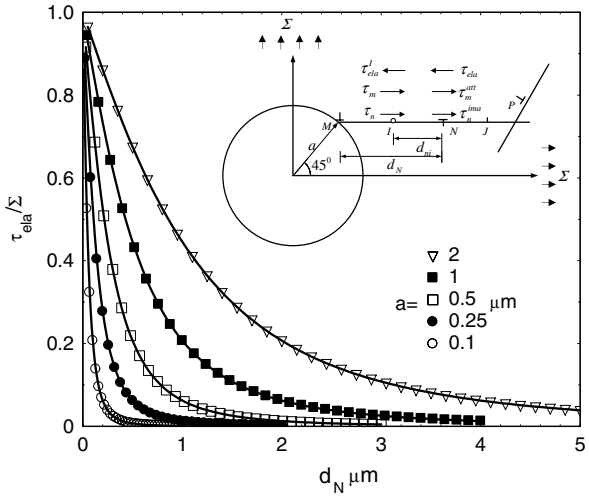

Figure 2.30: Typical curves for the Peach-Koehler force as a function of the distance to the void surface for different void radii a. The Peach-Koehler force was estimated to be equal to $f_N \approx \tau_{\text{ela}} b$, where b is the norm of Burgers vector (Huang et al., 2007)

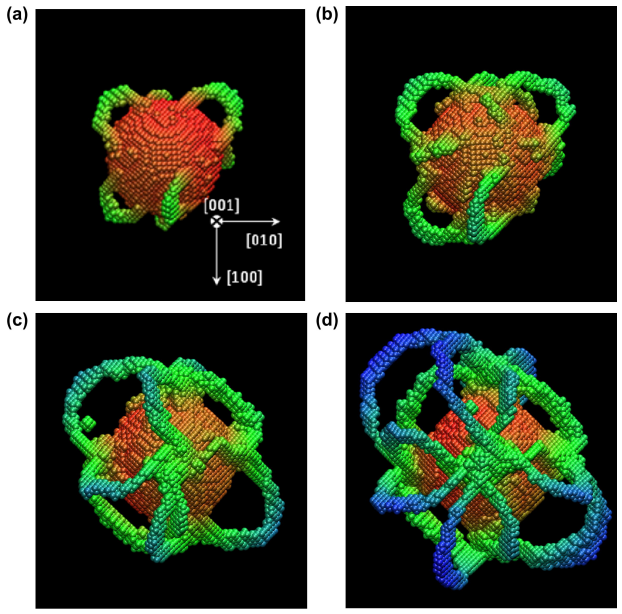

Figure 2.31: Propagation of multiple shear loops in hydrostatic tensile loading at a strain rate of $10^8\,\text{s}^{-1}$. The radii of void is 3.3 nm. (Tang et al., 2011)

size leads to an increase in the void growth rate (see fig. 2.29), which was explained as a matter of availability of dislocation sources near the void. As the void size increases, the number of active sources increases. As a result, for a bigger void, a larger amount of dislocations can reach the void surface, which leads to a higher void growth rate. In addition, Huang et al. (2007) estimated the driven force of dislocations, i.e., the Peach-Koehler force, as a function of distance to the void surface. It was found that the force is larger at the same distance to the void for

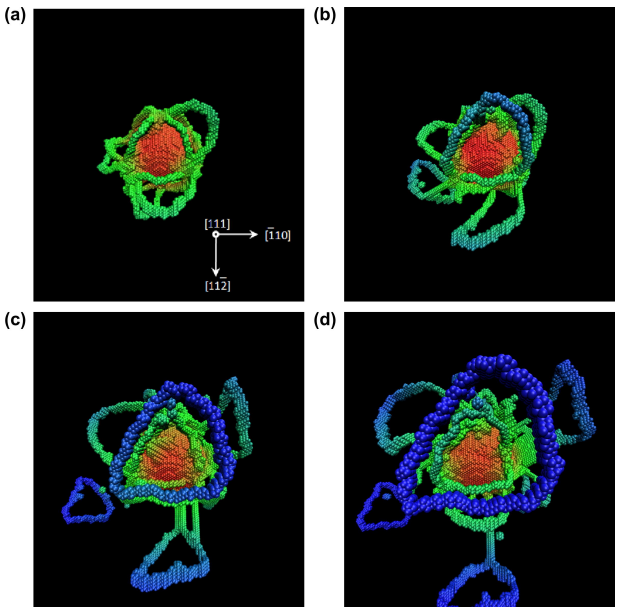

Figure 2.32: Sequence showing formation of shear and prismatic loops in hydrostatic tensile loading at a strain rate of $10^8\,s^{-1}$. (Tang et al., 2011)

larger voids and that thus the dislocation mobility is higher. This was believed to be the second reason for the size effect on the void growth rate. Moreover, Segurado and Llorca (2009) found a size effect on the strain hardening rate. In their simulations, the external boundaries of the single crystal were assumed to be impenetrable. This barrier mimics the effect of grain boundaries or of passivation layers in a microcrystal. When dislocations move towards the external boundaries, they stop at the boundaries and form pile-ups. They generate then back-stresses, reduce the mobility of following dislocations and also the activity of sources. This process results in an increasing flow stress. In this case, the strain hardening rate was found to be higher in the single crystal with smaller void. This effect was explained by two mechanisms. Firstly, dislocation density increases more rapidly as the size decreases, which indicates more dislocations within the pile-ups and leads to a higher strain hardening rate. Secondly, dislocations available in small crystals are limited by crystal size and the applied strain has to be partially absorbed through elastic deformation which causes a higher strain hardening rate.

MD simulations were applied for nano-sized voids rather than micro-sized ones, limited by the computationally expensive simulation process. At this scale, the amount of dislocation sources around the void is limited and dislocations nucleating from sources in the matrix are no longer sufficient for its growth. In this case, void growth by dislocation emission at the void surface was widely observed. It was found in the MD simulations that dislocations begin to nucleate at the void surface,

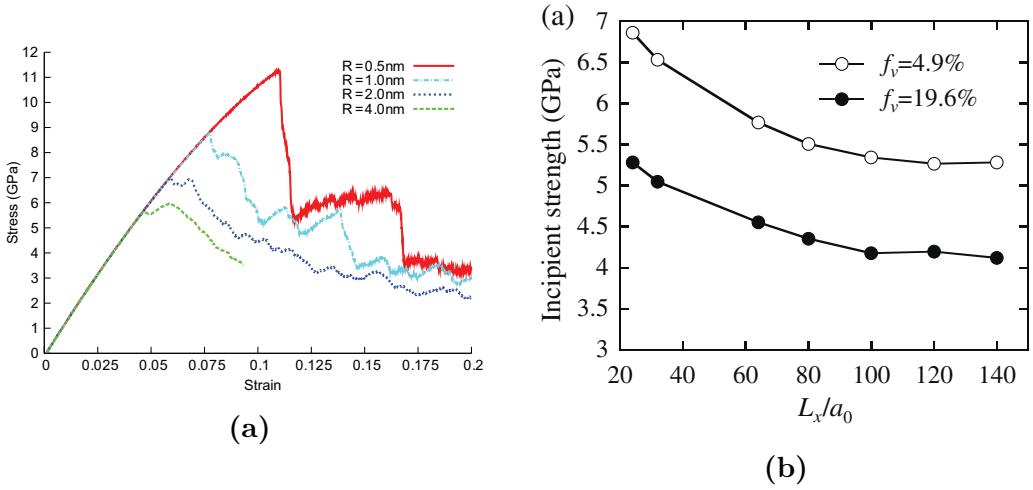

Figure 2.33: Typical MD simulations results showing size effects on porous single crystals. (a) Stress-strains curves for different void sizes. R denotes radius of the void. (Traiviratana et al., 2008). (b) Yield strength of nano-voided single crystals as a function of cell size L_x. a_0 is the lattice constant and f_v is the void volume fraction. (Zhao et al., 2009)

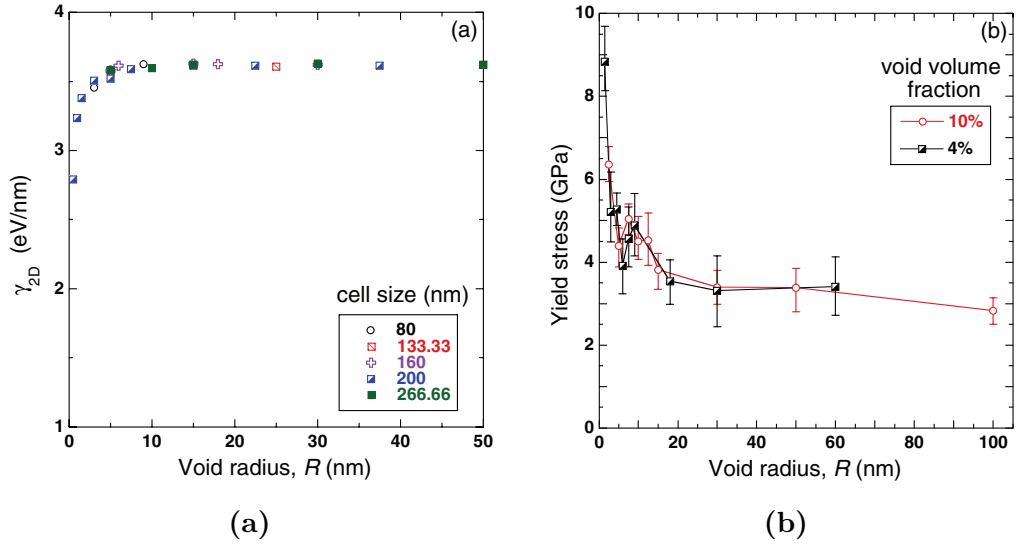

Figure 2.34: (a) Energy density associated with the void surface as a function of the void radius; (b) influence of void radius on the yield strength. (Chang et al., 2013)

allowing the significant growth of void. Concerning the kinetics of dislocation evolution, there is still a debate (Bulatov et al., 2010). The evolution of generated dislocations differs in details, which depends on various aspects, such as crystal structure considered (BCC, FCC or HCP) (Rudd, 2009), strain rate (Potirniche et al., 2006; Rudd, 2009; Tang et al., 2010; Xu et al., 2011; Tang et al., 2014), stress triaxiality (Seppälä et al., 2004), crystallographic orientation (Zhu et al., 2007; Bringa et al., 2010) and so on. However, it was widely observed that, following

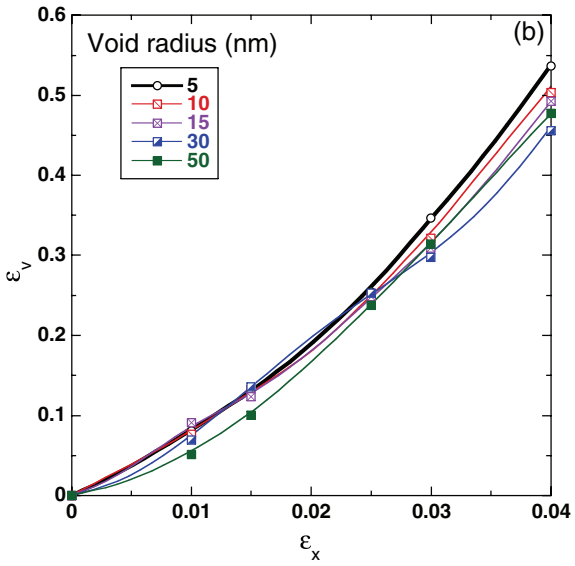

Figure 2.35: Evolution of the void volume fraction as a function of strain under biaxial deformation for different void radii. (Chang et al., 2013)

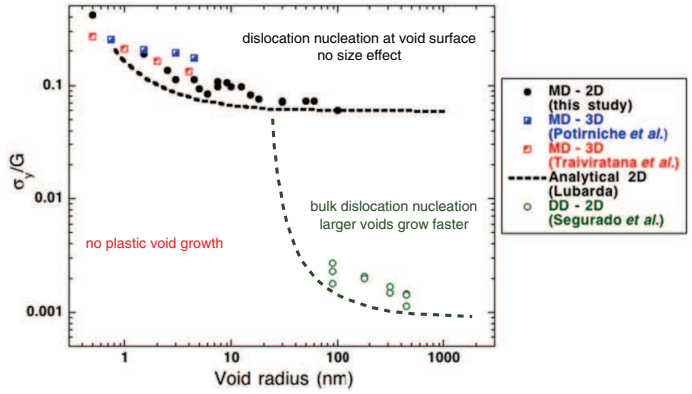

Figure 2.36: A map of mechanisms of void growth by plastic deformation: normalized yield strength as a function of void radius. (Chang et al., 2013)

the generation of dislocations at the surface and their interactions,

1. partial shear loops formed and expanded with the extremities attached to the void surface;
2. prismatic loops formed and were punched out from the void surface.

As a result, atoms are moved away from the void leading to the growth of the void. These two mechanisms are presented in figs. 2.31 and 2.32 (Tang et al., 2011). In addition, twinning was also found by (Tang et al., 2012; Rudd, 2009) to be a possible mechanism for void growth. More details concerning physical mechanisms of void growth at nano-scale under high strain rate are not discussed here. Nevertheless, it should be pointed out that strong size effects were reported by MD simulations

(see Potirniche et al., 2006; Traiviratana et al., 2008; Zhao et al., 2009; Xu et al., 2011; Tang et al., 2012; Chang et al., 2013; Krasnikov and Mayer, 2015):

- yield strength increased with decreasing void size;
- dislocation evolution patterns were influenced by void size.

It should be noticed that the definition of the yield strength can be different. The overall stress needed to nucleate the first dislocation from the void surface was often used for the yield strength. As shown in figs. 2.33a and 2.33b, the yield strength decreases with increasing void size and asymptotically approaches a constant value. The size dependence of yield strength is associated with the surface energy of the void. For 2D simulations, Chang et al. (2013) calculated the energy γ_{2D} per unit length at the void perimeter for various void radii presented in fig. 2.34a. They argued that the surface energy becomes small for voids with a radius below 5 nm, meaning that the void becomes more stable. It is thus more difficult to nucleate dislocations at void surface for the very small voids, which can be confirmed by higher yield strength for void radius smaller than 5 nm (see fig. 2.34b). However, **the size effect on void growth rate was quite limited** according to Potirniche et al. (2006) and Chang et al. (2013) (see fig. 2.35). No explanation is given for this negligible effect.

Combining the investigations at micro and nano-scale, a map of mechanisms and size effects for plastic void growth can be established, according to Chang et al. (2013), which is presented in fig. 2.36. It can be summarized as follows. For voids with radius larger than 100 nm, plastic deformation occurs by the nucleation of dislocation in the bulk from dislocation sources. Larger voids grow faster than small one, because the higher number of dislocation sources around the void increases the number of available dislocations, leading to faster void growth. For voids below 50 nm, few dislocation sources are available around the void, voids can only grow by the nucleation of dislocations at the void surface. This mechanism requires higher stress to initiate plastic deformation around the void and the void growth rate is independent of its size. In this regime, the yield stress does not depend on void size. The surface energy density remains constant for the radius in the range from 10 to 50 nm. For voids with radius smaller than 10 nm, the void surface becomes more stable and higher stress is necessary to nucleate dislocations from the void surface. These argument are in agreement with the micromechanics analysis of Ahn et al. (2007) based on the interaction between a void and emitted dislocations. They reported that the surface energy plays a significant role only for voids with radius smaller than 100 nm.

2.5.3 Investigations by strain gradient plasticity

Strain gradient plasticity theories have been widely used to study size effects in plasticity, among which size dependent void growth at micron-scale is frequently concerned. In the literature, two modeling approaches can be encountered:

- an isolated void in an infinite medium;
- a void in a finite medium (unit cell).

The first kind of model considers a spherical or cylindrical void embedded in an finite matrix subjected to a uniform remote loading, as shown in fig. 2.37. The model is usually used in analytical analysis to obtain a relation between the void growth rate and the remote loading, as in the well-known work of Rice and Tracey (1969). In contrast to the first type of model, the second accounts for a finite matrix, i.e., unit cell, which can be regarded as a representative volume element (RVE). The RVE is often supposed to be a cube in three dimension (3D) or a square in two dimension (2D) (see fig. 2.38a). This kind of model is frequently used in finite element analysis to study influences of different aspects on void growth rate, such as effects of stress triaxiality, initial void volume fraction, etc. However, the unit cell can also be of other shapes, especially spherical or spheroidal as considered in the well-known work of Gurson and in those for extending the Gurson model (see fig. 2.38b).

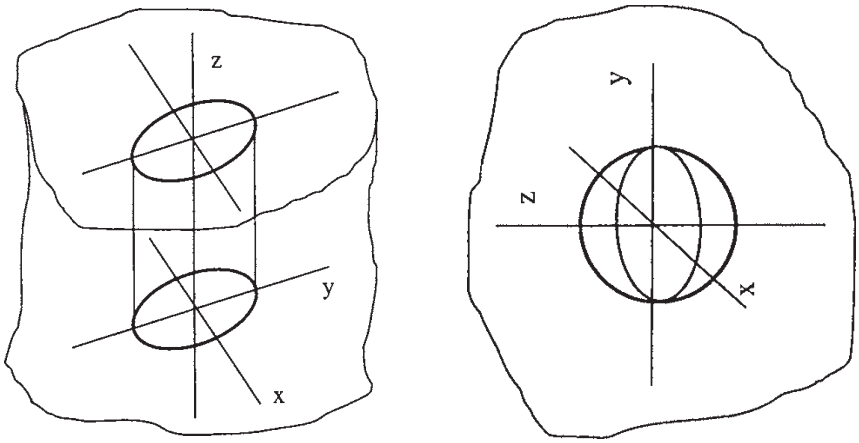

(a) **(b)**

Figure 2.37: Illustration for the model of an isolated void in an infinite medium: (a) a cylindrical void, (b) a spherical void. (Huang and Wang, 2006)

In early works, the matrix is assumed to be isotropic in order to simply analysis process. However, as radii of voids are reduced to several microns, whose size is

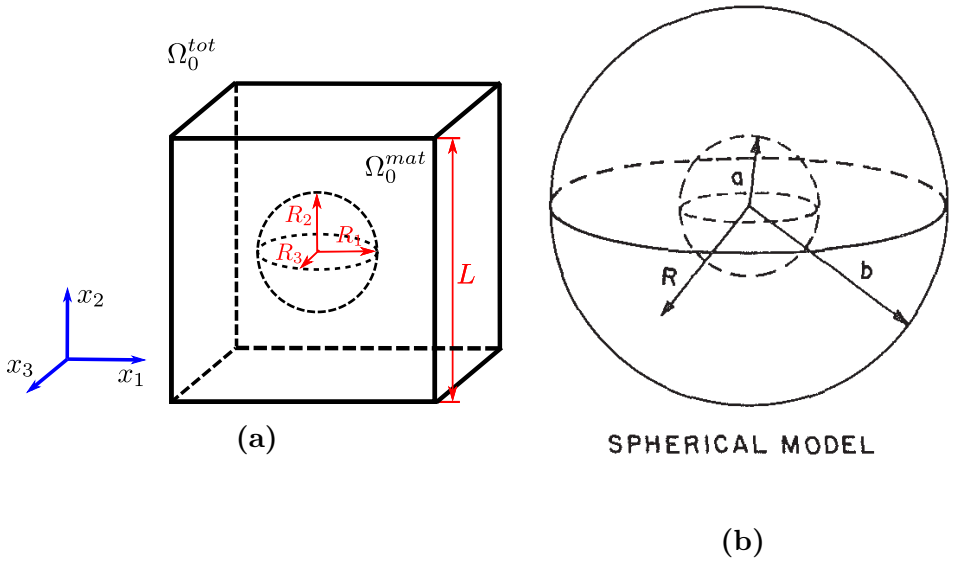

Figure 2.38: Illustration for (a) a cubic unit cell containing an initially spherical void, and (b) a spherical unit cell containing an initially spherical void (Gurson, 1977).

smaller than that of the grain, it is more reasonable to consider voids embedded inside a grain whose properties are naturally anisotropic (or at the grain boundary for some special cases). It means that as the size of the void is comparable with that of the grain, the matrix should assume to be anisotropic. This particular aspect attracts an increasing attention in recent years (see, e.g., Kysar et al., 2005; Gan et al., 2006; Borg and Kysar, 2007; Borg et al., 2008; Hussein et al., 2008).

Even though the approach used is different from one study to another, some common results are predicted by strain gradient theories:

1. smaller is stronger;
2. smaller is slower.

It implies that, with a given void volume fraction but a decreasing void size, loading carrying capacity of porous materials increases and void growth rate decreases, which are in agreement with the observations in DDD and MD simulations.

Apart from the very conclusions, some specific issues were addressed in different works, which will be presented in the following. Results obtained by the two models (a void in an infinite matrix and in a finite matrix) are described separately. Besides, works regarding the extension of the Gurson model accounting for the size effect will be exclusively summarized in section 2.5.5.

A void in an infinite matrix

Fleck and Hutchinson (Fleck and Hutchinson, 1993; Fleck and Hutchinson, 1997; Fleck and Hutchinson, 2001) established in their works the termed phenomenological strain gradient plasticity theory, where size effects in void growth were concerned as an implication of their theories. The problem was solved based on a variational principle established for an infinite matrix containing an isolated spherical void. The matrix is subjected to uniform remote axisymmetric loading specified by $\sigma_{33}^{\infty} = S$ and $\sigma_{11}^{\infty} = \sigma_{22}^{\infty} = T$. Results for the normalized void growth rate have the functional form

$$\frac{\dot{V}}{\dot{\varepsilon}_{33}^{\infty} V} = F\left(X, \frac{l}{a}, n\right) \tag{2.18}$$

where $\varepsilon_{33}^{\infty}$ denotes the remote strain, X the remote stress triaxiality, l the material length parameter, a the radius of the void and n the parameter of power law. Representative results (Fleck and Hutchinson, 1997) are given in fig. 2.39, which illustrates the variation of void growth rate with respect to the relative size of the void l/a. A pronounced size effect is predicted by the Toupin-Mindlin theory (SG) [1] which accounts for both the rotation and stretch gradients: the void growth is constrained when the void radius a is of the same order with the material length scale l. However, a much weaker effect is predicted by the couple stress theory (CS) [2] that only considers the rotation gradients, which implies that the rotation gradients do not play a significant role in the size dependent void growth.

The problem of an isolated void in an infinite matrix was also investigated by Huang et al. (2000) based on the termed mechanism-based strain gradient plasticity of Gao et al. (1999). Analyzing a spherical void in the matrix subjected to remote spherically symmetric tension, the authors showed, as presented in fig. 2.40, the remote stress σ^{∞} normalized by the yield strength σ_Y as a function of the normalized displacement on the void surface u_0/R_0, where R_0 is the initial void radius. It was concluded that small voids (large value of l/R_0) are less susceptible to growth at a given stress state than larger ones.

Because of the nonlinear nature and complexities of the problem, it is not always possible to derive an analytical result. Instead, numerical approaches, especially the finite element method, offer an efficient way to explore the size effects under different conditions.

[1] In the Toupin-Mindlin theory, the yield strength of the solid is taken to depend upon strain and second gradient of displacement.

[2] In the couple stress theory, the yield strength of the solid is taken to depend upon strain and curvature (spatial gradient of the material rotation).

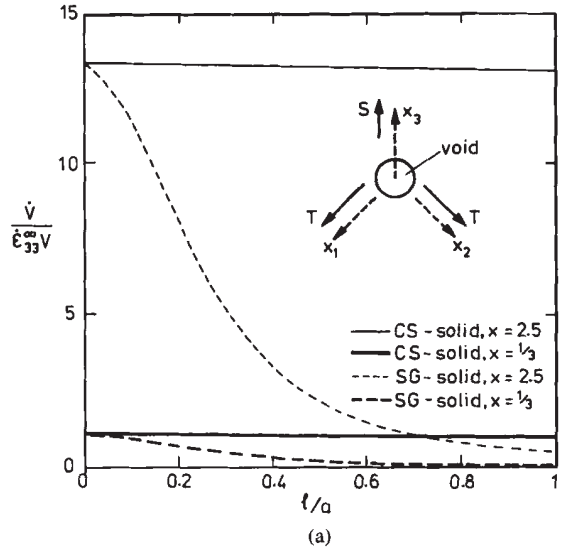

Figure 2.39: Effect of void radius a on normalized void growth rate. (Fleck and Hutchinson, 1997)

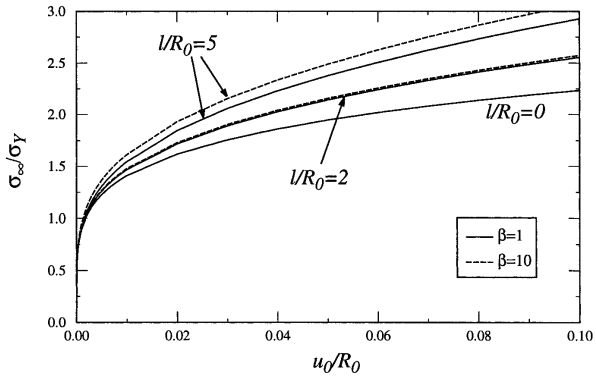

Figure 2.40: The remote applied stress normalized by the yield stress vs the normalized displacement on the surface of a spherical void. l is the material length parameter. β is a parameter of the strain gradient model to be determined from experiments. (Huang et al., 2000)

Unit cell model

Based on unit cell models, finite element simulations with strain gradient plasticity have been performed for both isotropic materials (see, e.g., Niordson, 2008) and anisotropic single crystals (see Shu, 1998; Borg and Kysar, 2007; Borg et al., 2008; Hussein et al., 2008). Basically, most of the works predicted reduced void growth rate and increased loading carrying capacity with decreasing void size (see, e.g., fig. 2.41 by Niordson (2008) for an isotropic material, fig. 2.42 by Shu (1998) for a single crystal with two planar slip systems, and fig. 2.43 by Borg et al. (2008) for a single crystal with three planar slip systems). These works are summarized in table 2.2 by indicating the material assumption of the matrix and the void

Reference	Isotropic or single crystal	Crystal structure	Void shape	Small or finite strains
(Niordson, 2008)	isotropic	—	spherical (axi-symmetry)	finite strains
(Shu, 1998)	single crystal	2 planar slip systems	cylindrical	small strains
(Borg and Kysar, 2007)	single crystal	3 planar slip systems	cylindrical	small strains
(Borg et al., 2008)	single crystal	3 planar slip systems	cylindrical	finite strains
(Hussein et al., 2008)	single crystal	3 planar slip systems	square (2D)	finite strains

Table 2.2: Unit cell simulations in the literature on size dependent void growth in isotropic or single crystal matrix.

shape. Besides, some more implications can be found from this numerical approach, which are outlined in the following.

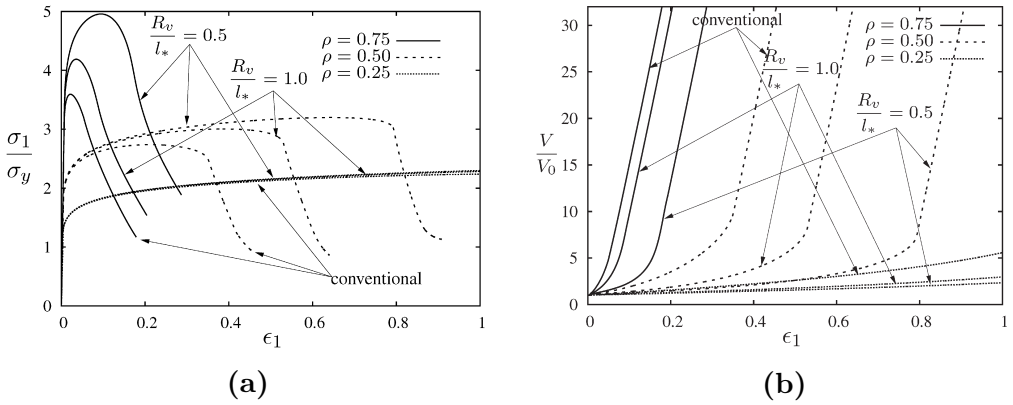

Figure 2.41: Size effects on (a) the overall stress strain response and (b) the evolution of the normalized void volume fraction for a material with $f_0 \approx 5.33 \times 10^{-3}$. Both conventional and size dependent results with $R_v/l_* = 1.0$ and $R_v/l_* = 0.5$ are shown for three stress ratios ρ. R_v denotes the void radius and l_* the material length parameter. (Niordson, 2008)

Niordson (2008) has studied size effects on both void growth and coalescence in isotropic materials. The strain gradient theory of Fleck and Hutchinson (2001) with its extension to finite strains by Niordson and Redanz (2004) was utilized. In addition to the common results, the author also showed that, for decreasing void size, the onset of coalescence is significantly delayed and the void volume fraction at the onset of coalescence decreases. Furthermore, it was also found that the size effect is negligible at low stress triaxialities, e.g., $T = 0.67$.

Given the anisotropy of the grain, a series of studies have been performed to understand size effects in single crystals. Shu (1998) applied the model of Shu

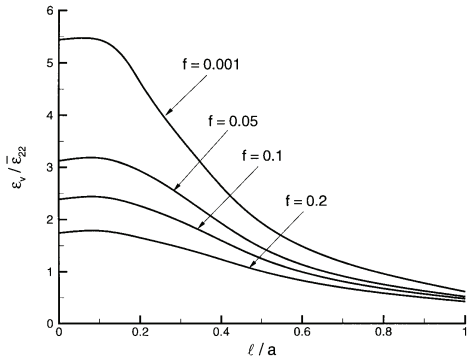

Figure 2.42: The normalized void growth rate ε_v at $\bar{\varepsilon}_{22} = 1\%$ as a function of l/a. l is a length scale parameter and a the void radius. (Shu, 1998)

and Fleck (1999), which fits within the framework of Mindlin (1964) and of Fleck and Hutchinson (1997), to a unit cell with a cylindrical void. Different initial void volume fractions and loading conditions were considered. It was found that the size effect is more significant under biaxial loadings than that at uniaxial loadings. In addition, the effect on the void growth is reduced and that on the macroscopic stress is enhanced with increasing void volume fraction. Note that even though the simulations were performed at small strains, the influence of strain gradients on void shape evolution was not concerned.

Borg and Kysar (2007) analyzed a unit cell with a cylindrical void accounting for 3 in-plane slip systems. The model of Borg (2007) based on the principle of virtual power introduced by Gurtin (2002) with the constitutive equations motivated from Fleck and Hutchinson (2001) was used. Borg (2007) assumed that plastic slips and plastic slip gradients contribute to plastic work and the plastic dissipation d^p per unit volume writes:

$$d^p = \sum_{s=1}^{N} Q^s \dot{\gamma}^s + \xi_l^s \underline{\boldsymbol{l}}^s . \boldsymbol{\nabla} \dot{\gamma}^s + \xi_m^s \underline{\boldsymbol{m}}^s . \boldsymbol{\nabla} \dot{\gamma}^s, \tag{2.19}$$

where Q^s $(s = 1, 2, \cdots, N)$ are the generalized stresses work-conjugate to the plastic slips, ξ_l^s and ξ_m^s are the generalized stresses work-conjugate to the slip gradients along the slip direction $\underline{\boldsymbol{l}}^s$ and the slip transverse direction $\underline{\boldsymbol{m}}^s$. The slip transverse direction vector $\underline{\boldsymbol{m}}^s$ forms a triad with the slip direction vector $\underline{\boldsymbol{l}}^s$ and the normal vector to the slip plane $\underline{\boldsymbol{n}}^s$. The power of internal forces p^i are written as

$$p^i = \underset{\sim}{\boldsymbol{\sigma}} : \underset{\sim}{\boldsymbol{D}} + \sum_{s=1}^{N} (Q^s - \tau^s) \dot{\gamma}^s + \sum_{s=1}^{N} \left(\xi_l^s \underline{\boldsymbol{l}}^s + \xi_m^s \underline{\boldsymbol{m}}^s \right) . \boldsymbol{\nabla} \dot{\gamma}^s \tag{2.20}$$

with the strain rate tensor $\underset{\sim}{\boldsymbol{D}}$ and the resolved shear stress τ^s. In the study, the authors focused on deformation and stress fields around the void and void growth

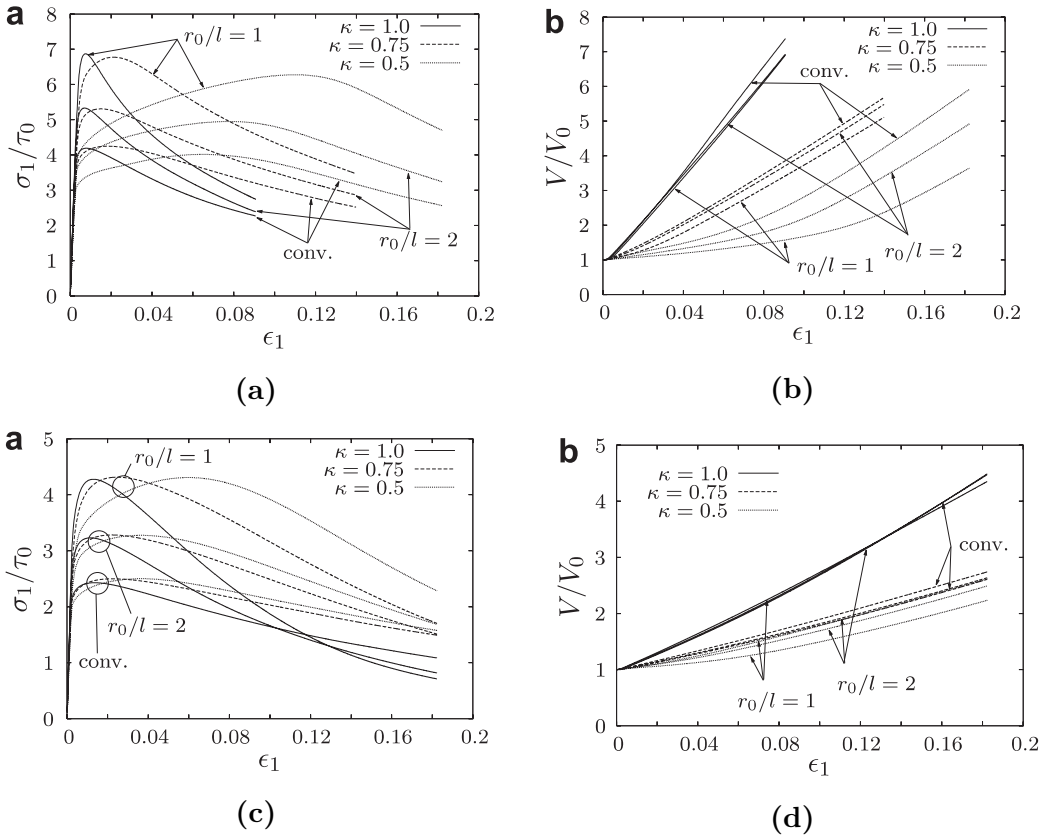

Figure 2.43: Size effects on the evolution of the relative void growth ((b),(d)) and that of the overall response in terms of the true stress ((a),(c)) with respect to the logarithmic strain. Figs. (a) and (b) are for the initial void volume fraction $f_0 = 3.1\%$ and fig. (c) and (d) for $f_0 = 12.6\%$. l denotes a length scale parameter and r_0 the void radius, and κ the stress ratio $\overline{\sigma}_{22}/\overline{\sigma}_{11}$. (Borg et al., 2008)

was not studied. It has been found that the angular structure of plastic slip around the void is different when using the classical theory and the strain gradient crystal plasticity. Especially, the double slip sectors are bigger with the non-local theory. The authors also found that the applied stress to activate plastic slip at the void is up to three times higher for smaller voids than for larger ones. Hussein et al. (2008) compared the results obtained by the strain gradient crystal plasticity model of Borg (2007) with those by DDD. The work was done at small strains considering plane strain conditions with planar slip systems. The internal length scale of the strain gradient theory was fixed according to the DDD simulations. The two theories predicted similar results for two loading conditions: shearing and equi-biaxial straining. For the equi-biaxial straining, the results obtained were consistent with the common conclusion, however, under shearing, an overall stress independent on the void size was found. Note that void growth was not considered in this work. Borg et al. (2008) analyzed the growth of cylindrical voids under plane strain conditions

within finite strain framework. Two levels of initial void volume fractions (12.6%, 3.1%), two crystal orientations and three stress ratios ($\overline{\sigma}_{22}/\overline{\sigma}_{11} = 0.5, 0.75, 1.0$) were considered. The simulations predicted a strong size effect on the overall stress strain response for all the cases considered. However, the effect on void growth is more pronounced for lower initial void volume fraction and higher stress ratios. The authors also found that using the strain gradient theory changes the symmetric structure of plastic slip, and that it makes the deformed void shape smoother.

2.5.4 Effects of surface energy

When material length scale reduces to nano-scale, surface energy can be introduced in continuum mechanics for investigating size effects. Energy associated with the void surface is believed to play a role in void growth when it is nano-sized.

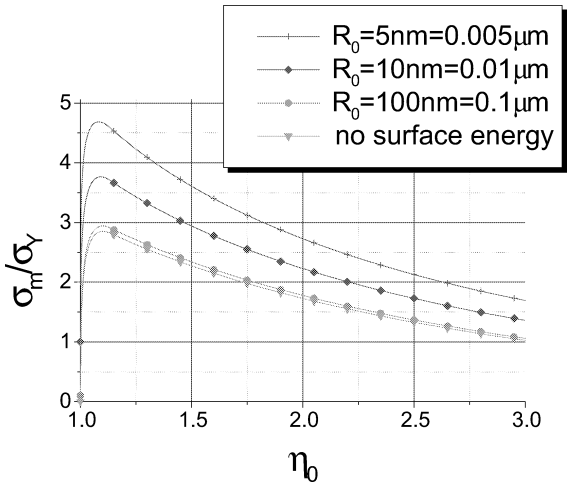

Figure 2.44: The effect of initial void radius R_0 on loading-deformation curves. (Huo et al., 1999)

To this purpose, the problem of a spherical void of radius R_0 in a finite (spherical) elasto-plastic matrix subjected to uniform remote hydrostatic tensile stress σ_m was considered by Huo et al. (1999). The matrix was supposed to be isotropic and obey a power hardening law. It is solved based on a variational principle accounting for the contribution of surface energy to void growth. Typical results for the initial void volume fraction $f = 0.01$ are given in fig. 2.44, where the remote stress σ_m normalized by the yield strength σ_Y is plotted as a function of the actual radius r_0 of the void normalized by its initial value R_0, i.e., $\eta_0 = r_0/R_0$. It can be seen that small voids are less susceptible to growth than larger ones. The authors also concluded for typical metals that the effect of the surface energy is negligible for voids larger than 100 nm in size, while may become significant when the void size is of 10 nm.

In addition, some efforts have also been devoted to development of homogenization models for voided materials accounting for surface energy. The details of the models are presented in the next section.

2.5.5 Extension of the Gurson model accounting for void size effects

In the past years, efforts have been dedicated to extend the Gurson model in order to account for effects of void size. All the models predict a reduced void growth rate and an increased loading carrying capacity. The models are summarized in the following.

Model based on Taylor dislocation model

Wen et al. (2005) introduced the intrinsic material length l:

$$l = 18\alpha^2 \left(\frac{\mu}{\sigma_0}\right)^2 b \tag{2.21}$$

with an empirical material constant α around 0.3, the shear modulus μ, the Burgers vector b and the yield stress σ_0, based on the Taylor dislocation model (Taylor, 1934), which associates the shear flow stress τ with the dislocation density ρ:

$$\tau = \alpha\mu b\sqrt{\rho}, \tag{2.22}$$

Considering an axisymmetric macroscopic strain rate case, the authors obtained the yield surface for a rigid perfectly plastic material containing void given by

$$\frac{1}{3}\operatorname{tr}\underset{\sim}{\boldsymbol{\Sigma}} = \frac{\sigma_0}{6\pi}\int_\Omega d\Omega \int_f^1 [2D + \frac{\lambda}{2}(1-3\cos^2\phi)]\sqrt{\frac{1+\sqrt{\frac{5}{2}}L\left(\frac{f}{\lambda^4}\right)^{1/3}}{\lambda^2+2D\lambda(1-3\cos^2\phi)+4D^2}}\frac{d\lambda}{\lambda} \tag{2.23}$$

$$\Sigma_e = \frac{\sigma_0}{6\pi}\left|\int_\Omega d\Omega \int_f^1 [(1-3\cos^2\phi)D+\lambda]\sqrt{\frac{1+\sqrt{\frac{5}{2}}L\left(\frac{f}{\lambda^4}\right)^{1/3}}{\lambda^2+2D\lambda(1-3\cos^2\phi)+4D^2}}\,d\lambda\right| \tag{2.24}$$

where f denotes the void volume fraction, D is the ratio of macroscopic volumetric strain rate to the effective strain rate, and $\lambda = r^3/b^3$ with the external radius of the matrix b. $\int_\Omega d\Omega = \int_0^\pi \sin\theta\, d\theta \int_0^{2\pi} d\phi$ is the integration over spherical angles θ and ϕ. L, a parameter associated with the intrinsic material length l, is defined by

$$L = \frac{l \operatorname{tr}\underset{\sim}{\boldsymbol{E}}}{a} \tag{2.25}$$

with the trace of the macroscopic strain $\underset{\sim}{\boldsymbol{E}}$ and the radius of the void a. Based on the yield stress, a set of constitutive equations has been established for an

elastic-plastic work hardening solid following the approach of Tvergaard (1989). However, this model predicts a very weak size effect on the overall stress-strain curves in uniaxial tension.

Model considering an von Mises interface

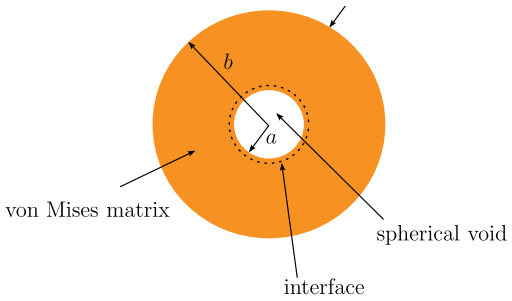

Figure 2.45: Unit cell with the consideration of interface stress for incorporating the void size effect into the Gurson model. (Morin et al., 2015)

Dormieux and Kondo (2010) introduced the size effect into the Gurson model by considering an interface at the void surface (see fig. 2.45). Assume that the solid matrix obeys the von Mises yield criterion

$$\sigma_{eq}^2 = \frac{3}{2}\underset{\sim}{\boldsymbol{\sigma}}' : \underset{\sim}{\boldsymbol{\sigma}}' \leqslant \sigma_0^2 \tag{2.26}$$

with the von Mises equivalent stress σ_{eq}, the stress tensor deviator $\underset{\sim}{\boldsymbol{\sigma}}'$ and the yield stress in simple tension σ_0, and that the interface obeys a 2D plane stress von Mises-type criterion

$$\frac{3}{2}\underset{\sim}{\boldsymbol{\sigma}}'_S : \underset{\sim}{\boldsymbol{\sigma}}'_S \leqslant k_{int}^2 \tag{2.27}$$

with the plane stress deviator tensor $\underset{\sim}{\boldsymbol{\sigma}}'_S$ and the yield limit of the interface k_{int}. A non-dimensional parameter Γ is therefore introduced, characterizing the void size effect:

$$\Gamma = \frac{k_{int}}{a\sigma_0} \tag{2.28}$$

with the void radius a. Through the limit analysis, the authors obtained a yield surface given by

$$\operatorname{tr}\underset{\sim}{\boldsymbol{\Sigma}} = \sigma_0 \left[2 \left(\operatorname{arcsinh}(\xi) - \operatorname{arcsinh}(f\xi) + \Gamma \frac{6\xi}{\sqrt{\xi^2 + 3/5}} \right) \right] \tag{2.29}$$

and

$$\Sigma_{\text{eq}} = \sigma_0 \left[\sqrt{1 + f^2\xi^2} - f\sqrt{1 + \xi^2} + \Gamma \frac{9f}{5\sqrt{\xi^2 + 3/5}} \right], \tag{2.30}$$

where f denote the void volume fraction and the parameter $\xi = (2/f)(D_m/D_{eq})$ is define from the mean and the equivalent deviatoric parts D_m, D_{eq} of the macroscopic strain rate $\underset{\sim}{\boldsymbol{D}}$. Based on this yield surface, a set of constitutive equations was formulated and implemented in a finite element code by Morin et al. (2015). The same approach was also used by Monchiet and Kondo (2013) for a matrix containing a spheroidal void.

Model based on Fleck–Hutchinson strain gradient plasticity theory

Monchiet and Bonnet (2013) extended the Gurson model considering the phenomenological strain gradient plasticity theory of Fleck and Hutchinson (1997) for the solid matrix. Note that the macroscopic strain gradient was not taken into account in the macroscopic dissipation, which was justified by the hypothesis that the size of the representative volume element is large compared with the internal length scales and the size of the voids. With some approximations, an explicit expression of the macroscopic yield surface was obtained, defined by

$$\Phi(\underset{\sim}{\boldsymbol{\Sigma}}, f, \eta) = \frac{\Sigma_{eq}^2}{\sigma_0^2} + 2f \cosh\left(\frac{3}{2\eta}\frac{\Sigma_m}{\sigma_0}\right) - 1 - f^2 = 0, \tag{2.31}$$

where η is a coefficient related to the material length parameter evaluated by

$$\eta = \frac{3}{\ln(f)} \left[\operatorname{arcsinh}\left(\frac{\alpha}{u}\right) - \sqrt{1 + \frac{u^2}{\alpha^2}} \right]_{u=f^{1/3}}^{u=1} \tag{2.32}$$

with

$$\alpha = \frac{1}{3}\sqrt{\frac{2}{5}}\frac{a}{l_1}. \tag{2.33}$$

Here, a denotes the void radius and l_1 is the material length parameter in the strain gradient plasticity theory of Fleck and Hutchinson (1997). A plastic model was also derive based on the yield surface, which predicted a strong size effect on both the stress-strain response and the void growth rate for relatively high stress triaxiality $T = 3$.

2.6 Conclusions

Austenitic stainless steels of 300 series are widely used as structural materials in nuclear power plants, because of their good mechanical properties. However, irradiation produces in the materials different microstructural defects, e.g., Frank loops, voids, etc, resulting in a modification of mechanical properties of the materials. It has been observed that the fracture toughness of the steels decreases rapidly with radiation dose, especially for the radiation damage less than 10 dpa. In stainless steels irradiated up to 10 dpa, ductile fracture is a dominant fracture mechanisms. Besides the decrease of fracture toughness with irradiation, a transition from classical dimple fracture to channel fracture and nano-dimple fracture has been observed with increasing dose in stainless steels. The physical foundation of the transition of fracture mechanism is still not well understood.

Dimple fracture, i.e., ductile fracture due to void growth and coalescence, is a dominant fracture mechanism in unirradiated stainless steels. Ductile fracture has being studied in numerous studies. Among various works, FE unit cell simulations are often used to investigate the process of void growth and coalescence under different conditions, e.g., different stress states and initial void volume fractions; Analytical models are proposed for simulating ductile damage/fracture at structure level. A large number of works were devoted to materials assumed to be isotropic (von Mises materials).

The fracture due to void growth and coalescence remains in stainless steels after irradiation with a trend of decreasing dimple size. These smaller dimples could result from irradiation-induced micro-sized precipitates or nano-sized cavities. Although voids involved in the ductile fracture process of irradiated steels may have different origins, they are usually intragranular voids, i.e., voids located inside a grain. Few works were devoted to growth and coalescence of intragranular voids, and this problem attracts increasing attentions in recent years. Intragranular voids can be equivalently considered as voids embedded in a single crystal matrix. In this case, effects of the anisotropy of single crystal matrix on void evolution (void growth and coalescence) need to be investigated. In addition, as presented in this section, irradiated stainless steels exhibit a particular strain hardening/softening behavior, whose effects on void evolution is still not clear. Moreover, different approaches were recently adopted for obtaining the effective yield surface of single crystals containing voids. However, there is currently no model for voided single crystals, which is able to describe the void growth up to coalescence and can be used to carry out structural computations.

As mentioned above, voids that are involved in ductile fracture process of irradiated stainless steels have potentially different size (nano to micrometers). Size effects have been predicted by different approaches for voided materials. In general, it has been found that "smaller is stronger" and "smaller is slower". It implies that, with a given void volume fraction but a decreasing void size, loading carrying capacity of porous materials increases and void growth rate decreases. It is thus necessary to investigate size effects on void growth in FCC single crystals. Moreover, for taking into account size effects, the Gurson model has been extended through different approaches, such as introducing strain gradient plasticity, interface energy, etc. However, there is currently no ductile fracture model incorporating size effects at single crystal scale.

In the following, ductile fracture due to void growth and coalescence at grain scale will be investigated. FE unit cell simulations will be performed for studying void growth and coalescence in a matrix governed by single crystal plasticity (chapter 3). Effects of some basic aspects, including crystal orientation and stress triaxiality, will be first studied in the case of unirradiated crystals. Effects of post-irradiation hardening/softening behavior will assessed in a second step. Following the simulations, an elastoviscoplastic model at finite strains will be proposed for single crystals containing voids (chapter 4). The model incorporates heuristically influences of hardening behavior of single crystal matrix and is able to describe void growth up to coalescence. The model will then be assessed based on the results of the unit cell simulations in the case of unirradiated single crystals. Size effects on void growth and coalescence in single crystals will be investigated (chapter 5). For this purpose, a strain gradient crystal plasticity model at finite strains will be derived following the micromorphic approach. FE unit cell simulations will be performed with this model for size dependent void growth. This model can be further coupled with the model for porous single crystals, resulting a non-local ductile fracture model for single crystals.

3

Porous single crystals: unit cell simulations

Résumé

Ce chapitre présente les simulations par éléments finis pour étudier la croissance et la coalescence des cavités dans le monocristal. Pour cela, des cellules unitaires tri-dimensionnelles avec une cavité sphérique sont utilisées. Le modèle de plasticité cristalline utilisé est présenté. Les simulations sont d'abord réalisées pour comprendre l'influence de l'orientation cristallographique, de la triaxialité et de la porosité initiale sur la croissance et la coalescence des cavités. L'effet de l'irradiation est ensuite introduit par un écrouissage post-irradiation. On montre que la croissance de cavité est plus rapide et que la coalescence commence à une déformation plus petite dans un monocristal irradié.

Contents

The aim of the section is to study mechanical behaviors of voided FCC single crystals, including effective stress–strain relations, void growth and coalescence, by 3D UC simulations. The single crystal plasticity model for the matrix of voided single crystals in described in a first step, followed by the presentation of the FE formulation of UC simulations. The first part of simulations will be devoted to assessment of effects of several parameters, including stress triaxiality, initial void volume fraction and crystal orientation of the matrix, in unirradiated single crystals. The second part of simulations will be devoted to irradiated single crystals. Effects of the post-irradiation hardening law on void growth and coalescence are investigated, by comparison with results obtained by the hardening law for unirradiated single crystals.

3.1 Crystal plasticity model for void-free single crystals

3.1.1 FCC single crystals

In the present work, face-centered cubic (FCC) single crystals are considered, since the crystal structure of austenitic stainless steels corresponds to this type. FCC lattice structure, as shown in fig. 3.1, has lattice points on the faces of the cube in addition to the corner lattice points. In FCC single crystals, plastic slip occurs on 12 slip systems, which are specified by the slip direction vector $\underline{\boldsymbol{m}}^s$ and the normal vector $\underline{\boldsymbol{n}}^s$ to the slip plane as summarised in table 3.1 (Schmid and Boas, 1935).

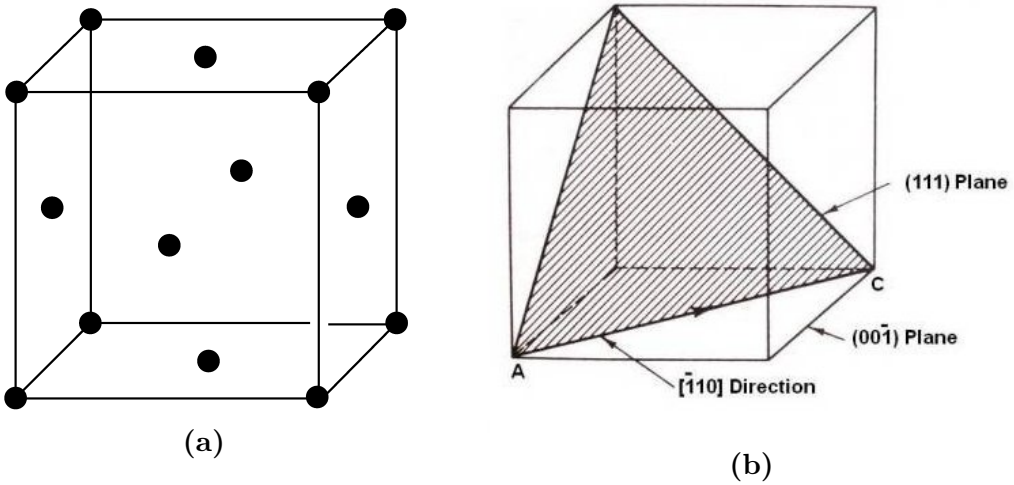

Figure 3.1: (a) FCC lattice structure; (b) Plastic slip systems for FCC single crystals.

s	1	2	3	4	5	6	7	8	9	10	11	12
label	B4	B2	B5	D4	D1	D6	A2	A6	A3	C5	C3	C1
$\underline{\boldsymbol{n}}^s$	(111)			$(1\bar{1}1)$			$(\bar{1}11)$			$(\bar{1}\bar{1}1)$		
$\underline{\boldsymbol{m}}^s$	$[\bar{1}01]$	$[0\bar{1}1]$	$[\bar{1}10]$	$[\bar{1}01]$	$[011]$	$[110]$	$[0\bar{1}1]$	$[110]$	$[101]$	$[\bar{1}10]$	$[101]$	$[011]$

Table 3.1: Slip systems in FCC single crystals. The labels are given according to the Schmid–Boas convention (Schmid and Boas, 1935).

p	1	2	3	4
plane(p)	(111)	$(1\bar{1}1)$	$(\bar{1}11)$	$(\bar{1}\bar{1}1)$

Table 3.2: Frank loop systems. Plane(p) denotes the normal to the plane of system p.

Frank loops are one of irradiation-induced microstructural defects in austenitic stainless steels and will be considered in the hardening laws in the following. In the present work, Frank loops are supposed to remain on the four {111} dislocation slip planes (see table 3.2).

3.1.2 Kinematics

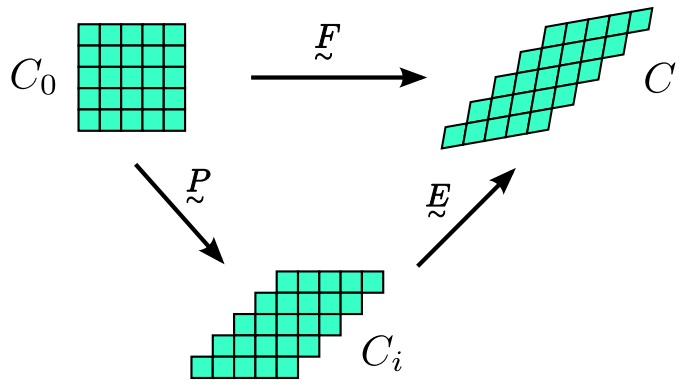

Figure 3.2: Multiplicative decomposition of the deformation gradient.

For void-free single crystals, a lattice orientation is attributed to each material point. The existence of directors[1] associated with lattice orientation allows for the definition of a unique isoclinic intermediate local configuration C_i, as recommended by Mandel (1973). This ensures the uniqueness of the multiplicative decomposition of the deformation gradient $\underset{\sim}{\boldsymbol{F}}$ (see. fig. 3.2) adopted within the finite strain framework:

$$\underset{\sim}{\boldsymbol{F}} = \underset{\sim}{\boldsymbol{E}}.\underset{\sim}{\boldsymbol{P}}, \tag{3.1}$$

[1]Director vectors are the notion that Mandel (1973) used for define the plastic media. According to Mandel, the plastic deformation is the result of the discontinuity of displacement or rotation between micro-elements which constitute the macroscopic media. Within one micro-element, there is no discontinuity. In order to describe movement of a micro-element, a triplet of director vectors $\underline{\boldsymbol{d}}^k$ $(k = 1, 2, 3)$ is attached to the center of each micro-element, whose position indicates the orientation of the micro-element.

with the elastic part $\underset{\sim}{\boldsymbol{E}}$ and the plastic part $\underset{\sim}{\boldsymbol{P}}$ of the deformation gradient $\underset{\sim}{\boldsymbol{F}}$. The crystal orientation is the same in the initial local configuration C_0 and the intermediate local configuration C_i. The determinants of $\underset{\sim}{\boldsymbol{F}}$, $\underset{\sim}{\boldsymbol{E}}$ and $\underset{\sim}{\boldsymbol{P}}$ describe the change of volume and of density of a material point:

$$J = \det\left(\underset{\sim}{\boldsymbol{F}}\right) = \frac{V}{V_0} = \frac{\rho_0}{\rho}, \tag{3.2}$$

$$J_e = \det\left(\underset{\sim}{\boldsymbol{E}}\right) = \frac{V}{V_i} = \frac{\rho_i}{\rho}, \tag{3.3}$$

$$J_p = \det\left(\underset{\sim}{\boldsymbol{P}}\right) = \frac{V_i}{V_0} = \frac{\rho_0}{\rho_i}, \tag{3.4}$$

where V_0, V_i and V denote the volume at the reference configuration C_0, the intermediate configuration C_i and the current configuration C; ρ_0, ρ_i and ρ represent the density at the reference configuration C_0, the intermediate configuration C_i and the current configuration C. Note that $J_p = 1$ due to the incompressible plasticity of void-free single crystals undergoing plastic slip.

The velocity gradient $\underset{\sim}{\boldsymbol{L}}$ can be expressed as

$$\underset{\sim}{\boldsymbol{L}} = \dot{\underset{\sim}{\boldsymbol{F}}}.\underset{\sim}{\boldsymbol{F}}^{-1} = \underset{\sim}{\boldsymbol{L}}^e + \underset{\sim}{\boldsymbol{E}}.\underset{\sim}{\boldsymbol{L}}^p.\underset{\sim}{\boldsymbol{E}}^{-1}, \tag{3.5}$$

with the elastic part of the velocity gradient $\underset{\sim}{\boldsymbol{L}}^e$ in the current configuration C

$$\underset{\sim}{\boldsymbol{L}}^e = \dot{\underset{\sim}{\boldsymbol{E}}}.\underset{\sim}{\boldsymbol{E}}^{-1}, \tag{3.6}$$

and the plastic part of the velocity gradient $\underset{\sim}{\boldsymbol{L}}^p$ in the intermediate configuration C_i

$$\underset{\sim}{\boldsymbol{L}}^p = \dot{\underset{\sim}{\boldsymbol{P}}}.\underset{\sim}{\boldsymbol{P}}^{-1}. \tag{3.7}$$

3.1.3 Definition of stresses

According to the approach of Mandel (1973) (see also Sabnis et al. (2012) and Sabnis et al. (2013)), stress tensors are defined as follows.

The second Piola–Kirchhoff stress tensor $\underset{\sim}{\boldsymbol{\Pi}}^e$, defined with respect to the intermediate configuration C_i, is given by

$$\underset{\sim}{\boldsymbol{\Pi}}^e = J_e \underset{\sim}{\boldsymbol{E}}^{-1}.\underset{\sim}{\boldsymbol{\sigma}}.\underset{\sim}{\boldsymbol{E}}^{-T}, \tag{3.8}$$

where $\underset{\sim}{\boldsymbol{\sigma}}$ is the Cauchy stress defined in the current configuration C.

The elastic Green–Lagrange strain tensor $\underset{\sim}{\boldsymbol{E}}^e_{GL}$ is defined as

$$\underset{\sim}{\boldsymbol{E}}^e_{GL} = \frac{1}{2}\left(\underset{\sim}{\boldsymbol{E}}^T.\underset{\sim}{\boldsymbol{E}} - \underset{\sim}{\mathbf{1}}\right). \tag{3.9}$$

$\underset{\sim}{\boldsymbol{\Pi}}^e$ is related to $\underset{\sim}{\boldsymbol{E}}^e_{GL}$ by the elasticity law:

$$\underset{\sim}{\boldsymbol{\Pi}}^e = \underset{\approx}{\boldsymbol{C}} : \underset{\sim}{\boldsymbol{E}}^e_{GL}, \tag{3.10}$$

where $\underset{\approx}{\boldsymbol{C}}$ is the fourth-order anisotropic elasticity tensor, which can be expressed in terms of three parameters C_{11}, C_{12} and C_{44} for cubic elasticity.

In addition, the driving force for single crystal plasticity is known as the Mandel stress $\underset{\sim}{\boldsymbol{M}}$, which is defined in the intermediate configuration and is work-conjugate to $\underset{\sim}{\boldsymbol{L}}^p$:

$$\underset{\sim}{\boldsymbol{M}} = J_e \underset{\sim}{\boldsymbol{E}}^T . \underset{\sim}{\boldsymbol{\sigma}} . \underset{\sim}{\boldsymbol{E}}^{-T} = \underset{\sim}{\boldsymbol{E}}^T . \underset{\sim}{\boldsymbol{E}} . \underset{\sim}{\boldsymbol{\Pi}}^e. \tag{3.11}$$

3.1.4 Flow rule

For each slip system, s, a yield function can be defined as:

$$\phi^s = \tau^*_s - \tau^s_c, \text{ with } \tau^*_s \geqslant 0 \tag{3.12}$$

where τ^*_s is a scalar stress and τ^s_c is the critical resolved shear stress (CRSS). For void-free single crystals, the scalar stress τ^*_s for system s is given by

$$\tau^*_s = \sqrt{\tau^s \tau^s} = |\tau^s|, \tag{3.13}$$

where τ^s is the resolved shear stress defined as:

$$\tau^s = \underset{\sim}{\boldsymbol{M}} : \underset{\sim}{\boldsymbol{N}}^s, \tag{3.14}$$

with the Schmid tensor $\underset{\sim}{\boldsymbol{N}}^s = \underline{\boldsymbol{m}}^s \otimes \underline{\boldsymbol{n}}^s$ ($\underline{\boldsymbol{m}}^s$ is the slip direction vector and $\underline{\boldsymbol{n}}^s$ is the normal vector to the slip plane of slip system s). For each slip system, yielding occurs for $\phi^s \geqslant 0$. The definition of τ^*_s provides a possibility for formulating the void-free and porous single crystal model in a unified form (see section 4.1).

The plastic strain rate $\underset{\sim}{\boldsymbol{L}}^p$ can be defined as

$$\underset{\sim}{\boldsymbol{L}}^p = \dot{\underset{\sim}{\boldsymbol{P}}} . \underset{\sim}{\boldsymbol{P}}^{-1} = \sum_{s=1}^{N} \dot{\gamma}^s \frac{\partial \phi^s}{\partial \underset{\sim}{\boldsymbol{M}}} = \sum_{s=1}^{N} \dot{\gamma}^s \underset{\sim}{\boldsymbol{N}}^{*s}, \tag{3.15}$$

with $\underset{\sim}{\boldsymbol{N}}^{*s}$

$$\underset{\sim}{\boldsymbol{N}}^{*s} = \frac{\partial \phi^s}{\partial \underset{\sim}{\boldsymbol{M}}} = \frac{\partial |\tau^s|}{\partial \tau^s} \frac{\partial \tau^s}{\partial \underset{\sim}{\boldsymbol{M}}} = \operatorname{sign}(\tau^s)\, \underset{\sim}{\boldsymbol{N}}^s \tag{3.16}$$

and the plastic slip rate $\dot{\gamma}^s$ given by

$$\dot{\gamma}^s = \dot{\gamma}_{\text{ref}} \left\langle \frac{\tau^*_s - \tau^s_c}{\tau_{\text{ref}}} \right\rangle^n, \tag{3.17}$$

where $\dot{\gamma}_{\text{ref}}$ is the reference slip rate and τ_{ref} is a reference resolved shear stress. Note that $\langle \bullet \rangle = \bullet$ if $\bullet > 0$, else $\langle \bullet \rangle = 0$. Here, $\dot{\gamma}^s$ is non-negative by its definition. The sign of plastic slip is given in Eq. (3.15).

3.1.5 Hardening rule

Unirradiated single crystals

For the hardening rule of unirradiated single crystals, an evolution law involving dislocation densities as the only source of hardening is chosen. Following Kubin et al., 2008, the slip resistance τ_c^s, i.e., the critical resolved shear stress, on a particular slip system s is decomposed into a thermal part τ_T^s and an athermal part τ_A^s:

$$\tau_c^s = \tau_T^s + \tau_A^s. \tag{3.18}$$

τ_T^s corresponds to lattice friction which is dependent on temperature and assumed to be constant at a given temperature. τ_A^s represents the athermal contribution of the flow stress. For unirradiated single crystals, only the interaction of dislocation network contribute to τ_A^s (Franciosi and Zaoui, 1982), which is expressed as

$$\tau_A^s = \mu b_D \sqrt{\sum_u^{12} a^{su} \rho_D^u}, \tag{3.19}$$

where b_D is the norm of the Burgers vector of dislocations, μ the shear modulus, ρ_D^u the dislocation density of system u, and a^{su} the matrix of long-range interactions between dislocations. The form of interaction matrix a^{su} is given in appendix A for FCC crystals.

The description of the evolution of dislocation densities is based on two mechanisms: the multiplication and the annihilation of dislocations (Mecking and Lücke, 1970; Essmann and Rapp, 1973; Teodosiu and Sidoroff, 1976; Tabourot et al., 1997; Cheong and Busso, 2004). The dislocation density ρ_D^s follows:

$$\dot{\rho}_D^s = \frac{1}{b_D} \left(\frac{1}{L^s} - g_c \rho_D^s \right) \dot{\gamma}^s, \tag{3.20}$$

where L_s is the mean free path of the dislocation segment before being stopped at obstacles in the form of forest dislocations and g_c is the critical distance controlling the annihilation of dislocations with opposite signs. For unirradiated crystals, L^s is written as

$$L^s = L_D^s = \frac{\kappa}{\sqrt{\sum_u^{12} b^{su} \rho_D^u}}. \tag{3.21}$$

The κ parameter is proportional to the number of obstacles crossed by a dislocation before being pinned. The matrix b^{su} describes the interaction between dislocations; it has the same form as the interaction matrix a^{su} (see appendix A).

Irradiated single crystals

For irradiated single crystals, the slip resistance τ_c^s is also decomposed, following Eq. (3.18), into the thermal part τ_T^s, which assumes to be a constant at a given temperature, and the athermal part τ_A^s . For the athermal contribution of the flow stress τ_A^s, in addition to the dislocation term (Eq. (3.19)), two more terms are considered to contribute to the athermal slip resistance for the irradiated material:

$$\tau_A^s = \underbrace{\mu b_D \sqrt{\sum_u^{12} a^{su} \rho_D^u}}_{\text{dislocation term}} + \underbrace{\alpha_L \mu b_L \sqrt{\sum_p^4 \phi_L \rho_L^p}}_{\text{loop term}} + \underbrace{\tau_a \exp\left(-\frac{\gamma^s}{\gamma_0}\right)}_{\text{unpinning term}}, \tag{3.22}$$

where α_L denotes a parameter setting the relative contribution of Frank loops to the hardening, b_L the norm of the Burgers vector of Frank loops, ϕ_L the mean diameter of Frank loops, ρ_L^p the density of Frank loops in the slip plane p, τ_a a reference shear stress for dislocation unpinning and γ_0 a coefficient to adjust the avalanche speed after unpinning the dislocations.[1]

The first term (called the dislocation term in the following) on the right-hand side of Eq. (3.22) is the slip resistance provided by the interaction of dislocation network (Franciosi and Zaoui, 1982). The second term (loop term) accounts for the effect of Frank loops generated by irradiation impeding dislocation motion. Based on Mughrabi's observation (Mughrabi, 1996) that the junction energy of dislocations and loops is significantly greater than that of thermal activation, the hardening due to Frank loops is considered to contribute to the athermal part. The third term (unpinning term) is introduced based on the observation of Tanguy et al. (2013) that the hardening effect is under-estimated if only the hardening due to Frank loops is considered as a dispersed barrier hardening. This unpinning term aims at modeling the static ageing effects arising once irradiation defect cascades are present in the material microstructure (Trinkaus et al. (1997a), Trinkaus et al. (1997b), and Singh et al. (1997)). For the unirradiated material, only the dislocation term is considered.

In irradiated stainless steels, the evolution of dislocation densities also follows the form of Eq. (3.20) but with modified mean free path L^s. In fact, Frank loops produced by irradiation are not rigid obstacles. Molecular dynamics simulations by Rodney and Martin (1999) showed that Frank loops can interact with dislocations, resulting in the unfaulting of the loops. According to Yang et al. (2003), dislocations can be emitted from the circumference of the loop during the interaction. These

[1] A more complex equation taking into account the effect of voids on hardening can be derived as proposed in Tanguy et al. (2013). However, considering the dose range of interest in this study, the effect of voids on hardening is considered negligible.

results motivate the modification of the mean free path L^s in order to include the influence of Frank loops; it is assumed to take the following form:

$$\frac{1}{L^s} = \frac{1}{L^s_D} + \frac{1}{L_L}, \tag{3.23}$$

where L^s_D is still given by Eq. (3.21) and the Frank loop contribution to the mean free path writes

$$L_L = \frac{\kappa}{\sqrt{k_{dl} \sum_p^4 \phi_L \rho^p_L}}, \tag{3.24}$$

where k_{dl} is a coefficient setting the effective interaction between Frank loops and dislocations.

The model proposed by Krishna and his co-workers (Krishna et al., 2010; Krishna and De, 2011) is adopted to describe the evolution of Frank loop densities. It is based on the mechanism of annihilation of Frank loops by dislocations gliding in the loop's plane. The probability and frequency of the annihilation of a Frank loop are taken into account. The decrease rate of Frank loop density $\dot{\rho}^p_L$ on plane p is

$$\dot{\rho}^p_L = -A \left(\sum_{s \in \text{plane}(p)} \rho^s_D \right) \frac{\phi_L}{b_D} \left(\rho^p_L - \rho^{\text{sat}}_L \right) \left(\sum_{s \in \text{plane}(p)} \dot{\gamma}^s \right), \tag{3.25}$$

where A denotes the annihilation area and ρ^{sat}_L the stabilized effective density of Frank loops. $s \in \text{plane}(p)$ represents all the dislocation slip systems having the same slip plane as the Frank loop p.

3.2 FE formulation of unit cell simulations

The simulations are performed with the FE software `Zset` (Besson and Foerch, 1998). Throughout the section, variables at microscopic and macroscopic scale are distinguished. The variables with an overline symbol (e.g., $\underset{\sim}{\overline{\boldsymbol{F}}}$) are used for macroscopic scale at which an effective behavior of the unit cell is observed, while the variables without the overline symbol describe the behavior at the microscopic scale, i.e., at each material point inside the unit cell.

The problem setup is shown in fig. 3.3. It is assumed that the distribution of voids in the single crystal is homogeneous. Thus, a unit cell, i.e., a representative elementary volume, Ω^{tot}_0 can be considered as a cube of length L_0 with a spherical void of radius R_0 at its center (see fig. 3.4a). Notice that L_0 characterizes the average distance between voids. Thus, the initial void volume fraction f_0 is

$$f_0 = \frac{4}{3}\pi \frac{R^3_0}{L^3_0}. \tag{3.26}$$

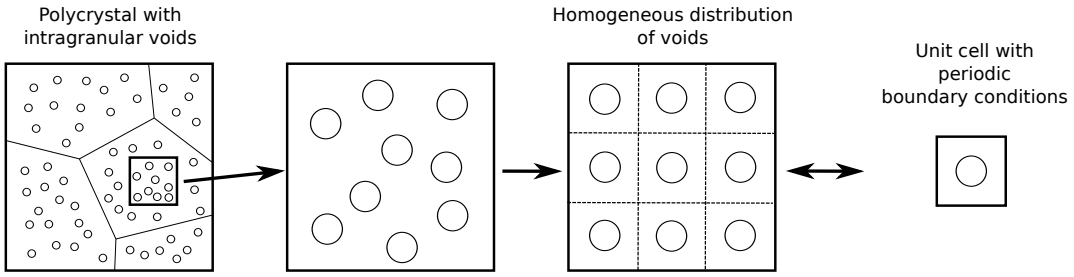

Figure 3.3: Problem setup for unit cell simulations.

In this work, 5 different initial void volume fractions are taken into account for the simulations: $f_0 = 0.005$, 0.01, 0.02, 0.05 and 0.1. In addition, the edges of the unit cell are initially parallel to the Cartesian coordinate x_i axes.

The unit cell is meshed with reduced-integration quadratic hexahedral elements (see fig. 3.4b). Numerical periodic homogenization at finite strains is used for the simulations and the elements are enhanced by introducing average strains ($\overline{F}_{ij}$) as degrees of freedom. The unit cell is subjected to periodic boundary conditions expressed by:

$$\underline{\boldsymbol{u}} = \underset{\sim}{\overline{\boldsymbol{F}}}.\underline{\boldsymbol{X}} + \underline{\boldsymbol{v}}\,, \tag{3.27}$$

where $\underset{\sim}{\overline{\boldsymbol{F}}}$ denotes the macroscopic deformation gradient, $\underline{\boldsymbol{u}}$ the displacement vector and $\underline{\boldsymbol{v}}$ a periodic fluctuation vector which obey the following periodicity condition:

$$\underline{\boldsymbol{v}}\,(\underline{\boldsymbol{x}}^{+}) = \underline{\boldsymbol{v}}\,(\underline{\boldsymbol{x}}^{-}) \tag{3.28}$$

where $\underline{\boldsymbol{x}}^{+}$ and $\underline{\boldsymbol{x}}^{-}$ denote the position of homologous nodes on opposite faces of the unit cell.

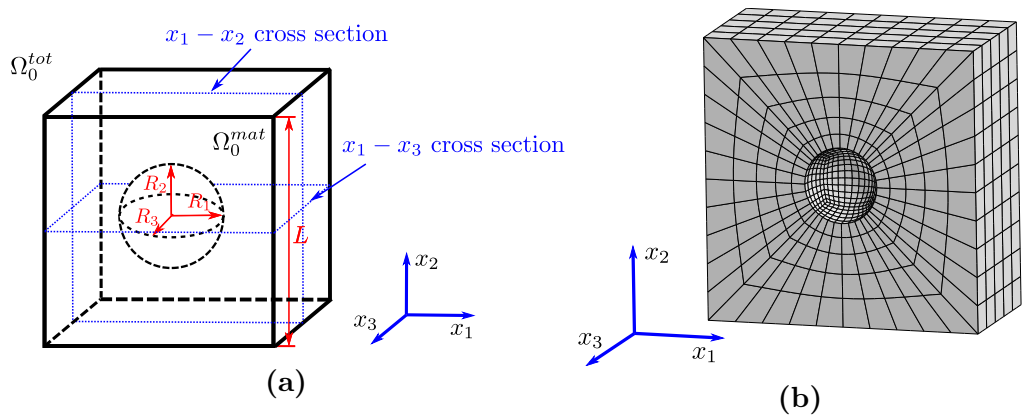

Figure 3.4: Unit cell: (a) the geometry, (b) half of a typical FE mesh with $f_0 = 0.01$.

The microscopic first Piola–Kirchhoff stress tensor $\underset{\sim}{\boldsymbol{S}}$ and the associated macroscopic tensor $\overline{\underset{\sim}{\boldsymbol{S}}}$ are related by

$$\overline{\underset{\sim}{\boldsymbol{S}}} = \frac{1}{V_0^{\text{tot}}} \int_{\Omega_0^{\text{tot}}} \underset{\sim}{\boldsymbol{S}}\, dV_0 = (1 - f_0) \frac{1}{V_0^{\text{mat}}} \int_{\Omega_0^{\text{mat}}} \underset{\sim}{\boldsymbol{S}}\, dV_0, \tag{3.29}$$

where V_0^{tot} and V_0^{mat} denote respectively the total volume of the unit cell and the volume of the matrix in the reference configuration. In uniaxial tension, the first Piola–Kirchhoff stress corresponds to the so-called engineering stress.

The macroscopic Cauchy stress tensor $\overline{\underset{\sim}{\boldsymbol{\sigma}}}$ is related to the macroscopic first Piola–Kirchhoff stress tensor by:

$$\overline{\underset{\sim}{\boldsymbol{\sigma}}} = \frac{1}{\overline{J}} \overline{\underset{\sim}{\boldsymbol{S}}} . \overline{\underset{\sim}{\boldsymbol{F}}}^T, \tag{3.30}$$

with $\overline{J} = \det\left(\overline{\underset{\sim}{\boldsymbol{F}}}\right)$. The Cauchy stress tensor corresponds to the true stress in the uniaxial tension case.

The microscopic deformation gradient $\underset{\sim}{\boldsymbol{F}}$ and the macroscopic tensor $\overline{\underset{\sim}{\boldsymbol{F}}}$ are related by:

$$\overline{\underset{\sim}{\boldsymbol{F}}} = \frac{1}{V_0^{\text{tot}}} \int_{\Omega_0^{\text{tot}}} \underset{\sim}{\boldsymbol{F}}\, dV_0. \tag{3.31}$$

Constant macroscopic Cauchy stress triaxiality T is imposed with

$$\overline{\underset{\sim}{\boldsymbol{\sigma}}} = \begin{bmatrix} \overline{\sigma}_{11} & 0 & 0 \\ 0 & \overline{\sigma}_{22} & 0 \\ 0 & 0 & \overline{\sigma}_{33} \end{bmatrix} = \overline{\sigma}_{11} \begin{bmatrix} 1 & 0 & 0 \\ 0 & \eta_2 & 0 \\ 0 & 0 & \eta_3 \end{bmatrix} = \overline{\sigma}_{11} \underset{\sim}{\boldsymbol{\eta}} \tag{3.32}$$

with

$$\eta_2 = \frac{\overline{\sigma}_{22}}{\overline{\sigma}_{11}},\ \eta_3 = \frac{\overline{\sigma}_{33}}{\overline{\sigma}_{11}},\ 0 \leqslant \eta_2, \eta_3 \leqslant 1, \tag{3.33}$$

such that

$$T = \frac{\overline{\sigma}_m}{\overline{\sigma}_{eq}} = \frac{1 + \eta_2 + \eta_3}{3\sqrt{1 - \eta_2 - \eta_3 - \eta_2\eta_3 + \eta_2^2 + \eta_3^2}}. \tag{3.34}$$

In the present study, axisymmetric loadings are mainly considered, which implies $\eta_2 = \eta_3 = \eta$ so that the imposed macroscopic Cauchy stress triaxiality is given by

$$T = \frac{1 + 2\eta}{3(1 - \eta)}. \tag{3.35}$$

Moreover, moderate to high stress triaxialities are investigated (see table 3.3), as they correspond to the stress triaxialities encountered in ductile failure process zones, such as in the vicinity of a crack tip. The method used to impose a constant triaxiality with periodic boundary conditions is described in appendix B.

T	1.0	1.5	2.0	3.0
η	0.4	0.538	0.625	0.727

Table 3.3: Values of the stress triaxiality T and corresponding η for axisymmetric loadings used in the simulations.

Each unit cell has a different crystal orientation characterized by the lattice orientations aligned with the three coordinate axes x_1–x_2–x_3. Five crystal orientations are considered: [100]–[010]–[001], [110]–[$\bar{1}$10]–[001], [111]–[$\bar{2}$11]–[0$\bar{1}$1], [210]–[$\bar{1}$20]–[001] and [$\bar{1}$25]–[1$\bar{2}$1]–[210]. They have different symmetry about the coordinate planes and correspond to different number of primary slip systems activated in uniaxial tension (see table 3.4). For the sake of brevity, the crystal orientations are named in the following by the lattice orientation along the main loading direction (axis x_1), i.e., [100], [110], [111], [210] and [$\bar{1}$25].

Orientation name	Crystallographic orientation along x_1–x_2–x_3	Number of primary slip systems	Schmid factor
[100]	[100] – [010] – [001]	8	$\frac{1}{\sqrt{6}} \approx 0.408$
[110]	[110] – [$\bar{1}$10] – [001]	4	$\frac{1}{\sqrt{6}} \approx 0.408$
[111]	[111] – [$\bar{2}$11] – [0$\bar{1}$1]	6	$\frac{2}{3\sqrt{6}} \approx 0.272$
[210]	[210] – [$\bar{1}$20] – [001]	2	$\frac{\sqrt{6}}{5} \approx 0.490$
[$\bar{1}$25]	[$\bar{1}$25] – [1$\bar{2}$1] – [210]	1	$\frac{\sqrt{6}}{5} \approx 0.490$

Table 3.4: Crystal orientations, number and Schmid factor of primary slip systems activated in uniaxial tension along x_1.

3.3 Results for unirradiated single crystals

The simulations are first performed for unirradiated single crystals. The material parameters used are closely related to those of a solution annealed 304 austenitic stainless steel at 340 °C (see Han (2012)).Among the parameters, a^{su} and b^{su} are two matrices (12×12 for FCC single crystal), describing the interaction between dislocations. Each of them is constructed by 6 independent parameters: $a_1, a_2, \cdots, a_6$ for a^{su} and $b_1, b_2, \cdots, b_6$ for b^{su} (see appendix A). The matrix a^{su} is assumed to be identical for all $s, u = 1, ..., 12$ (this is different from the matrix used in the work of Han (2012) which is identified by DDD simulations) to avoid some numerical bifurcation problems maybe encountered later in section 4.1; b^{su} is set equal to 0 if $s = u$ and equal to 1 if $s \neq u$. Due to the crystal structure and to the considered slip systems, τ_T^s can be considered as having the same value for all systems. The initial dislocation density is supposed to be equal for every system.

Hence, the initial value of the dislocation density for system s is $\rho_D^s|_{\text{ini}} = \rho_D^{\text{tot}}/12$, where ρ_D^{tot} is the total dislocation density measured in experiments. b_D is the norm of the Burgers vector $\frac{1}{2}a\langle 110\rangle$ of dislocations. All the material parameters used for the simulations are given in table 3.5.

C_{11}	C_{12}	C_{44}	τ_T^s	n
199 GPa	136 GPa	105 GPa	88 MPa	15
$\dot{\gamma}_{\text{ref}}$	τ_{ref}	μ	g_c	κ
1.47×10^{14} s^{-1}	88 MPa	65.6 GPa	2.6×10^{-9} m	42.8
a^{su}	b^{su} $(s \neq u)$	b^{su} $(s = u)$	b_D	ρ_0^s
0.124	1	0	2.54 $\mathring{A}$	8.33×10^8 m^{-2}

Table 3.5: Material parameters for the unit cell simulations.

The most relevant results could be discussed after choosing the three following orientations: [100], [111] and [$\bar{1}$25] (see table 3.4). In uniaxial tension, [100] is a multiple slip (8 primary slip systems) orientation with mirror symmetry about three coordinate planes; [111] is a multiple slip (6 primary slip systems) orientation with mirror symmetry about the x_1–x_2 coordinate plane, and [$\bar{1}$25] represents single slip orientation with no mirror symmetry about the coordinate planes. Note that the same primary slip systems are activated in axisymmetric loading as in uniaxial tension along axis x_1. Schmid factors calculated for the different orientations in the case of uniaxial tension along axis x_1 (see table 3.4) will be used to interpret the results.

3.3.1 FE discretisation effect

Before discussing simulation results, a study of the effect of finite element discretisation was first conducted to optimise computation time while keeping sufficient accuracy. Due to the anisotropy of the matrix, complete unit cells are used for the simulations. Two different finite element discretisations are considered as shown in fig. 3.5a and fig. 3.5b for one eighth of the FE mesh. The total number of elements used for the meshes can by calculated by $24 \times n^3$, where $n = 5$ (3000 elements) for the coarse mesh (fig. 3.5a) and $n = 10$ (24000 elements) for the fine mesh (fig. 3.5b). The variable n is used to characterize the number of elements of the unit cell as shown in fig. 3.5b. The crystallographic orientation [100] is chosen for this study with initial void volume fraction $f_0 = 0.01$ and two levels of stress triaxiality are considered: $T \in \{1, 3\}$.

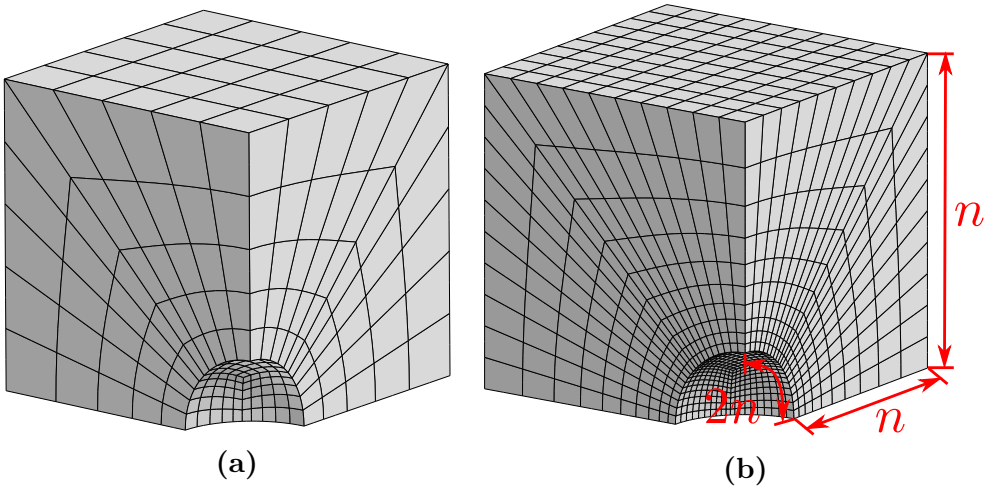

Figure 3.5: Different FE discretisation: (a) the coarse mesh ($n = 5$) for 1/8 of the full geometry (d) the fine mesh ($n = 10$) for 1/8 of the full geometry.

The influence of the FE discretisation on the overall stress strain behaviour and the void volume fraction evolution is evaluated. The overall Cauchy stress $\overline{\underset{\sim}{\boldsymbol{\sigma}}}$ is

$$\overline{\underset{\sim}{\boldsymbol{\sigma}}} = \frac{1}{V^{tot}} \int_{\Omega^{tot}} \underset{\sim}{\boldsymbol{\sigma}} \, dV = (1-f) \frac{1}{V^{mat}} \int_{\Omega^{mat}} \underset{\sim}{\boldsymbol{\sigma}} \, dV, \tag{3.36}$$

where V^{tot} and V^{mat} denote respectively the total volume of the unit cell Ω^{tot} and the volume of the matrix Ω^{mat} in the current configuration, and the void volume fraction f is calculated by

$$f = \frac{V^{tot} - V^{mat}}{V^{tot}}, \tag{3.37}$$

where the volume of the matrix V^{mat} in the current configuration is calculated by a post-processing of Zset software and the total volume of the unit cell V^{tot} in the current configuration can be obtained as

$$V^{tot} = \det\left(\overline{\underset{\sim}{\boldsymbol{F}}}\right) V_0^{tot}, \tag{3.38}$$

with V_0^{tot} the initial volume of the unit cell.

The evolution of normalised macroscopic Cauchy stress component $\overline{\sigma}_{11}/\tau_T^s$ and the void volume fraction f with respect to the deformation in the main loading direction $\overline{F}_{11} - 1$ are shown in fig. 3.6. It can be seen that the influence of FE discretisation on the overall stress strain behaviour and the evolution of void volume fraction is negligible for both low stress triaxiality ($T = 1$) and high stress triaxiality ($T = 3$). Even in the softening regime at $T = 3$, its influence is weak.

Based on this result, the coarse mesh ($n = 5$) will be used in the following, except otherwise stated, to obtain the curves of the macroscopic Cauchy stress

$\overline{\sigma}_{11}$ and the void volume fraction f. In particular, the fine mesh ($n = 10$) will be used to investigate local plastic slip fields in section 3.3 but the coarse mesh ($n = 5$) will be used later in section 3.4.

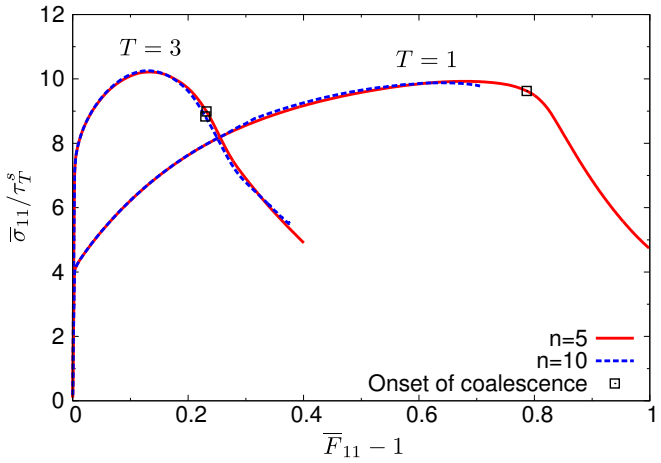

(a)

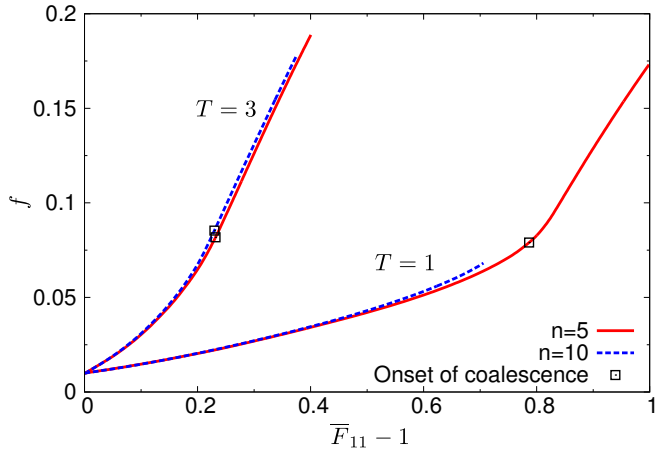

(b)

Figure 3.6: FE discretisation effect on (a) the overall stress strain behaviour (b) the void volume fraction for the [100] orientation and $f_0 = 0.01$.

3.3.2 Overall stress–strain response

Figure 3.7a shows the overall stress strain response of the unit cell for the [100] orientation with $f_0 = 0.01$ and the stress triaxiality T varying from 1 to 3. The macroscopic stress $\overline{\sigma}_{11}$ is normalised with respect to τ_T^s. It can be seen that the behaviour consists of a hardening regime followed by a softening regime, resulting from the competition between the strain hardening of matrix, the softening due to void growth and the softening due to void coalescence. The softening occurs

earlier at high stress triaxiality compared to that at low stress triaxiality. This can be explained by faster void growth at higher stress triaxiality.

Moreover, a transition from triaxial to uniaxial straining associated with the localization of the plastic flow in the intervoid ligament is observed, which corresponds to the onset of void coalescence according to Koplik and Needleman (1988). In this work, it is determined by plotting the transverse macroscopic strain $\overline{F}_{33} - 1$ as a function of the longitudinal macroscopic strain $\overline{F}_{11} - 1$. It is observed that $\overline{F}_{33} - 1$ reaches a stabilized value. In this study, by convention, the time step for which the transverse strain $\overline{F}_{33} - 1$ reaches 99% of its stabilized value, is regarded as the onset of coalescence. The corresponding longitudinal

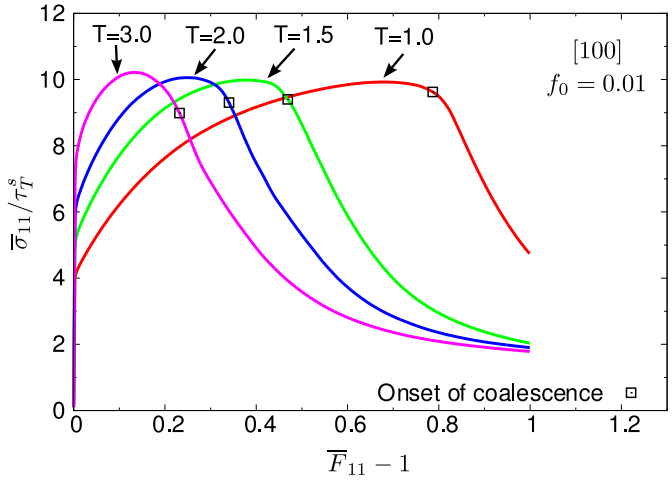

(a)

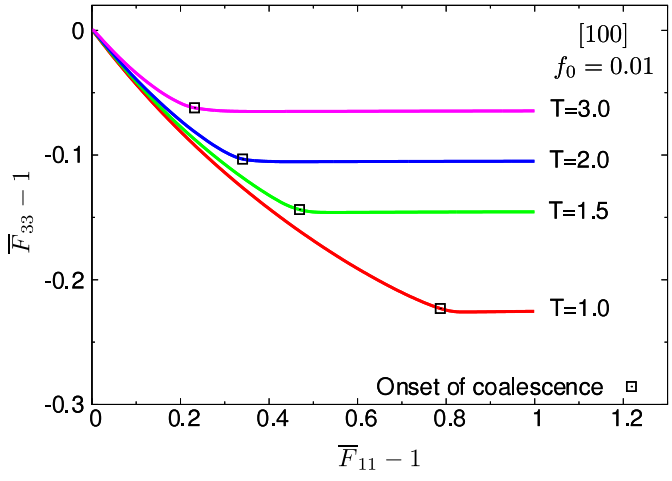

(b)

Figure 3.7: Effect of stress triaxiality on the overall behaviour of the unit cell for the crystallographic orientation [100], $f_0 = 0.01$ and triaxiality T from 1 to 3: (a) overall stress–strain curves and (b) evolution of the transverse strain $\overline{F}_{33} - 1$ vs. longitudinal strain $\overline{F}_{11} - 1$.

$\overline{F}_{11} - 1$ and porosity are defined as the critical strain $\overline{F}_{11c} - 1$ and critical porosity f_c at the onset of coalescence. The onset of void coalescence is indicated by a hollow square on each curve. It can be observed that the critical strain $\overline{F}_{11c} - 1$ decreases when the stress triaxiality T increases. Void coalescence will be discussed in more details later in this section.

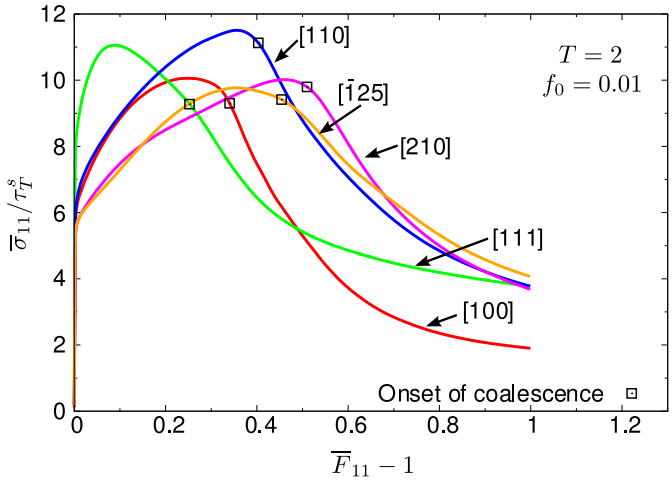

(a)

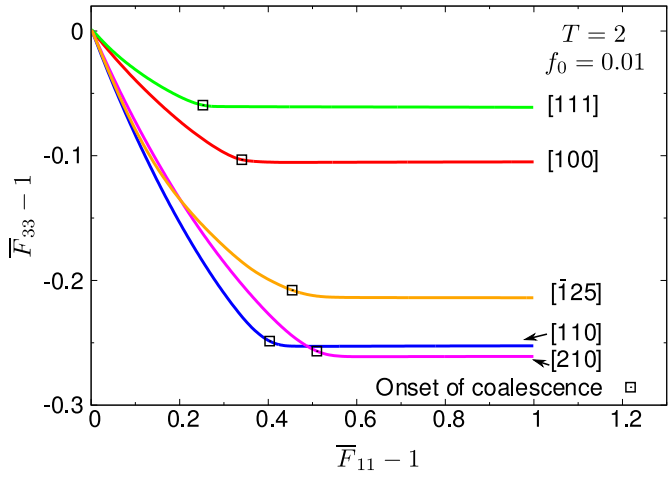

(b)

Figure 3.8: Effect of crystallographic orientation on the overall behaviour of the unit cell for $f_0 = 0.01$, triaxiality $T = 2$ and different crystallographic orientations: (a) overall stress–strain curves and (b) evolution of the transverse strain vs. longitudinal strain.

The effect of crystallographic orientation on the overall behaviour is presented in fig. 3.8, where the five crystallographic orientations are considered with the initial void volume fraction $f_0 = 0.01$ and the stress triaxiality $T = 2$. The [111] orientation shows the hardest response and the orientations [210] and [$\bar{1}$25] exhibit the softest response (see fig. 3.8a). The peak stress depends on the orientation

and this agrees with the results obtained by Ha and Kim (2010) for FCC single crystals and by Yerra et al. (2010) for BCC single crystals. In particular, the [110] orientation exhibits the highest peak stress and this is also observed by Ha and Kim (2010). As a general result, the softening regime starts earlier for the orientation [111] compared with the other orientations, which implies the fastest void growth for the [111] orientation, as will be confirmed in fig. 3.10.

For the asymmetric orientations, especially [210] and [$\bar{1}$25], the straining of the unit cell along the loading axis is accompanied by shearing, and the transverse straining of the unit cell may stop only along one transverse axis (x_2 or x_3 axis), which is interpreted as the preferred direction of coalescence. In that case, the onset of coalescence is determined in the "preferred coalescence direction", where void coalescence occurs first. As shown in fig. 3.8b, the [111] orientation leads to the earliest onset of coalescence.

3.3.3 Void growth

Figure 3.9 shows the effect of stress triaxiality on the evolution of void volume fraction f for the [100] orientation with the initial void volume fraction $f_0 = 0.01$ and the stress triaxiality T varying from 1 to 3. The results confirm the previous analysis: higher stress triaxiality leads to faster void growth, which induces earlier softening of the unit cell. These results are consistent with the observation of Ha and Kim (2010) for FCC single crystals.

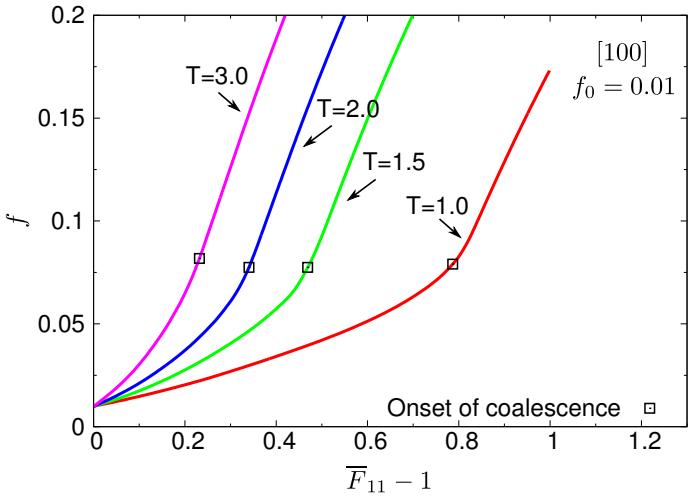

Figure 3.9: Evolution of void volume fraction: effect of stress triaxiality for crystallographic orientation [100], $f_0 = 0.01$ and triaxiality T from 1 to 3.

The evolution of void volume fraction for different orientations with $f_0 = 0.01$ is presented in fig. 3.10a for the stress triaxiality $T = 1$ and in fig. 3.10b for

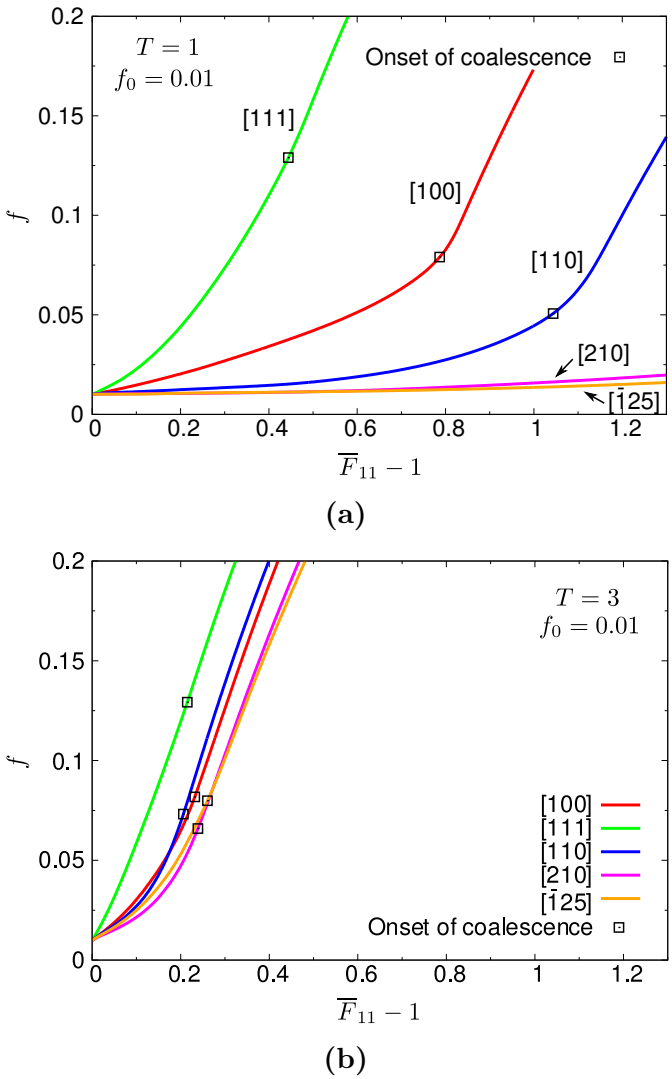

Figure 3.10: Evolution of void volume fraction: (a) effect of stress triaxiality for crystallographic orientation [100], $f_0 = 0.01$ and triaxiality T from 1 to 3, (b) effect of crystallographic orientation for $f_0 = 0.01$ and stress triaxiality $T = 1$ and (c) effect of crystallographic orientation for $f_0 = 0.01$ and stress triaxiality $T = 3$.

the stress triaxiality $T = 3$. Generally, the void growth rate depends on the crystallographic orientation. The effect of crystallographic orientation is significant when the stress triaxiality is small ($T = 1$ as in fig. 3.10a), which is in agreement with the results of Yerra et al. (2010) for BCC single crystals and those of Ha and Kim (2010) for FCC single crystals. However, the influence of the orientation becomes much weaker at high stress triaxiality ($T = 3$ as in fig. 3.10b). Moreover, in both cases of $T = 1$ and $T = 3$, the void growth rate is significantly higher in the [111] orientation than the other orientations, which is in good agreement with the previous analysis. A significant result from this calculation is the very limited void growth and the quasi-incompressible response for the [210] and [$\bar{1}$25]

orientations at low stress triaxiality $T = 1$.

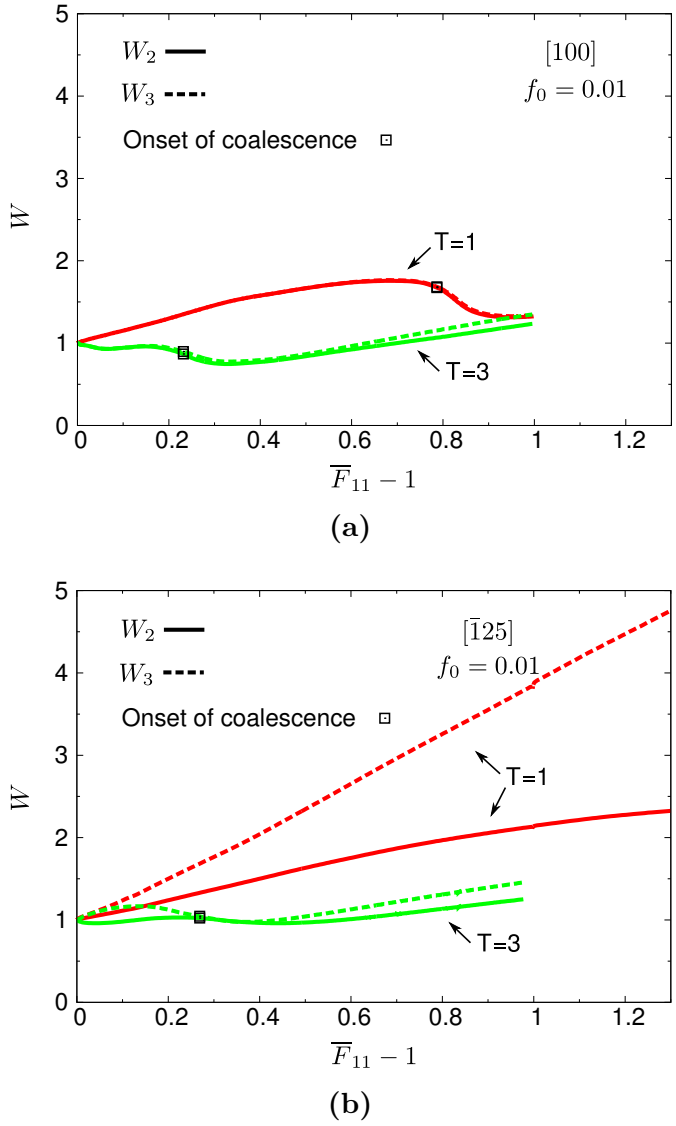

Figure 3.11: Evolution of void aspect ratios W_2 and W_3 for (a) the crystallographic orientation [100] and (b) [$\bar{1}$25] with triaxiality $T = 1$ and $T = 3$.

Void aspect ratios are also investigated, allowing to characterise the evolution of the void shape. The evolution of two aspect ratios $W_2 = \frac{R_1}{R_2}$ and $W_3 = \frac{R_1}{R_3}$ are presented in fig. 3.11a for the [100] orientation and in fig. 3.11b for the [$\bar{1}$25] orientation with the initial void volume fraction $f_0 = 0.01$. R_i $(i = 1, 2, 3)$ is the length from the centre of void to the node at the initial pole of the void surface in the x_i direction. Two levels of stress triaxiality $T = 1$ and $T = 3$ are considered here. For both orientations, the aspect ratios become larger than 1 before void coalescence at $T = 1$, which implies a void elongation in the main loading direction at low stress triaxiality. For the [100] orientation at $T = 3$, the void aspect ratios

decrease without exceeding the value of 1 before the onset of coalescence, which leads to an oblate shape of the void. For the $[\bar{1}25]$ orientation at $T = 3$, the void aspect ratio W_2 remains close to 1 and W_3 becomes somewhat larger than 1 before the onset of coalescence. For symmetry reasons, W_2 is equal to W_3 for the [100] orientation at both high and low stress triaxiality. However, W_3 becomes much larger than W_2 for the $[\bar{1}25]$ especially at low stress triaxiality, which can be explained by the anisotropy in the transverse plane x_2–x_3 of the unit cell. It can also be observed that the difference in the evolution of the void aspect ratios between the [100] orientation and the $[\bar{1}25]$ orientation is much more significant at low stress triaxiality than that at high stress triaxiality.

3.3.4 Field of total accumulated slip

The total accumulated slip γ_{cum}, defined as

$$\gamma_{cum} = \sum_{s=1}^{12} \gamma^s, \tag{3.39}$$

is used to display the field of plastic slip around the void, and to explain some results obtained about void growth. The total accumulated slip fields in the middle x_1–x_2 and x_1–x_3 cross sections (the definition of the cross sections is shown in fig. 3.4a) of the unit cell are shown for the stress triaxialities $T = 1$ in fig. 3.12 and $T = 3$ in fig. 3.13 with the [100], [111] and $[\bar{1}25]$ orientations and the initial void volume fraction $f_0 = 0.01$ at $\overline{F}_{11} - 1 = 0.1$. The fine mesh ($n = 10$, see fig. 3.5b) is used here to obtain the plastic slip field with more accurate local results. Recall that the macroscopic responses obtained with the fine mesh are identical to those with the coarse mesh, as shown in fig. 3.6. For symmetry reasons, the surfaces of the unit cell remain planes and the unit cell keeps its cubic shape during loading for the [100] orientation. For the other orientations, the unit cell does not remain cubic during loading, as a result of lattice re-orientation and shearing of the mesh.

It is observed that for each configuration (crystallographic orientation and stress triaxiality) a different pattern of plastic slip localisation develops. For example, for the [100] orientation at $T = 1$ and $T = 3$, the unit cell shows a symmetric cross shaped localisation zone and the field in the x_1–x_2 cross section is the same as that in the x_1–x_3 cross section, as expected from matrix material symmetries. However, such symmetry is not observed for the two other orientations. For almost all six cases, the plastic slip is highly localised around the void, i.e., the red zone, except for the $[\bar{1}25]$ orientation at $T = 1$, where the localisation around the void is much weaker. A zone where no slip system is activated, i.e., the blue zone,

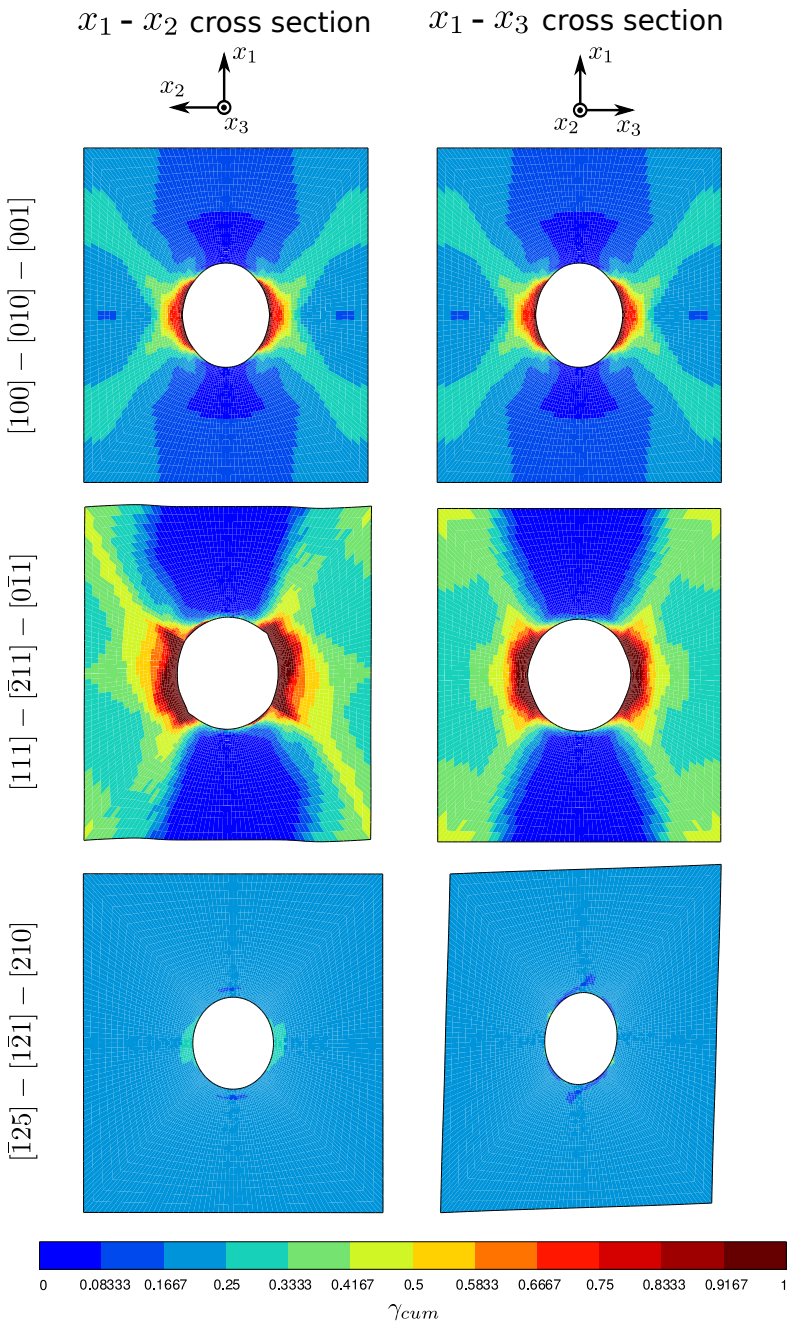

Figure 3.12: Fields of accumulated plastic slip γ_{cum} in the x_1–x_2 (left column) and x_1–x_3 (right column) cross sections of the fine unit cell mesh ($n = 10$) for three crystallographic orientations and stress triaxiality $T = 1$ with the overall deformation $\overline{F}_{11} - 1 = 0.1$. The initial void fraction is $f_0 = 0.01$.

is observed in all cases, except for the $[\bar{1}25]$ orientation at $T = 1$. In the case of the $[\bar{1}25]$ orientation at $T = 1$, the activation of the slip systems is nearly homogeneous in the matrix and it is found that only one slip system is activated

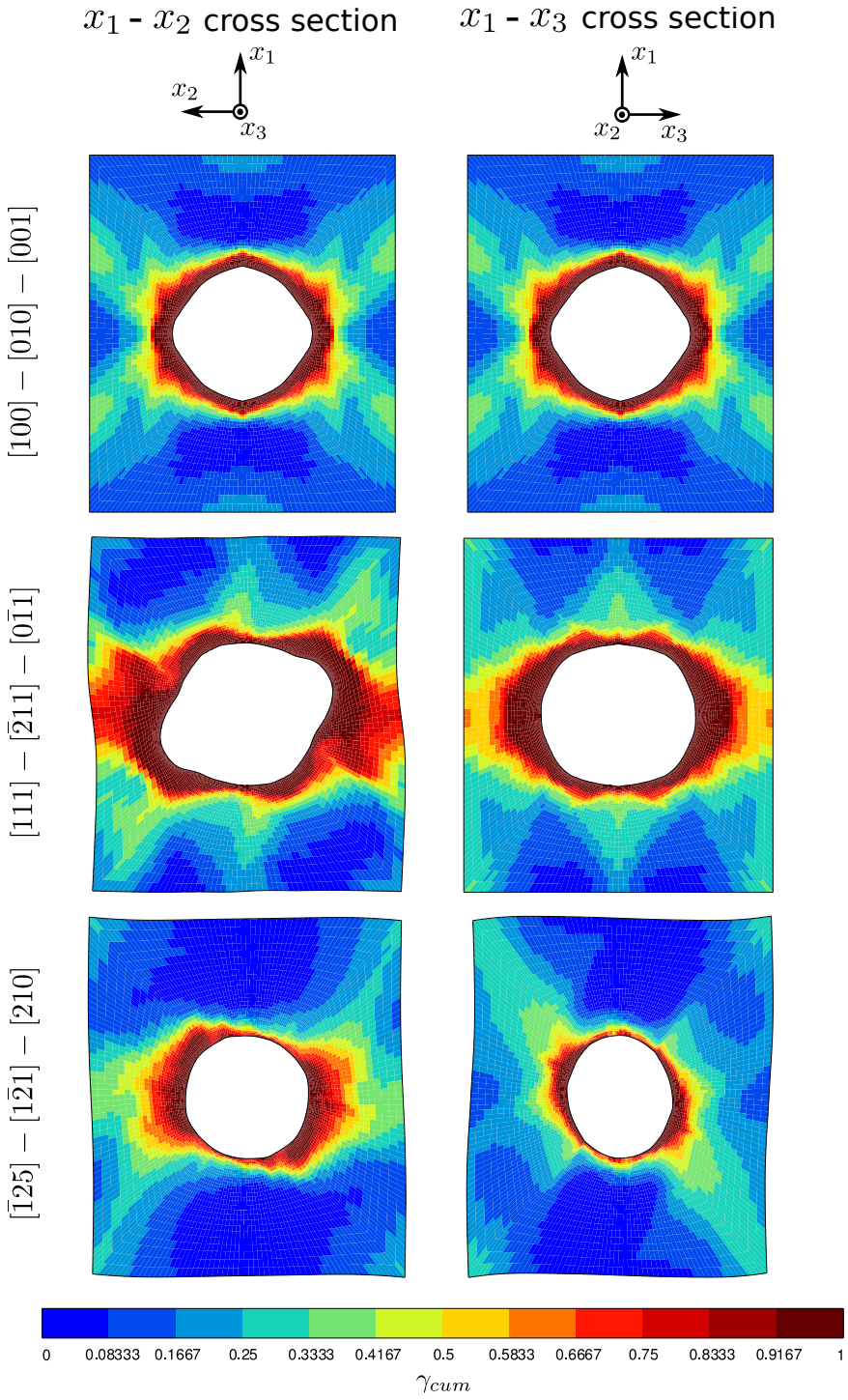

Figure 3.13: Fields of accumulated plastic slip γ_{cum} in the x_1–x_2 (left column) and x_1–x_3 (right column) cross sections of the fine unit cell mesh ($n = 10$) for three crystallographic orientations and stress triaxiality $T = 3$ with the overall deformation $\overline{F}_{11} - 1 = 0.1$. The initial void fraction is $f_0 = 0.01$.

almost everywhere in the matrix except in the vicinity of the void. One can conclude that the plastic slip heterogeneity introduced by the void in the matrix is negligible for the [$\bar{1}$25] orientation at low stress triaxiality, but that the plastic slip heterogeneity will increase with stress triaxiality.

Figure 3.12 and fig. 3.13 also show the void shape at $\overline{F}_{11} - 1 = 0.1$. The elongation of the void in the x_1 axes can be observed at $T = 1$ for the three orientations. For the [100] orientation at $T = 3$, the void evolves into a polygon-like shape. For [111] at $T = 3$, the void is of lemon-like shape in the x_1–x_2 cross section and polygon-like in the x_1–x_2 cross section. For [$\bar{1}$25] at $T = 3$, one can see that the cut of the void in the x_1–x_2 cross section is almost a circle, i.e. $R_1 = R_2$ remains, however the void is elongated in the x_1–x_3 cross section. These results are in good agreement with the results shown in fig. 3.11.

3.3.5 Field of lattice rotation

The polar decomposition of the elastic part of deformation gradient $\underset{\sim}{\boldsymbol{E}}$ follows

$$\underset{\sim}{\boldsymbol{E}} = \underset{\sim}{\boldsymbol{R}}.\underset{\sim}{\boldsymbol{U}}, \tag{3.40}$$

with the rotation tensor $\underset{\sim}{\boldsymbol{R}}$ and the right stretch tensor $\underset{\sim}{\boldsymbol{U}}$. Neglecting the elastic distortion $\underset{\sim}{\boldsymbol{U}}$, $\underset{\sim}{\boldsymbol{R}}$ can be interpreted as the lattice rotation. The corresponding rotation angle θ is given by

$$\theta = \arccos \frac{1}{2}(\operatorname{trace} \underset{\sim}{\boldsymbol{R}} - 1). \tag{3.41}$$

The fields of θ (in radian) in the middle x_1–x_2 and x_1–x_3 cross sections are shown for the [100], [111] and [$\bar{1}$25] orientations with the initial void volume fraction $f_0 = 0.01$ and the stress triaxiality $T = 1$ in fig. 3.14 and $T = 3$ in fig. 3.15 at $\overline{F}_{11} - 1 = 0.1$. At $T = 1$, lattice rotation occurs mainly around the void for [100] and [111], while it is almost homogeneous in the matrix for [$\bar{1}$25]. This is consistent with the fields of total accumulated slip observed in section 3.3.4. For [$\bar{1}$25], the quasi-homogeneous lattice rotation in the matrix leads to void-free-like macroscopic behaviour of the unit cell, i.e., the unit cell exhibits nearly pure shear, for a single slip orientation, in terms of macroscopic deformation pattern. At $T = 3$, the lattice rotation around the void is more significant compared with that at $T = 1$. In particular, the field of θ is no longer quasi-homogeneous for the [$\bar{1}$25] orientation and the macroscopic deformation deviates from homogeneous shear.

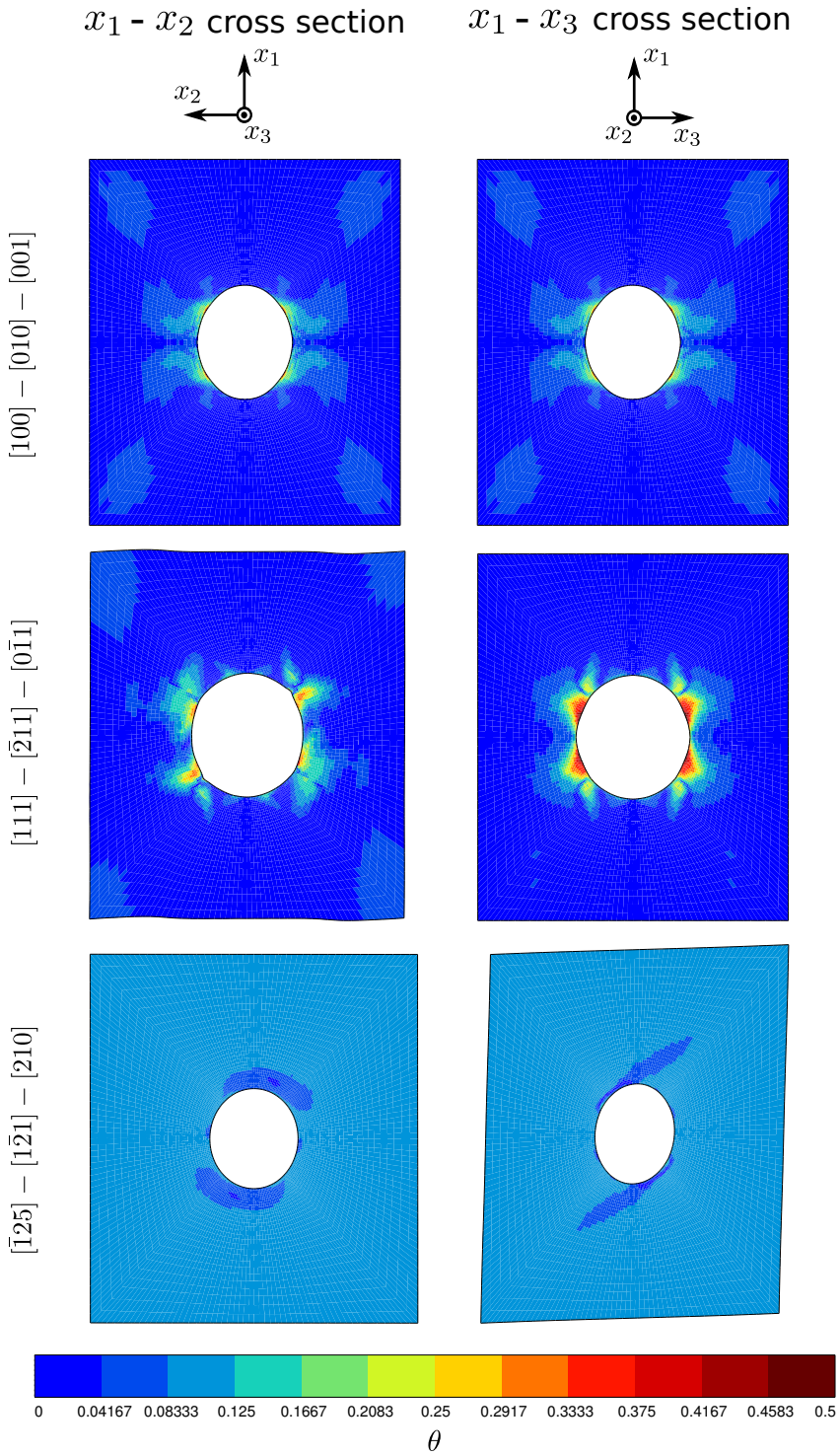

Figure 3.14: Lattice rotation θ (in radian) in the x_1–x_2 (left column) and x_1–x_3 (right column) cross sections of the fine unit cell mesh ($n = 10$) for three crystallographic orientations and stress triaxiality $T = 1$ with the overall deformation $\overline{F}_{11} - 1 = 0.1$. The initial void fraction is $f_0 = 0.01$.

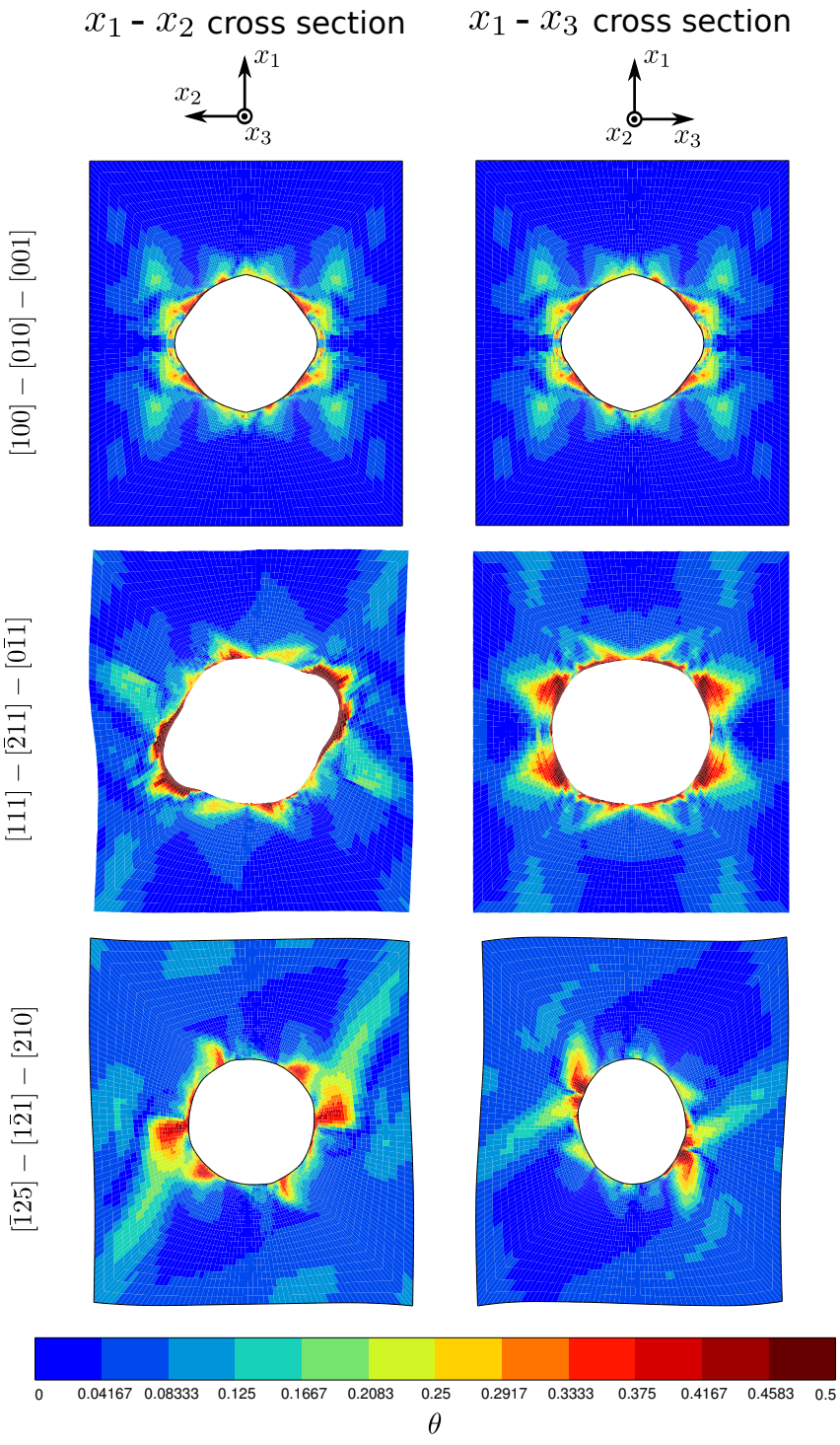

Figure 3.15: Lattice rotation θ (in radian) in the x_1–x_2 (left column) and x_1–x_3 (right column) cross sections of the fine unit cell mesh ($n = 10$) for three crystallographic orientations and stress triaxiality $T = 3$ with the overall deformation $\overline{F}_{11} - 1 = 0.1$. The initial void fraction is $f_0 = 0.01$.

3.3.6 Slip sectors

The number of activated slip systems is investigated. In all the simulations, plastic deformation always begins in single slip in some regions near the void. The plastic regions expand and single slip quickly evolves into multiple slip. These results are different from the observation of Kysar et al. (2005) who showed the slip sectors in the regions near the void within which the material points deformed plastically in single slip. The transition of slip sectors from single slip to multiple slip in the present work is closely related to the hardening laws that are used.

In fig. 3.16, the number of activated slip systems are shown in the elements bounding the void at $\overline{F}_{11} - 1 = 0.005$ for $T = 1$ and at $\overline{F}_{11} - 1 = 0.003$ for $T = 3$, before a dramatic change of the void shape. The [100], [111] and [$\bar{1}$25] orientations are considered. The slip sectors display regular structures determined by the crystallographic orientation and the stress triaxiality. For the three orientations with the stress triaxiality $T = 1$, the plastic slip occurs in some parts near the void but the rest remains elastic. The structures of slip sectors, including their geometry and the number of activated systems, vary from one to another. Under the high stress triaxiality $T = 3$, the slip sectors cover the whole void for the three orientations. Notice that the the slip sectors of the different orientations display very similar structure (both the geometry and the number of activated systems) with only an orientation deviation between them.

For the different orientations, the multiple slip sectors are shown to be different at $T = 1$ but similar at $T = 3$. This observation is consistent with that on the total accumulated slip in section 3.3.4, which shows the different slip localisation modes at $T = 1$ but the slip localisation covering the void for all the orientations considered at $T = 3$. These results may be one of possible reasons explaining the observation of significant orientation effects on void growth at $T = 1$ but reduced effects at $T = 3$.

3.3.7 Void coalescence

Figure 3.17a presents the evolution of the critical strain $\overline{F}_{11c} - 1$ for the onset of void coalescence with respect to the stress triaxiality T for different orientations with the initial void volume fraction $f_0 = 0.01$. For the [210] and [$\bar{1}$25] orientations, the simulations are not able to provide coalescence at low stress triaxiality, even though the longitudinal macroscopic strain $\overline{F}_{11c} - 1$ reaches 130%. This is related to extremely low void growth rate for these two orientations at low stress triaxiality. For all the orientations, the critical strain $\overline{F}_{11c} - 1$ decreases with increasing stress triaxiality T. This result agrees with the observation of Yerra et al. (2010)

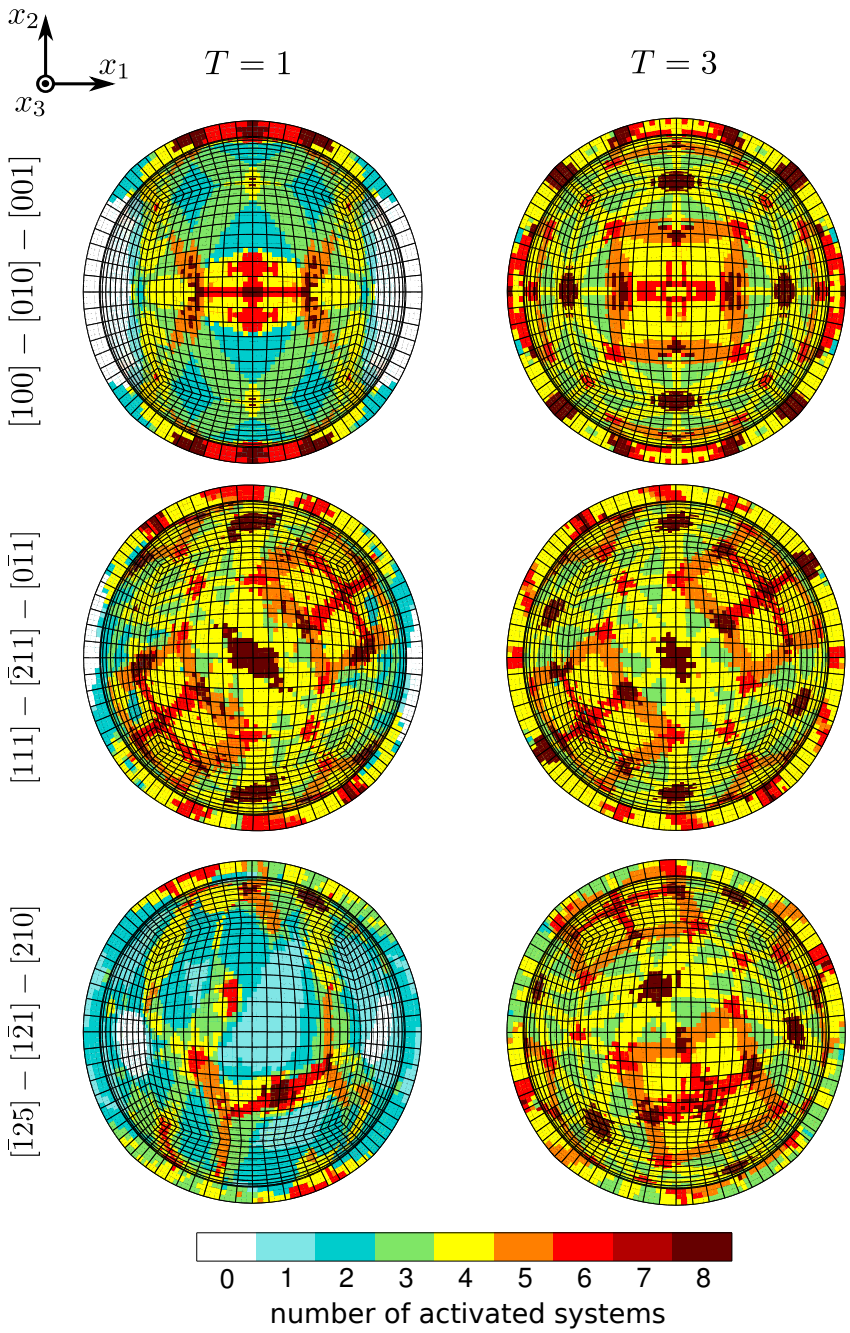

Figure 3.16: Slip sectors for the different orientations in the elements bounding the void for $T = 1$ at $\overline{F}_{11} - 1 = 0.005$ and for $T = 3$ at $\overline{F}_{11} - 1 = 0.003$. Half of the void is shown.

for BCC single crystals. The difference of the critical strain $\overline{F}_{11c} - 1$ between different orientations is significant at low stress triaxiality, but less pronounced at high stress triaxiality.

Once the critical strain $\overline{F}_{11c} - 1$ for the onset of void coalescence has been determined, the corresponding critical void volume fraction f_c for the void coalescence can readily be obtained. In fig. 3.17b, the critical void volume fraction

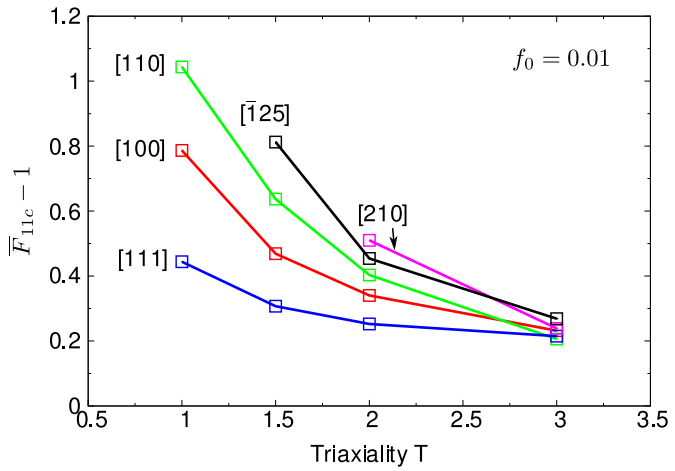

(a)

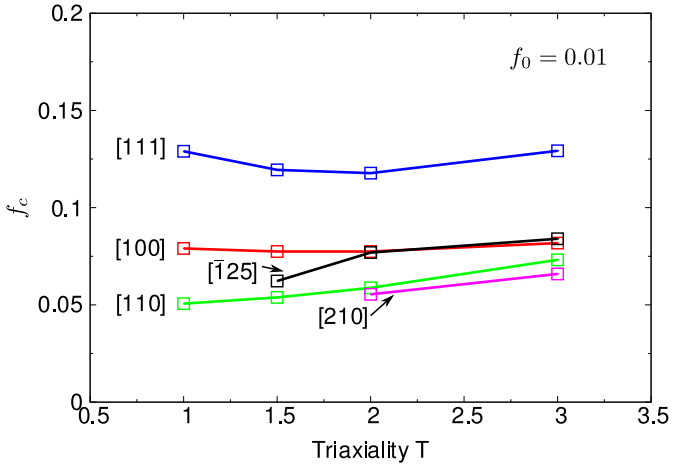

(b)

Figure 3.17: Effect of stress triaxiality and crystallographic orientation on (a) the critical deformation $\overline{F}_{11c} - 1$ and (b) the critical void volume fraction f_c at the onset of coalescence for various crystallographic orientations and fixed initial void volume fraction $f_0 = 0.01$.

f_c is plotted as a function of stress triaxiality T for different orientations with $f_0 = 0.01$. With the stress triaxiality T varying from 1 to 3, the critical void volume fraction f_c appears sensitive to the orientation but almost not sensitive to triaxiality. As f_c is nearly constant and void growth is more rapid at high stress triaxiality, the onset of coalescence occurs at smaller values of macroscopic deformation for high stress triaxiality. These results motivate the introduction of a criterion for the onset of void coalescence in single crystals which can incorporate the strong dependence of the critical void volume fraction on the crystallographic orientation.

The above results are presented only for one initial void volume fraction $f_0 = 0.01$. Unit cell simulations with larger or smaller initial void volume fractions show similar

influences of stress triaxiality and crystallographic orientation on the overall stress strain response and void evolution. For the sake of clarity, these results have not been reported in this section, but they will be used for the assessment of the macroscopic porous single crystal model presented in the next section.

3.3.8 Conclusions

Unit cell simulations have been performed in this section for investigating void growth and coalescence in unirradiated FCC single crystals. Effects of two parameters, i.e., stress triaxiality and crystal orientation, are studied.

The unit cell simulations have shown the dependence of overall stress strain response on the stress triaxiality and the crystallographic orientation. The [111] orientation exhibits harder response compared to the other orientations considered. Void growth rate has been found to increase with stress triaxiality for a given crystal orientation. The void growth also displays an orientation dependence which is more significant at lower stress triaxialities than higher stress triaxialities. In particular, a quasi absence of void growth is observed for the $[\bar{1}25]$ orientation with small initial void volume fraction at low stress triaxiality, which leads to quasi-incompressible overall behaviour. In addition, the critical void volume fraction f_c for the onset of coalescence highly depends on crystallographic orientation, while it is almost not influenced by stress triaxiality varying from 1 to 3 for a given crystallographic orientation.

Having understood mechanical behaviors of voided single crystals whose matrix is governed by hardening laws for unirradiated crystals, effects of post-irradiation hardening/softening laws on void growth and coalescence will be studied in the next section.

3.4 Results for irradiated single crystals

UC simulations are also carried out for irradiated single crystals with the coarse mesh ($n = 5$, see fig. 3.5a). Three crystal orientations are considered: [100], [111] and $[\bar{1}25]$. The material parameters used in the simulations were identified in the work of Han (2012) for 304L stainless steels irradiated up to 13 dpa.

The identification of the material parameters was performed by fitting a polycrystalline aggregate FE model response to the tensile test results of Pokor and his co-workers (Pokor et al., 2004a; Pokor et al., 2004b) at 340 °C. Note that, different from in section 3.3, the values of $a_1, a_2, \cdots, a_6$ are obtained by discrete dislocation dynamics (Monnet, 2009). The initial dislocation density is supposed to

C_{11}	C_{12}	C_{44}	n	τ_{ref}	$\dot{\gamma}_{\text{ref}}$
199 GPa	136 GPa	105 GPa	15	6.3 MPa	$10^{-3}\,\text{s}^{-1}$
τ_T^s	μ	g_c	κ	b_D	b_L
88 MPa	66 GPa	2.64 nm	42.8	2.54 Å	2.08 Å
a_1	a_2	a_3	a_4	a_5	a_6
0.124	0.124	0.07	0.625	0.137	0.122
b_1	b_2	b_3	b_4	b_5	b_6
0	1	1	1	1	1

	0 dpa	13 dpa
ϕ_L	-	7.3 nm
α_L	-	0.57
k_{dl}	-	1.7×10^{-7}
A	-	1.25×10^{-12} m^2
ρ_L^{sat}	-	10^{22} m^{-3}
τ_a	-	61.2 MPa
γ_0	-	5×10^{-3}
$\rho_D^s\|_{\text{ini}}$	8.3×10^8 m^{-2}	1.6×10^8 m^{-2}
$\rho_L^p\|_{\text{ini}}$	-	1.6×10^{22} m^{-3}

Table 3.6: Material parameters for the simulations (Han, 2012).

be equal for every system. Hence, the initial value of the dislocation density for system s is $\rho_D^s|_{\text{ini}} = \rho_D^{\text{tot}}/12$, where ρ_D^{tot} is the total dislocation density measured in experiments. The same hypothesis is made for the density of Frank loops and each system has an initial value of Frank loop density following $\rho_L^p|_{\text{ini}} = \rho_L^{\text{tot}}/4$ with the total Frank loop density being ρ_L^{tot} (Renault et al., 2010). b_D is the norm of the Burgers vector $\frac{1}{2}a\langle 110\rangle$ of dislocations and b_L is the norm of the Burgers vector $\frac{1}{2}a\langle 111\rangle$ of Frank loops. Two cases, unirradiated (0 dpa) and irradiated (13 dpa), are taken into account in the following simulations for emphasizing effects of the post-irradiation hardening/softening behavior on void growth and coalescence. The parameters for the two cases are listed in table 3.6.

3.4.1 Void-free single crystal: a reference

Simulations are first performed using a single finite element. The results will provide a reference for comparisons with the porous single crystal. Figure 3.18a shows the evolution of the overall first Piola–Kirchhoff stress component $\overline{S}_{11}$ with respect to the strain measure $\overline{F}_{11} - 1$ of the void-free single crystal (dashed lines) for the unirradiated state (0 dpa) and the irradiated state (13 dpa) for the [100] orientation at $T = 1$. Recall that the first Piola–Kirchhoff stress corresponds to the engineering stress in uniaxial tension, which can be directly compared with experimental results.

For 0 dpa, a strain hardening regime can be observed, which is related to the interaction among dislocations considered in Eqs. (3.20) and (3.22). With increasing strain, $\overline{S}_{11}$ decreases slightly, since $\overline{S}_{11}$ is evaluated on the undeformed section. This corresponds to the cross section area reduction of the unit cell due to finite strains. Note that the Cauchy stress $\overline{\sigma}_{11}$ is increasing in that case due to hardening and to the absence of damage. Compared to the behavior at 0 dpa, the void-free single crystal at 13 dpa displays a marked increase of the yield stress and a sharp softening at the beginning of the plastic regime followed by a slight hardening. This sharp softening corresponds, according to the observation in the experiments (Pokor et al., 2004a; Pokor et al., 2004b), to the unpinning term in Eq. (3.22). In fig. 3.18b, stress–strain curves are presented for $T = 3$. As expected, the maximum stresses at $T = 3$ are larger than those at $T = 1$.

The stress–strain curves are also shown in fig. 3.19 for the [111] orientation and fig. 3.20 for $[\bar{1}25]$. The [111] orientation exhibits similar stress–strain response as the [100] orientation. A higher stress level is reached due to the lower Schmid factor of primary slip systems (see table 3.4). However, the $[\bar{1}25]$ orientation displays a different response. Recall that the $[\bar{1}25]$ orientation has only one primary slip system ($s = 1$) and one secondary slip system ($s = 12$). For 0 dpa, a change in the hardening rate can be observed, which is associated with the activation of the secondary slip system leading to greater strain hardening. At 13 dpa and before the activation of the second slip system, results show the initial load drop (unpinning term) followed by a limited hardening. The activation of the secondary system at about $\overline{F}_{11} - 1 = 0.25$ has several consequences: (1) it activates the unpinning term of Eq. (3.22) for $s = 12$, as γ^{12} starts to increase, causing a dramatic drop in its slip resistance (indicated by a arrow in fig. 3.22b); (2) it annihilates Frank loops in the slip plane $p = 4$, resulting in a decrease in the Frank loop density ρ_D^4 (see fig. 3.21b); (3) the decreasing Frank loop density leads to a small reduction in the component of the athermal slip resistance related with the dislocation-loop interaction, i.e., loop term in Eq. (3.22), for the slip system $s = 1$ and $s = 12$ (see the blue lines in figs. 3.22a and 3.22b). After this transient evolution, a smooth load decrease is once again observed due to cross section reduction.

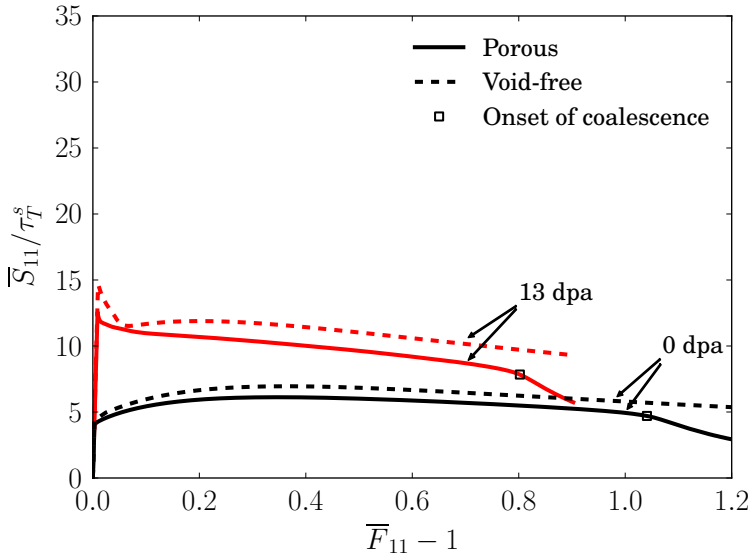

(a)

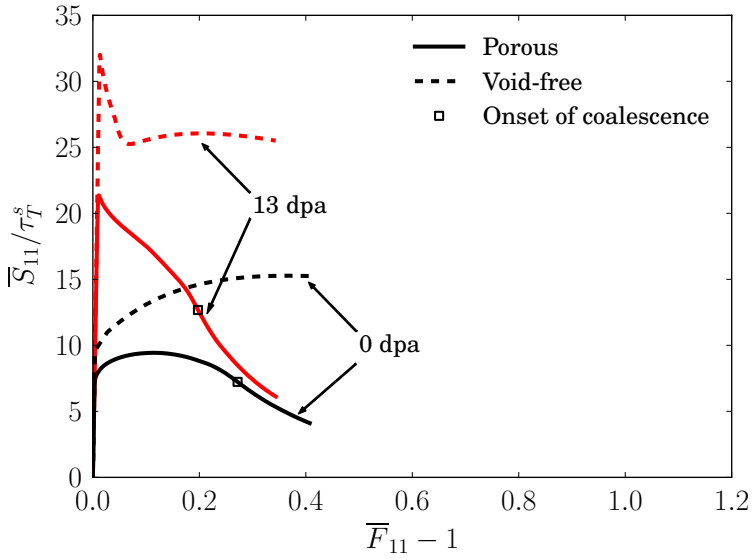

(b)

Figure 3.18: Overall stress–strain curves of unit cells with void ($f_0 = 0.01$, solid lines) and without void (dashed lines) at irradiated and unirradiated state. The crystallographic orientation is [100]–[010]–[001]. (a) $T = 1$, (b) $T = 3$.

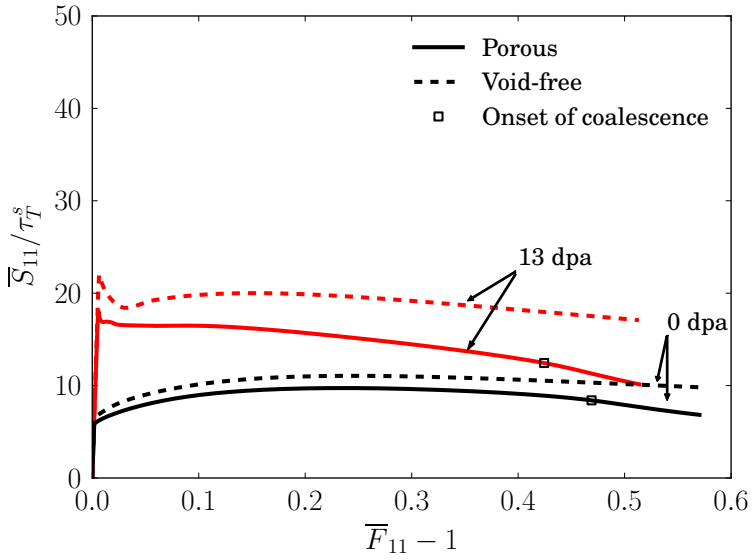

(a)

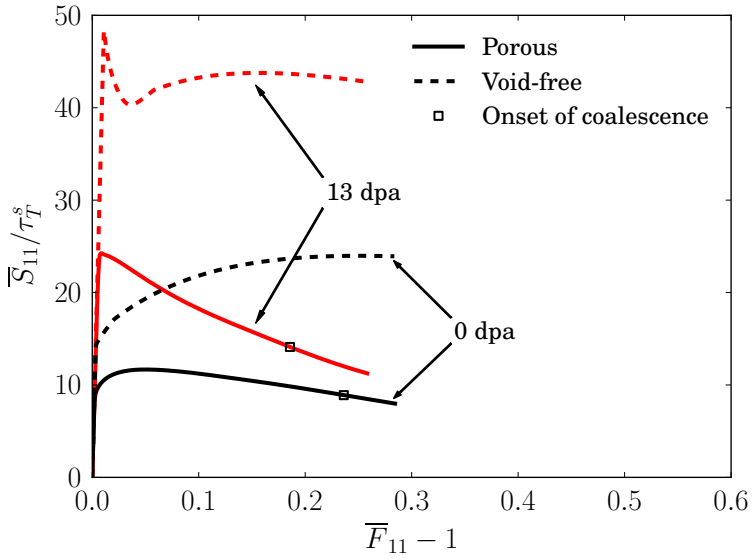

(b)

Figure 3.19: Overall stress–strain curves of unit cells with void ($f_0 = 0.01$, solid lines) and without void (dashed lines) at irradiated and unirradiated state. The crystallographic orientation is [111]–[$\bar{2}$11]–[0$\bar{1}$1]. (a) $T = 1$, (b) $T = 3$.

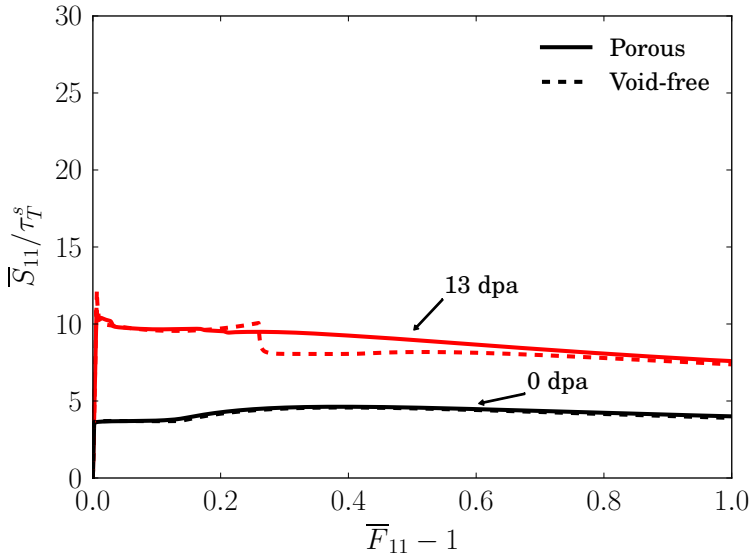

(a)

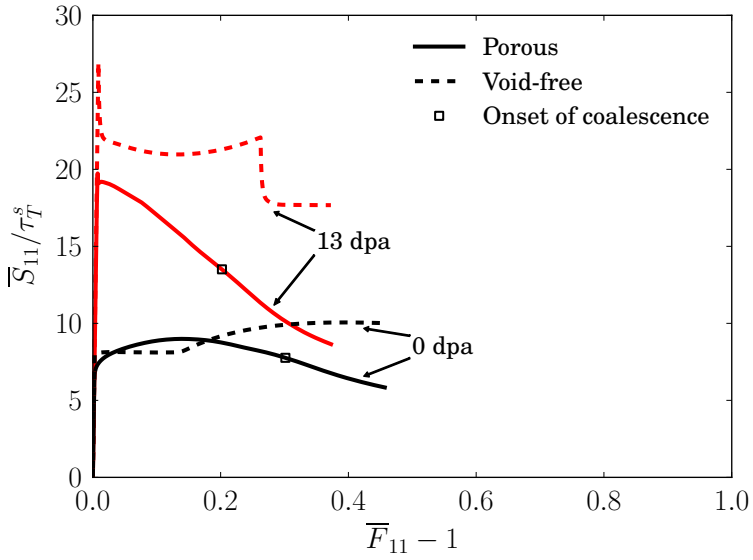

(b)

Figure 3.20: Overall stress–strain curves of unit cells with void ($f_0 = 0.01$, solid lines) and without void (dashed lines) at irradiated and unirradiated state. The crystallographic orientation is $[\bar{1}25]$–$[1\bar{2}1]$–[210]. (a) $T = 1$, (b) $T = 3$.

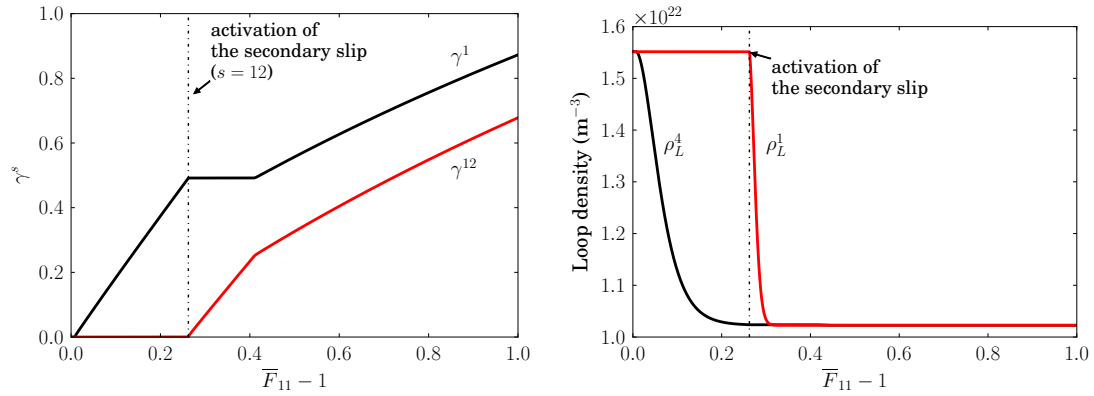

(a) **(b)**

Figure 3.21: Evolution of (a) plastic slip and (b) Frank loop density for the activated systems in irradiated void-free single crystal for $[\bar{1}25]$ at $T = 3$.

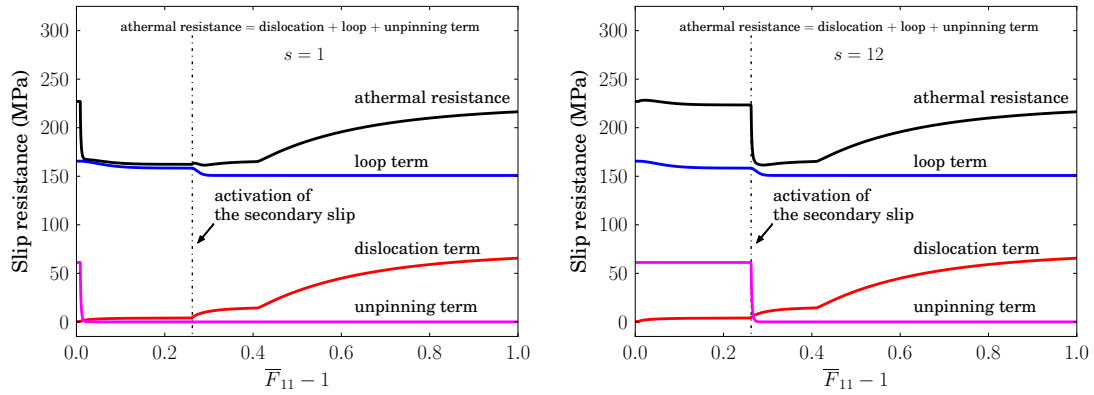

(a) **(b)**

Figure 3.22: Evolution of the athermal slip resistance τ_A^s and its components for the activated systems (a) $s = 1$ and (b) $s = 12$ in irradiated void-free single crystal for $[\bar{1}25]$ at $T = 3$.

3.4.2 Irradiation effects on stress–strain response of the unit cell

Figure 3.18a also presents overall stress–strain responses of the voided single crystal (solid lines) for the [100] orientation at $T = 1$. For the voided single crystal, the stress level that can be reached is reduced compared to the void-free one at both 0 dpa and 13 dpa. Moreover, strain hardening at 0 dpa is weakened and the strain softening at 13 dpa is enhanced because of void growth. After reaching a certain strain level, the stress decreases dramatically due to void coalescence with a greater void growth rate. This trend is in agreement with the work of Koplik and Needleman (1988) on a von Mises material: the onset of void coalescence is characterised by the transition to a uniaxial straining associated to the localization of the plastic flow in the intervoid ligament and a sharp load drop.

With stress triaxiality increasing up to $T = 3$ as shown in fig. 3.18b, strain softening begins earlier than at $T = 1$. Voids also lead to the decrease of the yield stress. This effect is stronger for the irradiated material. The presence of the void induces a plastic strain gradient so that the cell is progressively yielded, which prevents the macroscopic sharp peak load associated with the unpinning term. In addition, the strain hardening regime following initial softening which was observed on the void-free material completely disappears. Instead, the voided single crystal exhibits a strong softening. At the structural level this kind of behavior can lead to strain localization (so called "shear bands") and consequently to a quasi-brittle behavior.

The stress–strains curves are also shown in fig. 3.19 for the [111] orientation and fig. 3.20 for $[\bar{1}25]$. Effects of the voids shown at 0 dpa and 13 dpa for both orientations are similar to those for [100]. However some differences were observed and are described in the following.

For [111], the peak stress drops by about 50% at 13 dpa at $T = 3$ due to the presence of voids. This peak drop is more severe than that observed for [100] and $[\bar{1}25]$. This effect is related to the low Schmid factor of this orientation. As already outlined above, the presence of voids creates a plastic strain gradient so that the local Schmid factor in areas close to the void boundary is higher than the nominal Schmid factor; this promotes an early yielding of the cell.

The presence of the plastic strain gradient around the void strongly influences the cell behavior for the $[\bar{1}25]$ orientation. In the voided single crystal, different slip systems are activated in the vicinity of the void and multiple slip occurs whereas single slip prevails in the sound material. As a result, the single to double slip transition is not observed. In addition, latent hardening is locally triggered at the

early stages of deformation so that the voided crystal may exhibit a higher flow stress up to a given strain where void growth will induce softening (see fig. 3.20b for 0 dpa).

3.4.3 Irradiation effects on void growth

The evolution of the void volume fraction f under a fixed stress triaxiality $T \in \{1, 1.5, 2, 3\}$ is presented in fig. 3.23. As expected, void growth rate increases with the stress triaxiality for whatever orientation. For both unirradiated and irradiated voided single crystals, the void growth rate is the highest for the [111] orientation for all considered triaxialities and a quasi-absence of void growth is predicted for $\bar{1}25$ with $T = 1$. As shown in Ling et al. (2016), this is due to single slip which cannot lead to void growth. For the $[\bar{1}25]$ orientation, however, void growth becomes significant and cannot be neglected as the stress triaxiality reaches $T = 1.5$ as shown in fig. 3.23b.

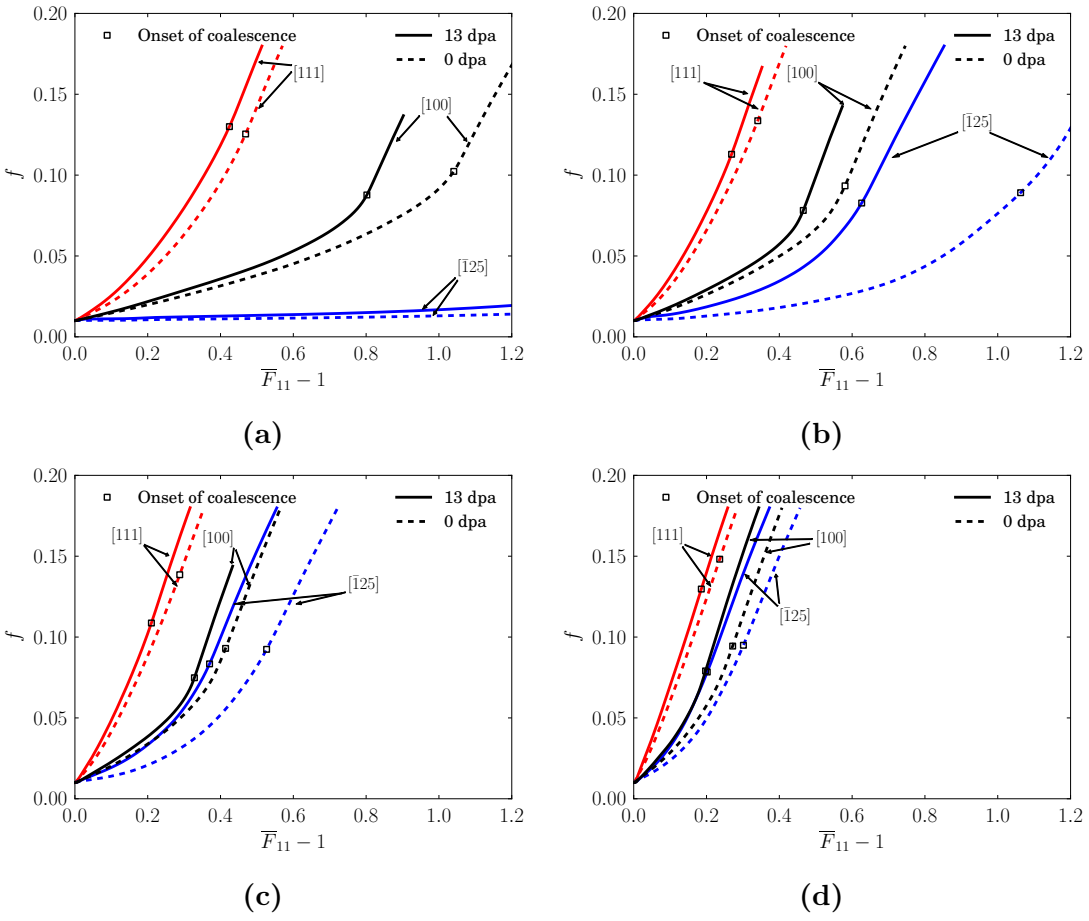

Figure 3.23: Evolution of void volume fraction for three crystallographic orientations under four stress triaxialities: (a) $T = 1.0$, (b) $T = 1.5$, (c) $T = 2.0$ and (d) $T = 3.0$. Solid lines are for irradiated materials and dashed lines for unirradiated materials.

Compared with unirradiated single crystal, a higher growth rate (with respect to the overall strain $\overline{F}_{11}$) is systematically observed in the irradiated crystal before the onset of coalescence for all investigated orientations and triaxialities. The effect of the irradiation is particularly strong at moderate stress triaxialities (i.e. $T = 1.5$ (see fig. 3.23b) and $T = 2$ (see fig. 3.23c)) for the $[\bar{1}25]$ orientation. In those cases, the void growth rate at the beginning of plastic regime is multiplied by 2.5 and 1.7 for the irradiated crystal.

3.4.4 Irradiation effects on onset of coalescence

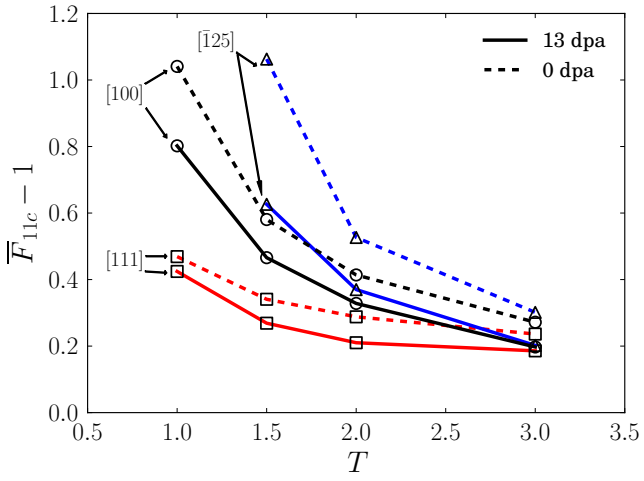

(a)

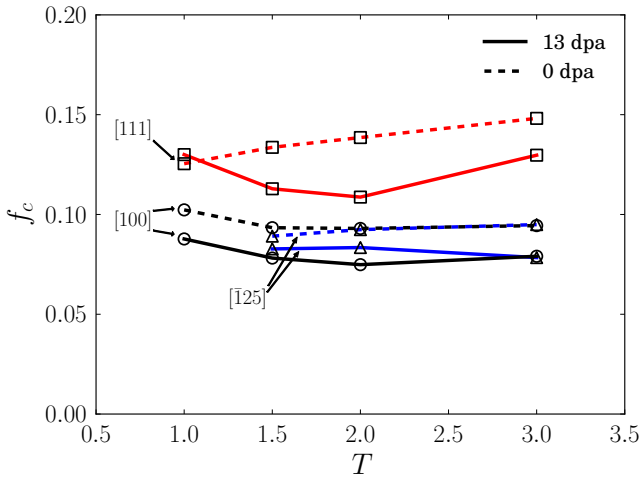

(b)

Figure 3.24: Influence of stress triaxiality and crystallographic orientation on (a) the critical deformation $\overline{F}_{11c} - 1$ and (b) the critical void volume fraction f_c at the onset of coalescence for various crystallographic orientations. $f_0 = 0.01$. Solid lines are for irradiated materials and dashed lines for unirradiated materials.

The onset of void coalescence is determined in the same way as in sections 3.3.2 and 3.3.7: it is determined by plotting the transverse macroscopic strain $\overline{F}_{33} - 1$ as a function of the longitudinal macroscopic strain $\overline{F}_{11} - 1$. It is observed that $\overline{F}_{33} - 1$ reaches a stabilized value. By convention, the time step for which the transverse strain $\overline{F}_{33} - 1$ reaches 99% of its stabilized value, is regarded as the onset of coalescence. The corresponding longitudinal $\overline{F}_{11} - 1$ and porosity are defined as the critical strain $\overline{F}_{11c} - 1$ and critical porosity f_c at the onset of coalescence. The onset of void coalescence is indicated by a hollow square on each curve. In the void coalescence regime, the void growth rate is fully determined by the coalescence kinematics (uniaxial straining).

The critical strain $\overline{F}_{11c} - 1$ for the onset of coalescence is plotted as a function of stress triaxiality T for the three orientations in fig. 3.24a. The decrease of $\overline{F}_{11c} - 1$ with increasing stress triaxiality can be observed for a given orientation. Compared with the unirradiated cases, the onset of coalescence occurs at a smaller strain in the irradiated single crystals. Especially for the $[\bar{1}25]$ orientation, the decrease of $\overline{F}_{11c} - 1$ even reaches about 40% at $T = 1.5$.

The evolution of critical void volume fraction f_c for the onset of coalescence as a function of stress triaxiality T is presented in fig. 3.24b. Considering one crystallographic orientation, f_c is almost unchanged for a given irradiation level. The [111] orientation shows a higher f_c than the [100] and $[\bar{1}25]$ orientations. With stress triaxialities varying from 1.5 to 3, similar values of f_c are predicted for [100] and $[\bar{1}25]$. Given one orientation, the value of f_c of the irradiated single crystals is lower than that of unirradiated ones.

3.4.5 Irradiation effects on fields of accumulated plastic slip

The fields of γ_{cum} in the middle x_1–x_2 cross section (fig. 3.4a) are shown in fig. 3.25 for [100] with $T = 1.5$ ($\overline{F}_{11} - 1 = 0.35$) and $T = 3$ ($\overline{F}_{11} - 1 = 0.2$). The evolution of the void shape is different at different stress triaxialities. In particular, at a relatively low stress triaxiality $T = 1.5$, the void becomes elongated along the loading axis x_1. Moreover, at the same stress triaxiality, a more significant localization of plastic slip is observed in the irradiated case than that in the unirradiated case, especially in the horizontal region near the void. This leads to a larger deformation of the void along the horizontal axis in the irradiated case, resulting in a faster void growth and an earlier void coalescence as shown previously (see fig. 3.23). These results for the irradiated porous single crystal, combined with the rather brittle overall behavior shown previously, are consistent with the experimental observations of Neustroev and Garner (2009) in AISI 321 stainless steels irradiated in BOR-60,

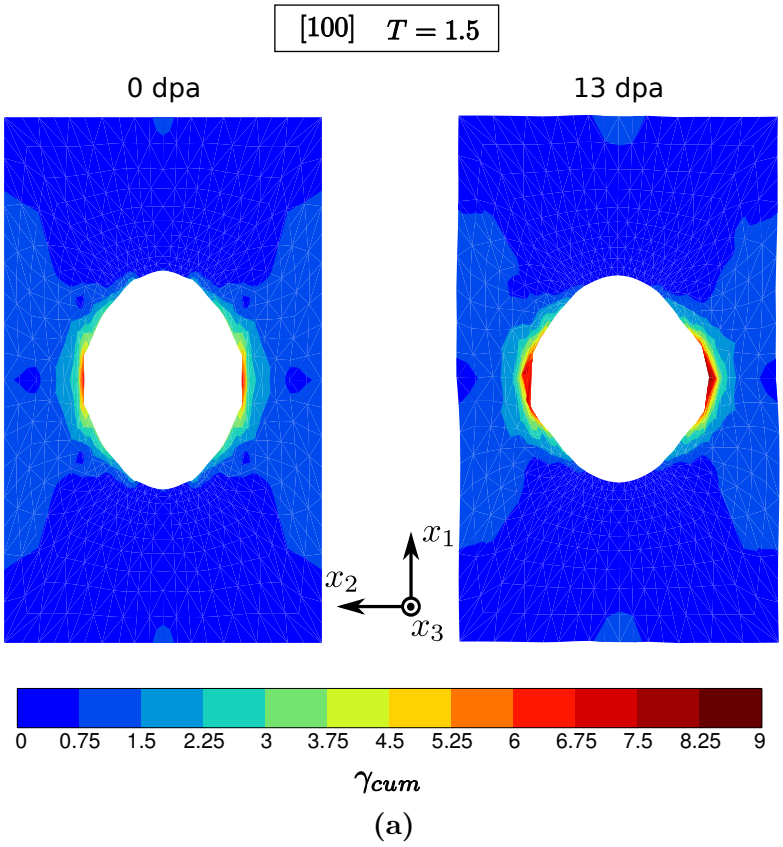

(a)

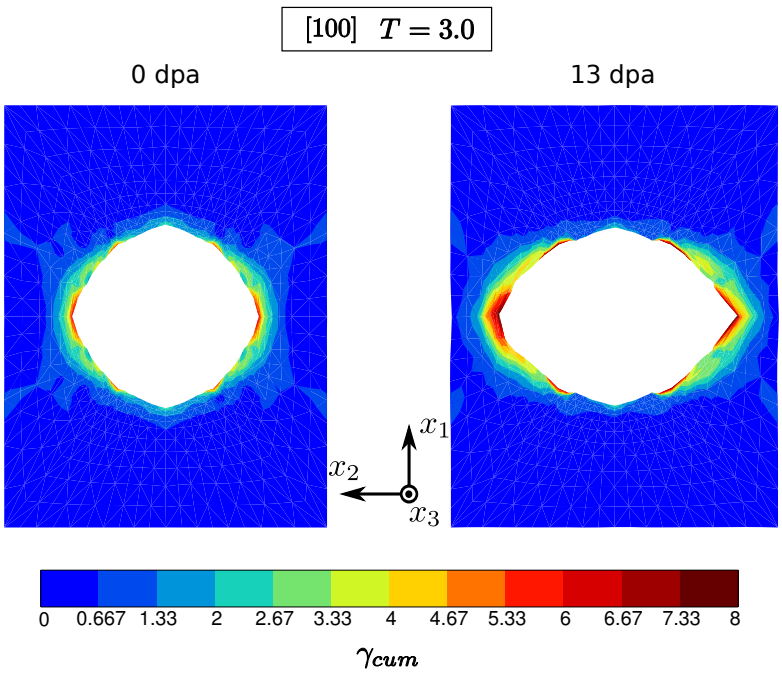

(b)

Figure 3.25: Field of accumulated slip on x_1–x_2 middle cross section on of the unit cell for [100]. (a) $T = 1.5$ and $\overline{F}_{11} - 1 = 0.35$, (b) $T = 3.0$ and $\overline{F}_{11} - 1 = 0.2$.

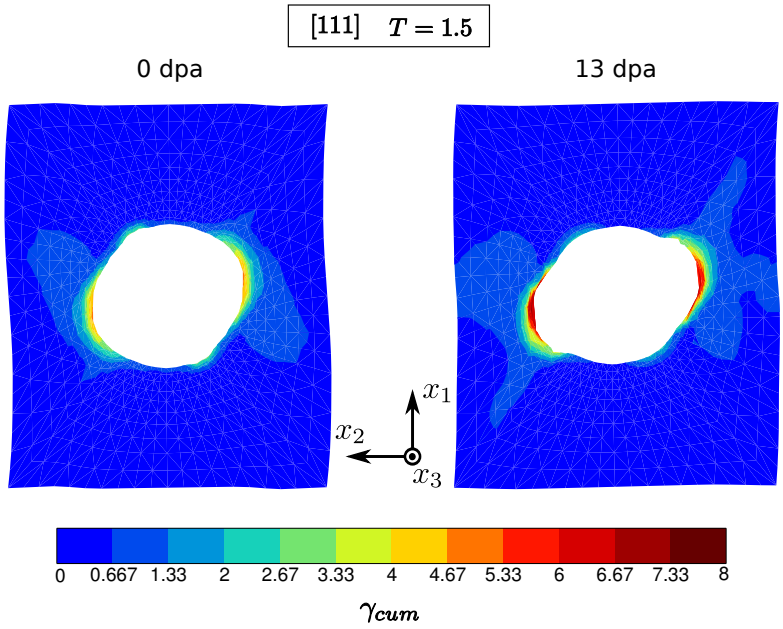

(a)

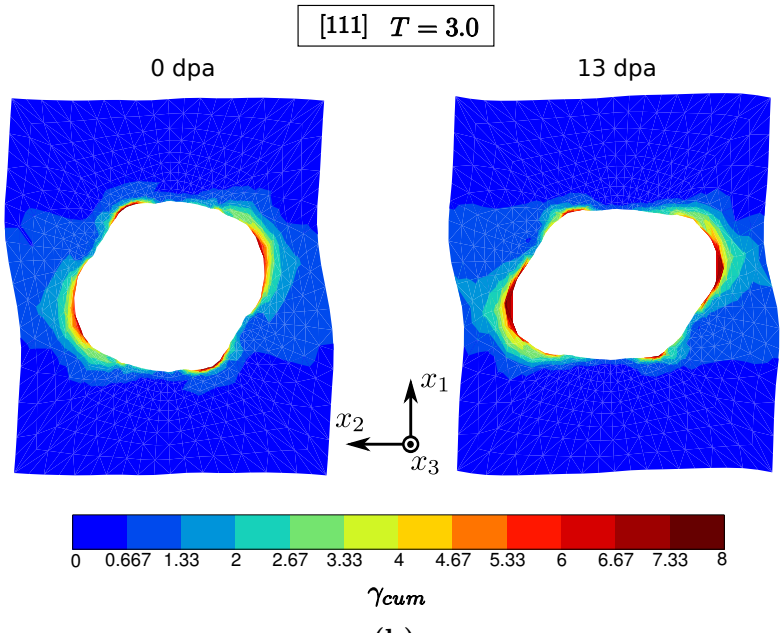

(b)

Figure 3.26: Field of accumulated slip on x_1–x_2 middle cross section on of the unit cell for [111] with (a) $T = 1.5$ and (b) $T = 3.0$. $\overline{F}_{11} - 1 = 0.14$.

which showed an embrittlement after irradiation at the macroscopic level but a large amount of deformation at the failure site showing fine dimples.

The fields of γ_{cum} are presented for [111] and [$\bar{1}$25] in figs. 3.26 and 3.27. For these two orientations, the voids develop different deformed shapes. Especially for [111], a rotation of the void is observed which is caused by the shearing of

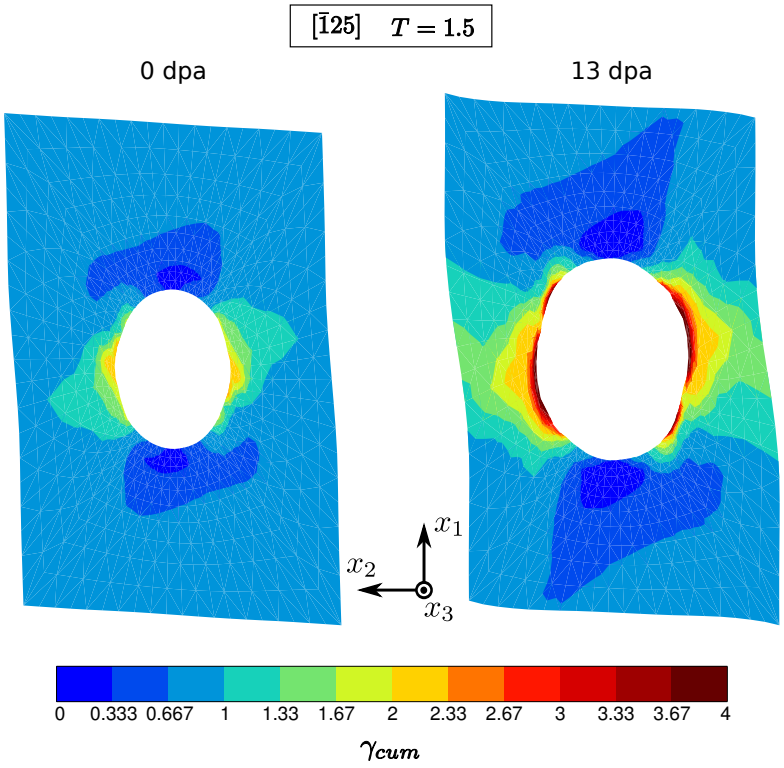

Figure 3.27: Field of accumulated slip on x_1–x_2 middle cross section of the unit cell for $[\bar{1}25]$. (a) $T = 1.5$ and $\overline{F}_{11} - 1 = 0.50$, (b) $T = 3.0$ and $\overline{F}_{11} - 1 = 0.2$.

the matrix, associated with the anisotropy of the single crystal. Besides, the void displays different shapes in other cross sections, e.g., the x_1–x_3 cross section, which has been discussed in section 3.3 and is not discussed here. Furthermore, in the irradiated case, again, more significant plastic slip localization can be seen for [111] and [$\bar{1}$25] than that in the unirradiated cases. Larger voids can be observed in the irradiated cases, especially for [125] at $T = 1.5$ (fig. 3.27a) which is consistent with faster void growth presented in fig. 3.23.

3.4.6 Conclusions

In this section, the void growth and coalescence at constant stress triaxiality in irradiated FCC single crystals are investigated using unit cell FE simulations. A single crystal plasticity model is used accounting for the modification of mechanical properties associated to the irradiation-induced defects. From these unit cell simulations, the following conclusions can be drawn:

- Voids grow at a higher rate in the irradiated single crystal.
- The onset of void coalescence occurs at a smaller value of the overall strain and at a smaller value of the void volume fraction in the irradiated crystals .
- More significant plastic strain localization in the region near the void is predicted in the irradiated crystal, correlated with the faster void growth and earlier onset of void coalescence.
- Brittle-like overall behavior is predicted at high level of stress triaxiality, i.e. $T = 3$, in the voided irradiated crystal, while a large amount of plastic deformation is reached in the vicinity of the void.

It is worth emphasizing that the numerical results showing faster void growth and earlier onset of void coalescence in irradiated single crystals are in agreement with the experimental observation of decreasing fracture toughness with irradiation. Furthermore, enhanced plastic strain localization predicted for irradiated single crystals is also in good agreement with the observations of Neustroev and Garner (2009) in AISI 321 stainless steels irradiated in BOR-60.

3.5 Concluding remarks

In this chapter, unit cell simulations have been performed to investigate void growth in FCC single crystals. Effects of stress triaxiality, crystal orientation and post-irradiation strain hardening/softening have been studied.

In order to investigate influences of irradiation on the fracture toughness of stainless steels, a fracture model is needed. As explained above, voids involved

in ductile fracture process of irradiated steels are often located within grains, i.e., intragranular voids. Due to this fact, a micromechanics model of ductile fracture model will be proposed at the scale of a grain, i.e., a single crystal, in the next chapter. The model aims to account for the effects of different parameters (stress triaxiality, crystal orientation and post-irradiation strain hardening/softening) outlined in this chapter. The model will be assessed based on the results of the unit cell simulations and then applied to study ductile fracture in single crystals and polycrystals.

4

Porous single crystals: an elastoviscoplastic model at finite strains

Résumé

Un modèle élastoviscoplastique en grandes transformations est proposé pour le monocristal poreux dans ce chapitre. Le modèle prend en compte l'effet de l'orientation cristallographique, de la triaxialité des contraintes et de la porosité initiale. En comparant avec les simulations de cellules unitaires, on montre que le modèle est capable de décrire qualitativement la croissance de cavité et la réponse mécanique macroscopique du monocristal poreux. Le modèle est ensuite appliqué à la simulation l'endommagement ductile dans un agrégat polycrystallin et dans une éprouvette monocristalline entaillée.

Contents

A first yield function for single crystals containing voids has been derived by Han et al. (2013) based on a variational approach at infinitesimal strains. The model accounts for the effects of initial void volume fraction, stress triaxiality and crystal orientation. In order to describe ductile fracture in single crystals due to void growth and coalescence, it is needed to introduce finite strain framework. In the present section, only void growth is considered and the porous single crystal model is extended to finite strain by introducing flow rule and evolution law for void growth. In this section, an elastoviscoplastic model at finite strains is formulated based on the model of Han et al. (2013). The model also incorporates heuristically strain hardening of single crystal matrix, in the same manner as that proposed by Tvergaard and Needleman (1984). It is then assessed through three-dimensional unit cell finite element simulations based on periodic homogenisation with prescribed constant stress triaxiality. Axisymmetric and non-axisymmetric loadings are taken into account for the assessment. The model is then applied to simulate ductile damage in polycrystalline aggregates and a single-edge-notch tension test on a single crystal.

4.1 Porous single crystal plasticity model

The porous single crystal plasticity model is formulated within the framework presented in section 3.1. For the sake of brevity, only new notions related to porous single crystals are outlined.

For porous single crystals, it is assumed that, in spite of the presence of pores inside the single crystal volume element and associated inhomogeneous deformation, a unique single crystal lattice orientation can be attributed to each material point. The definition of a unique isoclinic intermediate local configuration C_i is allowed by the existence of directors[1] associated with lattice orientation. The uniqueness of the multiplicative decomposition of the deformation gradient $\underset{\sim}{\boldsymbol{F}} = \underset{\sim}{\boldsymbol{E}}.\underset{\sim}{\boldsymbol{P}}$ thus remains. As a result, the **kinematics** of porous single crystals follows what is described in section 3.1.2, except that $\det(\underset{\sim}{\boldsymbol{P}}) \neq 1$ as a result of compressibility of porous single crystals. The initial porous single crystal orientation is taken that of the undeformed single crystal matrix.

The same number of slip systems N are attributed to each material point of the porous single crystal as the single crystal matrix. They have the same crystallographic definition as that of the undeformed single crystal matrix. For the **flow rule**, the yield criterion developed in the work of Han et al. (2013) for porous single crystals is used. The definition of effective resolved shear stress τ_s^*,

[1] See the footnote in page 56

derived by Han et al. (2013) in the infinitesimal strain framework, is extended to finite strain framework:

$$\Psi^s = \frac{\tau^{s2}}{\tau_s^{*2}} + \alpha\frac{2}{45}f_i\frac{M_{eq}^2}{\tau_s^{*2}} + 2q_1 f_i \cosh\left\{q_2\sqrt{\frac{3}{20}}\frac{M_m}{\tau_s^*}\right\} - 1 - q_1^2 f_i^2 \overset{\text{def}}{=} 0, \tau_s^* \geqslant 0, \quad (4.1)$$

where M_m is the mean stress of Mandel stress defined as $M_m = \frac{1}{3}\text{trace}\,\underset{\sim}{\boldsymbol{M}}$; M_{eq} is the equivalent stress of Mandel stress defined as $M_{eq} = \sqrt{\frac{3}{2}\underset{\sim}{\boldsymbol{M}}' : \underset{\sim}{\boldsymbol{M}}'}$ with the deviatoric part of Mandel stress $\underset{\sim}{\boldsymbol{M}}' = \underset{\sim}{\boldsymbol{M}} - M_m\underset{\sim}{\boldsymbol{1}}$; f_i is the void volume fraction in the intermediate configuration and can be calculated as

$$f_i = 1 - \frac{1 - f_0}{\det\left(\underset{\sim}{\boldsymbol{P}}\right)} \quad (4.2)$$

with the initial void volume fraction f_0. Note that α, q_1 and q_2 are parameters to be identified. The yield function for each slip system, taking the same form of Eq. (3.12), follows

$$\phi^s = \tau_s^* - \tau_c^s \quad (4.3)$$

with the effective resolved shear stress τ_s^* defined above.

The plastic strain rate $\underset{\sim}{\boldsymbol{L}}^p$ can be defined by

$$\underset{\sim}{\boldsymbol{L}}^p = \dot{\underset{\sim}{\boldsymbol{P}}}.\underset{\sim}{\boldsymbol{P}}^{-1} = (1 - f_i)\sum_{s=1}^{N}\dot{\gamma}^s\frac{\partial\phi^s}{\partial\underset{\sim}{\boldsymbol{M}}} = (1 - f_i)\sum_{s=1}^{N}\dot{\gamma}^s\underset{\sim}{\boldsymbol{N}}^{*s}, \quad (4.4)$$

with $\underset{\sim}{\boldsymbol{M}}$ still defined by Eq. (3.11) and

$$\underset{\sim}{\boldsymbol{N}}^{*s} = \frac{\partial\tau_s^*}{\partial\underset{\sim}{\boldsymbol{M}}} = -\left(\frac{\partial\Psi^s}{\partial\tau_s^*}\right)^{-1}\frac{\partial\Psi^s}{\partial\underset{\sim}{\boldsymbol{M}}}, \quad (4.5)$$

where

$$\frac{\partial\Psi^s}{\partial\tau_s^*} = -2\frac{\tau^{s2}}{\tau_s^{*3}} - \frac{4}{45}\alpha f_i\frac{{M_{eq}}^2}{\tau_s^{*3}} - 2\sqrt{\frac{3}{20}}q_1q_2f_i\frac{M_m}{\tau_s^{*2}}\sinh\left(q_2\sqrt{\frac{3}{20}}\frac{M_m}{\tau_s^*}\right) \quad (4.6)$$

and

$$\frac{\partial\Psi^s}{\partial\underset{\sim}{\boldsymbol{M}}} = 2\frac{\tau^s}{\tau_s^{*2}}\underset{\sim}{\boldsymbol{N}}^s + \frac{2}{15}\alpha f_i\frac{1}{\tau_s^{*2}}\underset{\sim}{\boldsymbol{M}}' + \frac{2}{3}\sqrt{\frac{3}{20}}q_1q_2f_i\frac{\sinh\left(q_2\sqrt{3/20}M_m/\tau_s^*\right)}{\tau_s^*}\underset{\sim}{\boldsymbol{1}}. \quad (4.7)$$

Note that $\underset{\sim}{\boldsymbol{L}}^p$ is corrected by the factor $1 - f_i$ resulting from the definition of τ_s^* in Eq. (4.1) which is obtained by the homogenisation in the matrix of porous single crystal excluding the pores. It corresponds to the vanishing plastic work in the pores (Besson, 2009; Besson, 2010). When $f_i = 0$, the model of porous single crystals is reduced to that of void-free single crystals.

The plastic slip rate $\dot{\gamma}^s$, the same as Eq. (3.17), is given by

$$\dot{\gamma}^s = \dot{\gamma}_{\text{ref}}\left\langle\frac{\tau_s^* - \tau_c^s}{\tau_{\text{ref}}}\right\rangle^n, \quad (4.8)$$

where $\dot{\gamma}_{\text{ref}}$ is the reference slip rate and τ_{ref} is a reference resolved shear stress.

The **hardening rule** described in section 3.1.5 holds for porous single crystals.

4.2 Numerical assessment

The simulations results presented in section 3.3 for unirradiated single crystals combined with some additional simulations with non-axisymmetric loadings are used to assess the proposed porous single crystal model at finite strains.

4.2.1 Calibration of model parameters

The overall stress strain curves and the evolution of the void volume fraction obtained by the unit cell simulations with axisymmetric loading are used for calibrating the parameters α, q_1 and q_2 in Eq. (4.1) of the macroscopic porous single crystal model. The calibration has been conducted with the material parameters given in table 3.5 which aim to represent the behavior of a solution annealed 304 austenitic stainless steel. The crystallographic orientations, the initial void volume fractions f_0 and the stress triaxialities T considered for the calibration are summarised in table 4.1.

Test number	Crystallographic orientation	Initial void volume fractions	Stress triaxialities
1	$[100]-[0\bar{1}0]-[001]$	0.005, 0.01, 0.02, 0.05, 0.1	1.0, 1.5, 2.0, 3.0
2	$[110]-[\bar{1}10]-[001]$	0.005, 0.01, 0.02	1.0, 1.5, 2.0, 3.0
3	$[111]-[\bar{2}11]-[0\bar{1}1]$	0.005, 0.01, 0.02, 0.05, 0.1	1.0, 1.5, 2.0, 3.0
4	$[210]-[\bar{1}20]-[001]$	0.005, 0.01, 0.02	1.0, 1.5, 2.0, 3.0
5	$[\bar{1}25]-[1\bar{2}1]-[210]$	0.005, 0.01, 0.02, 0.05, 0.1	1.0, 1.5, 2.0, 3.0

Table 4.1: Crystallographic orientations, initial void volume fractions and stress triaxialities used for the calibration of material parameters α, q_1 and q_2, see Eq. (4.1).

The parameters α, q_1 and q_2 have been identified using Levenberg–Marquardt algorithm and taking into account at the same time the stress–strain response and the evolution of void volume fraction by minimizing the cost function:

$$\mathcal{F} = \frac{1}{F_{11}^t} \int_0^{F_{11}^t} w_1(\sigma_{11} - \overline{\sigma}_{11})^2 + w_2(f_i - f)^2 \, dF_{11}, \tag{4.9}$$

where σ_{11} denotes the component of Cauchy stress tensor of the porous single crystal model, $\overline{\sigma}_{11}$ the component of the macroscopic Cauchy stress tensor of the unit cell, f_i the void volume fraction of the porous single crystal model defined by Eq. (4.2) and f the void volume fraction determined from the unit cell simulations (see Eq. (3.37)). F_{11}^t is chosen to be 1.1, i.e., the calibration is done from the beginning of the loading to the strain value $F_{11} - 1 = 0.1$ (for the porous single crystal model) and $\overline{F}_{11} - 1 = 0.1$ (for the unit cell). This level of macroscopic deformation corresponds to the regime before void coalescence for all the cases considered. In addition, the weight w_1 and w_2 are chosen in such a way that stress and void volume fraction have the same order of contribution to the cost function.

Optimised values of the parameters are given in table 4.2. Note that the obtained calibrated parameters, accounting for the hardening of the matrix and the evolution of the void volume fraction, are slightly different from those determined by Han et al. (2013), where only the yield surface was taken into account. Comparison between the predictions of the porous single crystal model and the results obtained by the unit cell will be presented in the next sections.

	α	q_1	q_2
the present work	5.69	1.60	1.19
Han et al. (2013)	6.46	1.47	1.33

Table 4.2: Identified values of the porous single crystal model parameters, see Eq. (4.1).

4.2.2 Assessment for axisymmetric loading cases

In this part, the porous single crystal model is assessed for axisymmetric loading cases, which were used to calibrate the model parameters.

Figure 4.1 shows the evolution of the normalised Cauchy stress σ_{11}/τ_T^s with respect to the strain $F_{11} - 1$ for the porous single crystal model and that of the normalised macroscopic Cauchy stress $\overline{\sigma}_{11}/\tau_T^s$ with respect to the macroscopic strain $\overline{F}_{11} - 1$ for the unit cell for [100], [111] and [$\bar{1}$25] orientations with $f_0 = 0.01$ at (a) $T = 1$ and (b) $T = 3$. To simplify the notation, the overline for the macroscopic variables of the unit cell will be dropped in the following (e.g., F_{11} instead of $\overline{F}_{11}$). As void coalescence is not incorporated in the porous single crystal model, the curves are plotted before void coalescence predicted by the unit cell simulations. At low stress triaxiality $T = 1$, the porous single crystal model successfully predicts the tendency of the orientation effect on the stress strain response. However the model slightly overestimates the strain hardening for the [100] and [111] orientations and underestimates the strain hardening for the [$\bar{1}$25] orientation. This can imply that the model will underestimate the void growth for the [100] and [111] orientations and overestimate the void growth for the [$\bar{1}$25] orientation, which will be confirmed in the next section. At high stress triaxiality $T = 3$, the prediction of the model for the [111] orientation is generally in good agreement with the unit cell simulations, while the difference between the model and the unit cell simulation for the [$\bar{1}$25] orientation is more significant.

The comparison of the stress strain response is also shown in fig. 4.2 for larger initial void volume fraction $f_0 = 0.05$. Similar trends can be observed, except for an increased difference between the unit cell and the model for the [125] orientation at low triaxiality $T = 1$ for this higher initial void volume fraction.

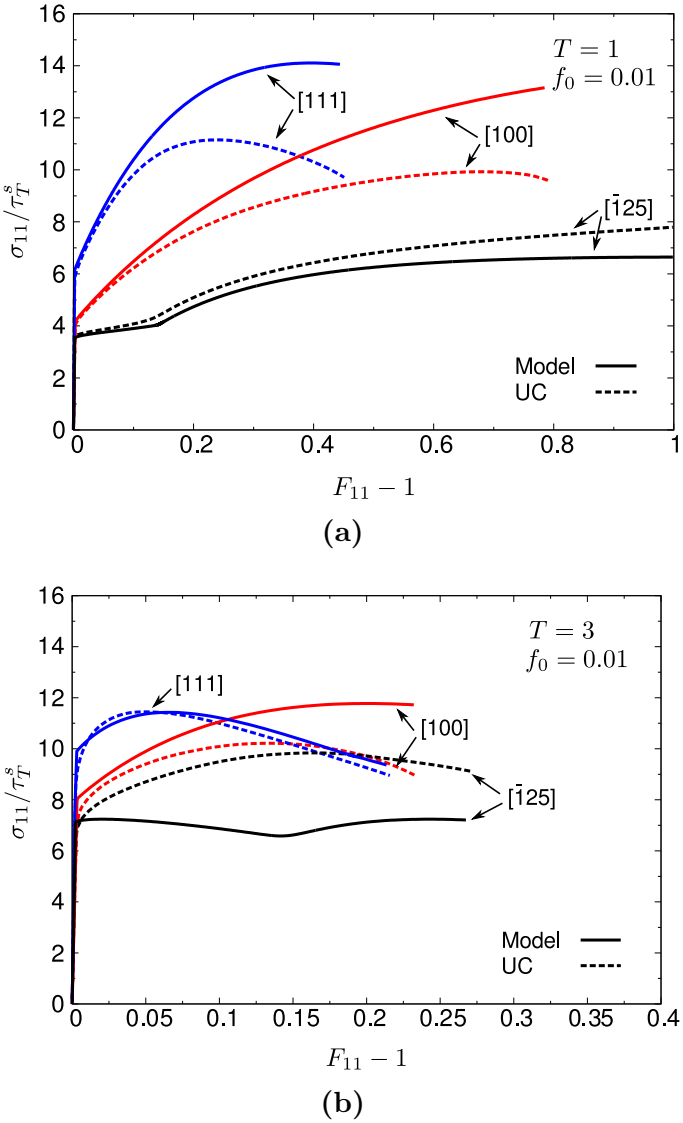

Figure 4.1: Comparison between the unit cell (UC) simulations and the porous single crystal model predictions: evolution of normalised macroscopic stress σ_{11}/τ_T^s with respect to axial strain $F_{11} - 1$ for different crystallographic orientations with fixed triaxiality, (a) $T = 1$ and (b) $T = 3$, and initial void volume fraction $f_0 = 0.01$.

Figure 4.3 shows the comparison of the evolution of the void volume fraction f for three orientations with $f_0 = 0.01$ at stress triaxiality (a) $T = 1$ and (b) $T = 3$. It can be observed that the porous single crystal model satisfactorily describes the tendency of the orientation effect on the evolution of the void volume fraction at both low and high stress triaxiality. However, the model underestimates the void growth for the [100] and [111] orientations, and overestimates the void growth for the [$\bar{1}$25] orientation at low stress triaxiality $T = 1$. These discrepancies are consistent with those presented in the previous section. At high stress triaxiality $T = 3$, the model well predicts the void growth for the [100] and [$\bar{1}$25] orientations,

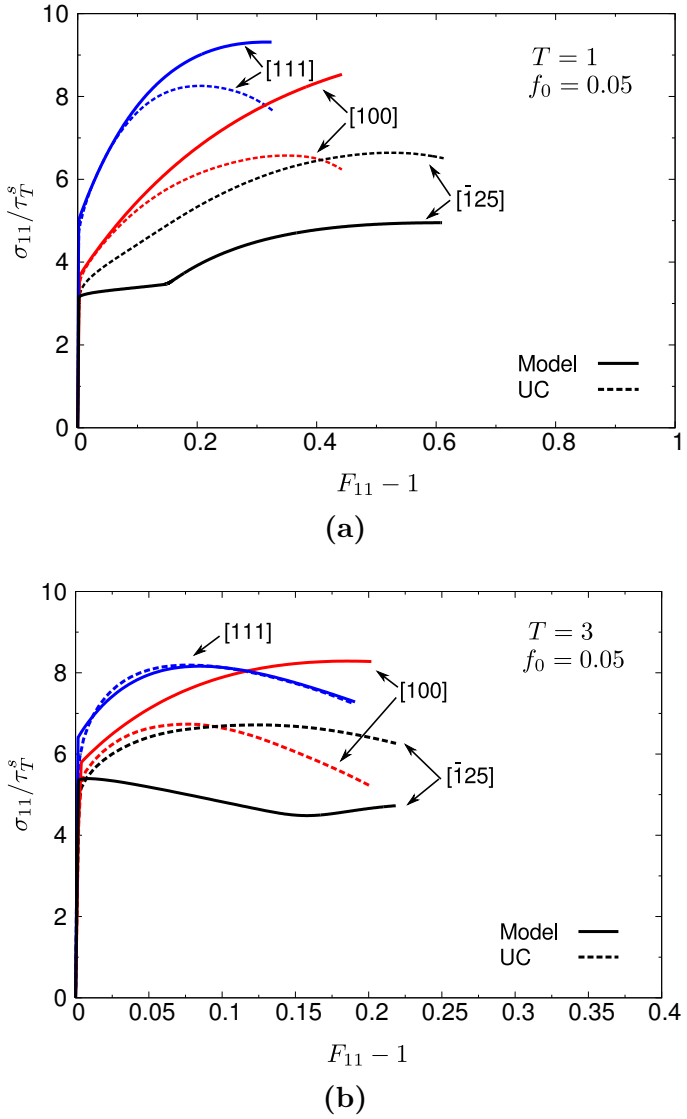

Figure 4.2: Comparison between the unit cell simulations and the porous single crystal model predictions: evolution of normalised macroscopic stress σ_{11}/τ_T^s with respect to axial strain $F_{11}-1$ for various crystallographic orientations with fixed triaxiality, (a) $T=1$ and (b) $T=3$, and initial void volume fraction $f_0=0.05$.

but overestimates the void growth for the [111] orientation, which is probably related to the void rotation shown in fig. 3.12.

The same comparison for larger initial void volume fraction $f_0=0.05$ is shown in fig. 4.4. Similar results are found, i.e., the model well predicts the orientation effect on the evolution of void volume fraction. However, the model underestimates the void growth in the case of the [$\bar{1}$25] orientation at low stress triaxiality $T=1$.

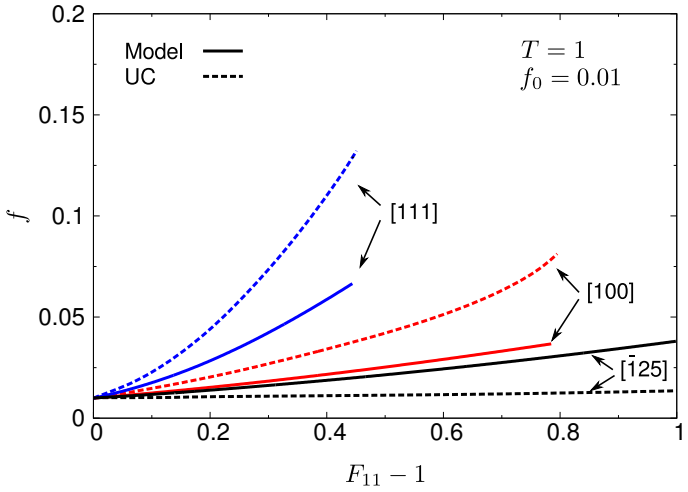

(a)

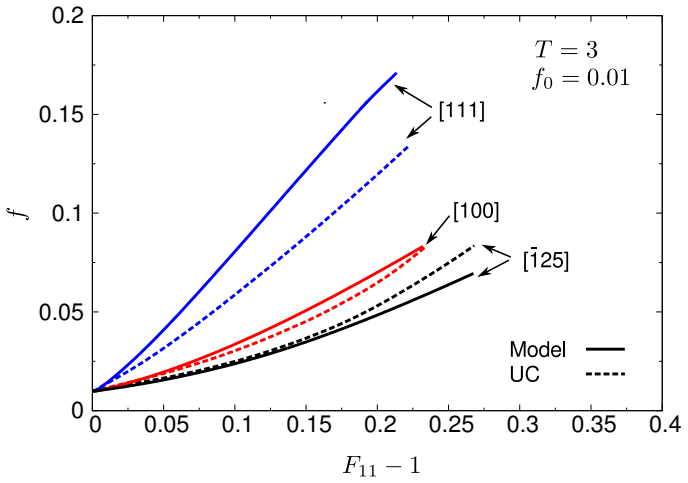

(b)

Figure 4.3: Comparison between the unit cell simulations and the porous single crystal model predictions: evolution of void volume fraction f with respect to axial strain $F_{11} - 1$ for various crystallographic orientations with fixed triaxiality, (a) $T = 1$ and (b) $T = 3$, and initial void volume fraction $f_0 = 0.01$.

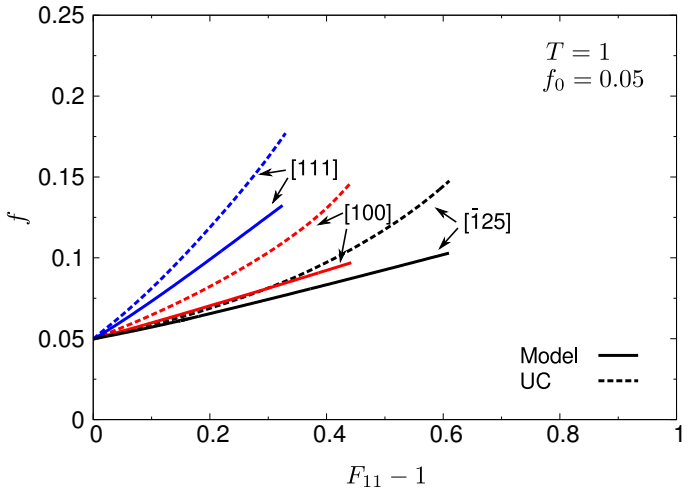

(a)

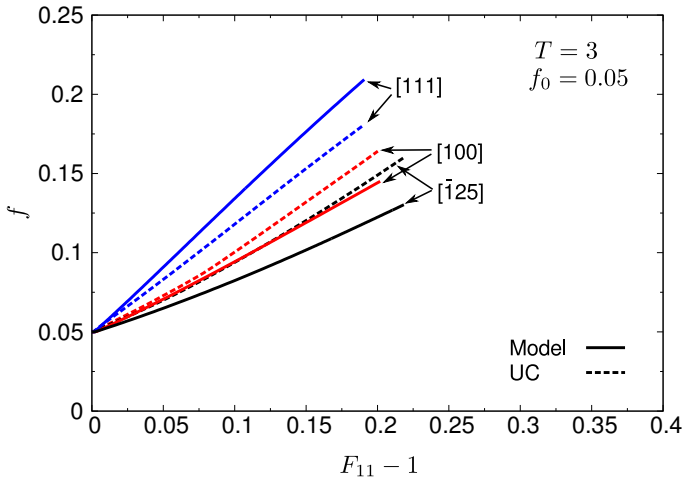

(b)

Figure 4.4: Comparison between the unit cell simulations and the porous single crystal model predictions: evolution of void volume fraction f with respect to axial strain $F_{11} - 1$ for various crystallographic orientations with fixed triaxiality, (a) $T = 1$ and (b) $T = 3$, and initial void volume fraction $f_0 = 0.05$.

4.2.3 Assessment for non-axisymmetric loading cases

The porous single crystal model calibrated from the axisymmetric loading cases is used to predict macroscopic stress–strain behaviour and void volume fraction evolution under non-axisymmetric loadings in this part. The loadings with $\eta_2 = 0.727$ and $\eta_3 \in \{0.4, 0.538, 0.625\}$ are considered for the [100], [111] and [$\bar{1}$25] orientations with $f_0 = 0.01$.

The stress–strain responses predicted by the porous single crystal are compared to those of unit cell simulations in fig. 4.5. In spite of insufficient strain hardening for the [111] and the [$\bar{1}$25] orientations, the model satisfactorily describes, for the non-axisymmetric loadings considered, the hierarchy of stress–strain response with respect to crystallographic orientation. For example, the [111] orientation shows the hardest response while the [$\bar{1}$25] orientation has the softest response.

The assessment of the porous single crystal model in terms of void volume fraction evolution is presented in fig. 4.6. The hierarchy of void volume fraction evolution with respect to crystallographic orientation is well predicted by the model. In addition, for the [111] orientation with $\eta_2 = 0.727$ and $\eta_3 = 0.4$, the unit cell simulation displays low void growth. This situation is poorly captured by the model that predicts significant void growth and in turn insufficient hardening. This discrepancy has not been observed for the axisymmetric loading cases with this orientation at $\eta_2 = \eta_3 = 0.4$ ($T = 1$) in fig. 4.1a and fig. 4.3a and at $\eta_2 = \eta_3 = 0.4$ ($T = 3$) in fig. 4.1b and fig. 4.3b. This can probably be explained by the potential influence of the third invariant of the macroscopic stress tensor, which is not yet taken into account in the porous single crystal model.

4.2.4 Discussion

The comparisons between the porous single crystal model and the unit cell simulations have been presented. The model with the identified parameters successfully predicts the hierarchy of the macroscopic stress strain behaviour and the evolution of void volume fraction with respect to (i) crystallographic orientation, (ii) stress triaxiality, and (iii) initial void volume fraction. An exhaustive list of initial conditions for the simulations was considered. While the model has been verified for most conditions, specific modeling issues have been highlighted.

The most significant difference between the porous single crystal model and the UC simulations is observed for the [$\bar{1}$25] orientation. It has been observed that the porous single crystal model underestimates the strain hardening of the unit cell for the [$\bar{1}$25] with $f_0 = 0.01$ and $f_0 = 0.05$ at high stress triaxiality $T = 3$.

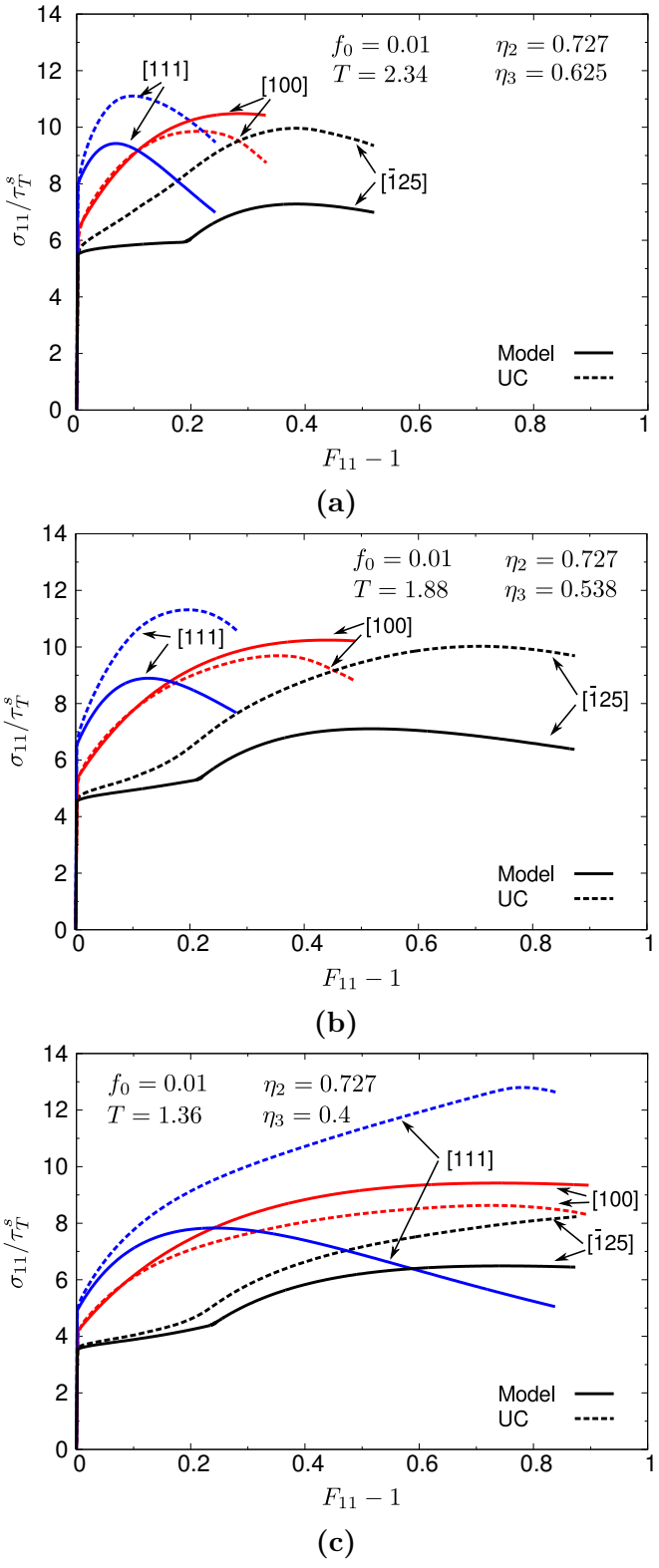

Figure 4.5: Assessment of porous single crystal model for non-axisymmetric cases: evolution of normalised macroscopic stress σ_{11}/τ_T^s with respect to axial strain $F_{11} - 1$ for different crystallographic orientations with initial void volume fraction $f_0 = 0.01$, $\eta_2 = 0.727$ and (a) $\eta_3 = 0.625$, (b) $\eta_3 = 0.538$ and (c) $\eta_3 = 0.4$.

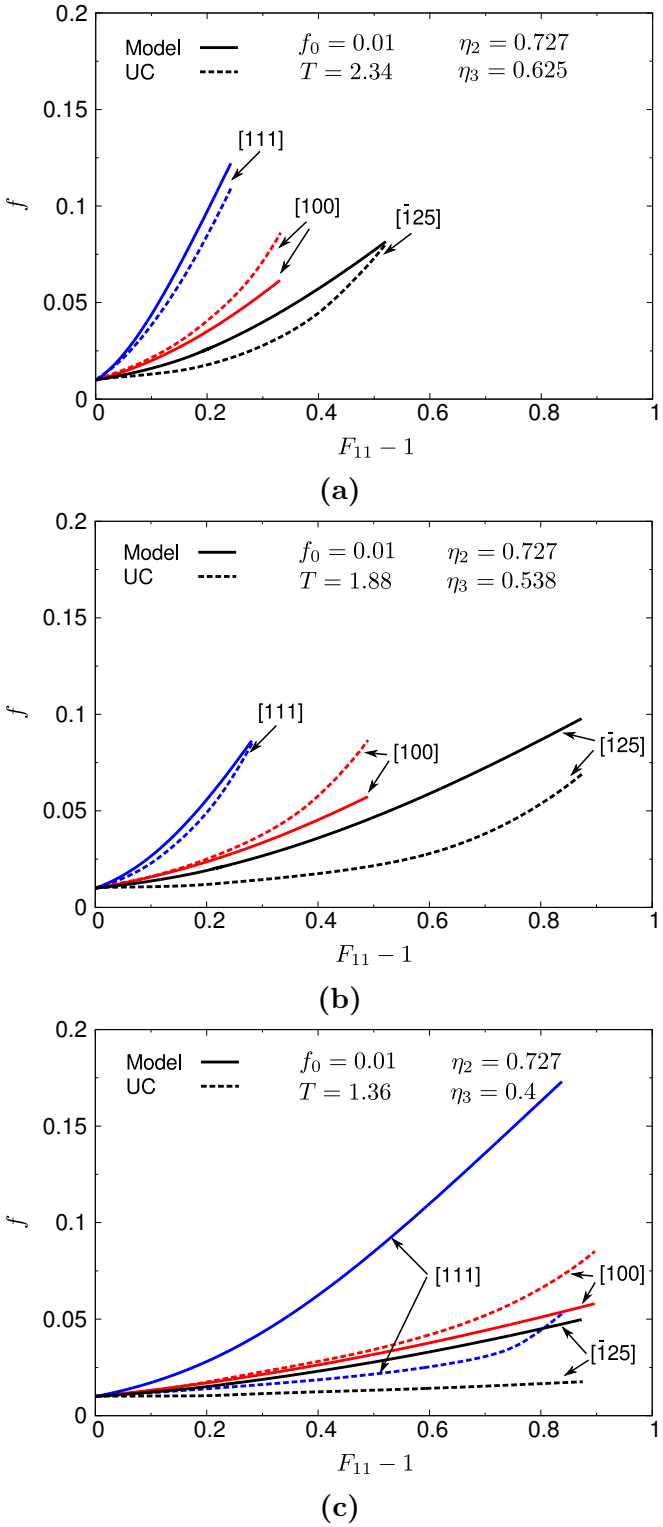

Figure 4.6: Assessment of porous single crystal model for non-axisymmetric cases: evolution of void volume fraction f with respect to axial strain $F_{11} - 1$ for different crystallographic orientations with initial void volume fraction $f_0 = 0.01$, $\eta_2 = 0.727$ and (a) $\eta_3 = 0.625$, (b) $\eta_3 = 0.538$ and (c) $\eta_3 = 0.4$.

The overall stress strain response of the unit cell simulation and that predicted by the porous model are replotted in fig. 4.7 for $f_0 = 0.01$ with the stress strain response of the void-free single crystal at the same stress triaxiality. For the void-free single crystal, the plastic deformation begins with small hardening rate due to the fact that only one slip system is activated. A change of hardening rate occurs when a secondary slip system being activated. For the voided single crystal (the unit cell simulation), on the contrary, the plastic part begins with a significant hardening rate, which is related to an important latent hardening as a result of the multiple slip in the regions near the void as shown in fig. 3.13 and fig. 3.16. To be more precise, an indicator is proposed as

$$I = \frac{1}{V}\int_V \sum_{s=1}^{12} H\left(\frac{|\dot{\gamma}^s|}{\dot{F}_{11}}\right) dV, \tag{4.10}$$

where the Heaviside function $H(x) = 1$ if $x > 0$, else $H(x) = 0$. This quantity indicates the effective number of activated slip systems depending on crystallographic orientation and the stress triaxiality in both the model and the unit cell. In fig. 4.8, the evolution of the indicator with respect to the strain $F_{11} - 1$ is presented for the $[\bar{1}25]$ orientation with $f_0 = 0.01$. It reveals that the macroscopic porous model predicts single slip pattern for the $[\bar{1}25]$ orientation at $T = 3$. However the factor reaches 4 before void coalescence in the unit cell simulation, which significantly deviates from the single slip pattern. This is confirmed by fig. 3.13 and fig. 3.15. Since fewer activated slip systems are predicted by the porous model, strain hardening is underestimated by the model. The enhancement of latent hardening by the high stress triaxiality observed in the unit cell simulation for the single-slip orientation is difficult to be incorporated in the homogenisation model.

For the $[\bar{1}25]$ orientation with small initial void volume fraction $f_0 = 0.01$ at the low stress triaxiality $T = 1$, the porous model overestimates the void growth rate as compared to the unit cell simulation (see fig. 4.3a). The unit cell shows nearly no void growth in terms of void volume fraction. Notice that the $[\bar{1}25]$ orientation corresponds to single slip orientation for a void-free FCC single crystal. For this type of orientation with small initial void volume fraction at low stress triaxiality, the void does not induce significant plastic slip heterogeneity in the single crystal matrix, as shown in section 3.3.4. As a result, the voided single crystal behaves like a void-free single crystal and exhibits a nearly single slip pattern with quasi-incompressible overall behaviour. No void growth is predicted by the unit cell simulation in this case. In contrast, the macroscopic model predicts a weak void growth for this case, due to the term $2q_1 f_i \cosh\left\{q_2\sqrt{\frac{3}{20}}\frac{M_m}{\tau_s^*}\right\}$ in Eq. (4.1), which is strictly positive even

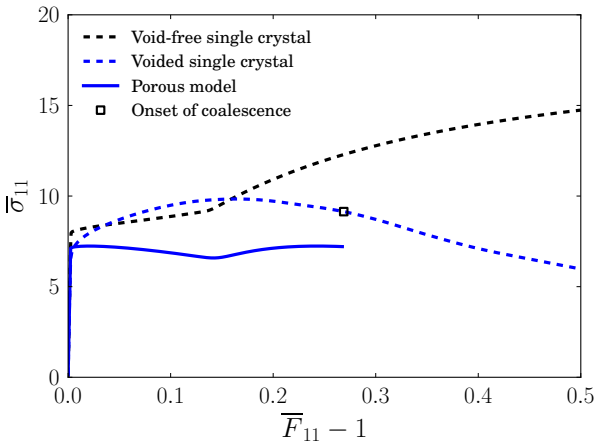

Figure 4.7: Stress-strain curves of the void-free and the voided single crystals for the $[\bar{1}25]$ orientation. $T = 3$ and $f_0 = 0.01$.

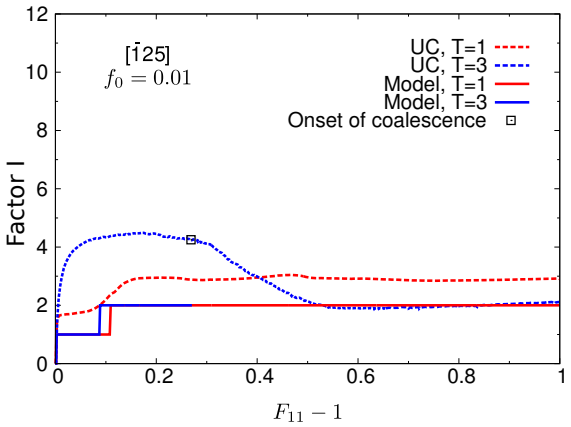

Figure 4.8: Comparison between the unit cell simulation and the porous single crystal model: evolution of plastic slip indicator I with respect to axial strain $F_{11} - 1$ for the $[\bar{1}25]$ orientation.

in the case of single slip and, by virtue of normality rule, induces void growth. As the initial void volume fraction increases to $f_0 = 0.05$, the plastic slip heterogeneity introduced by the void becomes significant even at low stress triaxiality. The porous single crystal deviates significantly from single slip and much more slip systems are activated around the void. As a result, in the unit cell simulation, the strain hardening rate is increased and the void growth is accelerated. As the model only considers a single slip situation, it underestimates the strain hardening and the void growth for the $[\bar{1}25]$ orientation with $f_0 = 0.05$ even at low stress triaxiality $T = 1$.

4.2.5 Conclusions

An elastoviscoplastic model is proposed for porous single crystals undergoing finite deformations. The effective resolved shear stress defined in the work of Han

et al. (2013) at infinitesimal strains is extended to finite strains and the work hardening of the matrix of porous single crystals is incorporated. To the best knowledge of the author, the proposed macroscopic model is the first model for porous single crystals at finite strains.

The model is calibrated from unit cell simulations for unirradiated single crystals, presented in section 3.3. Compared with the unit cell simulations, the porous single crystal model satisfactorily describes the hierarchy of porous single crystal responses with respect to crystal orientation and void volume fraction. However, the model cannot predict the quasi-incompressible behaviour observed for strongly asymmetric orientations, e.g., $[\bar{1}25]$, with small initial void volume fraction at low stress triaxiality. The model underestimates the strain hardening for strongly asymmetric orientations with small initial void volume fraction at high stress triaxiality and with large f_0 at all levels of stress triaxiality considered.

4.3 Application to simulations of ductile damage in a polycrystalline aggregate

The final goal of the modeling tools developed in this study is their application to evaluate fracture toughness of austenitic strainless steels. A first attempt is done in this section to simulate polycristal aggreggates with the developed porous crystal model. For the sake of simplicity, the stress state ahead of a crack is represented by applying different stress triaxiality levels to a simplified polycristal aggregate.

4.3.1 Problem setup

The FE mesh of a polycrystalline aggregate with 343 cubic grains ($7 \times 7 \times 7$) is used for the simulations, shown in fig. 4.9a. Each cubic grain is meshed with 27 20-node quadratic brick elements with reduced integration. A random distribution of crystal orientations , as indicated in the inverse pole figure (fig. 4.9b), is attributed to the aggregate. Axisymmetric loadings are applied on the aggregate with constant stress triaxialities ($T = 1, 2, 3$). The surfaces of the aggregate are kept plane during the loading. The material parameters for unirradiated single crystals (see table 3.6) are used for the simulations with the parameters $\alpha = 5.69$, $q_1 = 1.60$ and $q_2 = 1.19$ identified in table 4.2. It is assumed that the initial void volume fraction of the grains takes the same value $f_0 = 0.01$. Effects of post-irradiation hardening/softening are not yet investigated in this section.

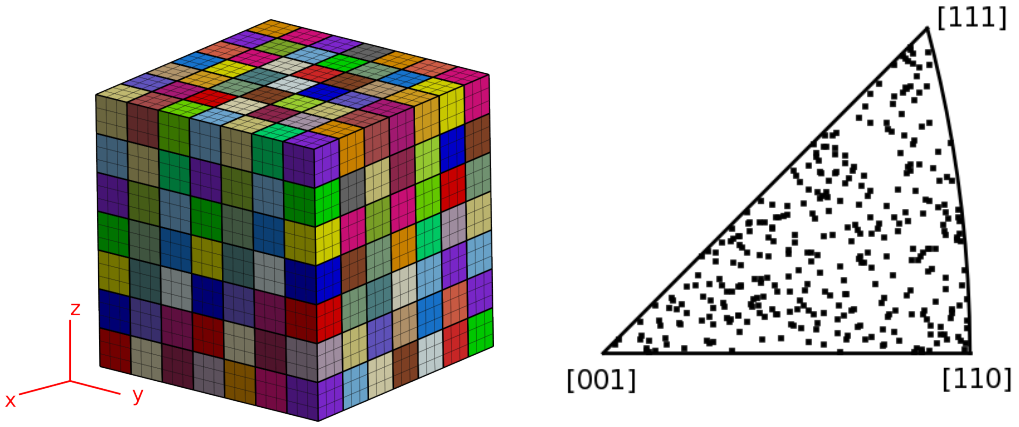

Figure 4.9: (a) FE mesh of the polycrystalline aggregate with 343 cubic grains. Each grain is meshed with 27 elements; (b) Inverse pole figure showing the random distribution of the grain orientations.

4.3.2 Results

The evolution of overall Cauchy stress as a function of overall strain $\overline{F}_{11} - 1$ is shown in fig. 4.10 for different stress triaxialities. A softening regime is predicted at the aggregate scale for the stress triaxialities $T = 2$ and 3. For $T = 1$, the simulation diverged before strain softening. The strain softening begins at a smaller overall strain for $T = 3$ than $T = 1$. The strain softening observed at the aggregate scale is associated with the evolution of void volume fraction at the grain scale.

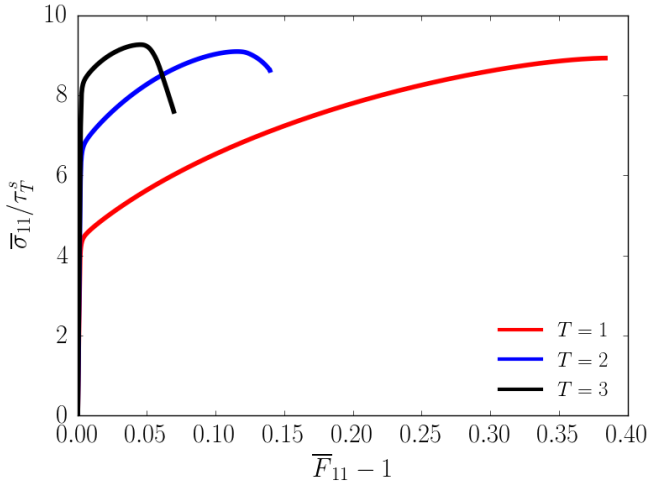

Figure 4.10: Overall stress-strain curves for different stress triaxialities.

The evolution of local void volume fraction f_i with the overall strain $\overline{F}_{11} - 1$ is first shown in fig. 4.11 for the stress triaxiality $T = 3$. At the beginning of the

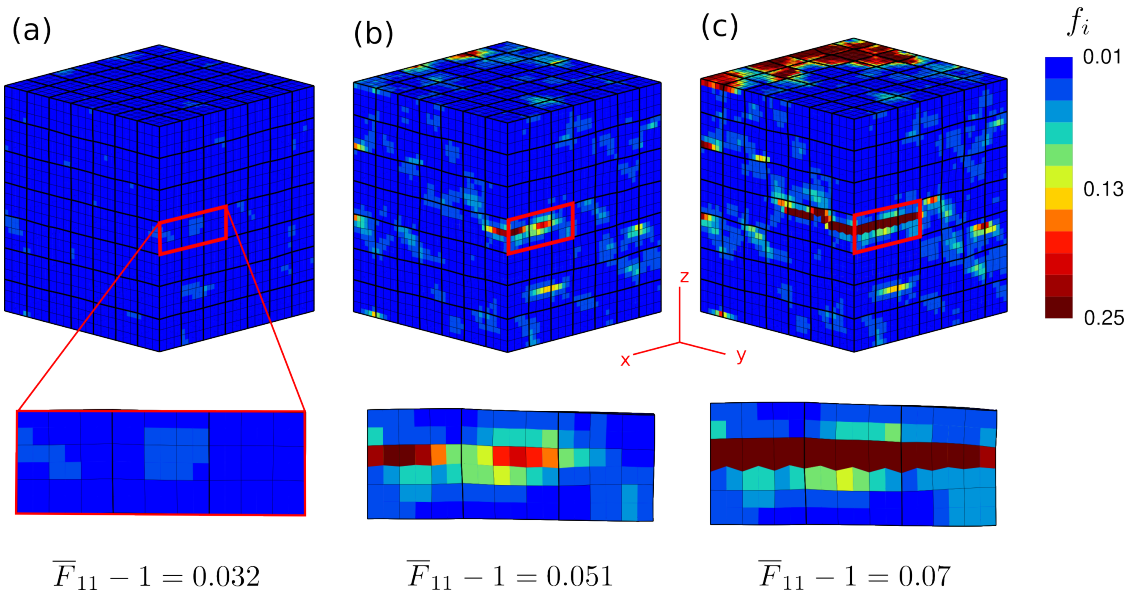

Figure 4.11: Evolution of void volume fraction f_i with the overall strain $\overline{F} - 1$ for the imposed stress triaxiality $T = 3$, showing a propagation of ductile damage between grains.

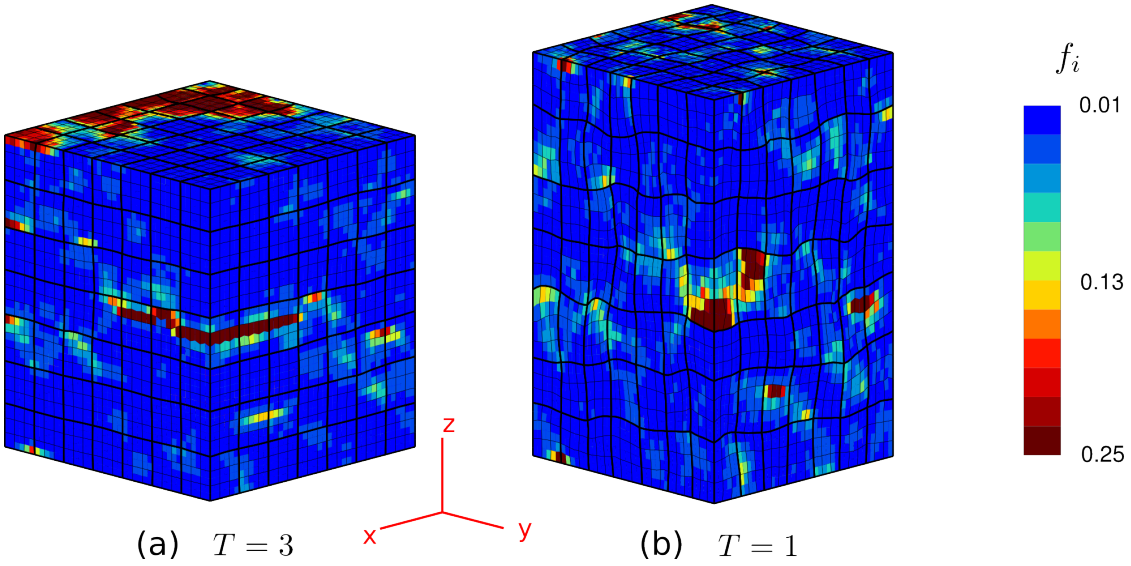

Figure 4.12: Stress triaxiality effects: void volume fraction f_i for (a) $T = 3$ at $\overline{F}_{11} - 1 = 0.07$ and (b) $T = 1$ at $\overline{F}_{11} - 1 = 0.38$.

straining, e.g., $\overline{F}_{11} - 1 = 0.032$, the local void volume fraction f_i remains around its initial value (0.01). As the straining continues, void volume fraction increases inhomogeneously in the aggregate. For example, in the zoomed region of three grains, the void volume fraction at $\overline{F}_{11} - 1 = 0.051$ is higher than in the surrounding grains. A propagation of ductile damage (void volume fraction is regarded as a damage parameter) from one grain to another is also observed, as shown in the zoomed region, which results in a crack on the edge of the aggregate. The damage

intensively formed on the top of the aggregate is associated with the boundary condition used, which may increase locally the stress triaxiality on the boundary.

The void volume fraction for $T = 1$ at $\overline{F}_{11} - 1 = 0.38$ is compared with $T = 3$ at $\overline{F}_{11} - 1 = 0.07$ in fig. 4.12. A inhomogeneous evolution of ductile damage is also observed for $T = 1$. However, the damage is localized in grains and the damage propagation from grain to grain is not observed at this relatively low level of stress triaxiality.

4.3.3 Conclusions

In this section, the porous single crystal model is applied to simulate ductile damage of polycrystalline aggregates containing intragranular voids. The evolution of void volume fraction is studied by the simulations. A strain softening behavior due to the increase of the porosity inside grains has been predicted. A propagation of ductile damage has been observed at a relatively high stress triaxiality $T = 3$, while ductile damage is localized inside grains for the stress triaxiality $T = 1$.

As cracking criterion is not introduced in the simulations, crack propagation and fracture cannot be simulated. This will be done in future works. In addition, more realistic FE meshes, such as Voronoi-type polycrystalline aggregates or meshes obtained from the X-ray tomography, can also be used in future works.

4.4 Application to simulations of the single-edge-notch tension

4.4.1 Experiment and simulation

A single-edge-notch tension (SENT) was performed on a single crystal of 316L stainless steel in the Material Aging Institute of EDF. The test provides experimental data to validate the porous single crystal model (a ductile damage model for single crystal).

The geometry of the specimen is shown in fig. 4.13 with the length of the reduced section $L = 8$ mm, the width of the reduced section $W = 3$ mm and the thickness $T = 1.02 \pm 0.02$ mm. A notch of length $d = 605 \pm 5\,\mu$m with a round tip is machined in the center of the specimen with a wire saw. The initial value of the notch opening is $a = 164.5 \pm 1.5\,\mu$m. The crystallographic orientation of the specimen was measured by electron backscatter diffraction (EBSD) shown in fig. 4.14. The orientation corresponds to Euler angles $(\phi_1, \Phi, \phi_2) = (175.65°, 33.64°, 146.94°)$ following the **zxz** convention. The Euler angles rotate the spatial basis to the crystal basis. Then,

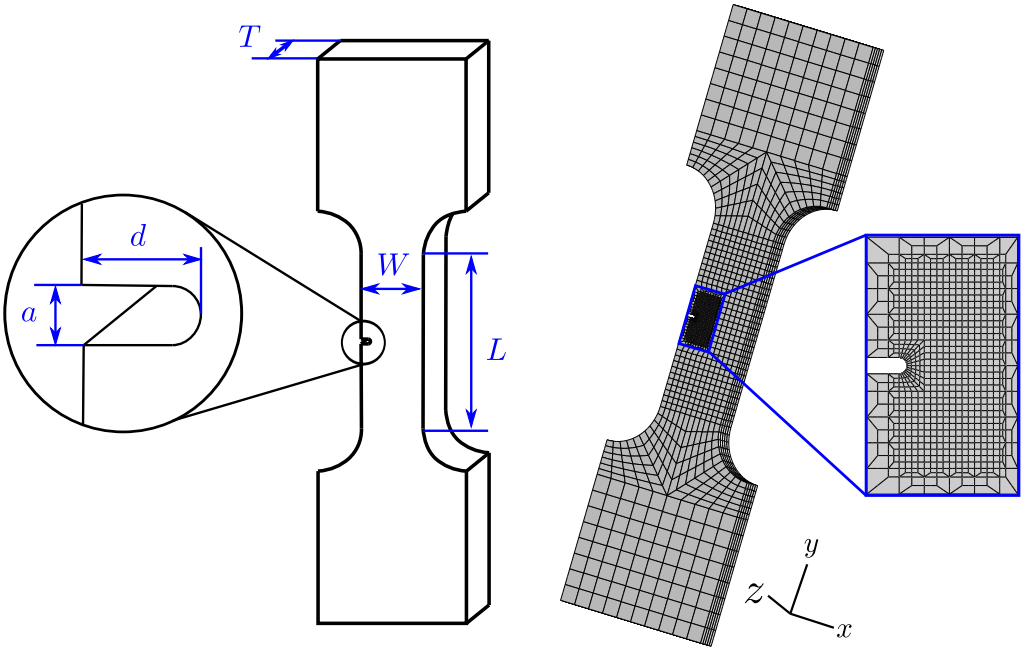

Figure 4.13: The geometry and a 3D FE mesh of the specimen for SENT.

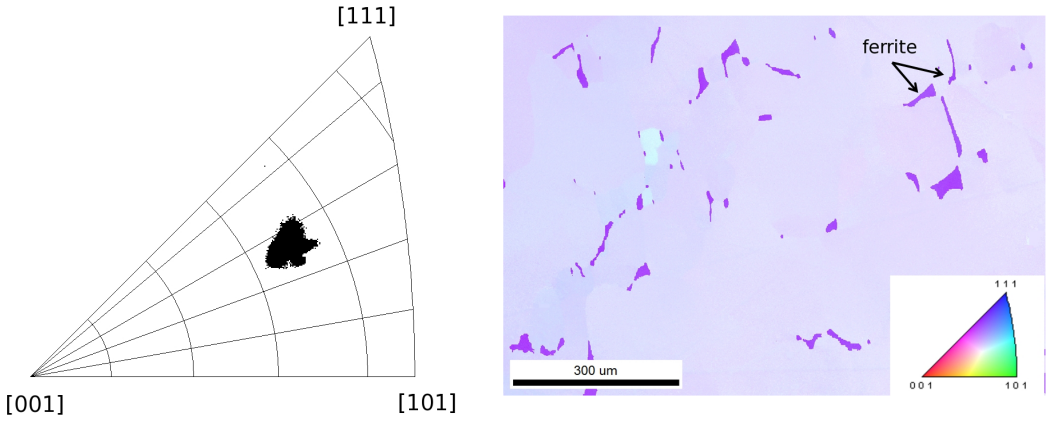

Figure 4.14: Crystal orientation measured by EBSD: (a) the inverse pole figure for the direction normal to the specimen along the z axis; (b) a map showing microstructure of the single crystal with some inclusions of ferrite.

speckles of gold were created by electron-beam lithography on a zone of the specimen surface near the notch tip in order to measure surface strain fields by digital image correlation (DIC) methods (see fig. 4.15). An *in-situ* SENT test was performed in a scanning electron microscope (SEM) with a loading speed of $2 \times 10^{-6}\,\mathrm{m\,s^{-1}}$ at 20 °C. The notch opening displacement Δa, corresponding to the increase of a, is measured using SEM micrographs. The imposed straining is planned to be large enough so that ductile fracture can occur. However, it was not achieved, partly because of the

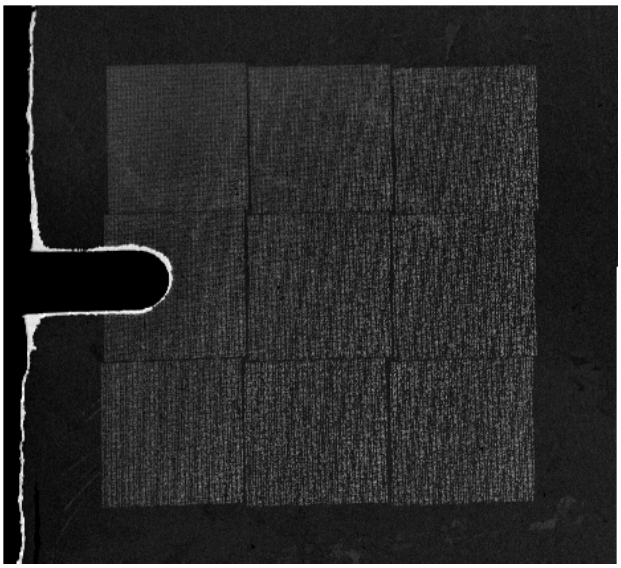

Figure 4.15: SEM micrograph showing gold speckles created on a zone of the specimen surface near the notch tip for the digital image correlation.

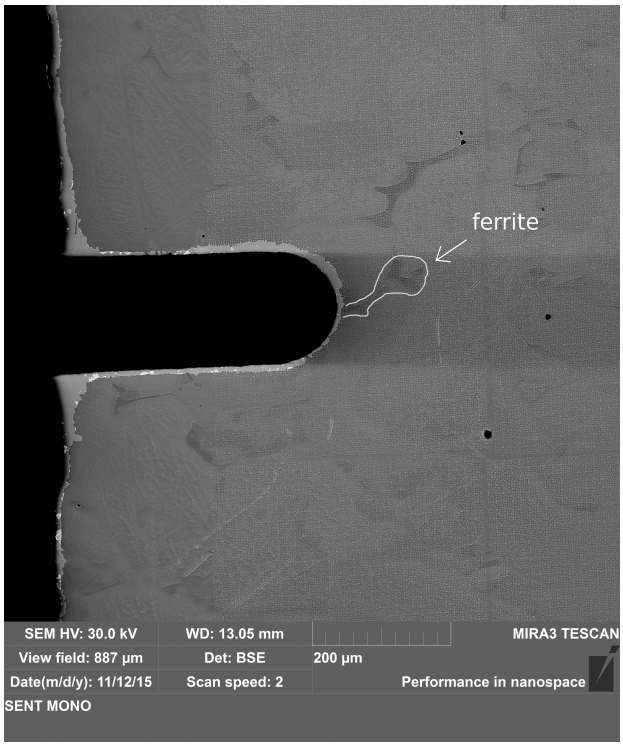

Figure 4.16: SEM micrograph showing inclusions of ferrite at the front of the notch tip.

high ductility of the material. Besides, it is important to note that inclusions of ferrite were observed (see fig. 4.14b) including one located in the front of the notch tip (see fig. 4.16), which may have an influence on the experiment results.

A 3D FE mesh with five elements in the thickness is created according to the geometry of the specimen to simulate the test (see fig. 4.13). The mesh is refined in

the region near the notch tip where a high level of strain is expected. In terms of boundary conditions, the bottom is fixed in three directions; the top is fixed in the directions of x and z axes and the displacement is prescribed along the y-axis. The crystallographic orientation measured by EBSD is considered for the simulation. In absence of the material parameters for the 316L single crystal, those identified for the unirradiated polycrystalline 304L steel at 340 °C (table 3.6) are used with two levels of initial void volume fraction: $f_0 = 0$ and 0.01. Even though damage/fracture does not occur during the experiment, the simulation with porous single crystal model, as a preliminary study, can offer some implications for further studies.

4.4.2 Results: surface slip traces

During the test, slip traces are observed on the surface of the specimen as a result of dislocation glide, as shown in fig. 4.17 for different normalized notch opening displacements $\Delta a/a_0$ (a_0 is the initial value of a). A few traces of three slip planes can be observed around the notch tip at the beginning of plastic deformation (indicated by black lines in fig. 4.17a) and they become more pronounced with larger notch opening (fig. 4.17b).

slip trace	$p1$			$p2$			$p3$			$p4$		
slip system	1	2	3	4	5	6	7	8	9	10	11	12
$\underline{\boldsymbol{n}}^s$	(111)			$(1\bar{1}1)$			$(\bar{1}11)$			$(\bar{1}\bar{1}1)$		
$\underline{\boldsymbol{m}}^s$	$[\bar{1}01]$	$[0\bar{1}1]$	$[\bar{1}10]$	$[\bar{1}01]$	[011]	[110]	$[0\bar{1}1]$	[110]	[101]	$[\bar{1}10]$	[101]	[011]

Table 4.3: Slip systems and slip traces for FCC single crystals.

The surface slip traces can be theoretically predicted. According to the Euler angles measured by EBSD, four types of surface slip traces are expected and their angles with respect to the x-axis are calculated and shown in fig. 4.18. One type of slip traces corresponds to dislocations with the same slip plane. In the case of FCC single crystals, there are four types of slip planes and the normal to the planes are respectively: (111), $(1\bar{1}1)$, $(\bar{1}11)$ and $(\bar{1}\bar{1}1)$ (see table 4.3). The four types of slip traces are denoted respectively by $p1$, $p2$, $p3$ and $p4$. Comparing the theoretical predictions and the experimental observations, we conclude that three types, i.e., $p1$, $p2$ and $p3$, are activated. Theoretical and experimental angles of surface slip traces with respect to the x-axis are in good agreement.

To better illustrate the results, accumulated plastic slip for four slip planes are defined:

$$\gamma^{p1} = \gamma^1 + \gamma^2 + \gamma^3,\ \gamma^{p2} = \gamma^4 + \gamma^5 + \gamma^6, \tag{4.11}$$

$$\gamma^{p3} = \gamma^7 + \gamma^8 + \gamma^9,\ \gamma^{p4} = \gamma^{10} + \gamma^{11} + \gamma^{12}. \tag{4.12}$$

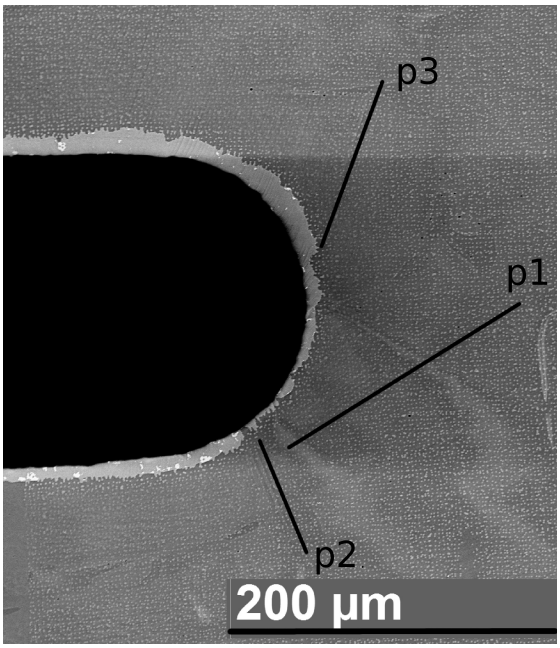

(a)

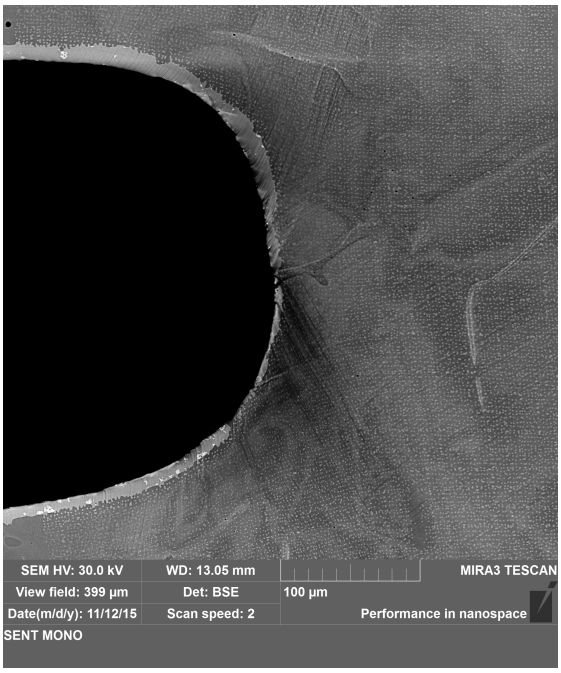

(b)

Figure 4.17: SEM micrographs showing surface slip traces with different notch opening displacements: (a) $\Delta a/a_0 = 0.18$; (b)$\Delta a/a_0 = 0.95$.

Plastic slip predicted by FE simulations is shown in fig. 4.19 with $f_0 = 0$ and $f_0 = 0.01$. Note that plastic slips vary in the direction of thickness, the results in fig. 4.19 correspond to plastic slips which can be observed on specimen surface. The simulations predict that two types of slip traces, i.e., $p1$ and $p2$, are intensively

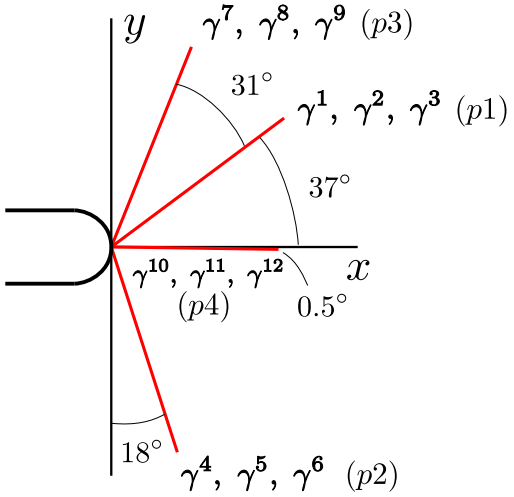

Figure 4.18: Theoretical prediction of slip traces on the free surfaces.

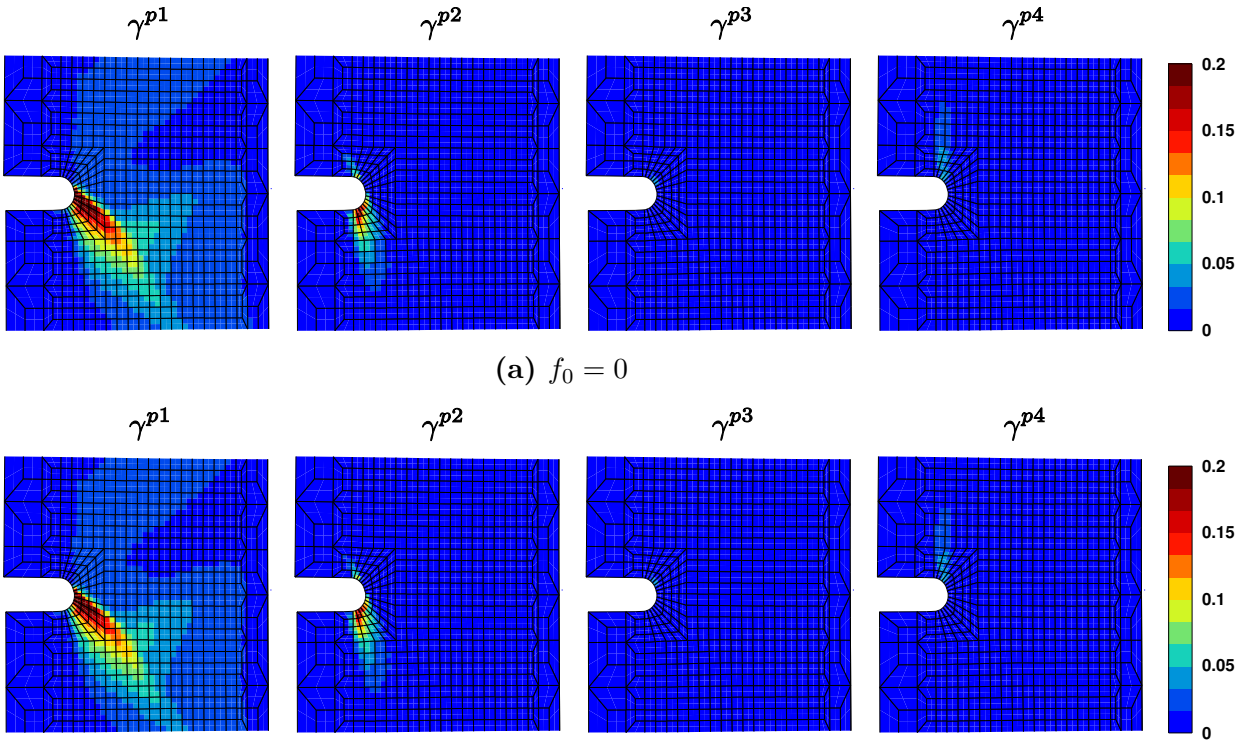

(a) $f_0 = 0$

(b) $f_0 = 0.01$

Figure 4.19: Simulations showing plastic slip of four families with (a) $f_0 = 0$ and (b) $f_0 = 0.01$. $\Delta a/a_0 = 0.18$.

activated in front of the notch tip. The intensive activation of slip traces $p1$ and $p2$ and their position are in agreement with the experiment observation. The other two types $p3$ and $p4$ are very weakly activated in the simulations, which is different from experimental observations. In the experiment, slip traces $p4$ are not observed and slip traces $p3$ is relatively dense in front of the notch tip (these are more visible with

DIC, see fig. 4.20 in the next section). These differences between the experiment and the simulation are probably related to the ferrite inclusions located in front of the notch tip. The inclusions can change activation of plastic slip at the notch tip.

4.4.3 Results: strain fields at the notch tip

Strain fields on the surface of the specimen during loading were measured by DIC. The measured field of the strain $E_{22} = F_{22} - 1$ for the normalized notch opening $\Delta a/a_0 = 0.95$ in the region near the notch tip is shown in fig. 4.20a. The obtained result shows a discontinuous strain field which is related to the discrete nature of plastic slip. Furthermore, a strong strain localization is observed in front of the notch tip; three types ($p1$, $p2$ and $p3$) of slip traces display which is in agreement with the observation in section 4.4.2. Besides, slip traces of type $p1$ and $p2$ are very intensive even in the region relatively far from the notch tip, while slip traces of type $p3$ are found only in the region near the notch tip. This is consistent with the FE predictions shown in fig. 4.19.

The damage f_i predicted by the porous single crystal model with the initial void volume fraction $f_0 = 0.01$ is presented in fig. 4.21 for $\Delta a/a_0 = 0.95$. The evolution of the damage parameter f_i is not homogeneous in the direction of the thickness around the notch. The maximum value of f_i, reaching 0.06, is not found on the surface of the specimen. Since the ductile fracture does not occur in the experiment, this simulation result about ductile damage is not compared with the experiment.

The results of the simulations, presented in fig. 4.20b, succeed in predicting basic characteristics of the strain field observed in the experiment: a strong strain localization in an asymmetric region near the notch tip; an asymmetric mode of notch opening; an activation of plastic slip in the region relatively far from the notch tip.

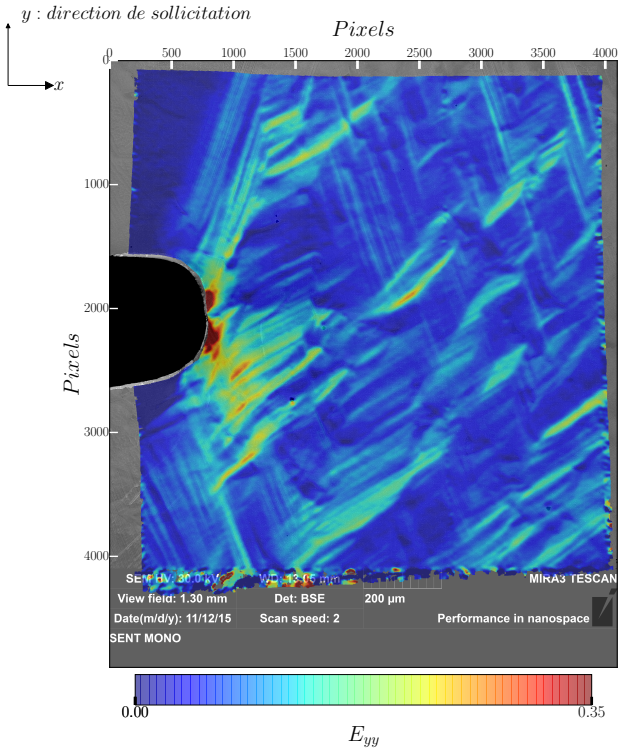

(a)

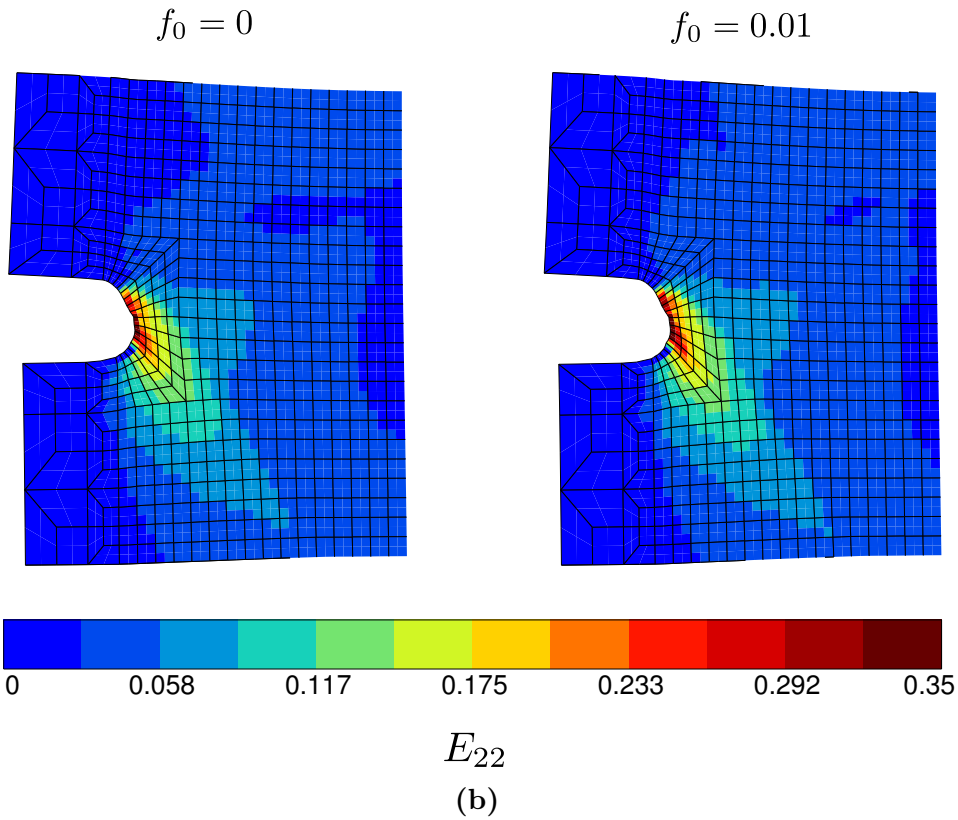

(b)

Figure 4.20: Surface strain filed E_{22} for $\Delta a/a_0 = 0.95$: (a) experimental result measured by DIC; (b) simulation predictions.

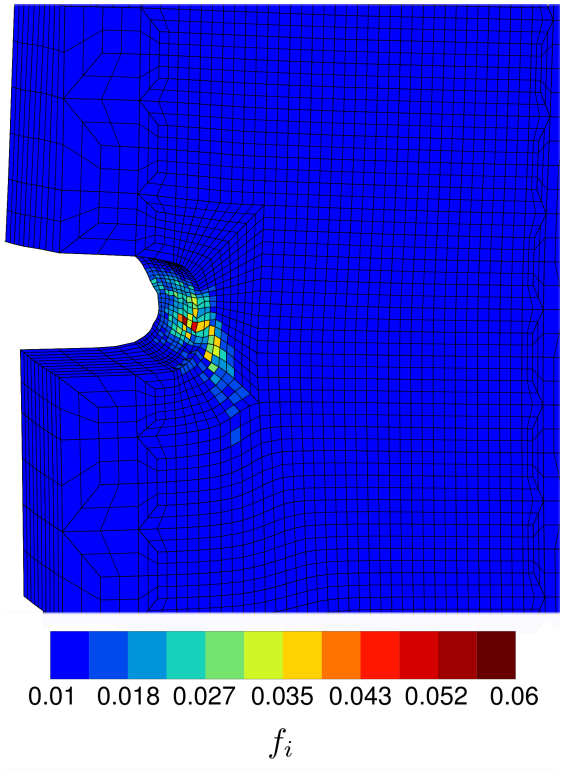

Figure 4.21: Void volume fraction f_i in the region near the notch tip at $\Delta a/a_0 = 0.95$ predicted by the porous single crystal model with the initial porosity $f_0 = 0.01$

4.4.4 Results: force–notch-opening-displacement relation

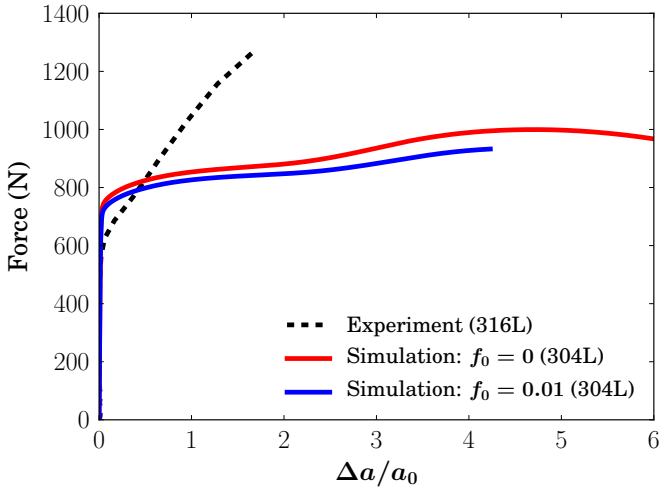

Figure 4.22: Evolution of loading force as a function of normalized notch opening displacement: comparison experiment–simulations.

The evolution of loading force is plotted in fig. 4.22 as a function of normalized notch opening displacement $\Delta a/a_0$ for the experiment and the simulations. For

the simulations with $f_0 = 0$ and 0.01, a first hardening regime is observed followed by a second one with a higher hardening rate. The activation of the second hardening regime is related to an increase in the number of activated slip systems with increasing notch opening displacement. In the case of $f_0 = 0$, a strain softening regime following the hardening regimes is also observed. Compared with the simulations, the experiment exhibits a lower yield stress and a much higher strain hardening rate.

The differences between the experiment and the simulations are closely related to the material parameters used for the simulations which are not calibrated for the material of the test. In particular, in the single crystal plasticity models, the yield stress is directly associated with the initial dislocation densities (see Eq. (3.22)). Hence, the dislocation densities in the single crystal of 316L should be carefully measured/estimated before the test. In addition, the under-estimation of the hardening by the simulations is not well understood. It is probably associated with the interaction matrices of the hardening law, i.e., a^{su} in Eq. (3.22) and b^{su} in Eq. (3.21). The components of the matrix a^{su} were evaluated by DD simulations, while a strong assumption has been made about the matrix b^{su} due to a lack of studies. Further works are needed for accurate calibration of the two matrices.

4.4.5 Conclusions and outlook

The model is applied to simulate the SENT test performed on a single crystal of 316L stainless steel in this section. The prediction of the model about plastic slip activation on the specimen surface and plastic strain filed in front of the notch tip is in good agreement with the experimental observation. However, compared with the experiment, the simulation predicts a notch-opening-displacement relation showing a higher yield stress and a much lower strain hardening rate. These differences are probably related to: 1) the material parameters used for the simulations is identified on polycrystalline 304L stainless steels, not the material used for the SENT test; 2) the ferrite inclusions in the 316L stainless steel single crystal may have an influence on mechanical behaviors of the material, which is not taken into account in the simulation.

Note that this work is not finished yet. The ongoing works concentrate on the improvement of the simulations. Two aspects are being studied:

1. Decrease the initial value of dislocation densities and investigate its influences on strain hardening rate;

2. Introduce inclusions of ferrite by some particles with higher yield stress than the matrix in the FE mesh and study their influences on strain hardening rate;
3. Investigate influences of boundary conditions prescribed in the simulations on the results.

4.5 Concluding remarks

In this chapter, an elastoviscoplastic model at finite strains has been formulated porous single crystals based on the work of Han et al. (2013). The model incorporates heuristically strain hardening of single crystal matrix. The model has been shown to be able to predict ductile damage due to void growth to coalescence in single crystals with different orientations. The model has then been applied to simulate ductile damage in polycrystalline aggregates and a single-edge-notch tension test on a single crystal.

In this chapter, effects of post-irradiation hardening/softening behavior is not taken into account. This will be considered in future works. Crack propagation due to ductile fracture at the scale of grains can also be investigated with the proposed model and simulations. To this end, a cracking criterion should be introduced in the future.

The model proposed in this chapter accounts for intragranular voids in polycrystalline materials. As presented in the previous chapters, in irradiated stainless steels, intragranular voids can correspond to irradiation-induced swelling voids or to voids nucleated on irradiation-induced precipitates during plastic straining. The former can lead to nano-sized fracture dimples and their size can be as small as 20–30 nm according to Margolin et al., 2016. The latter, as reported in Little, 1986, can result in fracture dimples of size $< 10\,\mu m$ in irradiated steels, which is smaller than in unirradiated materials (size $> 25\,\mu m$). In a word, voids of different sizes exist in irradiated steels. Moreover, it is well known that size effects in plasticity exist at the crystal level (see, e.g., Fleck et al., 1994; Stelmashenko et al., 1993; Poole et al., 1996; Suresh et al., 1999; Stölken and Evans, 1998) and size effects in turn are also expected on void growth and coalescence Fleck and Hutchinson, 2001; Borg et al., 2008. It is hence of importance to investigate the effect of void size on the ductile fracture process and fracture toughness at the grain scale. This aspect will be treated in the next chapter.

5

Micromorphic single crystal plasticity model and its applications

Résumé

Dans les aciers irradiés, la rupture ductile peut avoir lieu en raison des cavités de tailles différentes. La taille des cavités peut avoir une influence sur la cinétique de la croissance et la coalescence des cavités. Pour étudier cet effet, un modèle micromorphe de plasticité cristalline en grandes transformations est proposé dans ce chapitre. Le modèle est basé sur une variable scalaire et il est donc numériquement efficace. Selon les variables d'état choisies, deux formulations sont présentées et l'une est implémentée dans le code par éléments finis. Le modèle est d'abord utilisé pour étudier la localisation de la déformation dans le monocristal. On montre que le modèle peut régulariser à la fois la bande de glissement et la bande en genou. Le modèle est ensuite appliqué à la croissance de cavité. Les simulations des cellules unitaires montrent que les petites cavités croissent moins vite que les grandes.

Contents

In irradiated stainless steels, ductile fracture can probably occur due to intragranular voids of size varying from nano to micrometers. Plasticity size effects could thus be involved in the particular fracture process associated with void growth and coalescence in irradiated steels. In order to study influence of void size on the ductile fracture process at grain scale, a micromorphic single crystal plasticity model at finite deformation is proposed. The first part of this section is devoted to the formulations of the model. FE implementation of one of the formulations is described in the second part. Then, the model is first applied to study analytically and numerically strain localization in single crystals with single slip, where a material length scale is derived for the model. Finally, UC simulations are performed for investigating size dependent void growth and coalescence in single crystals.

5.1 Micromorphic single crystal plasticity at finite deformation

5.1.1 Kinematics of a micromorphic single crystal

We consider a crystalline body occupying the region $\mathbf{B_0}$ in a fixed reference configuration. A point $\underline{\boldsymbol{X}}$ in $\mathbf{B_0}$ is referred to as a material point. Following the micromorphic approach (see Germain (1973), see also Forest (2009) and Aslan et al. (2011)), two types of degrees of freedom (DOF) are attributed to a material point, i.e., the displacement $\underline{\boldsymbol{u}}\,(\underline{\boldsymbol{X}}\,,t)$ and an additional strain type DOF $\gamma_\chi(\underline{\boldsymbol{X}}\,,t)$:

$$\text{DOF} = \{\underline{\boldsymbol{u}}\,, \gamma_\chi\}. \tag{5.1}$$

In the present work, the additional DOF, γ_χ, is a scalar variable called microslip variable.

At time t, the deformed body occupies the region $\mathbf{B}$ in space, called the current configuration. The Lagrangian gradients of the degrees of freedom are

$$\underset{\sim}{\boldsymbol{H}}(\underline{\boldsymbol{x}}\,,t) = \frac{\partial \underline{\boldsymbol{u}}}{\partial \underline{\boldsymbol{X}}} = \text{Grad}\,\underline{\boldsymbol{u}}\,, \tag{5.2}$$

$$\underline{\boldsymbol{K}}\,(\underline{\boldsymbol{x}}\,,t) = \frac{\partial \gamma_\chi}{\partial \underline{\boldsymbol{X}}} = \text{Grad}\,\gamma_\chi, \tag{5.3}$$

where $\underset{\sim}{\boldsymbol{H}}$ is the displacement gradient which is related to the deformation gradient $\underset{\sim}{\boldsymbol{F}}$ by $\underset{\sim}{\boldsymbol{F}} = \underset{\sim}{\mathbf{1}} + \underset{\sim}{\boldsymbol{H}}$, and $\underline{\boldsymbol{K}}$ is referred to as the microslip gradient vector. Besides, the Eulerian gradient of γ_χ, which is useful in the following, follows

$$\underline{\boldsymbol{k}} = \frac{\partial \gamma_\chi}{\partial \underline{\boldsymbol{x}}} = \text{grad}\,\gamma_\chi, \tag{5.4}$$

where $\underline{\boldsymbol{x}}$ is the current position of material point $\underline{\boldsymbol{X}}$ at time t. $\underline{\boldsymbol{K}}$ and $\underline{\boldsymbol{k}}$ are related to each other by

$$\underline{\boldsymbol{k}} = \underline{\boldsymbol{K}} . \underset{\sim}{\boldsymbol{F}}^{-1} = \underset{\sim}{\boldsymbol{F}}^{-T} . \underline{\boldsymbol{K}} . \tag{5.5}$$

Taking the time derivative of the DOFs gives the generalized velocities $\{\underline{\dot{\boldsymbol{u}}}, \dot{\gamma}_\chi\}$:

$$\underline{\dot{\boldsymbol{u}}} = \frac{\partial \underline{\boldsymbol{u}}(\underline{\boldsymbol{X}}, t)}{\partial t}, \tag{5.6}$$

$$\dot{\gamma}_\chi = \frac{\partial \gamma_\chi(\underline{\boldsymbol{X}}, t)}{\partial t}. \tag{5.7}$$

The Eulerian gradient of the generalized velocities is computed as

$$\operatorname{grad} \underline{\dot{\boldsymbol{u}}} = \operatorname{Grad} \underline{\dot{\boldsymbol{u}}} . \underset{\sim}{\boldsymbol{F}}^{-1} = \overline{\operatorname{Grad} \underline{\boldsymbol{u}}}^{\cdot} . \underset{\sim}{\boldsymbol{F}}^{-1} = \dot{\underset{\sim}{\boldsymbol{F}}} . \underset{\sim}{\boldsymbol{F}}^{-1}, \tag{5.8}$$

$$\operatorname{grad} \dot{\gamma}_\chi = \operatorname{Grad} \dot{\gamma}_\chi . \underset{\sim}{\boldsymbol{F}}^{-1} = \overline{\operatorname{Grad} \gamma_\chi}^{\cdot} . \underset{\sim}{\boldsymbol{F}}^{-1} = \dot{\underline{\boldsymbol{K}}} . \underset{\sim}{\boldsymbol{F}}^{-1}, \tag{5.9}$$

where the commutativity between the Lagrangian gradient and time derivatives is used. Note that Eq. (5.8) represents the classical velocity gradient $\underset{\sim}{\boldsymbol{L}} = \dot{\underset{\sim}{\boldsymbol{F}}} . \underset{\sim}{\boldsymbol{F}}^{-1}$.

5.1.2 Principle of virtual power and generalized balance of moment

The principle of virtual power is formulated in the static case following the approach of Germain, 1973. Consider the virtual motion of a subdomain D of the body $\mathbf{B}$ specified by the generalized virtual velocity $\mathcal{V} = \{\underline{\dot{\boldsymbol{u}}}, \dot{\gamma}_\chi\}$. The principle of virtual power asserts that, given any subdomain D, the virtual power of internal forces P^i is equal to the virtual power of external forces P^e for any virtual motion $\mathcal{V}$.

The virtual power of internal forces P^i is assumed to comprise three parts, which are associated respectively to the strain of the subdomain, the microslip and its gradient:

$$P^i = \int_D p^i \, dV = \int_D \left(\underset{\sim}{\boldsymbol{\sigma}} : (\operatorname{grad} \underline{\dot{\boldsymbol{u}}}) + s\dot{\gamma}_\chi + \underline{\boldsymbol{m}} \cdot \operatorname{grad} \dot{\gamma}_\chi \right) dV, \quad \forall D \subset \mathbf{B}, \tag{5.10}$$

where s and $\underline{\boldsymbol{m}}$ are generalized stresses.

In the absence of body forces, the virtual power of external forces is presumed to arise from a surface traction $\underline{\boldsymbol{t}}$ related to the macroscopic motion and a generalized surface traction m related to the microslip. P^e is thus written in the current configuration as

$$P^e = \int_{\partial D} p^c \, dS = \int_{\partial D} \left(\underline{\boldsymbol{t}} . \underline{\dot{\boldsymbol{u}}} + m\dot{\gamma}_\chi \right) dS, \quad \forall D \subset \mathbf{B}. \tag{5.11}$$

Applying the principle of virtual power with Eq. (5.10) and Eq. (5.11) yields

$$\int_D \left(\underset{\sim}{\boldsymbol{\sigma}} : (\operatorname{grad} \underline{\dot{\boldsymbol{u}}}) + s\dot{\gamma}_\chi + \underline{\boldsymbol{m}} \,.\, \operatorname{grad} \dot{\gamma}_\chi\right) dV = \int_{\partial D} \left(\underline{\boldsymbol{t}} \,.\, \underline{\dot{\boldsymbol{u}}} + m\dot{\gamma}_\chi\right) dS, \quad \forall \underline{\dot{\boldsymbol{u}}}, \forall \dot{\gamma}_\chi, \forall D. \tag{5.12}$$

Using the divergence theorem, it can be found that

$$\int_D \left((\operatorname{div} \underset{\sim}{\boldsymbol{\sigma}}) . \underline{\dot{\boldsymbol{u}}} + (\operatorname{div} \underline{\boldsymbol{m}} - s)\, \dot{\gamma}_\chi\right) dV + \int_{\partial D} \left((\underline{\boldsymbol{t}} - \underset{\sim}{\boldsymbol{\sigma}} . \underline{\boldsymbol{n}})\, \underline{\dot{\boldsymbol{u}}} + (m - \underline{\boldsymbol{m}} \,.\, \underline{\boldsymbol{n}})\, \dot{\gamma}_\chi\right) dS = 0, \quad \forall \underline{\dot{\boldsymbol{u}}}, \forall \dot{\gamma}_\chi, \forall D, \tag{5.13}$$

where $\underline{\boldsymbol{n}}$ is the normal to the surface element dS of the boundary ∂D of the subdomain D in the current configuration. Since this relation must hold for all D, all $\underline{\dot{\boldsymbol{u}}}$ and all $\dot{\gamma}_\chi$, one gets the balances

$$\operatorname{div} \underset{\sim}{\boldsymbol{\sigma}} = 0, \quad \forall \underline{\boldsymbol{x}} \in D, \tag{5.14}$$

$$\operatorname{div} \underline{\boldsymbol{m}} - s = 0, \quad \forall \underline{\boldsymbol{x}} \in D, \tag{5.15}$$

and the Neumann boundary conditions

$$\underline{\boldsymbol{t}} = \underset{\sim}{\boldsymbol{\sigma}} . \underline{\boldsymbol{n}}, \quad \forall \underline{\boldsymbol{x}} \in \partial D, \tag{5.16}$$

$$m = \underline{\boldsymbol{m}} \,.\, \underline{\boldsymbol{n}}, \quad \forall \underline{\boldsymbol{x}} \in \partial D. \tag{5.17}$$

Analogously, one can derive the balance laws in the reference configuration:

$$\operatorname{Div} \underset{\sim}{\boldsymbol{S}} = 0, \quad \forall \underline{\boldsymbol{X}} \in D_0, \tag{5.18}$$

$$\operatorname{Div} \underline{\boldsymbol{M}} - S = 0, \quad \forall \underline{\boldsymbol{X}} \in D_0, \tag{5.19}$$

where $\underset{\sim}{\boldsymbol{S}}$ is the Boussinesq stress tensor which generates power over $\dot{\underset{\sim}{\boldsymbol{F}}}$ in any subdomain D_0 of the body $\mathbf{B_0}$, $\underline{\boldsymbol{M}}$ is the generalized stress which generates power over $\underline{\dot{\boldsymbol{K}}}$ in D_0 and S is the generalized stress which generates power over $\dot{\gamma}_\chi$ in D_0. In addition,

$$\underset{\sim}{\boldsymbol{S}} = \frac{\rho_0}{\rho} \underset{\sim}{\boldsymbol{\sigma}} . \underset{\sim}{\boldsymbol{F}}^{-T}; \tag{5.20}$$

$$\underline{\boldsymbol{M}} = \frac{\rho_0}{\rho} \underset{\sim}{\boldsymbol{F}}^{-1} . \underline{\boldsymbol{m}}; \tag{5.21}$$

$$S = \frac{\rho_0}{\rho} s. \tag{5.22}$$

The Neumann boundary conditions then become

$$\underline{\boldsymbol{T}} = \underset{\sim}{\boldsymbol{S}} . \underline{\boldsymbol{n}}_0, \quad \forall \underline{\boldsymbol{X}} \in \partial D_0, \tag{5.23}$$

$$M = \underline{\boldsymbol{M}} \,.\, \underline{\boldsymbol{n}}_0, \quad \forall \underline{\boldsymbol{X}} \in \partial D_0. \tag{5.24}$$

where $\underline{\boldsymbol{T}}$ is the surface traction measured with respect to ∂D_0, M is the generalized surface traction which generates power over $\dot{\gamma}_\chi$ in D_0 and $\underline{\boldsymbol{n}}_0$ is the normal to the surface element of the subdomain D_0.

5.1.3 Second law of thermodynamics

The second law of thermodynamics asserts non-negative energy dissipation rate d for any subdomain D of the crystalline body B in the current configuration, which writes

$$d = \int_D p^i \, dV - \overset{\cdot}{\overline{\int_D \rho\psi \, dV}} \geqslant 0 \tag{5.25}$$

with the free energy density ψ measured per unit mass and the mass density ρ measured in the current configuration. The second term represents the temporal increase in the free energy of subdomain D, which follows

$$\overset{\cdot}{\overline{\int_D \rho\psi \, dV}} = \overset{\cdot}{\overline{\int_{D_0} \rho_0\psi \, dV_0}} = \int_{D_0} \rho_0\dot{\psi} \, dV_0 = \int_D \rho\dot{\psi} \, dV, \tag{5.26}$$

where D_0 denotes the considered subdomain in the reference configuration and ρ_0 the reference mass density. Thus Eq. (5.25) can be written as

$$\int_D \left(p^i - \rho\dot{\psi}\right) dV \geqslant 0. \tag{5.27}$$

As D is arbitrary, the local form of the entropy imbalance is

$$p^i - \rho\dot{\psi} \geqslant 0. \tag{5.28}$$

5.1.4 Constitutive equations

The goal is to propose a set of constitutive equations accounting for the generalized stress variables and the microslip variables, fulfilling the entropy inequality. To this end, we first consider the multiplicative decomposition of the deformation gradient $\underset{\sim}{\boldsymbol{F}}$:

$$\underset{\sim}{\boldsymbol{F}} = \underset{\sim}{\boldsymbol{E}}.\underset{\sim}{\boldsymbol{P}}, \tag{5.29}$$

where $\underset{\sim}{\boldsymbol{E}}$ denotes the elastic part and $\underset{\sim}{\boldsymbol{P}}$ the plastic part of the deformation gradient $\underset{\sim}{\boldsymbol{F}}$. By this decomposition, a local intermediate configuration $C_\sharp$ is introduced (Mandel, 1973). The reference and current local configuration at $\underline{\boldsymbol{X}}$ are called C_0 and C respectively. It is assumed that plastic deformation takes place through the slip of dislocations on prescribed slip planes with normal $\underline{\boldsymbol{n}}^s$ along prescribed slip direction $\underline{\boldsymbol{l}}^s$, and that the evolution of $\underset{\sim}{\boldsymbol{P}}$ is governed by the plastic slip γ^s on slip systems s via the relation

$$\dot{\underset{\sim}{\boldsymbol{P}}}.\underset{\sim}{\boldsymbol{P}}^{-1} = \sum_{s=1}^{N} \dot{\gamma}^s \underset{\sim}{\boldsymbol{N}}^s \tag{5.30}$$

with the Schmid tensor $\underset{\sim}{\boldsymbol{N}}^s = \underline{\boldsymbol{l}}^s \otimes \underline{\boldsymbol{n}}^s$ and the total number of slip systems N. The uniqueness of the decomposition (Eq. (5.29)) is obtained by choosing the isoclinic local configuration $C_\sharp$ where the crystal lattice has the same orientation as in C_0 (Mandel, 1973). A cumulative total slip variable γ_{cum} is introduced as

$$\gamma_{cum} = \int_0^t \sum_{s=1}^{12} |\dot{\gamma}^s| \, dt. \tag{5.31}$$

γ_{cum} is related to the microslip variable γ_χ via a variable $e(\underline{\boldsymbol{X}}, t)$ called relative plastic slip and given by

$$e(\underline{\boldsymbol{X}}, t) = \gamma_{cum} - \gamma_\chi. \tag{5.32}$$

The relative plastic slip variable e measures the deviation of γ_χ from γ_{cum} and will be associated with an energy cost in the free energy potential in the following.

Considering Eq. (5.29), $\underset{\sim}{\boldsymbol{L}}$ can be expressed as

$$\underset{\sim}{\boldsymbol{L}} = \dot{\underset{\sim}{\boldsymbol{F}}}\underset{\sim}{\boldsymbol{F}}^{-1} = \underset{\sim}{\boldsymbol{L}}^e + \underset{\sim}{\boldsymbol{E}}.\underset{\sim}{\boldsymbol{L}}^p.\underset{\sim}{\boldsymbol{E}}^{-1} \tag{5.33}$$

with

$$\underset{\sim}{\boldsymbol{L}}^e = \dot{\underset{\sim}{\boldsymbol{E}}}.\underset{\sim}{\boldsymbol{E}}^{-1}, \quad \underset{\sim}{\boldsymbol{L}}^p = \dot{\underset{\sim}{\boldsymbol{P}}}.\underset{\sim}{\boldsymbol{P}}^{-1}. \tag{5.34}$$

With the consideration of Eqs. (5.32) and (5.33), the internal power density p^i in Eq. (5.10) can be further developed as

$$p^i = \frac{\rho}{\rho_\sharp}\underset{\sim}{\boldsymbol{\Pi}}^e : \dot{\underset{\sim}{\boldsymbol{E}}}^e_{GL} + \frac{\rho}{\rho_\sharp}\underset{\sim}{\boldsymbol{\Pi}}^M : (\dot{\underset{\sim}{\boldsymbol{P}}}.\underset{\sim}{\boldsymbol{P}}^{-1}) + s(\dot{\gamma}_{cum} - \dot{e}) + \underline{\boldsymbol{m}} \,.\, \mathrm{grad}\, \dot{\gamma}_\chi. \tag{5.35}$$

with

$$\underset{\sim}{\boldsymbol{\Pi}}^e = \frac{\rho_\sharp}{\rho}\underset{\sim}{\boldsymbol{E}}^{-1}.\underset{\sim}{\boldsymbol{\sigma}}.\underset{\sim}{\boldsymbol{E}}^{-T}, \; \underset{\sim}{\boldsymbol{\Pi}}^M = \frac{\rho_\sharp}{\rho}\underset{\sim}{\boldsymbol{E}}^T.\underset{\sim}{\boldsymbol{\sigma}}.\underset{\sim}{\boldsymbol{E}}^{-T} = \underset{\sim}{\boldsymbol{E}}^T.\underset{\sim}{\boldsymbol{E}}.\underset{\sim}{\boldsymbol{\Pi}}^e, \; \underset{\sim}{\boldsymbol{E}}^e_{GL} = \frac{1}{2}\left(\underset{\sim}{\boldsymbol{E}}^T.\underset{\sim}{\boldsymbol{E}} - \underset{\sim}{\mathbf{1}}\right) \tag{5.36}$$

where $\rho_\sharp$ is the density measured w.r.t. the intermediate configuration $C_\sharp$, $\underset{\sim}{\boldsymbol{E}}^e_{GL}$ denotes the Green-Lagrange elastic strain tensor, $\underset{\sim}{\boldsymbol{\Pi}}^e$ the Piola stress tensor w.r.t. $C_\sharp$ and $\underset{\sim}{\boldsymbol{\Pi}}^M$ the Mandel stress tensor. Note that $\rho_\sharp = \rho_0$, because of the plastic incompressibility of the crystalline body. As Eulerian gradient and time derivative do not generally commute, it is more convenient to express $\underline{\boldsymbol{m}} \,.\, \mathrm{grad}\, \dot{\gamma}_\chi$ in Eq. (5.35) in terms of Lagrangian gradient. Considering Eqs. (5.9) and (5.21), one obtains

$$\begin{aligned} \underline{\boldsymbol{m}} \,.\, \mathrm{grad}\, \dot{\gamma}_\chi &= \underline{\boldsymbol{m}} \,.\, \left(\mathrm{Grad}\, \dot{\gamma}_\chi.\underset{\sim}{\boldsymbol{F}}^{-1}\right) = \left(\underset{\sim}{\boldsymbol{F}}^{-1}.\underline{\boldsymbol{m}}\right) \,.\, \mathrm{Grad}\, \dot{\gamma}_\chi \\ &= \frac{\rho}{\rho_0}\left(\frac{\rho_0}{\rho}\underset{\sim}{\boldsymbol{F}}^{-1}.\underline{\boldsymbol{m}}\right) \,.\, \mathrm{Grad}\, \dot{\gamma}_\chi = \frac{\rho}{\rho_0}\underline{\boldsymbol{M}} \,.\, \mathrm{Grad}\, \dot{\gamma}_\chi. \end{aligned} \tag{5.37}$$

Because of the commutativity between Lagrangian gradient and time derivative, one gets

$$\frac{\rho}{\rho_0}\underline{\boldsymbol{M}}\,.\,\mathrm{Grad}\,\dot{\gamma}_\chi = \frac{\rho}{\rho_0}\underline{\boldsymbol{M}}\,.\,\overline{\mathrm{Grad}\,\gamma_\chi}^{\cdot} = \frac{\rho}{\rho_0}\underline{\boldsymbol{M}}\,.\,\dot{\underline{\boldsymbol{K}}}\,. \tag{5.38}$$

As a result, Eqs. (5.35) and (5.38) yield

$$p^i = \frac{\rho}{\rho_\sharp}\underset{\sim}{\boldsymbol{\Pi}}^e : \dot{\underset{\sim}{\boldsymbol{E}}}^e_{GL} + \frac{\rho}{\rho_\sharp}\underset{\sim}{\boldsymbol{\Pi}}^M : (\dot{\underset{\sim}{\boldsymbol{P}}}.\underset{\sim}{\boldsymbol{P}}^{-1}) + s(\dot{\gamma}_{cum} - \dot{e}) + \frac{\rho}{\rho_0}\underline{\boldsymbol{M}}\,.\dot{\underline{\boldsymbol{K}}} \tag{5.39}$$

In the present model, the vector microslip variable $\underline{\boldsymbol{K}}$ and the relative plastic slip e are assumed to be state variables in addition to the usually considered term — elastic strain $\underset{\sim}{\boldsymbol{E}}_{GL}$. The free energy density ψ is hence a function of $\underset{\sim}{\boldsymbol{E}}_{GL}$, $\underline{\boldsymbol{K}}$ and e:

$$\psi = \psi\left(\underset{\sim}{\boldsymbol{E}}^e_{GL}, e, \underline{\boldsymbol{K}}\right). \tag{5.40}$$

Thus, $\rho\dot{\psi}$ yields

$$\rho\dot{\psi} = \rho\frac{\partial\psi}{\partial\underset{\sim}{\boldsymbol{E}}^e_{GL}} : \dot{\underset{\sim}{\boldsymbol{E}}}^e_{GL} + \rho\frac{\partial\psi}{\partial e}\dot{e} + \rho\frac{\psi}{\underline{\boldsymbol{K}}}\,.\dot{\underline{\boldsymbol{K}}}\,. \tag{5.41}$$

Considering Eqs. (5.28), (5.39) and (5.41) yields

$$\rho\left(\frac{\underset{\sim}{\boldsymbol{\Pi}}^e}{\rho_\sharp} - \frac{\partial\psi}{\partial\underset{\sim}{\boldsymbol{E}}^e_{GL}}\right) : \dot{\underset{\sim}{\boldsymbol{E}}}^e_{GL} + \frac{\rho}{\rho_\sharp}\underset{\sim}{\boldsymbol{\Pi}}^M : \left(\dot{\underset{\sim}{\boldsymbol{P}}}\underset{\sim}{\boldsymbol{P}}^{-1}\right) - \left(s + \rho\frac{\partial\psi}{\partial e}\right)\dot{e} + \rho\left(\frac{\underline{\boldsymbol{M}}}{\rho_0} - \frac{\partial\psi}{\partial\underline{\boldsymbol{K}}}\right).\dot{\underline{\boldsymbol{K}}} + s\dot{\gamma}_{cum} \geqslant 0. \tag{5.42}$$

Following the Coleman-Noll procedure, we require that Eq. (5.42) holds for all arbitrarily prescribed $\dot{\underset{\sim}{\boldsymbol{E}}}^e_{GL}$, $\dot{e}$ and $\dot{\underline{\boldsymbol{K}}}$. In order to satisfy this requirement, the coefficients associated with the three terms mush vanish, which gives the state laws:

$$\underset{\sim}{\boldsymbol{\Pi}}^e = \rho_\sharp\frac{\partial\psi}{\partial\underset{\sim}{\boldsymbol{E}}^e_{GL}}, \tag{5.43}$$

$$s = -\rho\frac{\partial\psi}{\partial e}, \tag{5.44}$$

$$\underline{\boldsymbol{M}} = \rho_0\frac{\partial\psi}{\partial\underline{\boldsymbol{K}}}. \tag{5.45}$$

Note that, as the free energy potential is assumed to depend on the Lagrangian term $\underline{\boldsymbol{K}}$, a constitutive relation is thus directly obtained for the work-conjugate pair $\underline{\boldsymbol{K}}$ and $\underline{\boldsymbol{M}}$ in the reference configuration C_0. Furthermore, Eq. (5.42) yields the residual dissipation (also called reduced dissipation) inequality:

$$d^{res} = \frac{\rho}{\rho_\sharp}\underset{\sim}{\boldsymbol{\Pi}}^M : \left(\dot{\underset{\sim}{\boldsymbol{P}}}\underset{\sim}{\boldsymbol{P}}^{-1}\right) + s\dot{\gamma}_{cum} \geqslant 0. \tag{5.46}$$

Given Eq. (5.30), the term $\underset{\sim}{\boldsymbol{\Pi}}^M : \left(\dot{\underset{\sim}{\boldsymbol{P}}}\underset{\sim}{\boldsymbol{P}}^{-1}\right)$ yields

$$\underset{\sim}{\boldsymbol{\Pi}}^M : \left(\dot{\underset{\sim}{\boldsymbol{P}}}\underset{\sim}{\boldsymbol{P}}^{-1}\right) = \underset{\sim}{\boldsymbol{\Pi}}^M : \left(\sum_{s=1}^{12} \dot{\gamma}^s \underset{\sim}{\boldsymbol{N}}^s\right) = \sum_{s=1}^{12} \left(\underset{\sim}{\boldsymbol{\Pi}}^M : \underset{\sim}{\boldsymbol{N}}^s\right) \dot{\gamma}^s = \sum_{s=1}^{12} \tau^s \dot{\gamma}^s, \tag{5.47}$$

with the resolved shear stress $\tau^s = \underset{\sim}{\boldsymbol{\Pi}}^M : \underset{\sim}{\boldsymbol{N}}^s$ in $C_\sharp$. Thus, the residual dissipation inequality writes

$$d^{res} = \frac{\rho}{\rho_\sharp} \sum_{s=1}^{12} \tau^s \dot{\gamma}^s + s\dot{\gamma}_{cum} \geqslant 0. \tag{5.48}$$

With γ_{cum} defined by Eq. (5.31), Eq. (5.48) can be written as

$$d^{res} = \frac{\rho}{\rho_\sharp} \sum_{s=1}^{12} \tau^s \dot{\gamma}^s + s \sum_{s=1}^{12} |\dot{\gamma}^s| \geqslant 0. \tag{5.49}$$

Noticing that $\text{sign}\,(\tau^s) = \text{sign}\,(\gamma^s)$, one has $\tau^s\dot{\gamma}^s = |\tau^s||\dot{\gamma}^s|$. Eq. (5.49) can be further written as

$$d^{res} = \frac{\rho}{\rho_\sharp} \sum_{s=1}^{12} |\tau^s||\dot{\gamma}^s| + s \sum_{s=1}^{12} |\dot{\gamma}^s| = \frac{\rho}{\rho_\sharp} \sum_{s=1}^{12} \left(|\tau^s| + \frac{\rho_\sharp}{\rho} s\right) |\dot{\gamma}^s| \geqslant 0. \tag{5.50}$$

Considering the term $|\tau^s| + \dfrac{\rho_\sharp}{\rho} s$ in Eq. (5.50), we propose to introduce the following yield function:

$$f^s = |\tau^s| + \frac{\rho_\sharp}{\rho} s - \tau_c^s = |\tau^s| - \left(\tau_c^s - \frac{\rho_\sharp}{\rho} s\right) \leqslant 0, , \ \forall s = 1, 2, ..., N, \tag{5.51}$$

where τ_c^s is the critical resolved shear stress (CRSS) for the slip system s. As can be seen from the yield function, the generalized stress s is regarded as a source of isotropic hardening and changes the yield limit of slip systems. Accordingly, a rate-dependent law is chosen for the plastic slip γ^s, expressed as

$$\dot{\gamma}^s = \left\langle \frac{|\tau^s| - \left(\tau_c^s - \frac{\rho_\sharp}{\rho} s\right)}{K} \right\rangle^n \text{sign}\,(\tau^s)\,. \tag{5.52}$$

5.1.5 Alternative formulation of constitutive equations

In the previous sections, the constitutive equations are derived by accounting for $\underline{\boldsymbol{K}}$, or equivalently $\underline{\boldsymbol{k}}$, as an argument of the free energy potential. However, other choices exist. Inspired from the Green-Lagrange elastic tensor $\underset{\sim}{\boldsymbol{E}}^e_{GL}$ which is measured in the intermediate configuration $C_\sharp$, we push forward $\underline{\boldsymbol{K}}$ into $C_\sharp$, or equivalently pull back $\underline{\boldsymbol{k}}$ into $C_\sharp$, and define $\underline{\boldsymbol{K}}^\sharp$ as:

$$\underline{\boldsymbol{K}}^\sharp = \underset{\sim}{\boldsymbol{P}}^{-T}.\underline{\boldsymbol{K}} = \underset{\sim}{\boldsymbol{E}}^T.\underline{\boldsymbol{k}}\,. \tag{5.53}$$

The generalized stress $\underline{\boldsymbol{M}}^{\sharp}$ work-conjugate to $\underline{\boldsymbol{K}}^{\sharp}$ in the intermediate configuration $C_{\sharp}$ can be found according to the requirement that the work generated by $\underline{\boldsymbol{M}}$ over the vector microslip variable $\underline{\boldsymbol{K}}$ on a volume element dV_0 in C_0 is equal to that by $\underline{\boldsymbol{M}}^{\sharp}$ over $\underline{\boldsymbol{K}}^{\sharp}$ on the volume element $dV_{\sharp}$ in $C_{\sharp}$. Thus, $\underline{\boldsymbol{M}}.\underline{\boldsymbol{K}}$ follows

$$\underline{\boldsymbol{M}}.\underline{\boldsymbol{K}}\, dV_0 = \frac{\rho_{\sharp}}{\rho_0}\underline{\boldsymbol{M}}.\underline{\boldsymbol{K}}\, dV_{\sharp} = \frac{\rho_{\sharp}}{\rho_0}\underline{\boldsymbol{M}}.\underset{\sim}{\boldsymbol{P}}^{T}.\underset{\sim}{\boldsymbol{P}}^{-T}.\underline{\boldsymbol{K}}\, dV_{\sharp} = \frac{\rho_{\sharp}}{\rho_0}\underline{\boldsymbol{M}}.\underset{\sim}{\boldsymbol{P}}^{T}.\underline{\boldsymbol{K}}^{\sharp}\, dV_{\sharp} = \underline{\boldsymbol{M}}^{\sharp}.\underline{\boldsymbol{K}}^{\sharp}\, dV_{\sharp}, \tag{5.54}$$

where

$$\underline{\boldsymbol{M}}^{\sharp} = \frac{\rho_{\sharp}}{\rho_0}\underline{\boldsymbol{M}}.\underset{\sim}{\boldsymbol{P}}^{T} = \frac{\rho_{\sharp}}{\rho_0}\underset{\sim}{\boldsymbol{P}}.\underline{\boldsymbol{M}}\,. \tag{5.55}$$

Substituting Eq. (5.21) into the previous equation leads to

$$\underline{\boldsymbol{M}}^{\sharp} = \frac{\rho_{\sharp}}{\rho}\underset{\sim}{\boldsymbol{E}}^{-1}.\underline{\boldsymbol{m}} \tag{5.56}$$

Accordingly, an alternative constitutive formulation can be proposed for which the free energy potential depends on $\underline{\boldsymbol{K}}^{\sharp}$ instead of $\underline{\boldsymbol{K}}$, i.e., $\psi = \psi\left(\underset{\sim}{\boldsymbol{E}}^{e}_{GL}, e, \underline{\boldsymbol{K}}^{\sharp}\right)$. It follows that

$$\rho\dot{\psi} = \rho\frac{\partial\psi}{\partial\underset{\sim}{\boldsymbol{E}}^{e}_{GL}} : \dot{\underset{\sim}{\boldsymbol{E}}}^{e}_{GL} + \rho\frac{\partial\psi}{\partial e}\dot{e} + \rho\frac{\psi}{\underline{\boldsymbol{K}}^{\sharp}}.\dot{\underline{\boldsymbol{K}}}^{\sharp}. \tag{5.57}$$

Substitution of Eqs. (5.53) and (5.55) into the power density of internal forces, Eq. (5.39), leads to

$$\begin{aligned}
p^i &= \frac{\rho}{\rho_{\sharp}}\underset{\sim}{\boldsymbol{\Pi}}^{e} : \dot{\underset{\sim}{\boldsymbol{E}}}^{e}_{GL} + \frac{\rho}{\rho_{\sharp}}\underset{\sim}{\boldsymbol{\Pi}}^{M} : (\dot{\underset{\sim}{\boldsymbol{P}}}.\underset{\sim}{\boldsymbol{P}}^{-1}) + s(\dot{\gamma}_{cum} - \dot{e}) + \frac{\rho}{\rho_0}\underline{\boldsymbol{M}}.\dot{\underline{\boldsymbol{K}}} && (5.58)\\
&= \frac{\rho}{\rho_{\sharp}}\underset{\sim}{\boldsymbol{\Pi}}^{e} : \dot{\underset{\sim}{\boldsymbol{E}}}^{e}_{GL} + \frac{\rho}{\rho_{\sharp}}\underset{\sim}{\boldsymbol{\Pi}}^{M} : (\dot{\underset{\sim}{\boldsymbol{P}}}.\underset{\sim}{\boldsymbol{P}}^{-1}) + s(\dot{\gamma}_{cum} - \dot{e}) + \\
&\frac{\rho}{\rho_{\sharp}}\underset{\sim}{\boldsymbol{P}}^{-1}.\underline{\boldsymbol{M}}^{\sharp}.(\dot{\underset{\sim}{\boldsymbol{P}}}^{T}.\underline{\boldsymbol{K}}^{\sharp} + \underset{\sim}{\boldsymbol{P}}^{T}.\dot{\underline{\boldsymbol{K}}}^{\sharp}) && (5.59)\\
&= \frac{\rho}{\rho_{\sharp}}\underset{\sim}{\boldsymbol{\Pi}}^{e} : \dot{\underset{\sim}{\boldsymbol{E}}}^{e}_{GL} + \frac{\rho}{\rho_{\sharp}}\underset{\sim}{\boldsymbol{\Pi}}^{M} : (\dot{\underset{\sim}{\boldsymbol{P}}}.\underset{\sim}{\boldsymbol{P}}^{-1}) + s(\dot{\gamma}_{cum} - \dot{e}) + \frac{\rho}{\rho_{\sharp}}\underset{\sim}{\boldsymbol{P}}^{-1}.\dot{\underset{\sim}{\boldsymbol{P}}}.\underline{\boldsymbol{M}}^{\sharp}.\underline{\boldsymbol{K}}^{\sharp}\\
&+ \frac{\rho}{\rho_{\sharp}}\underset{\sim}{\boldsymbol{P}}^{-1}.\underset{\sim}{\boldsymbol{P}}.\underline{\boldsymbol{M}}^{\sharp}.\dot{\underline{\boldsymbol{K}}}^{\sharp} && (5.60)\\
&= \frac{\rho}{\rho_{\sharp}}\underset{\sim}{\boldsymbol{\Pi}}^{e} : \dot{\underset{\sim}{\boldsymbol{E}}}^{e}_{GL} + \frac{\rho}{\rho_{\sharp}}\underset{\sim}{\boldsymbol{\Pi}}^{M} : (\dot{\underset{\sim}{\boldsymbol{P}}}.\underset{\sim}{\boldsymbol{P}}^{-1}) + s(\dot{\gamma}_{cum} - \dot{e}) + \frac{\rho}{\rho_{\sharp}}(\underline{\boldsymbol{K}}^{\sharp}\otimes\underline{\boldsymbol{M}}^{\sharp}) : (\dot{\underset{\sim}{\boldsymbol{P}}}.\underset{\sim}{\boldsymbol{P}}^{-1})\\
&+ \frac{\rho}{\rho_{\sharp}}\underline{\boldsymbol{M}}^{\sharp}.\dot{\underline{\boldsymbol{K}}}^{\sharp}. && (5.61)
\end{aligned}$$

Substituting Eqs. (5.57) and (5.61) into Eq. (5.28) writes

$$\begin{aligned}
p^i - \rho\dot{\psi} \;=\; & \rho\left(\frac{\underset{\sim}{\boldsymbol{\Pi}}^{e}}{\rho_{\sharp}} - \frac{\partial\psi}{\partial\underset{\sim}{\boldsymbol{E}}^{e}_{GL}}\right) : \dot{\underset{\sim}{\boldsymbol{E}}}^{e}_{GL} - \left(s + \rho\frac{\partial\psi}{\partial e}\right)\dot{e} + \rho\left(\frac{\underline{\boldsymbol{M}}^{\sharp}}{\rho_{\sharp}} - \frac{\partial\psi}{\partial\underline{\boldsymbol{K}}^{\sharp}}\right).\dot{\underline{\boldsymbol{K}}}^{\sharp}\\
& + \frac{\rho}{\rho_{\sharp}}\left(\underset{\sim}{\boldsymbol{\Pi}}^{M} + \underline{\boldsymbol{K}}^{\sharp}\otimes\underline{\boldsymbol{M}}^{\sharp}\right) : \left(\dot{\underset{\sim}{\boldsymbol{P}}}\underset{\sim}{\boldsymbol{P}}^{-1}\right) + s\dot{\gamma}_{cum} \geqslant 0. && (5.62)
\end{aligned}$$

Following the Coleman-Noll procedure results in the constitutive equations Eqs. (5.43) and (5.44) and another one connecting $\underline{\boldsymbol{M}}^{\sharp}$ and $\underline{\boldsymbol{K}}^{\sharp}$

$$\underline{\boldsymbol{M}}^{\sharp} = \rho_{\sharp} \frac{\partial \psi}{\partial \underline{\boldsymbol{K}}^{\sharp}}. \tag{5.63}$$

Then, the residual dissipation inequality writes

$$d^{res} = \frac{\rho}{\rho_{\sharp}} \left(\underset{\sim}{\boldsymbol{\Pi}}^{M} + \underline{\boldsymbol{K}}^{\sharp} \otimes \underline{\boldsymbol{M}}^{\sharp} \right) : \left(\underset{\sim}{\dot{\boldsymbol{P}}} \underset{\sim}{\boldsymbol{P}}^{-1} \right) + s \dot{\gamma}_{cum} \geqslant 0. \tag{5.64}$$

Considering Eqs. (5.30) and (5.31) yields

$$d^{res} = \frac{\rho}{\rho_{\sharp}} \left(\underset{\sim}{\boldsymbol{\Pi}}^{M} + \underline{\boldsymbol{K}}^{\sharp} \otimes \underline{\boldsymbol{M}}^{\sharp} \right) : \left(\sum_{s=1}^{12} \dot{\gamma}^{s} \underset{\sim}{\boldsymbol{N}}^{s} \right) + s \sum_{s=1}^{12} |\dot{\gamma}^{s}| \geqslant 0. \tag{5.65}$$

Given the resolved shear stress $\tau^{s} = \underset{\sim}{\boldsymbol{\Pi}}^{M} : \underset{\sim}{\boldsymbol{N}}^{s}$ with $\underset{\sim}{\boldsymbol{N}}^{s} = \underline{\boldsymbol{l}}^{s} \otimes \underline{\boldsymbol{n}}^{s}$, the previous inequality follows

$$\begin{aligned} d^{res} &= \frac{\rho}{\rho_{\sharp}} \sum_{s=1}^{12} \left\{ \left[\tau^{s} + (\underline{\boldsymbol{K}}^{\sharp}.\underline{\boldsymbol{l}}^{s})(\underline{\boldsymbol{M}}^{\sharp}.\underline{\boldsymbol{n}}^{s}) \right] \dot{\gamma}^{s} + \frac{\rho_{\sharp}}{\rho} s |\dot{\gamma}^{s}| \right\} && (5.66) \\ &= \frac{\rho}{\rho_{\sharp}} \sum_{s=1}^{12} \left(|\tau^{\sharp s}| + \frac{\rho_{\sharp}}{\rho} s \right) |\dot{\gamma}^{s}| \geqslant 0, && (5.67) \end{aligned}$$

where a generalized resolved shear stress is defined as

$$\tau^{\sharp s} = \tau^{s} + x^{s} \tag{5.68}$$

with

$$x^{s} = (\underline{\boldsymbol{K}}^{\sharp}.\underline{\boldsymbol{l}}^{s})(\underline{\boldsymbol{M}}^{\sharp}.\underline{\boldsymbol{n}}^{s}). \tag{5.69}$$

It can be seen that the residual dissipation section 5.1.5 takes the same form as Eq. (5.50), except that $\tau^{\sharp s}$ is used instead of τ^{s}. Moreover, x^{s} plays the role of a gradient induced back-stress for each slip system. Therefore, a second yield function is thus proposed in the form:

$$f^{s} = |\tau^{\sharp s}| - \left(\tau_{c}^{s} - \frac{\rho_{\sharp}}{\rho} s \right) = |\tau^{s} + (\underline{\boldsymbol{K}}^{\sharp}.\underline{\boldsymbol{l}}^{s})(\underline{\boldsymbol{M}}^{\sharp}.\underline{\boldsymbol{n}}^{s})| - \left(\tau_{c}^{s} - \frac{\rho_{\sharp}}{\rho} s \right) \leqslant 0, \ \forall s = 1, 2, ..., 12. \tag{5.70}$$

Compared with the previous formulation of the theory, gradient terms come into play not only through isotropic hardening but also kinematic hardening, as a result of introducing the gradient of microslip measured in the intermediate configuration. Accordingly, the rate-dependent law to determine the plastic slip writes

$$\dot{\gamma}^{s} = \left\langle \frac{|\tau^{\sharp s}| - \left(\tau_{c}^{s} - \frac{\rho_{\sharp}}{\rho} s \right)}{K} \right\rangle^{n} \operatorname{sign}(\tau^{s}). \tag{5.71}$$

5.1.6 Hardening laws

The hardening laws describe the evolution of the critical resolved shear stress τ_c^s with some internal variables. In the present work, the hardening laws based on the evolution of dislocation densities are taken into account. Since the thermodynamics of the evolution of dislocation densities is not known (Busso and Cailletaud, 2005), the hardening laws are not involved in the previous development of the present model.

Following Kubin et al. (2008), τ_c^s of the slip system s can be expressed as:

$$\tau_c^s = \tau_0 + \mu \sqrt{\sum_{s=1}^{12} a^{su} r^u}, \tag{5.72}$$

where τ_0 is the thermal component of the CRSS due to the lattice friction, r^s denotes adimensional dislocation density ($r^s = b^2\rho^s$ with the dislocation density ρ^s and the norm of Burgers vector of the dislocation b), μ is the shear modulus, and a^{su} is a matrix for describing long-range interactions between dislocations.

Considering the multiplication and the annihilation of dislocations due to the interactions among them, the evolution of adimensional dislocation densities r^s is governed by

$$\dot{r^s} = |\dot{\gamma}^s| \left(\frac{\sqrt{b^{su} r^u}}{\kappa} - G_c r^s \right), \tag{5.73}$$

where κ is proportional to the number of obstacles crossed by a dislocation before being immobilized, G_c is the critical distance controlling the annihilation of dislocations with opposite signs, and b^{su} describes the interactions between dislocations. The structure of the matrices a^{su} and b^{su} are given in appendix A for FCC crystals.

5.2 Constitutive choices for the free energy potential

Different free energy potentials can be chosen for the two formulations of the constitutive equations. Several potentials as well as resulting regularization equations are proposed in the following. The two formulations are discussed separately.

5.2.1 Formulation with free energy potential depending on $\underline{\boldsymbol{K}}$ or $\underline{\boldsymbol{k}}$

Choices of free energy potential are first discussed for the constitutive formulation presented in section 5.1.4. Choices of free energy potential leads to different state laws, yield functions and regularization functions as shown below.

Model based on the state law $\underline{\boldsymbol{M}} = \underset{\sim}{\boldsymbol{A}}.\underline{\boldsymbol{K}}$

A first quadratic potential is considered in the form:

$$\rho\psi = \frac{1}{2}\frac{\rho}{\rho_\sharp}\underset{\sim}{\boldsymbol{E}}^e_{GL} : \underset{\approx}{\boldsymbol{\Lambda}} : \underset{\sim}{\boldsymbol{E}}^e_{GL} + \frac{1}{2}\frac{\rho}{\rho_0}H_\chi e^2 + \frac{1}{2}\frac{\rho}{\rho_0}\underline{\boldsymbol{K}}\,.\underset{\sim}{\boldsymbol{A}}.\underline{\boldsymbol{K}}\,, \tag{5.74}$$

where $\underset{\approx}{\boldsymbol{\Lambda}}$ is the fourth rank tensor of elastic moduli, H_χ a penalty modulus and $\underset{\sim}{\boldsymbol{A}}$ a second rank tensor of high order moduli. With this potential, the constitutive relations Eqs. (5.43) to (5.45) yield

$$\underset{\sim}{\boldsymbol{\Pi}}^e = \underset{\approx}{\boldsymbol{\Lambda}} : \underset{\sim}{\boldsymbol{E}}^e_{GL}, \tag{5.75}$$

$$s = -\frac{\rho}{\rho_0}H_\chi e, \tag{5.76}$$

$$\underline{\boldsymbol{M}} = \underset{\sim}{\boldsymbol{A}}.\underline{\boldsymbol{K}}\,, \tag{5.77}$$

with $e = \gamma_{cum} - \gamma_\chi$. Noticing $S = \frac{\rho_0}{\rho}s$, one can write Eq. (5.76) as

$$S = -H_\chi e. \tag{5.78}$$

Substituting Eqs. (5.5) and (5.21) into Eq. (5.77) yields a nonlinear relation between the associated Eulerian vectors:

$$\underline{\boldsymbol{m}} = \frac{\rho}{\rho_0}\underset{\sim}{\boldsymbol{F}}.\underset{\sim}{\boldsymbol{A}}.\underset{\sim}{\boldsymbol{F}}^T.\underline{\boldsymbol{k}}\,. \tag{5.79}$$

Then, we consider the yield function Eq. (5.51). Noticing that $\rho_\sharp = \rho_0$ for crystal plasticity and that $S = \frac{\rho_0}{\rho}s$, one can obtain

$$f^s = |\tau^s| - \left(\tau^s_c - \frac{\rho_\sharp}{\rho}s\right) = |\tau^s| - \left(\tau^s_c - \frac{\rho_0}{\rho}s\right) = |\tau^s| - (\tau^s_c - S) \tag{5.80}$$

Substituting the balance law Eq. (5.19) into the previous yield function gives

$$f^s = |\tau^s| - (\tau^s_c - \mathrm{Div}\,\underline{\boldsymbol{M}}\,)\,. \tag{5.81}$$

In the present work, the model will be applied to crystals with cubic symmetry. It follows that $\underset{\sim}{\boldsymbol{A}}$ must be a spherical tensor, i.e., $\underset{\sim}{\boldsymbol{A}} = A\underset{\sim}{\mathbf{1}}$. The constitutive relations Eqs. (5.77) and (5.79) thus become

$$\underline{\boldsymbol{M}} = A.\underline{\boldsymbol{K}}\,, \tag{5.82}$$

$$\underline{\boldsymbol{m}} = \frac{\rho}{\rho_0}A\underset{\sim}{\boldsymbol{B}}.\underline{\boldsymbol{k}}\,, \tag{5.83}$$

where $\underset{\sim}{\boldsymbol{B}} = \underset{\sim}{\boldsymbol{F}}.\underset{\sim}{\boldsymbol{F}}^T$ is the left Cauchy–Green tensor. Taking into account the state law Eq. (5.82), one can further get

$$f^s = |\tau^s| - (\tau^s_c - A\mathrm{Div}\,(\mathrm{Grad}\,\gamma_\chi)) = |\tau^s| - (\tau^s_c - A\triangle_X\gamma_\chi) \tag{5.84}$$

As can be seen in this expression, the term Grad γ_χ comes into play as a source of isotropic hardening proportional to the Laplacian of microslip in the spirit of Aifantis model (Aifantis, 1987).

Moreover, one can obtain the regularization equation connecting γ_χ and γ_{cum}. Combining Eqs. (5.19), (5.32), (5.78) and (5.82) gives

$$\gamma_\chi - \frac{A}{H_\chi} \triangle_X \gamma_\chi = \gamma_{cum}. \tag{5.85}$$

Here, the regularization equation with a Lagrangian Laplace operator is thus obtained in the reference configuration. Besides, it is also possible to get a regularization function with an Eulerian Laplace operator by choosing a different free energy potential as shown below.

Model based on the state law $\underline{\boldsymbol{m}} = \underset{\sim}{\boldsymbol{A}}.\underline{\boldsymbol{k}}$

For obtaining an Eulerian Laplace operator in the regularization equation, a second potential is considered in the form:

$$\rho\psi = \frac{1}{2}\frac{\rho}{\rho_\sharp}\underset{\sim}{\boldsymbol{E}}^e : \underset{\approx}{\boldsymbol{\Lambda}} : \underset{\sim}{\boldsymbol{E}}^e + \frac{1}{2}H_\chi e^2 + \frac{1}{2}\underline{\boldsymbol{K}}.\underset{\sim}{\boldsymbol{F}}^{-1}\underset{\sim}{\boldsymbol{A}}.\underset{\sim}{\boldsymbol{F}}^{-T}.\underline{\boldsymbol{K}}. \tag{5.86}$$

By Eq. (5.43), the same constitutive equation as Eq. (5.75) is obtained, while Eqs. (5.44) and (5.45) lead to

$$s = -H_\chi e, \tag{5.87}$$

$$\underline{\boldsymbol{M}} = \frac{\rho_0}{\rho}\underset{\sim}{\boldsymbol{F}}^{-1}\underset{\sim}{\boldsymbol{A}}.\underset{\sim}{\boldsymbol{F}}^{-T}.\underline{\boldsymbol{K}}. \tag{5.88}$$

With Eqs. (5.5), (5.21) and (5.88), one can readily find

$$\underline{\boldsymbol{m}} = \underset{\sim}{\boldsymbol{A}}.\underline{\boldsymbol{k}}. \tag{5.89}$$

For crystals with cubic symmetric, i.e., $\underset{\sim}{\boldsymbol{A}} = A\underset{\sim}{\mathbf{1}}$, the constitutive relations Eqs. (5.88) and (5.89) become

$$\underline{\boldsymbol{M}} = \frac{\rho_0}{\rho}A\underset{\sim}{\boldsymbol{C}}^{-1}.\underline{\boldsymbol{K}}, \tag{5.90}$$

$$\underline{\boldsymbol{m}} = A\underline{\boldsymbol{k}}, \tag{5.91}$$

where $\underset{\sim}{\boldsymbol{C}} = \underset{\sim}{\boldsymbol{F}}^T.\underset{\sim}{\boldsymbol{F}}$ is the right Cauchy–Green tensor. Following the same derivation procedure as in the previous section, one can find that the yield function Eq. (5.51) writes

$$f^s = |\tau^s| - \left(\tau_c^s - \frac{\rho_\sharp}{\rho}A \operatorname{div}(\operatorname{grad}\gamma_\chi)\right) = |\tau^s| - \left(\tau_c^s - \frac{\rho_\sharp}{\rho}A \triangle_x \gamma_\chi\right). \tag{5.92}$$

and the regularization equation as

$$\gamma_\chi - \frac{A}{H_\chi} \triangle_x \gamma_\chi = \gamma_{cum}, \tag{5.93}$$

where the Eulerian Laplace operator appears.

5.2.2 Formulation with free energy potential depending on $\underline{\boldsymbol{K}}^\sharp$

In the following, the formulation presented in section 5.1.5 is developed. Three choices of free energy potential are shown.

Model based on the state law $\underline{\boldsymbol{K}}^\sharp = \underset{\sim}{\boldsymbol{A}}.\underline{\boldsymbol{M}}^\sharp$

A first quadratic free energy potential is considered in the form:

$$\rho\psi = \frac{1}{2}\frac{\rho}{\rho_\sharp}\underset{\sim}{\boldsymbol{E}}^e : \underset{\approx}{\boldsymbol{\Lambda}} : \underset{\sim}{\boldsymbol{E}}^e + \frac{1}{2}H_\chi e^2 + \frac{1}{2}\frac{\rho}{\rho_\sharp}\underline{\boldsymbol{K}}^\sharp.\underset{\sim}{\boldsymbol{A}}.\underline{\boldsymbol{K}}^\sharp. \tag{5.94}$$

Substituting the potential into Eqs. (5.44) and (5.63) gives:

$$s = -H_\chi e, \tag{5.95}$$

$$\underline{\boldsymbol{M}}^\sharp = \underset{\sim}{\boldsymbol{A}}.\underline{\boldsymbol{K}}^\sharp, \tag{5.96}$$

with $e = \gamma_{cum} - \gamma_\chi$. With $S = \frac{\rho_0}{\rho}s$, one has

$$S = -\frac{\rho_0}{\rho}H_\chi e. \tag{5.97}$$

We express the yield function in terms of γ_χ and first consider the Lagrangian treatment of the variables. Substituting Eqs. (5.53) and (5.55) into Eq. (5.96) yields

$$\underline{\boldsymbol{M}} = \frac{\rho_0}{\rho_\sharp}\underset{\sim}{\boldsymbol{P}}^{-1}.\underset{\sim}{\boldsymbol{A}}\underset{\sim}{\boldsymbol{P}}^{-T}.\underline{\boldsymbol{K}} \tag{5.98}$$

Noticing that $\rho_\sharp = \rho_0$ for crystal plasticity and that $S = \frac{\rho_0}{\rho}s$, one can write Eq. (5.70) as

$$f^s = |\tau^{\sharp s}| - \left(\tau_c^s - \frac{\rho_\sharp}{\rho}s\right) = |\tau^{\sharp s}| - \left(\tau_c^s - \frac{\rho_0}{\rho}s\right) = |\tau^{\sharp s}| - (\tau_c^s - S)\,. \tag{5.99}$$

In the case of $\underset{\sim}{\boldsymbol{A}} = A\underset{\sim}{\boldsymbol{1}}$, the constitutive equations Eqs. (5.96) and (5.98) become

$$\underline{\boldsymbol{M}}^\sharp = A\underline{\boldsymbol{K}}^\sharp,, \tag{5.100}$$

$$\underline{\boldsymbol{M}} = \frac{\rho_0}{\rho_\sharp}A\underset{\sim}{\boldsymbol{C}}^{p-1}.\underline{\boldsymbol{K}}\,, \tag{5.101}$$

with $\underset{\sim}{\boldsymbol{C}}^p = \underset{\sim}{\boldsymbol{P}}^T.\underset{\sim}{\boldsymbol{P}}$. Considering Eqs. (5.19) and (5.101), one can further write the yield function as

$$f^s = |\tau^{\sharp s}| - \left(\tau_c^s - A\ \mathrm{Div}\,(\frac{\rho_0}{\rho_\sharp}\underset{\sim}{\boldsymbol{C}}^{p-1}.\underline{\boldsymbol{K}}\,)\right), \tag{5.102}$$

with

$$\tau^{\sharp s} = \tau^s + x^s \quad \text{and} \quad x^s = (\underline{\boldsymbol{K}}^{\sharp}.\underline{\boldsymbol{l}}^{s})(\underline{\boldsymbol{M}}^{\sharp}.\underline{\boldsymbol{n}}^{s}) = (\underset{\sim}{\boldsymbol{P}}^{-T}.\underline{\boldsymbol{K}}.\underline{\boldsymbol{l}}^{s})(A\underset{\sim}{\boldsymbol{P}}^{-T}.\underline{\boldsymbol{K}}.\underline{\boldsymbol{n}}^{s}). \tag{5.103}$$

Combining Eqs. (5.19), (5.97) and (5.98), one can obtain the regularization function:

$$\gamma_\chi - \frac{A}{H_\chi}\frac{\rho}{\rho_0}\mathrm{Div}\,(\frac{\rho_0}{\rho_\sharp}\underset{\sim}{\boldsymbol{C}}^{p-1}.\,\mathrm{Grad}\,\gamma_\chi) = \gamma_{cum}. \tag{5.104}$$

It can be seen that the Lagrangian Laplace operator is not involved in the equation.

For the same formulation, we then consider the Eulerian treatment of the variables to see whether the Eulerian Laplace operator will be obtained. With Eqs. (5.21) and (5.55), $\underline{\boldsymbol{m}}$ follows

$$\underline{\boldsymbol{m}} = \frac{\rho}{\rho_0}\underset{\sim}{\boldsymbol{F}}.\underline{\boldsymbol{M}} = \frac{\rho}{\rho_\sharp}\underset{\sim}{\boldsymbol{E}}.\underline{\boldsymbol{M}}^{\sharp}. \tag{5.105}$$

Combining Eqs. (5.5) and (5.53) gives

$$\underline{\boldsymbol{K}}^{\sharp} = \underset{\sim}{\boldsymbol{E}}^{T}.\underline{\boldsymbol{k}}\,. \tag{5.106}$$

Hence, Eq. (5.96) yields

$$\underline{\boldsymbol{m}} = \frac{\rho}{\rho_\sharp}\underset{\sim}{\boldsymbol{E}}.\underset{\sim}{\boldsymbol{A}}.\underset{\sim}{\boldsymbol{E}}^{T}.\underline{\boldsymbol{k}}\,. \tag{5.107}$$

For crystals with cubic symmetry, the previous equation becomes

$$\underline{\boldsymbol{m}} = \frac{\rho}{\rho_\sharp}A\underset{\sim}{\boldsymbol{B}}^{e}.\underline{\boldsymbol{k}}\,, \tag{5.108}$$

with $\underset{\sim}{\boldsymbol{B}}^{e} = \underset{\sim}{\boldsymbol{E}}.\underset{\sim}{\boldsymbol{E}}^{T}$. The yield function Eq. (5.70) thus writes

$$f^s = |\tau^{\sharp s}| - \left(\tau_c^s - \frac{\rho_\sharp}{\rho}\mathrm{div}\left(\frac{\rho}{\rho_\sharp}A\underset{\sim}{\boldsymbol{B}}^{e}.\,\mathrm{grad}\,\gamma_\chi\right)\right) \leqslant 0. \tag{5.109}$$

According to Eqs. (5.15), (5.95) and (5.107), the regularization function writes

$$\gamma_\chi - \frac{A}{H_\chi}\mathrm{div}\,(\frac{\rho}{\rho_\sharp}\underset{\sim}{\boldsymbol{B}}^{e}.\,\mathrm{grad}\,\gamma_\chi) = \gamma_{cum}. \tag{5.110}$$

This function does not involve the Eulerian Laplace operator. It is thus demonstrated that the second formulation based on $\underline{\boldsymbol{K}}^{\sharp}$ with the potential Eq. (5.94) cannot lead to neither Lagrangian nor Eulerian Laplace operator in the regularization equation.

Model based on the state law $\underline{\boldsymbol{M}} = \underset{\sim}{\boldsymbol{A}}.\underline{\boldsymbol{K}}$

For involving the Lagrangian Laplace operator in the regularization equation, a second potential is proposed in the form:

$$\rho\psi = \frac{1}{2}\frac{\rho}{\rho_\sharp}\underset{\sim}{\boldsymbol{E}}^e : \underset{\approx}{\boldsymbol{\Lambda}} : \underset{\sim}{\boldsymbol{E}}^e + \frac{1}{2}\frac{\rho}{\rho_0}H_\chi e^2 + \frac{1}{2}\frac{\rho}{\rho_0}\underline{\boldsymbol{K}}^\sharp.\underset{\sim}{\boldsymbol{P}}.\underset{\sim}{\boldsymbol{A}}.\underset{\sim}{\boldsymbol{P}}^T.\underline{\boldsymbol{K}}^\sharp, \tag{5.111}$$

According to Eqs. (5.44) and (5.63), the potential leads to

$$s = -\frac{\rho}{\rho_0}H_\chi e, \tag{5.112}$$

$$\underline{\boldsymbol{M}}^\sharp = \frac{\rho_\sharp}{\rho_0}\underset{\sim}{\boldsymbol{P}}.\underset{\sim}{\boldsymbol{A}}.\underset{\sim}{\boldsymbol{P}}^T.\underline{\boldsymbol{K}}^\sharp. \tag{5.113}$$

With $S = \frac{\rho_0}{\rho}s$, one has

$$S = -H_\chi e. \tag{5.114}$$

Substituting Eqs. (5.53) and (5.55) into Eq. (5.113) yields

$$\underline{\boldsymbol{M}} = \underset{\sim}{\boldsymbol{A}}.\underline{\boldsymbol{K}}\,. \tag{5.115}$$

For crystals with cubic symmetry, the constitutive relations Eqs. (5.113) and (5.115) become

$$\underline{\boldsymbol{M}}^\sharp = A\underset{\sim}{\boldsymbol{B}}^p.\underline{\boldsymbol{K}}^\sharp, \tag{5.116}$$

$$\underline{\boldsymbol{M}} = A\underline{\boldsymbol{K}}\,, \tag{5.117}$$

with $\underset{\sim}{\boldsymbol{B}}^p = \underset{\sim}{\boldsymbol{P}}.\underset{\sim}{\boldsymbol{P}}^T$. The yield function can be written as:

$$f^s = |\tau^{\sharp s}| - (\tau_c^s - A\,\triangle_X\gamma_\chi) = |\tau^s + x^s| - (\tau_c^s - A\,\triangle_X\gamma_\chi) \leqslant 0, \tag{5.118}$$

with

$$x^s = (\underline{\boldsymbol{K}}^\sharp.\underline{\boldsymbol{l}}^{\,s})(\underline{\boldsymbol{M}}^\sharp.\underline{\boldsymbol{n}}^{\,s}) = (\underset{\sim}{\boldsymbol{P}}^{-T}.\underline{\boldsymbol{K}}\,.\underline{\boldsymbol{l}}^{\,s})(A\underset{\sim}{\boldsymbol{B}}^p.\underset{\sim}{\boldsymbol{P}}^{-T}.\underline{\boldsymbol{K}}\,.\underline{\boldsymbol{n}}^{\,s}). \tag{5.119}$$

Analogously, the regularization function is found to be

$$\gamma_\chi - \frac{A}{H_\chi}\triangle_X\gamma_\chi = \gamma_{cum}. \tag{5.120}$$

This regularization function involves the Lagrangian Laplace operator as expected. Note that this regularization function is the same as Eq. (5.85), but that the yield function is defined with the generalized resolved shear stress $\tau^{\sharp s}$ instead of τ^s.

Model based on the state law $\underline{\boldsymbol{m}} = \underset{\sim}{\boldsymbol{A}}.\underline{\boldsymbol{k}}$

Based on the idea to obtain a regularization equation with the Eulerian Laplace operator, a third potential considered follows:

$$\rho\psi = \frac{1}{2}\frac{\rho}{\rho_\sharp}\underset{\sim}{\boldsymbol{E}}^e : \underset{\approx}{\boldsymbol{\Lambda}} : \underset{\sim}{\boldsymbol{E}}^e + \frac{1}{2}H_\chi e^2 + \frac{1}{2}\underline{\boldsymbol{K}}^\sharp.\underset{\sim}{\boldsymbol{E}}^{-1}.\underset{\sim}{\boldsymbol{A}}.\underset{\sim}{\boldsymbol{E}}^{-T}.\underline{\boldsymbol{K}}^\sharp \tag{5.121}$$

The potential leads to

$$s = -H_\chi e, \tag{5.122}$$

$$\underline{\boldsymbol{M}}^\sharp = \underset{\sim}{\boldsymbol{E}}^{-1}.\underset{\sim}{\boldsymbol{A}}.\underset{\sim}{\boldsymbol{E}}^{-T}.\underline{\boldsymbol{K}}^\sharp. \tag{5.123}$$

Using Eqs. (5.105) and (5.106),one can obtain

$$\underline{\boldsymbol{m}} = \underset{\sim}{\boldsymbol{A}}.\underline{\boldsymbol{k}}\,. \tag{5.124}$$

For crystals with cubic symmetry, the constitutive relations become

$$\underline{\boldsymbol{M}}^\sharp = A\underset{\sim}{\boldsymbol{C}}^{e-1}.\underline{\boldsymbol{K}}^\sharp, \tag{5.125}$$

$$\underline{\boldsymbol{m}} = A\underline{\boldsymbol{k}}\,, \tag{5.126}$$

with $\underset{\sim}{\boldsymbol{C}}^e = \underset{\sim}{\boldsymbol{E}}^T.\underset{\sim}{\boldsymbol{E}}$. The yield function is found to be

$$f^s = |\tau^{\sharp s}| - \left(\tau_c^s - \frac{\rho_\sharp}{\rho}A\triangle_x\gamma_\chi\right) = |\tau^s + x^s| - \left(\tau_c^s - \frac{\rho_\sharp}{\rho}A\triangle_x\gamma_\chi\right) \leqslant 0. \tag{5.127}$$

with

$$x^s = (\underline{\boldsymbol{K}}^\sharp.\underline{\boldsymbol{l}}^{\,s})(\underline{\boldsymbol{M}}^\sharp.\underline{\boldsymbol{n}}^{\,s}) = (\underset{\sim}{\boldsymbol{P}}^{-T}.\underline{\boldsymbol{K}}\,.\underline{\boldsymbol{l}}^{\,s})(A\underset{\sim}{\boldsymbol{C}}^{e-1}.\underset{\sim}{\boldsymbol{P}}^{-T}.\underline{\boldsymbol{K}}\,.\underline{\boldsymbol{n}}^{\,s}). \tag{5.128}$$

The regularization function can readily be obtained:

$$\gamma_\chi - \frac{A}{H_\chi}\triangle_x\gamma_\chi = \gamma_{cum}. \tag{5.129}$$

Notice that the obtained regularization function is the same as Eq. (5.93) but the corresponding yield function is defined with the generalized resolved shear stress $\tau^{\sharp s}$ instead of τ^s.

5.3 Numerical implementation

5.3.1 Integration of constitutive equations

The formulation of the constitutive equations presented in section 5.1.4 is chosen for the numerical implementation. The free energy potential given by Eq. (5.74) is chosen for the implementation.

The problem of the numerical integration of constitutive equations can be stated as follows: given the initial values of the stress variables $\underset{\sim}{\boldsymbol{S}}$, S and $\underline{\boldsymbol{M}}$ and associated internal variables v_{int} to be integrated , if the strain variables $\underset{\sim}{\boldsymbol{F}}$, γ_χ, $\underline{\boldsymbol{K}}$ increase to $\underset{\sim}{\boldsymbol{F}} + \Delta\underset{\sim}{\boldsymbol{F}}$, $\gamma_\chi + \Delta\gamma_\chi$, $\underline{\boldsymbol{K}} + \Delta\underline{\boldsymbol{K}}$, what are the final values of the stress variables and the internal variables v_{int}? The strain variables are referred to as the input variables (v_{IN}) and the stress variables as the output variables (v_{OUT}), the problem is briefly depicted in fig. 5.1. For the sake of brevity, the increments of the variables are written in the rate form.

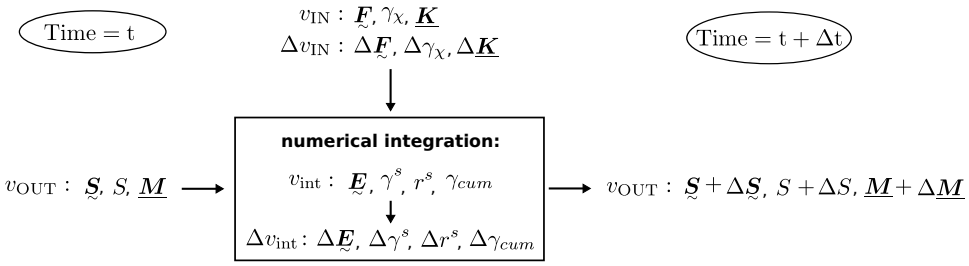

Figure 5.1: Problem setup of the numerical integration of the constitutive equations.

$\dot{S}$ and $\underline{\dot{\boldsymbol{M}}}$ can be given directly by Eqs. (5.77) and (5.78), while the calculation of $\dot{\underset{\sim}{\boldsymbol{S}}}$ requires some further derivation of equations. Combining Eqs. (5.20), (5.36) and (5.75) leading to

$$\underset{\sim}{\boldsymbol{S}} = J\underset{\sim}{\boldsymbol{\sigma}}.\underset{\sim}{\boldsymbol{F}}^{-T} = \frac{J}{J_e}\underset{\sim}{\boldsymbol{E}}.\left(\frac{\underset{\approx}{\boldsymbol{\Lambda}}}{2}(\underset{\sim}{\boldsymbol{E}}^T.\underset{\sim}{\boldsymbol{E}} - \underset{\sim}{\mathbf{1}})\right).\underset{\sim}{\boldsymbol{E}}^T.\underset{\sim}{\boldsymbol{F}}^{-T}, \tag{5.130}$$

which shows that $\underset{\sim}{\boldsymbol{S}}$ depends on $\underset{\sim}{\boldsymbol{E}}$ and $\underset{\sim}{\boldsymbol{F}}$. Since the current value of $\underset{\sim}{\boldsymbol{F}}$ is given, the problem of looking for the current value of $\underset{\sim}{\boldsymbol{F}}$ becomes to find that of $\underset{\sim}{\boldsymbol{E}}$. In order to obtain the equations governing $\underset{\sim}{\boldsymbol{E}}$, one can combine Eqs. (5.33) and (5.34) and get

$$\dot{\underset{\sim}{\boldsymbol{E}}} = \dot{\underset{\sim}{\boldsymbol{F}}}.\underset{\sim}{\boldsymbol{F}}^{-1}.\underset{\sim}{\boldsymbol{E}} - \underset{\sim}{\boldsymbol{E}}.\dot{\underset{\sim}{\boldsymbol{P}}}.\underset{\sim}{\boldsymbol{P}}^{-1}. \tag{5.131}$$

Notice that $\dot{\underset{\sim}{\boldsymbol{P}}}.\underset{\sim}{\boldsymbol{P}}^{-1}$ is given in Eq. (5.30) and governed by

$$\dot{\underset{\sim}{\boldsymbol{P}}}.\underset{\sim}{\boldsymbol{P}}^{-1} = \sum_{s=1}^{12} \dot{\gamma}^s \underset{\sim}{\boldsymbol{N}}^s. \tag{5.132}$$

With this relation, $\dot{\underset{\sim}{\boldsymbol{E}}}$ is expressed by

$$\dot{\underset{\sim}{\boldsymbol{E}}} = \dot{\underset{\sim}{\boldsymbol{F}}}.\underset{\sim}{\boldsymbol{F}}^{-1}.\underset{\sim}{\boldsymbol{E}} - \underset{\sim}{\boldsymbol{E}}.\left(\sum_{s=1}^{12} \dot{\gamma}^s \underset{\sim}{\boldsymbol{N}}^s\right). \tag{5.133}$$

Recall that $\dot{\gamma}^s$ is determined by Eq. (5.52):

$$\dot{\gamma}^s = \left\langle \frac{|\tau^s| - (\tau_c^s - S)}{K} \right\rangle^n \operatorname{sign}(\tau^s), \tag{5.134}$$

where $S = H_\chi(\gamma_\chi - \gamma_{cum})$ and τ_c^s is given by the hardening law. Note that $\tau_c^s - S \geqslant 0$ is considered. For γ_{cum}, we consider the rate form of Eq. (5.31)

$$\dot{\gamma}_{cum} = \sum_{s=1}^{12} |\dot{\gamma}^s|, \tag{5.135}$$

Therefore, for calculating the current value of $\underset{\sim}{\boldsymbol{E}}$, the differential equations that must be integrated are

$$\begin{cases} \dot{\underset{\sim}{\boldsymbol{E}}} = \dot{\underset{\sim}{\boldsymbol{F}}}.\underset{\sim}{\boldsymbol{F}}^{-1}.\underset{\sim}{\boldsymbol{E}} - \underset{\sim}{\boldsymbol{E}}.\left(\sum_{s=1}^{12} \dot{\gamma}^s \underset{\sim}{\boldsymbol{N}}^s\right) & (5.136) \\ \dot{\gamma}^s = \left\langle \dfrac{|\tau^s| - (\tau_c^s - S)}{K} \right\rangle^n \operatorname{sign}(\tau^s) & (5.137) \\ \dot{r}_D^s = |\dot{\gamma}^s| \left(\dfrac{\sqrt{b^{su} r_D^u}}{\kappa} - G_c r_D^s \right) & (5.138) \\ \dot{\gamma}_{cum} = \sum_{s=1}^{12} |\dot{\gamma}^s|, & (5.139) \end{cases}$$

For facilitating the description of the algorithm, the variables to integrate are denoted by v_{int} in the following, i.e., $v_{\text{int}} = \{\underset{\sim}{\boldsymbol{E}}, \gamma^s, r^s, \gamma_{cum}\}$. The numerical integration of the differential equations is performed with the Newton-Raphson method, which concerns solving the residual equations

$$\{R\} = \{\Delta v_{\text{int}}\} - \Delta t \{\dot{v}_{\text{int}}\}(t + \theta \Delta t) = \{0\}. \tag{5.140}$$

For the considered differential equations, the residual equations follow

$$\begin{cases} R_{\underset{\sim}{\boldsymbol{E}}} = \Delta\underset{\sim}{\boldsymbol{E}} - \Delta\underset{\sim}{\boldsymbol{F}}.\underset{\sim}{\boldsymbol{F}}^{-1}.\underset{\sim}{\boldsymbol{E}} + \underset{\sim}{\boldsymbol{E}}.\left(\sum_{s=1}^{12}\Delta\gamma^s\underset{\sim}{\boldsymbol{N}}^s\right) & (5.141)\\ R_{\gamma^s} = \Delta\gamma^s - \left\langle\frac{|\tau^s| - (\tau_c^s - S)}{K}\right\rangle^n \operatorname{sign}(\tau^s)\,\Delta t, & (5.142)\\ R_{r^s} = \Delta r^s - |\Delta\gamma^s|\left(\frac{\sqrt{b^{su}r^u}}{\kappa} - G_c r^s\right) & (5.143)\\ R_{\gamma_{cum}} = \Delta\gamma_{cum} - \sum_{s=1}^{12}|\Delta\gamma^s| & (5.144)\end{cases}$$

Within the Newton-Raphson algorithm, the Jacobian $[J]$ needs to be evaluated and writes

$$[J] = \frac{\partial\{R\}}{\partial\{\Delta v_{\text{int}}\}} = [1] - \Delta t\frac{\partial\{\dot{v}_{\text{int}}\}}{\partial\{\Delta v_{\text{int}}\}}. \tag{5.145}$$

The Jacobian for the previous residual equation system can be expressed in a partitioned matrix

$$\begin{pmatrix} \frac{\partial R_{\underset{\sim}{\boldsymbol{E}}}}{\partial\Delta_{\underset{\sim}{\boldsymbol{E}}}} & \frac{\partial R_{\underset{\sim}{\boldsymbol{E}}}}{\partial\Delta\gamma^p} & \frac{\partial R_{\underset{\sim}{\boldsymbol{E}}}}{\partial\Delta r^q} & \frac{\partial R_{\underset{\sim}{\boldsymbol{E}}}}{\partial\Delta\gamma_{cum}} \\ \frac{\partial R_{\gamma^s}}{\partial\Delta_{\underset{\sim}{\boldsymbol{E}}}} & \frac{\partial R_{\gamma^s}}{\partial\Delta\gamma^p} & \frac{\partial R_{\gamma^s}}{\partial\Delta r^q} & \frac{\partial R_{\gamma^s}}{\partial\Delta\gamma_{cum}} \\ \frac{\partial R_{r^s}}{\partial\Delta_{\underset{\sim}{\boldsymbol{E}}}} & \frac{\partial R_{r^s}}{\partial\Delta\gamma^p} & \frac{\partial R_{r^s}}{\partial\Delta r^q} & \frac{\partial R_{r^s}}{\partial\Delta\gamma_{cum}} \\ \frac{\partial R_{\gamma_{cum}}}{\partial\Delta_{\underset{\sim}{\boldsymbol{E}}}} & \frac{\partial R_{\gamma_{cum}}}{\partial\Delta\gamma^p} & \frac{\partial R_{\gamma_{cum}}}{\partial\Delta r^q} & \frac{\partial R_{\gamma_{cum}}}{\partial\Delta\gamma_{cum}} \end{pmatrix}. \tag{5.146}$$

Analytical expressions for each block is presented in appendix C.

5.3.2 Finite element formulation

The model is implemented in the finite element (FE) code `Zset` using a total Lagrangian finite element formulation in three dimensions. To this end, we first convert the principle of virtual power, given by Eq. (5.12) and expressed in the current configuration C:

$$\int_D \left(\underset{\sim}{\boldsymbol{\sigma}} : (\operatorname{grad}\underline{\dot{\boldsymbol{u}}}) + s\dot{\gamma}_\chi + \underline{\boldsymbol{m}}\,.\operatorname{grad}\dot{\gamma}_\chi\right) dV = \int_{\partial D}\left(\underline{\boldsymbol{t}}\,.\underline{\dot{\boldsymbol{u}}} + m\dot{\gamma}_\chi\right) dS, \tag{5.147}$$

to the formulation in the reference configuration C_0

$$\int_{D_0} \underset{\sim}{\boldsymbol{S}} : \dot{\underset{\sim}{\boldsymbol{F}}} + S\dot{\gamma}_\chi + \underline{\boldsymbol{M}}\,.\underline{\dot{\boldsymbol{K}}}\; dV_0 = \int_{\partial D_0}\left(\underline{\boldsymbol{T}}\,.\underline{\dot{\boldsymbol{u}}} + M\dot{\gamma}_\chi\right) dS_0. \tag{5.148}$$

Note that since the FE equations will be solved by an iterative method, the rate terms ($\dot{\underset{\sim}{\boldsymbol{F}}},\ \dot{\gamma}_\chi,\ \dot{\underline{\boldsymbol{K}}},\ \dot{\underline{\boldsymbol{u}}}$) correspond to their increments ($\Delta\underset{\sim}{\boldsymbol{F}},\ \Delta\gamma_\chi,\ \Delta\underline{\boldsymbol{K}},\ \Delta\underline{\boldsymbol{u}}$).

Next, we carry on the FE discretisation on the crystalline body considered. Tensors and vectors are written in index notation, except otherwise stated. Besides the displacement u_i, the microslip γ_χ is regarded as an additional nodal degree of freedom. Assuming that the considered crystalline body occupying the domain D_0 in C_0 is discretized by l finite elements, one can write the principle of virtual power (Eq. (5.148)) as

$$\int_{D_0} \left(S_{ij}\dot{F}_{ij} + S\dot{\gamma}_\chi + M_i\dot{K}_i\right)\, dV_0 = \int_{\partial D_0} \left(T_i\dot{u}_i + M\dot{\gamma_\chi}\right)\, dS_0 \tag{5.149}$$

$$\Longrightarrow \sum_{e=1}^{l} \int_{D_0^e} \left(S_{ij}\dot{F}_{ij} + S\dot{\gamma}_\chi + M_i\dot{K}_i\right)\, dV_0 = \sum_{e=1}^{l} \int_{\partial D_0^e} \left(T_i\dot{u}_i + M\dot{\gamma_\chi}\right)\, dS_0. \tag{5.150}$$

Here, the subdomain D_0^e corresponds to the space occupied by an individual element. The summation is done for the repeated subscripts, e.g., $S_{ij}\dot{F}_{ij}$ denotes $\sum_{i=1}^{3}\sum_{j=1}^{3} S_{ij}\dot{F}_{ij}$; for the sake of brevity, the summation operator will not be written for the subscripts. In general, it is assumed that, within one individual element, u_i is interpolated from the displacement values of p nodes and γ_χ from the values of q nodes. u_i and γ_χ within one element are given by

$$u_i = \sum_{a=1}^{p} {}^{u}N^a \widetilde{u}_i^a \tag{5.151}$$

$$\gamma_\chi = \sum_{b=1}^{q} {}^{\chi}N^b \widetilde{\gamma}_\chi^b, \tag{5.152}$$

where ${}^{u}N^a$ and ${}^{\chi}N^b$ are shape functions respectively for u_i and γ_χ, and $\widetilde{u}_i^a$ and $\widetilde{\gamma}_\chi^b$ respectively denote the nodal values of u_i on node a and those of γ_χ on node b. Unlike the subscripts, the summation operators are written explicitly for the superscripts denoting the nodes. The deformation gradient F_{ij} and the Lagrangian gradient of microslip K_i are given by

$$F_{ij} = \sum_{a=1}^{p} {}^{u}B_j^a \widetilde{u}_i^a \tag{5.153}$$

$$K_i = \sum_{b=1}^{q} {}^{\chi}B_i^b \widetilde{\gamma}_\chi^b \tag{5.154}$$

with ${}^{u}B^a_j = \dfrac{\partial {}^{u}N^a}{\partial X_j}$ and ${}^{\chi}B^b_i = \dfrac{\partial {}^{\chi}N^b}{\partial X_i}$. Using these relations in Eq. (5.150) leads to

$$\sum_{e=1}^{l}\int_{D_0^e}\left[S_{ij}\sum_{a=1}^{p}\left({}^{u}B^a_j\dot{\tilde{u}}^a_i\right)+\sum_{b=1}^{q}\left(S^{\chi}N^b\dot{\tilde{\gamma}}^b_{\chi}+M_i{}^{\chi}B^b_i\dot{\tilde{\gamma}}^b_{\chi}\right)\right]dV_0 = \sum_{e=1}^{l}\int_{\partial D_0^e}\left(T_i\sum_{a=1}^{p}{}^{u}N^a\dot{\tilde{u}}^a_i+M\sum_{b=1}^{q}{}^{\chi}N^b\dot{\tilde{\gamma}}^b_{\chi}\right)dS_0 \tag{5.155}$$

$$\Longrightarrow\sum_{e=1}^{l}\sum_{a=1}^{p}\left[\int_{D_0^e}\left(S_{ij}{}^{u}B^a_j\right)dV_0\right]\dot{\tilde{u}}^a_i+\sum_{e=1}^{l}\sum_{b=1}^{q}\left[\int_{D_0^e}\left(S^{\chi}N^b+M_i{}^{\chi}B^b_i\right)dV_0\right]\dot{\tilde{\gamma}}^b_{\chi} = \sum_{e=1}^{l}\sum_{a=1}^{p}\left[\int_{\partial D_0^e}\left(T_i{}^{u}N^a\right)dS_0\right]\dot{\tilde{u}}^a_i+\sum_{e=1}^{l}\sum_{b=1}^{q}\left[\int_{\partial D_0^e}\left(M^{\chi}N^b\right)dS_0\right]\dot{\tilde{\gamma}}^b_{\chi}. \tag{5.156}$$

According to Eq. (5.156), an internal reaction is associated with each degree of freedom. We thus refer to $R^a_{\mathrm{int}(u_i,e)}$ as the internal reaction on node a related to u_i

$$R^a_{\mathrm{int}(u_i,e)} = \int_{D_0^e}\left(S_{ij}{}^{u}B^a_j\right)dV_0 \tag{5.157}$$

and to $R^b_{\mathrm{int}(\gamma_\chi,\mathrm{e})}$ as the internal reaction on node b related to γ_χ

$$R^b_{\mathrm{int}(\gamma_\chi,\mathrm{e})} = \int_{D_0^e}\left(S^{\chi}N^b+M_i{}^{\chi}B^b_i\right)dV_0. \tag{5.158}$$

Analogously, an external reaction is associated with each degree of freedom. We refer to $R^a_{\mathrm{int}(u_i,e)}$ as the external reaction on node a related to u_i

$$R^a_{\mathrm{int}(u_i,e)} = \int_{\partial D_0^e}\left(T_i{}^{u}N^a\right)dS_0 \tag{5.159}$$

and to $R^b_{\mathrm{ext}(\gamma_\chi,\mathrm{e})}$ as the external reaction on node b related to γ_χ

$$R^b_{\mathrm{ext}(\gamma_\chi,\mathrm{e})} = \int_{\partial D_0^e}\left(M^{\chi}N^b\right)dS_0. \tag{5.160}$$

With these expressions, (5.156) writes

$$\sum_{e=1}^{l}\sum_{a=1}^{p}R^a_{\mathrm{int}(u_i,e)}\dot{\tilde{u}}^a_i+\sum_{e=1}^{l}\sum_{b=1}^{q}R^b_{\mathrm{int}(\gamma_\chi,\mathrm{e})}\dot{\tilde{\gamma}}^b_{\chi} = \sum_{e=1}^{l}\sum_{a=1}^{p}R^a_{\mathrm{int}(u_i,e)}\dot{\tilde{u}}^a_i+\sum_{e=1}^{l}\sum_{b=1}^{q}R^b_{\mathrm{ext}(\gamma_\chi,\mathrm{e})}\dot{\tilde{\gamma}}^b_{\chi}. \tag{5.161}$$

Note that, **in the terms associated with displacement u_i, the summation is done for the subscript i ($i = 1, 2, 3$) which is not written for the sake of brevity**. This is the FE equation for the entire FE mesh and can be solved by Newton's method.

5.3.3 Details on implementation in FE code

In order to facilitate the numerical implementation in FE code, we rewrite the previous equations in vector and matrix form. The rates of nodal degrees of freedom $\dot{\tilde{u}}^a$ and $\dot{\tilde{\gamma}}^b_\chi$ are arranged in vector form as

$$\{\dot{\tilde{u}}^a_i\} = \{\dot{\tilde{\mathbf{u}}}^e\} = \begin{Bmatrix} \dot{\tilde{u}}^1_1 \\ \dot{\tilde{u}}^1_2 \\ \dot{\tilde{u}}^1_3 \\ \vdots \\ \dot{\tilde{u}}^p_1 \\ \dot{\tilde{u}}^p_2 \\ \dot{\tilde{u}}^p_3 \end{Bmatrix} \quad \text{and} \quad \{\dot{\tilde{\gamma}}^b_\chi\} = \{\dot{\tilde{\boldsymbol{\gamma}}}^e_{\boldsymbol{\chi}}\} = \begin{Bmatrix} \dot{\tilde{\gamma}}^1_\chi \\ \dot{\tilde{\gamma}}^2_\chi \\ \vdots \\ \dot{\tilde{\gamma}}^q_\chi \end{Bmatrix}. \tag{5.162}$$

Here, we drop the superscripts a and b used for summation over the nodes of one element and add a superscript label e, in order to indicate that the vector is for one individual element and to distinguish it from vectors for the entire FE mesh. Recall that p is the number of nodes possessing displacement degrees of freedom and q is that for microslip γ_χ. Voigt's notation is used for writing tensors in the form of vectors and matrices. Especially, the second-order non-symmetric tensor $\underset{\sim}{\boldsymbol{F}}$ and the vector $\underline{\boldsymbol{K}}$ are arranged in the form:

$$\{\underset{\sim}{\boldsymbol{F}}\} = \begin{Bmatrix} F_{11} \\ F_{22} \\ F_{33} \\ F_{12} \\ F_{23} \\ F_{31} \\ F_{21} \\ F_{32} \\ F_{13} \end{Bmatrix} \quad \text{and} \quad \{\underline{\boldsymbol{K}}\} = \begin{Bmatrix} K_1 \\ K_2 \\ K_3 \end{Bmatrix}. \tag{5.163}$$

Thus, shape functions ${}^uN^a_i$ and ${}^\chi N^b$ can thus be written as

$$[{}^{\mathbf{u}}\mathbf{N}] = \begin{bmatrix} {}^uN^1 & 0 & 0 & \cdots & {}^uN^p & 0 & 0 \\ 0 & {}^uN^1 & 0 & \cdots & 0 & {}^uN^p & 0 \\ 0 & 0 & {}^uN^1 & \cdots & 0 & 0 & {}^uN^p \end{bmatrix} \tag{5.164}$$

and

$$[{}^{\chi}\mathbf{N}] = \begin{bmatrix} {}^\chi N^1 & {}^\chi N^2 & {}^\chi N^3 & \cdots & {}^\chi N^q. \end{bmatrix} \tag{5.165}$$

Accordingly, ${}^{u}B^{a}_{ij}$ and ${}^{\chi}B^{a}_{i}$ can also be written in matrix form denoted by $[{}^{\mathbf{u}}\mathbf{B}]$ and $[{}^{\chi}\mathbf{B}]$:

$$[{}^{\mathbf{u}}\mathbf{B}] = \begin{bmatrix} \frac{\partial {}^{u}N^1}{\partial X_1} & 0 & 0 & \cdots & \frac{\partial {}^{u}N^p}{\partial X_1} & 0 & 0 \\ 0 & \frac{\partial {}^{u}N^1}{\partial X_2} & 0 & \cdots & 0 & \frac{\partial {}^{u}N^p}{\partial X_2} & 0 \\ 0 & 0 & \frac{\partial {}^{u}N^1}{\partial X_3} & \cdots & 0 & 0 & \frac{\partial {}^{u}N^p}{\partial X_3} \\ \frac{\partial {}^{u}N^1}{\partial X_2} & 0 & 0 & \cdots & \frac{\partial {}^{u}N^p}{\partial X_2} & 0 & 0 \\ 0 & \frac{\partial {}^{u}N^1}{\partial X_3} & 0 & \cdots & 0 & \frac{\partial {}^{u}N^p}{\partial X_3} & 0 \\ 0 & 0 & \frac{\partial {}^{u}N^1}{\partial X_1} & \cdots & 0 & 0 & \frac{\partial {}^{u}N^p}{\partial X_1} \\ 0 & \frac{\partial {}^{u}N^1}{\partial X_1} & 0 & \cdots & 0 & \frac{\partial {}^{u}N^p}{\partial X_1} & 0 \\ 0 & 0 & \frac{\partial {}^{u}N^1}{\partial X_2} & \cdots & 0 & 0 & \frac{\partial {}^{u}N^p}{\partial X_2} \\ \frac{\partial {}^{u}N^1}{\partial X_3} & 0 & 0 & \cdots & \frac{\partial {}^{u}N^p}{\partial X_3} & 0 & 0 \end{bmatrix} \tag{5.166}$$

and

$$[{}^{\chi}\mathbf{B}] = \begin{bmatrix} \frac{\partial {}^{\chi}N^1}{\partial X_1} & \frac{\partial {}^{\chi}N^2}{\partial X_1} & \frac{\partial {}^{\chi}N^3}{\partial X_1} & \cdots & \frac{\partial {}^{\chi}N^q}{\partial X_1} \\ \frac{\partial {}^{\chi}N^1}{\partial X_2} & \frac{\partial {}^{\chi}N^2}{\partial X_2} & \frac{\partial {}^{\chi}N^3}{\partial X_2} & \cdots & \frac{\partial {}^{\chi}N^q}{\partial X_2} \\ \frac{\partial {}^{\chi}N^1}{\partial X_3} & \frac{\partial {}^{\chi}N^2}{\partial X_3} & \frac{\partial {}^{\chi}N^3}{\partial X_3} & \cdots & \frac{\partial {}^{\chi}N^q}{\partial X_3} \end{bmatrix} \tag{5.167}$$

The interpolation of increment of the displacement $\dot{u}_i$ and that of the microslip $\dot{\gamma}_\chi$ in one element thus write

$$\{\underline{\dot{\boldsymbol{u}}}\} = [{}^{\mathbf{u}}\mathbf{N}].\{\dot{\tilde{\mathbf{u}}}^e\} \tag{5.168}$$

$$\{\dot{\boldsymbol{\gamma}}_{\boldsymbol{\chi}}\} = [{}^{\chi}\mathbf{N}].\{\dot{\tilde{\boldsymbol{\gamma}}}^e_{\boldsymbol{\chi}}\} \tag{5.169}$$

and their Lagrangian gradients follows

$$\{\dot{\underset{\sim}{\boldsymbol{F}}}\} = [{}^{\mathbf{u}}\mathbf{B}].\{\dot{\tilde{\mathbf{u}}}^e\} \tag{5.170}$$

$$\{\underline{\dot{\boldsymbol{K}}}\} = [{}^{\chi}\mathbf{B}].\{\dot{\tilde{\boldsymbol{\gamma}}}^e_{\boldsymbol{\chi}}\}. \tag{5.171}$$

With stress and strain variables expressed with Voigt's notation, Eqs. (5.157) to (5.160) follow

$$\{\mathbf{R}^e_{\mathrm{int(u)}}\} = \int_{D^e_0} [{}^{\mathbf{u}}\mathbf{B}]^T.\{\underset{\sim}{\boldsymbol{S}}\}\, dV_0, \tag{5.172}$$

$$\{\mathbf{R}^e_{\mathrm{int}(\gamma_\chi)}\} = \int_{D^e_0} [{}^{\chi}\mathbf{N}]^T.\{S\} + [{}^{\chi}\mathbf{B}]^T.\{\underline{\boldsymbol{M}}\}\, dV_0, \tag{5.173}$$

$$\{\mathbf{R}^e_{\mathrm{ext(u)}}\} = \int_{\partial D^e_0} [{}^{\mathbf{u}}\mathbf{N}]^T.\{\underline{\boldsymbol{T}}\}\, dS_0, \tag{5.174}$$

$$\{\mathbf{R}^e_{\mathrm{ext}(\gamma_\chi)}\} = \int_{\partial D^e_0} [{}^{\chi}\mathbf{N}]^T.\{M\}\, dS_0, \tag{5.175}$$

where $[{}^{\mathrm{u}}\mathbf{B}]^T$ is the transpose of the matrix $[{}^{\mathrm{u}}\mathbf{B}]$ and the same notation is used for other matrix. The global FE equation is obtained by applying assembly operator $\mathcal{A}$ on internal reactions and external reactions:

$$\{\mathbf{R}_{\mathrm{int(u)}}\} = \mathcal{A}(\{\mathbf{R}^e_{\mathrm{int(u)}}\}) \tag{5.176}$$

$$\{\mathbf{R}_{\mathrm{int}(\gamma_\chi)}\} = \mathcal{A}(\{\mathbf{R}^e_{\mathrm{int}(\gamma_\chi)}\}) \tag{5.177}$$

$$\{\mathbf{R}_{\mathrm{ext(u)}}\} = \mathcal{A}(\{\mathbf{R}^e_{\mathrm{ext(u)}}\}) \tag{5.178}$$

$$\{\mathbf{R}_{\mathrm{ext}(\gamma_\chi)}\} = \mathcal{A}(\{\mathbf{R}^e_{\mathrm{ext}(\gamma_\chi)}\}). \tag{5.179}$$

The reader is referred to Besson et al. (2009) for the description of the assembly procedure. Thus, the global FE equation (Eq. (5.161)) to be solved can be written as

$$\left\{ \begin{array}{c} \{\mathbf{R}_{\mathrm{int(u)}}\} \\ \{\mathbf{R}_{\mathrm{int}(\gamma_\chi)}\} \end{array} \right\} \cdot \left\{ \begin{array}{c} \{\dot{\tilde{\mathbf{u}}}\} \\ \{\dot{\tilde{\boldsymbol{\gamma}}}_{\boldsymbol{\chi}}\} \end{array} \right\} = \left\{ \begin{array}{c} \{\mathbf{R}_{\mathrm{ext(u)}}\} \\ \{\mathbf{R}_{\mathrm{ext}(\gamma_\chi)}\} \end{array} \right\} \cdot \left\{ \begin{array}{c} \{\dot{\tilde{\mathbf{u}}}\} \\ \{\dot{\tilde{\boldsymbol{\gamma}}}_{\boldsymbol{\chi}}\} \end{array} \right\}. \tag{5.180}$$

Since the system is nonlinear, it can be solved by Newton's method which requires the calculation of the Jacobian matrix with respect to the internal reactions (Besson et al., 2009). The Jacobian matrix of an individual element, split into four blocks, writes

$$\left[\begin{array}{cc} [\mathbf{K}^e_{(\mathrm{uu})}] & [\mathbf{K}^e_{(\mathrm{ug})}] \\ [\mathbf{K}^e_{(\mathrm{gu})}] & [\mathbf{K}^e_{(\mathrm{gg})}] \end{array} \right] = \left[\begin{array}{cc} \left[\dfrac{\partial\{\mathbf{R}^e_{\mathrm{int(u)}}\}}{\partial\{\tilde{\mathbf{u}}^e\}}\right] & \left[\dfrac{\partial\{\mathbf{R}^e_{\mathrm{int(u)}}\}}{\partial\{\tilde{\boldsymbol{\gamma}}^e_{\boldsymbol{\chi}}\}}\right] \\ \left[\dfrac{\partial\{\mathbf{R}^e_{\mathrm{int}(\gamma_\chi)}\}}{\partial\{\tilde{\mathbf{u}}^e\}}\right] & \left[\dfrac{\partial\{\mathbf{R}^e_{\mathrm{int}(\gamma_\chi)}\}}{\partial\{\tilde{\boldsymbol{\gamma}}^e_{\boldsymbol{\chi}}\}}\right] \end{array} \right]. \tag{5.181}$$

Using the assembly operation $\mathcal{A}$, one can calculate the global Jacobian matrix $[\mathbf{K}]$

$$[\mathbf{K}] = \mathcal{A} \left[\begin{array}{cc} [\mathbf{K}^e_{(\mathrm{uu})}] & [\mathbf{K}^e_{(\mathrm{ug})}] \\ [\mathbf{K}^e_{(\mathrm{gu})}] & [\mathbf{K}^e_{(\mathrm{gg})}] \end{array} \right] \tag{5.182}$$

One calculates the blocks for an individual element and obtains the so-called element stiffness matrix:

$$[\mathbf{K}^e_{(\mathrm{uu})}] = \frac{\partial\{\mathbf{R}^e_{\mathrm{int(u)}}\}}{\partial\{\tilde{\mathbf{u}}^e\}} = \int_{D_0} [{}^{\mathrm{u}}\mathbf{B}]^T . \frac{\partial\{\underset{\sim}{\boldsymbol{S}}\}}{\partial\{\underset{\sim}{\boldsymbol{F}}\}} . \frac{\partial\{\underset{\sim}{\boldsymbol{F}}\}}{\partial\{\tilde{\mathbf{u}}^e\}}\, dV_0$$
$$= \int_{D_0} [{}^{\mathrm{u}}\mathbf{B}]^T . \frac{\partial\{\underset{\sim}{\boldsymbol{S}}\}}{\partial\{\underset{\sim}{\boldsymbol{F}}\}} . [{}^{\mathrm{u}}\mathbf{B}]\, dV_0 \tag{5.183}$$

$$[\mathbf{K}^e_{(\mathrm{ug})}] = \frac{\partial\{\mathbf{R}^e_{\mathrm{int(u)}}\}}{\partial\{\tilde{\boldsymbol{\gamma}}^e_{\boldsymbol{\chi}}\}} = \int_{D_0} \left([{}^{\mathrm{u}}\mathbf{B}]^T . \frac{\partial\{\underset{\sim}{\boldsymbol{S}}\}}{\partial\{\boldsymbol{\gamma}_{\boldsymbol{\chi}}\}} . \frac{\partial\{\boldsymbol{\gamma}_{\boldsymbol{\chi}}\}}{\partial\{\tilde{\boldsymbol{\gamma}}^e_{\boldsymbol{\chi}}\}} + [{}^{\mathrm{u}}\mathbf{B}]^T . \frac{\partial\{\underset{\sim}{\boldsymbol{S}}\}}{\partial\{\underline{\boldsymbol{K}}\}} . \frac{\partial\{\underline{\boldsymbol{K}}\}}{\partial\{\tilde{\boldsymbol{\gamma}}^e_{\boldsymbol{\chi}}\}} \right) dV_0$$
$$= \int_{D_0} \left([{}^{\mathrm{u}}\mathbf{B}]^T . \frac{\partial\{\underset{\sim}{\boldsymbol{S}}\}}{\partial\{\boldsymbol{\gamma}_{\boldsymbol{\chi}}\}} . [{}^{\chi}\mathbf{N}] + [{}^{\mathrm{u}}\mathbf{B}]^T . \frac{\partial\{\underset{\sim}{\boldsymbol{S}}\}}{\partial\{\underline{\boldsymbol{K}}\}} . [{}^{\chi}\mathbf{B}] \right) dV_0 \tag{5.184}$$

$$[\mathbf{K}^e_{(\mathrm{gu})}] = \frac{\partial\{\mathbf{R}^e_{\mathrm{int}(\gamma_\chi)}\}}{\partial\{\tilde{\mathbf{u}}^e\}} = \int_{D_0} \left([{}^{\chi}\mathbf{N}]^T . \frac{\partial\{S\}}{\partial\{\underset{\sim}{\boldsymbol{F}}\}} . \frac{\partial\{\underset{\sim}{\boldsymbol{F}}\}}{\partial\{\tilde{\mathbf{u}}^e\}} + [{}^{\chi}\mathbf{B}]^T . \frac{\partial\{\underline{\boldsymbol{M}}\}}{\partial\{\underset{\sim}{\boldsymbol{F}}\}} . \frac{\partial\{\underset{\sim}{\boldsymbol{F}}\}}{\partial\{\tilde{\mathbf{u}}^e\}} \right) dV_0$$
$$= \int_{D_0} \left([{}^{\chi}\mathbf{N}]^T . \frac{\partial\{S\}}{\partial\{\underset{\sim}{\boldsymbol{F}}\}} . [{}^{\mathrm{u}}\mathbf{B}] + [{}^{\chi}\mathbf{B}]^T . \frac{\partial\{\underline{\boldsymbol{M}}\}}{\partial\{\underset{\sim}{\boldsymbol{F}}\}} . [{}^{\mathrm{u}}\mathbf{B}] \right) dV_0 \tag{5.185}$$

$$[\mathbf{K}^e_{(\mathrm{gg})}] = \frac{\partial\{\mathbf{R}^e_{\mathrm{int}(\gamma_\chi)}\}}{\partial\{\tilde{\boldsymbol{\gamma}}^e_{\boldsymbol{\chi}}\}} = \int_{D_0} \left([{}^{\chi}\mathbf{N}]^T . \frac{\partial\{S\}}{\partial\{\boldsymbol{\gamma}_{\boldsymbol{\chi}}\}} . \frac{\partial\{\boldsymbol{\gamma}_{\boldsymbol{\chi}}\}}{\partial\{\tilde{\boldsymbol{\gamma}}^e_{\boldsymbol{\chi}}\}} + [{}^{\chi}\mathbf{B}]^T . \frac{\partial\{\underline{\boldsymbol{M}}\}}{\partial\{\boldsymbol{\gamma}_{\boldsymbol{\chi}}\}} . \frac{\partial\{\boldsymbol{\gamma}_{\boldsymbol{\chi}}\}}{\partial\{\tilde{\boldsymbol{\gamma}}^e_{\boldsymbol{\chi}}\}} \right.$$
$$\left. + [{}^{\chi}\mathbf{N}]^T . \frac{\partial\{S\}}{\partial\{\underline{\boldsymbol{K}}\}} . \frac{\partial\{\underline{\boldsymbol{K}}\}}{\partial\{\tilde{\boldsymbol{\gamma}}^e_{\boldsymbol{\chi}}\}} + [{}^{\chi}\mathbf{B}]^T . \frac{\partial\{\underline{\boldsymbol{M}}\}}{\partial\{\underline{\boldsymbol{K}}\}} . \frac{\partial\{\underline{\boldsymbol{K}}\}}{\partial\{\tilde{\boldsymbol{\gamma}}^e_{\boldsymbol{\chi}}\}} \right) dV_0$$
$$= \int_{D_0} \left([{}^{\chi}\mathbf{N}]^T . \frac{\partial\{S\}}{\partial\{\boldsymbol{\gamma}_{\boldsymbol{\chi}}\}} . [{}^{\chi}\mathbf{N}] + [{}^{\chi}\mathbf{B}]^T . \frac{\partial\{\underline{\boldsymbol{M}}\}}{\partial\{\boldsymbol{\gamma}_{\boldsymbol{\chi}}\}} . [{}^{\chi}\mathbf{N}] \right.$$
$$\left. + [{}^{\chi}\mathbf{N}]^T . \frac{\partial\{S\}}{\partial\{\underline{\boldsymbol{K}}\}} . [{}^{\chi}\mathbf{B}] + [{}^{\chi}\mathbf{B}]^T . \frac{\partial\{\underline{\boldsymbol{M}}\}}{\partial\{\underline{\boldsymbol{K}}\}} . [{}^{\chi}\mathbf{B}] \right) dV_0. \tag{5.186}$$

In the element stiffness matrix, one can find nine derivatives which will be evaluated by consistent tangent matrix $\{\mathbf{J}^*\}$ in the next section. The consistent tangent matrix $\{\mathbf{J}^*\}$ are defined as:

$$\begin{bmatrix} \frac{\partial\{\Delta\underset{\sim}{\boldsymbol{S}}\}}{\partial\{\Delta\underset{\sim}{\boldsymbol{F}}\}} & \frac{\partial\{\Delta\underset{\sim}{\boldsymbol{S}}\}}{\partial\{\Delta\boldsymbol{\gamma}_{\boldsymbol{\chi}}\}} & \frac{\partial\{\Delta\underset{\sim}{\boldsymbol{S}}\}}{\partial\{\Delta\underline{\boldsymbol{K}}\}} \\ \frac{\partial\{\Delta S\}}{\partial\{\Delta\underset{\sim}{\boldsymbol{F}}\}} & \frac{\partial\{\Delta S\}}{\partial\{\Delta\boldsymbol{\gamma}_{\boldsymbol{\chi}}\}} & \frac{\partial\{\Delta S\}}{\partial\{\Delta\underline{\boldsymbol{K}}\}} \\ \frac{\partial\{\Delta\underline{\boldsymbol{M}}\}}{\partial\{\Delta\underset{\sim}{\boldsymbol{F}}\}} & \frac{\partial\{\Delta\underline{\boldsymbol{M}}\}}{\partial\{\Delta\boldsymbol{\gamma}_{\boldsymbol{\chi}}\}} & \frac{\partial\{\Delta\underline{\boldsymbol{M}}\}}{\partial\{\Delta\underline{\boldsymbol{K}}\}} \end{bmatrix}. \tag{5.187}$$

In addition, it will be shown that $\frac{\partial\{\Delta S\}}{\partial\{\Delta\underline{\boldsymbol{K}}\}}$ and $\frac{\partial\{\Delta\underline{\boldsymbol{M}}\}}{\partial\{\Delta\boldsymbol{\gamma}_{\boldsymbol{\chi}}\}}$ vanish for the constitutive model implemented in this work.

5.3.4 Consistent tangent matrix

As presented in sections 5.3.2 and 5.3.3, the tangent operators are necessary for evaluating the element stiffness matrix. In the present work, they are estimated from

the incremental form of constitutive equations (Besson et al., 2009). In section 5.3.1, we have shown that the integration of the constitutive equations concerns solving the residual equations (Eqs. (5.141) to (5.144)). It is important to notice that the residual equations is expressed in terms of increments of the integration variables Δv_{int} and increments of the input variables Δv_{IN}. The calculation of the consistent tangent matrix is performed after the integration of the constitutive equations, and one has thus vanish residual equations

$$\{R(\Delta v_{\text{int}}, \Delta v_{\text{IN}})\} = \{0\} \tag{5.188}$$

with imposed Δv_{IN} and obtained Δv_{int}. If applying an infinitesimal variation to the increments Δv_{IN}, one can obtain a new Δv_{int} according to the requirement of vanish residual equations. The variation of Δv_{int} resulting from the variation of Δv_{IN} should make the variation of $\{R\}$ vanish, which follows

$$\{\delta R\} = \frac{\{\partial R\}}{\{\partial \Delta v_{\text{int}}\}}\{\delta \Delta v_{\text{int}}\} + \frac{\{\partial R\}}{\{\partial \Delta v_{\text{IN}}\}}\{\delta \Delta v_{\text{IN}}\} = \{0\}. \tag{5.189}$$

Therefore, one can have

$$\{\delta \Delta v_{\text{int}}\} = \left[-\left(\frac{\{\partial R\}}{\{\partial \Delta v_{\text{int}}\}} \right)^{-1} \frac{\{\partial R\}}{\{\partial \Delta v_{\text{IN}}\}} \right] \{\delta \Delta v_{\text{IN}}\}, \tag{5.190}$$

where $-\left(\frac{\{\partial R\}}{\{\partial \Delta v_{\text{int}}\}} \right)^{-1} \frac{\{\partial R\}}{\{\partial \Delta v_{\text{IN}}\}}$ gives an evaluation of $\frac{\{\delta \Delta v_{\text{int}}\}}{\{\delta \Delta v_{\text{IN}}\}}$, i.e., $\frac{\partial \{\Delta v_{\text{int}}\}}{\partial \{\Delta v_{\text{IN}}\}}$. Moreover, noticing the constitutive equations Eqs. (5.77), (5.78) and (5.130), one can find that v_{OUT} depends on not only v_{int}, but also v_{IN}, i.e.,

$$v_{\text{OUT}} = v_{\text{OUT}}(v_{\text{int}}, v_{\text{IN}}), \tag{5.191}$$

which can be written in incremental form as

$$\Delta v_{\text{OUT}} = \Delta v_{\text{OUT}}(\Delta v_{\text{int}}, \Delta v_{\text{IN}}). \tag{5.192}$$

The variation of Δv_{OUT} should follow

$$\delta \Delta v_{\text{OUT}} = \frac{\partial \Delta v_{\text{OUT}}}{\partial \Delta v_{\text{int}}} \delta \Delta v_{\text{int}} + \frac{\partial \Delta v_{\text{OUT}}}{\partial \Delta v_{\text{IN}}} \delta \Delta v_{\text{IN}}. \tag{5.193}$$

Substituting Eq. (5.190) into the previous equation leads to

$$\delta \Delta v_{\text{OUT}} = \left\{ \frac{\partial \Delta v_{\text{OUT}}}{\partial \Delta v_{\text{int}}} \left[-\left(\frac{\partial R}{\partial \Delta v_{\text{int}}} \right)^{-1} \frac{\partial R}{\partial \Delta v_{\text{IN}}} \right] + \frac{\partial \Delta v_{\text{OUT}}}{\partial \Delta v_{\text{IN}}} \right\} \delta \Delta v_I, \tag{5.194}$$

where $\left\{ \frac{\partial \Delta v_{\text{OUT}}}{\partial \Delta v_{\text{int}}} \left[-\left(\frac{\partial R}{\partial \Delta v_{\text{int}}} \right)^{-1} \frac{\partial R}{\partial \Delta v_{\text{IN}}} \right] + \frac{\partial \Delta v_{\text{OUT}}}{\partial \Delta v_{\text{IN}}} \right\}$, denoted by $\{\mathbf{J}^*\}$, is the consistent tangent matrix. As can be seen, $\{\mathbf{J}^*\}$ is calculated from four matrix: $\frac{\partial \Delta v_{\text{OUT}}}{\partial \Delta v_{\text{int}}}$, $\frac{\partial R}{\partial \Delta v_{\text{int}}}$, $\frac{\partial R}{\partial \Delta v_{\text{IN}}}$ and $\frac{\partial \Delta v_{\text{OUT}}}{\partial \Delta v_{\text{IN}}}$. Note that the inverse of $\frac{\partial R}{\partial \Delta v_{\text{int}}}$ is obtained numerically. Details concerning calculation of the matrix are given in appendix D.

5.3.5 Convergence improvement of integration of the power law

The integration of Eq. (5.52) displays some difficulties, because of the penalty parameter H_χ in Eq. (5.78) which should be of a large value. To improve the convergence, an improved algorithm for Newton's method has been proposed by Wulfinghoff and Böhlke, 2013. It is based on the fact that the solution τ^s of Eq. (5.52) is located around $\tau_c^s - J_e s$ with $J_e = \frac{\rho_\sharp}{\rho}$.

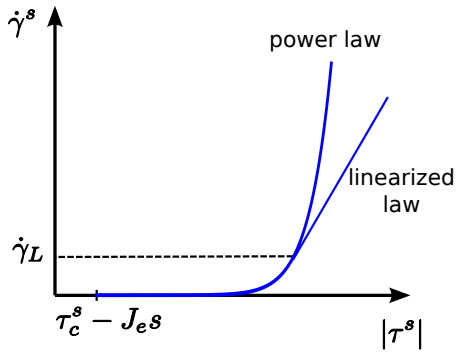

Figure 5.2: Improved algorithm for integrating the power law.

The algorithm is illustrated in fig. 5.2 and can be stated as follows: in first iterations, the power law is linearized for large values of τ^s; as soon as the slip rate $\dot{\gamma}^s$ calculated during an iteration is smaller than a critical value $\dot{\gamma}_L$, the original law is integrated. A smooth transition is considered at $\dot{\gamma}_L$. In another word, the modified law follows

$$\dot{\gamma}^s = \begin{cases} \left(\dfrac{f^s}{K}\right)^n \operatorname{sign}(\tau^s), \text{ if } \dot{\gamma}^s < \dot{\gamma}_L \\ \dfrac{n}{K}\dot{\gamma}_L^{\frac{n-1}{n}}\left(f^s - K\dot{\gamma}_L^{\frac{1}{n}}\right) + \dot{\gamma}_L, \text{ if } \dot{\gamma}^s \geqslant \dot{\gamma}_L \end{cases} \tag{5.195}$$

with

$$f^s = |\tau^s| - (\tau_c^s - J_e s)\,. \tag{5.196}$$

Notice that $\dot{\gamma}_L$ should be small enough for ensuring the convergence improvement but should not be too small for obtaining a correct solution of the original power law. In this study, $\dot{\gamma}_L = 2\,\mathrm{s}^{-1}$ is chosen. Some simple tests have been performed for showing the convergence improvement by the algorithm, as presented in appendix E.

5.4 Application to strain localization in single crystals

Strong strain gradients arise in particular in the presence of localization phenomena. Such a situation involving strain softening is investigated in this section using the proposed micromorphic model.

5.4.1 Shear banding with single slip

Analytical solutions

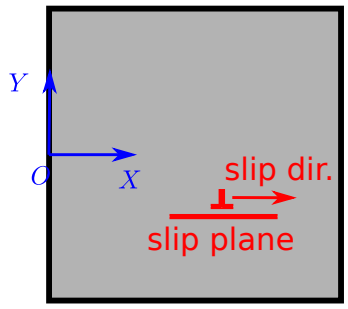

Figure 5.3: Single crystal with a single slip system.

Shear banding with single slip is analyzed within the framework of finite strains in 2D. The analysis is inspired from the work of Gurtin (2000) and Forest et al. (2005). Only one slip system is considered for the single crystal as shown in fig. 5.3. The slip direction $\underline{\boldsymbol{l}}$ and the normal to the slip plane $\underline{\boldsymbol{n}}$ are

$$\underline{\boldsymbol{l}} = (1,\ 0), \quad \underline{\boldsymbol{n}} = (0,\ 1). \tag{5.197}$$

Superscript $s = 1$ is dropped for brevity. Simple shearing is imposed on the single crystal and motions of material points of single crystal follow

$$\underline{\boldsymbol{x}} = \underline{\boldsymbol{X}} + u(Y)\underline{\boldsymbol{l}} \tag{5.198}$$

with the displacement $u(Y)$ of the material points in the direction of slip, which is taken as a function of Y. Thus, $\underset{\sim}{\boldsymbol{F}}$ takes the form

$$\underset{\sim}{\boldsymbol{F}} = \underset{\sim}{\mathbf{1}} + \kappa \underline{\boldsymbol{l}} \otimes \underline{\boldsymbol{n}}\,, \tag{5.199}$$

where $\kappa = \dfrac{\partial u}{\partial Y}$. As single slip is considered, we assume

$$\dot{\underset{\sim}{\boldsymbol{P}}}.\underset{\sim}{\boldsymbol{P}}^{-1} = \underset{\sim}{\mathbf{1}} + \dot{\gamma} \underline{\boldsymbol{l}} \otimes \underline{\boldsymbol{n}}\,, \tag{5.200}$$

with $\gamma = \gamma(Y)$. $\underset{\sim}{\boldsymbol{P}}$ obeys the following relation in the case of single slip:

$$\underset{\sim}{\boldsymbol{P}} = \underset{\sim}{\mathbf{1}} + \gamma \underline{\boldsymbol{l}} \otimes \underline{\boldsymbol{n}}\,, \tag{5.201}$$

because no lattice rotation takes place under the chosen conditions. Since $\underset{\sim}{\boldsymbol{F}} = \underset{\sim}{\boldsymbol{E}}.\underset{\sim}{\boldsymbol{P}}$, one obtains

$$\underset{\sim}{\boldsymbol{E}} = \underset{\sim}{\mathbf{1}} + \kappa^e \underline{\boldsymbol{l}} \otimes \underline{\boldsymbol{n}} \tag{5.202}$$

with $\kappa^e = \kappa - \gamma$, where $\kappa = \kappa(Y)$.

In the following, small elastic strains are assumed, i.e., small κ^e, which leads to

$$\underset{\sim}{\boldsymbol{C}}^e = \underset{\sim}{\boldsymbol{E}}^T.\underset{\sim}{\boldsymbol{E}} \approx \underset{\sim}{\mathbf{1}} + \kappa^e(\underline{\boldsymbol{l}} \otimes \underline{\boldsymbol{n}} + \underline{\boldsymbol{n}} \otimes \underline{\boldsymbol{l}}\,). \tag{5.203}$$

Thus, the Green-Lagrange elastic tensor $\underset{\sim}{\boldsymbol{E}}^e_{GL}$, the Mandel stress $\underset{\sim}{\boldsymbol{\Pi}}^M$ and the resolved shear stress τ have the following approximate forms:

$$\underset{\sim}{\boldsymbol{E}}^e_{GL} \approx \frac{1}{2}\kappa^e(\underline{\boldsymbol{l}} \otimes \underline{\boldsymbol{n}} + \underline{\boldsymbol{n}} \otimes \underline{\boldsymbol{l}}\,), \tag{5.204}$$

$$\underset{\sim}{\boldsymbol{\Pi}}^M = \underset{\sim}{\boldsymbol{C}}^e.\underset{\sim}{\boldsymbol{\Pi}}^e \approx \underset{\sim}{\boldsymbol{\Pi}}^e, \tag{5.205}$$

$$\tau \approx \underset{\sim}{\boldsymbol{\Pi}}^e : (\underline{\boldsymbol{l}} \otimes \underline{\boldsymbol{n}}\,). \tag{5.206}$$

Assuming that μ denotes the shear modulus and substituting Eq. (5.204) into Eq. (5.75), one can obtain $\underset{\sim}{\boldsymbol{\Pi}}^e$

$$\underset{\sim}{\boldsymbol{\Pi}}^e = \tau(\underline{\boldsymbol{l}} \otimes \underline{\boldsymbol{n}} + \underline{\boldsymbol{n}} \otimes \underline{\boldsymbol{l}}\,), \tag{5.207}$$

with $\tau = \mu\kappa^e$. In addition, the Boussinesq stress tensor $\underset{\sim}{\boldsymbol{S}}$ is approximated by

$$\underset{\sim}{\boldsymbol{S}} = J\underset{\sim}{\boldsymbol{\sigma}}.\underset{\sim}{\boldsymbol{F}}^{-T} = \underset{\sim}{\boldsymbol{E}}.\underset{\sim}{\boldsymbol{\Pi}}^e.\underset{\sim}{\boldsymbol{P}}^{-T} \approx \underset{\sim}{\boldsymbol{\Pi}}^e.\underset{\sim}{\boldsymbol{P}}^{-T} = \underset{\sim}{\boldsymbol{\Pi}}^e - \tau\gamma\underline{\boldsymbol{l}} \otimes \underline{\boldsymbol{l}}\,. \tag{5.208}$$

Since $\operatorname{Div}\underset{\sim}{\boldsymbol{S}} = 0$ (see Eq. (5.19)), one has

$$\frac{\partial \tau}{\partial Y} = 0, \tag{5.209}$$

which makes $\tau = \overline{\tau}$ spatially constant.

Consider the linear softening law:

$$\tau_c = \tau_0 + H\gamma \tag{5.210}$$

with $H < 0$. In the following, the derivation is carried out first for the formulation presented in section 5.1.3. The free energy potential given by Eq. (5.74) is chosen so that one has the following constitutive equations:

$$\underline{\boldsymbol{K}} = A\underline{\boldsymbol{M}} \tag{5.211}$$

and

$$S = -H_\chi e. \tag{5.212}$$

Given Eq. (5.212), the yield condition (Eq. (5.51)) writes

$$f = |\tau| - (\tau_c - S) = |\tau| - [\tau_0 + H\gamma - H_\chi(\gamma_\chi - \gamma)] = 0, \tag{5.213}$$

from which one can express γ as

$$\gamma = \frac{|\tau| - \tau_0 + H_\chi \gamma_\chi}{H + H_\chi}. \tag{5.214}$$

For the special case of single slip, we assume $\gamma_\chi = \gamma_\chi(Y)$. Considering Eq. (5.211), Div $\underline{\boldsymbol{M}}$ becomes

$$\text{Div}\,\underline{\boldsymbol{M}} = A\text{Div}\,\underline{\boldsymbol{K}} = A\text{Div}\,(\frac{\partial \gamma_\chi}{\partial X}\underline{\boldsymbol{l}} + \frac{\partial \gamma_\chi}{\partial Y}\underline{\boldsymbol{n}}) = A\frac{\partial^2 \gamma_\chi}{\partial Y^2}. \tag{5.215}$$

Combining the balance equation Eq. (5.19) with the previous equation and Eq. (5.212) leads to

$$A\frac{\partial^2 \gamma_\chi}{\partial Y^2} = H_\chi(\gamma_\chi - \gamma). \tag{5.216}$$

Substituting Eq. (5.214) into the previous equation, one gets

$$A\frac{\partial^2 \gamma_\chi}{\partial Y^2} - \frac{HH_\chi}{H + H_\chi}\gamma_\chi + \frac{HH_\chi}{H + H_\chi}(|\tau| - \tau_0) = 0. \tag{5.217}$$

Recall that τ is spatially constant (cf. Eq. (5.209)). One thus has the differential equation governing γ_χ:

$$A\frac{\partial^2 \gamma_\chi}{\partial Y^2} - \frac{HH_\chi}{H + H_\chi}\gamma_\chi + \frac{HH_\chi}{H + H_\chi}(|\overline{\tau}| - \tau_0) = 0. \tag{5.218}$$

One trivial solution of Eq. (5.218) is

$$\gamma_\chi = |\overline{\tau}| - \tau_0 = \text{constant}, \tag{5.219}$$

which results in a spatially constant shearing strain κ.

As H is negative, a general sinusoidal solution exists in the form:

$$\gamma_\chi = C_1 \sin\left(\frac{2\pi}{\lambda_c}Y\right) + C_2 \cos\left(\frac{2\pi}{\lambda_c}Y\right) + (|\overline{\tau}| - \tau_0), \tag{5.220}$$

with the integration constants C_1 and C_2, and the wave length

$$\lambda_c = 2\pi / \sqrt{\frac{H_\chi |H|}{A(H_\chi + H)}}. \tag{5.221}$$

Note that λ_c comes into play as a material length scale. Within one period, γ_χ increases to its maximum value and then decreases, which represents a **shear band**. Since a large value is usually taken for the penalty parameter H_χ such that $H_\chi \gg |H|$, $\lambda_c \sim \sqrt{\frac{A}{|H|}}$. Thus, increasing the value of A results in a wider shear band. Another form of periodic solution exists, which represents a periodic array of shear bands separated by nearly constant values.

Analysis with the alternative formulation

In this section, we consider the second formulation of the theory presented in section 5.1.5. The free energy potential given by Eq. (5.111) is considered so that one has the constitutive equations Eqs. (5.211) and (5.212). The yield function (Eq. (5.70)) writes

$$f = |\tau + (\underline{\boldsymbol{K}}^{\sharp}.\underline{\boldsymbol{l}})(\underline{\boldsymbol{M}}^{\sharp}.\underline{\boldsymbol{n}})| - [\tau_0 + H\gamma - H_\chi(\gamma_\chi - \gamma)]\,. \tag{5.222}$$

Noticing $\underline{\boldsymbol{K}}^{\sharp} = \underset{\sim}{\boldsymbol{P}}^{-T}.\underline{\boldsymbol{K}}$, $\underline{\boldsymbol{M}}^{\sharp} = \underset{\sim}{\boldsymbol{P}}.\underline{\boldsymbol{M}}$ and $\underline{\boldsymbol{M}} = A\underline{\boldsymbol{K}}$, one considers $\underset{\sim}{\boldsymbol{P}} = \underset{\sim}{\boldsymbol{1}} + \gamma\underline{\boldsymbol{l}} \otimes \underline{\boldsymbol{n}}$ and further obtains:

$$\underline{\boldsymbol{K}}^{\sharp} = \frac{\partial\gamma_\chi}{\partial X}\underline{\boldsymbol{l}} + \left(\frac{\partial\gamma_\chi}{\partial Y} - \gamma\frac{\partial\gamma_\chi}{\partial X}\right)\underline{\boldsymbol{n}}\,, \tag{5.223}$$

$$\underline{\boldsymbol{M}}^{\sharp} = A\left[\left(\frac{\partial\gamma_\chi}{\partial X} + \gamma\frac{\partial\gamma_\chi}{\partial Y}\right)\underline{\boldsymbol{l}} + \frac{\partial\gamma_\chi}{\partial Y}\underline{\boldsymbol{n}}\right]. \tag{5.224}$$

Substituting the previous equations into Eq. (5.222) results in

$$f = |\tau + x^s| - [\tau_0 + H\gamma - H_\chi(\gamma_\chi - \gamma)] \tag{5.225}$$

with

$$x^s = A\frac{\partial\gamma_\chi}{\partial X}\frac{\partial\gamma_\chi}{\partial Y}. \tag{5.226}$$

Here, a kinematic hardening is found. It can exhibit only in the presence of a gradient of slip in both directions X and Y. Since we assume $\gamma_\chi = \gamma_\chi(Y)$, $\dfrac{\partial\gamma_\chi}{\partial X} = 0$. Thus, the yield function is reduced to

$$f = |\tau| - [\tau_0 + H\gamma - H_\chi(\gamma_\chi - \gamma)]\,, \tag{5.227}$$

which is the same as in Eq. (5.213).

As the balance laws Eqs. (5.18) and (5.19) hold for the two formulations, one can obtain the same differential equation governing γ_χ as Eq. (5.218). It means that the two formulations lead to the same solution for the special case of single slip. However, it is important to notice that the term $A\dfrac{\partial\gamma_\chi}{\partial X}\dfrac{\partial\gamma_\chi}{\partial Y}$ in Eq. (5.225) will come into play for the case with $\dfrac{\partial\gamma_\chi}{\partial X} \neq 0$ in shear bands, e.g., pile-ups are considered. Further studies are needed for this term in the second formulation especially with FEM. This is out of the scope of the present study.

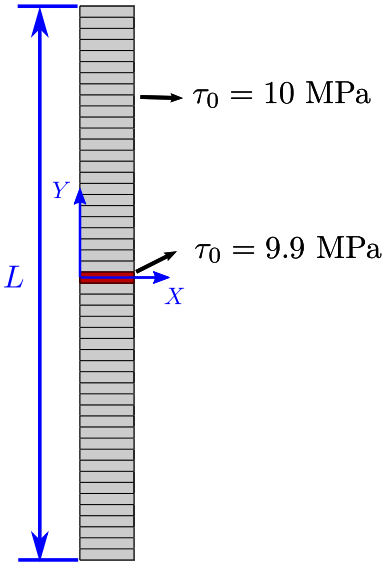

Figure 5.4: FE mesh for studying shear banding.

FE solutions

For the FE analysis, a single row of elements with side length $L = 1\,\text{mm}$ is considered and shown in fig. 5.4. Periodic boundary conditions are applied for the displacement field $\underline{\boldsymbol{u}}$ such that

$$\underline{\boldsymbol{u}} = \overline{\underset{\sim}{\boldsymbol{F}}}.\underline{\boldsymbol{X}} + \underline{\boldsymbol{v}} \tag{5.228}$$

with $\overline{\underset{\sim}{\boldsymbol{F}}}$ denotes the overall deformation gradient and $\underline{\boldsymbol{v}}$ a periodic fluctuation vector. The periodicity is also enhanced for the γ_χ field, i.e., γ_χ takes the same value at homologous points on the opposite sides of the strip. Simple shear is imposed by prescribing the overall deformation gradient $\overline{F}_{12}$.

As for the material parameters, the softening parameter is fixed to be $H = -10^3\,\text{MPa}$ the shear modulus $\mu = 104.7\,\text{GPa}$, and $\tau_0 = 10\,\text{MPa}$. The parameters of power law is chosen as $K = 0.1\,\text{MPa}$ and $n = 15$ such that the viscous effect is negligible. Note that, for triggering the localization, the value of τ_0 for a line of elements is set to be $\tau_0 = 9.9\,\text{MPa}$, which is slightly smaller than that of the others.

The effect of the penalty parameter H_χ is first studied. To this end, the higher order modulus is fixed to be $A = 5\,\text{N}$, and the value of H_χ is changed from 10^3 to $10^6\,\text{MPa}$. The overall stress-strain response and the distribution of γ_χ along axis Y at the shear strain $\overline{F}_{12} = 0.0005$ are shown in fig. 5.5. As can be seen, the overall stress–strain curves and the distribution of γ_χ converge to the same result with increasing H_χ. However, when H_χ is too small, i.e., $H_\chi = 10^3\,\text{MPa}$, a completely different solution of γ_χ is found. These results confirm the penalty

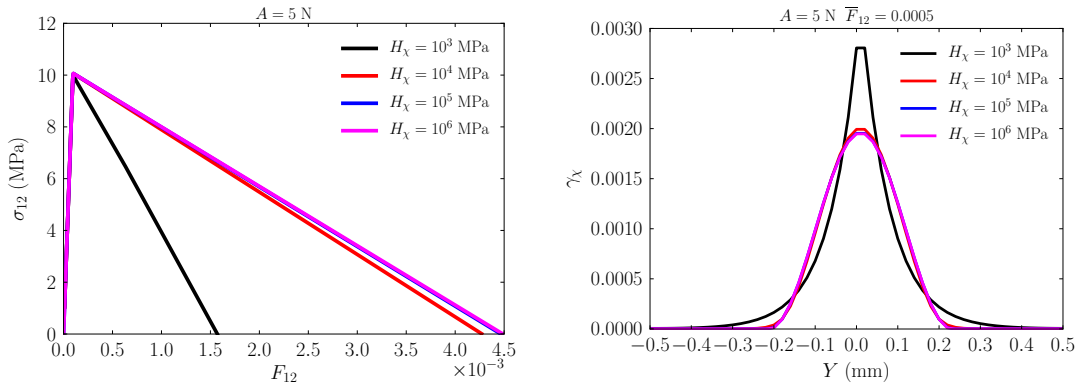

(a) **(b)**

Figure 5.5: Influence of H_χ on (a) overall stress-strain curve and (b) distribution of γ_χ along Y direction at $\overline{F}_{12} = 0.0005$. $A = 5\,\mathrm{N}$.

role of the parameter H_χ and shows the necessity of choosing a large value for H_χ. However, a too large value of H_χ will cause numerical problems. Thus, the value of H_χ should not be too large, neither too small.

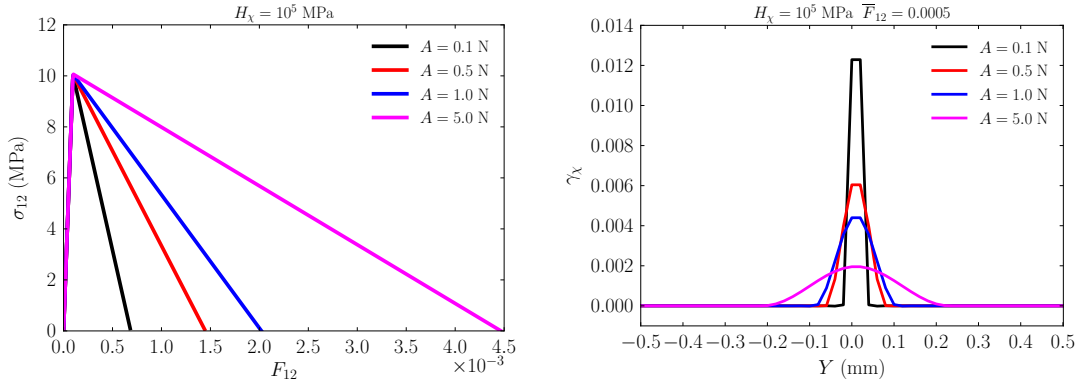

(a) **(b)**

Figure 5.6: Influence of A on (a) overall stress-strain curve and (b) distribution of γ_χ along Y direction at $\overline{F}_{12} = 0.0005$. $H_\chi = 10^5\,\mathrm{MPa}$.

The effect of A is then investigated by fixing $H_\chi = 10^5\,\mathrm{MPa}$ and varying A from 0.1 to 5 N. The stress-strain curves and γ_χ as a function of Y at the overall shear strain $\overline{F}_{12} = 0.0005$ are presented in fig. 5.6. The results show the regularization of the shear band, i.e., its finite width. The width of the band increases with increasing value of A, which is in good agreement with the analytical solution (cf. the material length scale λ_c by Eq. (5.221)). It can also been observed in fig. 5.6a that the hardening due to slip gradient is more significant with a large value of A, which counteracts the softening due to the term $H\gamma$ with $H < 0$ in Eq. (5.213).

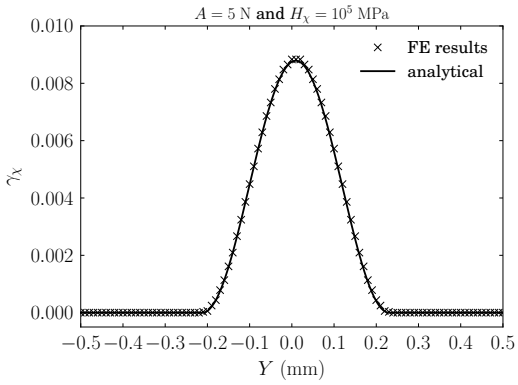

Figure 5.7: Comparison analytical and numerical results: distribution of γ_χ along Y direction at $\overline{F}_{12} = 0.002$. $A = 5\,\mathrm{N}$ and $H_\chi = 10^5\,\mathrm{MPa}$.

For obtaining the analytical solution for this problem, boundary conditions need to be considered. The solution corresponds to a shear band surrounded by elastic zones within which $\gamma_\chi = 0$. At the boundary between the elastic and the plastic region, $\gamma_\chi = 0$ and $\frac{\partial \gamma_\chi}{\partial Y} = 0$ are considered; the continuity of γ_χ and $\frac{\partial \gamma_\chi}{\partial Y}$ are guaranteed. The analytical solution obtained for $A = 5\,\mathrm{N}$ and $H_\chi = 10^5\,\mathrm{MPa}$ is compared with the numerical result in fig. 5.7 at the shear strain $\overline{F}_{12} = 0.002$. It shows a perfect agreement between the FE and the analytical result.

5.4.2 Strain localization with single slip under uniaxial tension

Strain localization in single crystals has been observed in many studies (see, e.g., Chang and Asaro, 1981). It was analyzed in a seminal work of Asaro and Rice (1977) by considering crystals deformed by single slip. The problem was then investigated by Peirce et al. (1982) using FE simulations for double slip. In the present work, we will study strain localization in single crystals using FE simulations with the micromorphic model and consider crystals deformed by single slip. Slip and kink bands are expected in the simulations, which have been investigated in different works (see Forest (1998) for analysis and simulations, and Kysar and Briant (2002), Flouriot et al. (2003), and Sabnis et al. (2012) for experimental observations of slip and kink bands at the crack tip or the notch tip). Mesh dependence of the simulations of slip and kink bands will be studied.

Problem setup

Simulations are performed with a plate as shown in fig. 5.8. The plate is meshed by brick elements with reduced integration (20 nodes for the displacement DOFs and 8

nodes for the microslip DOF) and one element is used in the thickness direction. An in-plane single slip system is defined, whose slip plane has an angle of 56.3° with respect to the vertical direction. The crystal orientation is chosen such that both the slip direction and the slip plane normal of the single slip system are parallel to the X–Y plane. This results in plane plastic strain conditions. The boundary conditions are considered as follows:

$$U_X(Y = L_0) = 0, \quad U_Y(Y = L_0) = U(t), \tag{5.229}$$

$$U_X(Y = 0) = 0, \quad U_Y(Y = 0) = 0. \tag{5.230}$$

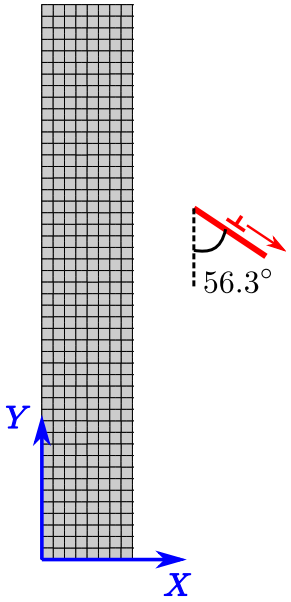

Figure 5.8: A typical FE mesh for simulations of strain localization. The total number of elements used is $n \times 6n$ with n for the width and $6n$ for the height. The mesh with $n = 8$ shown in the figure. An in-plane single slip system is also shown in the figure, whose slip direction has an angle of 56.3° with respect to the vertical direction.

The simulations are performed with both the conventional and micromorphic model. A linear hardening law is considered with τ_c given by:

$$\tau_c = \tau_0 + H\gamma \tag{5.231}$$

with $H > 0$. For the simulations, a weak hardening is considered with $H = 1\,\text{MPa}$. For the micromorphic model, $H_\chi = 5 \times 10^4\,\text{MPa}$ and $A = 0.1\,\text{N}$ are taken. Strain localization due to the prescribed boundary conditions and lattice rotation will be studied in the following.

Results

Different FE discretizations are considered with n elements for the width and $6n$ for the height, i.e., totally $6n^2$ elements. Four meshes with respectively $n = 8, 16, 24, 32$, are considered (see fig. 5.8 for a mesh with $n = 8$).

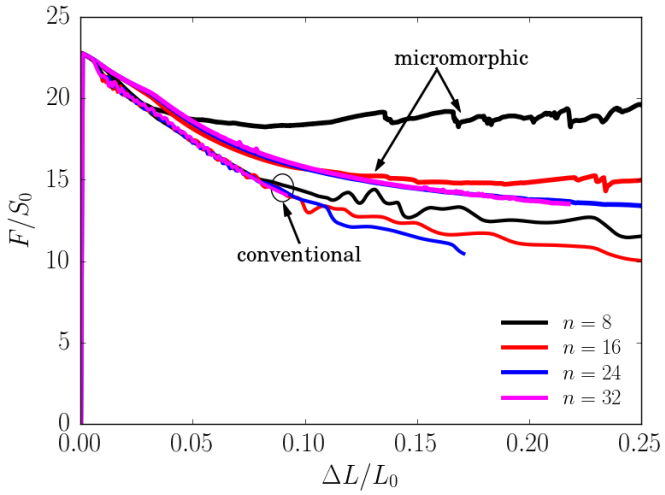

Figure 5.9: Stress–strain curves obtained by the conventional and micromorphic model with different FE meshes.

The evolution of the loading force F normalized by initial section area S_0 is plotted in fig. 5.9 as a function of the elongation ΔL (in the direction Y axis) normalized by the initial height L_0 of the mesh. For the simulations with the conventional model, a softening regime due to change in section and lattice rotation is found. Recall that a weak hardening is considered in the constitutive relation of the crystal. Zigzags are found are the curves and a mesh dependence of the curves is also observed. As the FE mesh is refined to $n = 32$, the simulation diverges at $\Delta L/L_0 = 0.1$ as a result of strong strain localization.

For the simulations with the micromorphic model, a softening regime is also observed. However, the stress level is higher than that obtained by the conventional model and it results from the strain gradient hardening taken into account in the micromorphic model. The mesh convergence is observed for the micromorphic model. Moreover, the curves obtained by the micromorphic model with $n = 24$ and $n = 32$ are smoother than those obtained by the conventional model.

The evolution of plastic slip γ field with $\Delta L/L_0$ is shown in fig. 5.10 for the conventional model and in fig. 5.11 for the micromorphic model. Complex localization modes are observed in the simulations with the conventional and micromorphic model. Both the models predict a formation of two kink bands at the

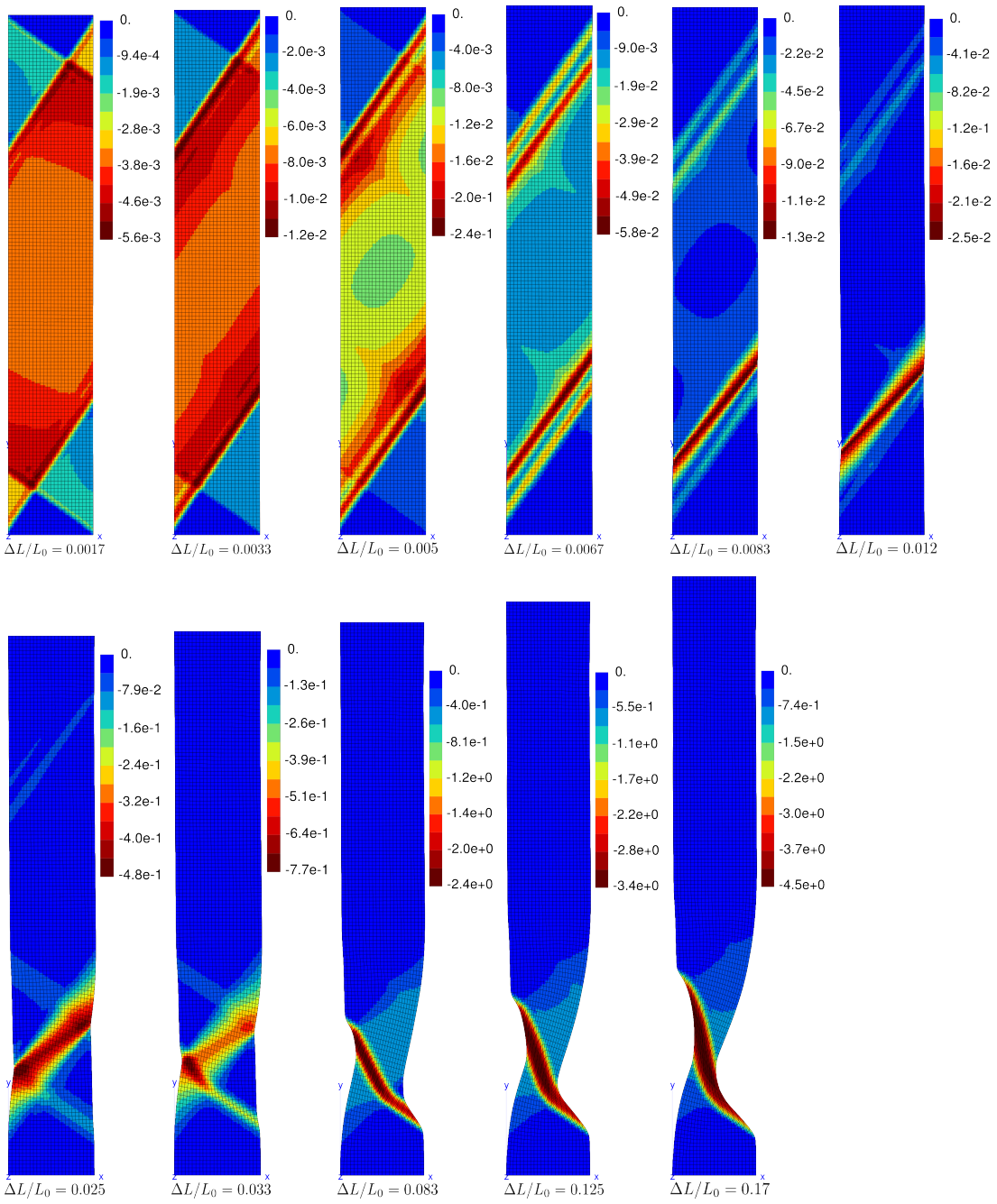

Figure 5.10: Evolution of plastic slip γ field with $\Delta L/L_0$ predicted by the conventional model with the FE mesh $n = 24$.

beginning of the loading. As the loading increases, strain localizes in the kink band located in the lower part of the crystal. Finally, intense slip bands form crossing the initial kink bands, leading to final necking of the plate. A slip band is a localization band parallel to the slip plane. A kink band is a localization band perpendicular to

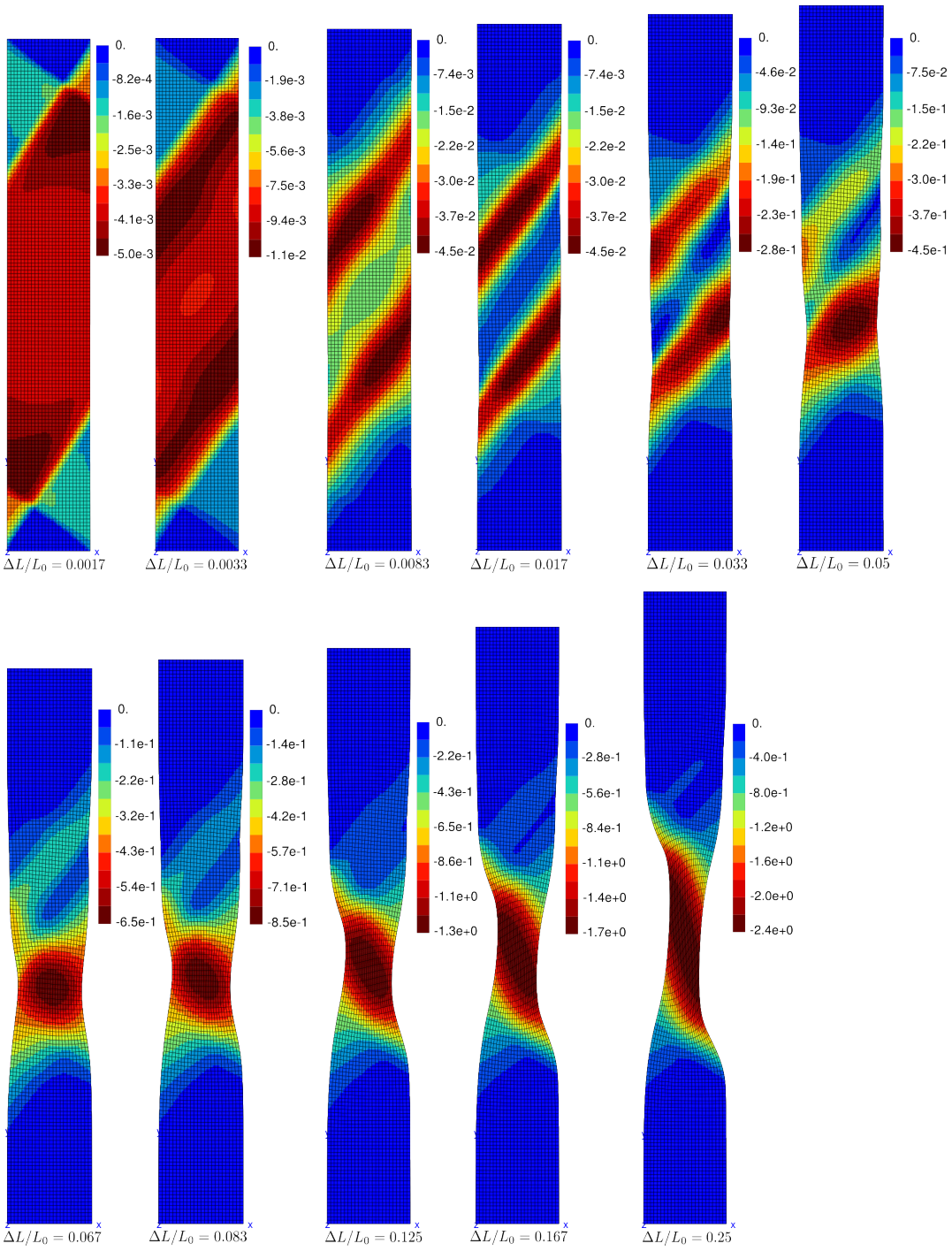

Figure 5.11: Evolution of plastic slip γ field with $\Delta L/L_0$ predicted by the micromorphic model with the FE mesh $n = 24$.

the slip direction. A major difference between slip and kink bands is that strong lattice curvature occurs at the kink band boundaries.

Some differences are noticed for the two simulations. Compared with the conventional model, the distance between the two kink bands predicted by the

micromorphic model is smaller. Besides, the band width (band size along Y direction) predicted by the micromorphic model is larger than that by the conventional model, i.e., the plastic slip field is more diffuse in the simulation with the micromorphic model than with the conventional model.

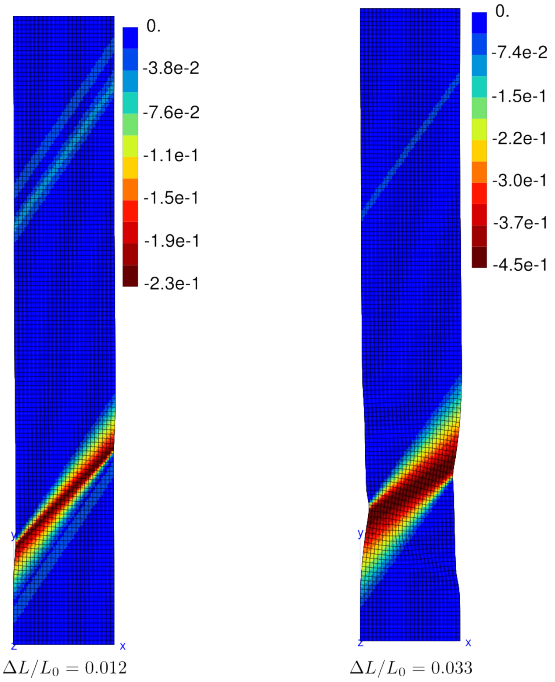

Figure 5.12: The lattice rotation angle θ predicted by the conventional model for (a) $\Delta L/L = 0.012$ and (b) $\Delta L/L = 0.033$

For further confirming the formation of kink bands, lattice rotation needs to be checked. The polar decomposition of the elastic part of deformation gradient $\underset{\sim}{\boldsymbol{E}}$ follows

$$\underset{\sim}{\boldsymbol{E}} = \underset{\sim}{\boldsymbol{R}}.\underset{\sim}{\boldsymbol{U}}, \tag{5.232}$$

with the rotation tensor $\underset{\sim}{\boldsymbol{R}}$ and the right stretch tensor $\underset{\sim}{\boldsymbol{U}}$. Neglecting the elastic distortion $\underset{\sim}{\boldsymbol{U}}$, $\underset{\sim}{\boldsymbol{R}}$ can be interpreted as the lattice rotation. The corresponding rotation angle θ is given by

$$\theta = \arccos \frac{1}{2}(\text{trace}\, \underset{\sim}{\boldsymbol{R}} - 1). \tag{5.233}$$

The field of θ is shown in fig. 5.12 for the simulation with the conventional model when $\Delta L/L_0 = 0.012$ and $\Delta L/L_0 = 0.033$. The formation of kink bands at $\Delta L/L_0 = 0.012$ is verified, because of relatively high level of θ within the bands. The formation of slip band crossing the kink band at $\Delta L/L_0 = 0.067$ is also checked, because significant plastic slip is observed in the band parallel with the

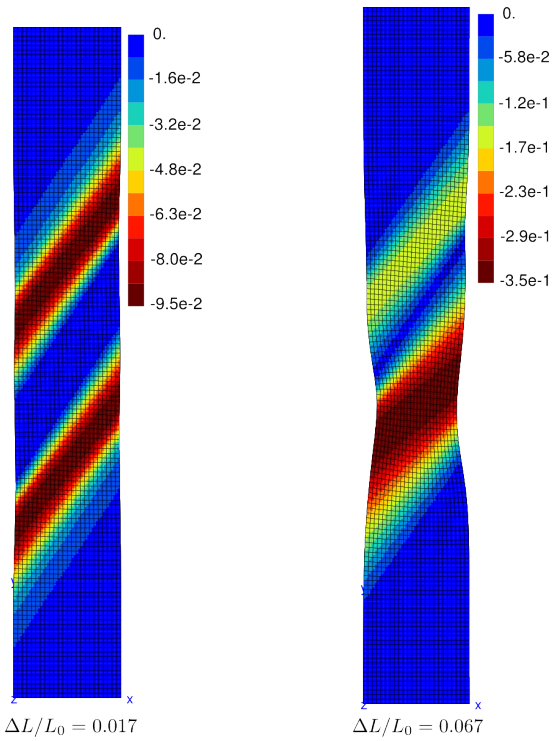

Figure 5.13: The lattice rotation angle θ predicted by the micromorphic model for (a) $\Delta L/L = 0.017$ and (b) $\Delta L/L = 0.067$

slip plane, where no lattice rotation is found. The formation of kink and slip band are verified in the same way for the micromorphic model as shown in fig. 5.13 for $\Delta L/L_0 = 0.017$ and $\Delta L/L_0 = 0.067$.

In addition, for the simulations with the micromorphic model, the material length scale, estimated by Eq. (5.221), is found to be $\lambda_c = 2\,\text{mm}$, which is larger than the width of the plate (1 mm). The element size ($\sim 0.04\,\text{mm}$ for $n = 24$ and $\sim 0.03\,\text{mm}$ for $n = 32$) should be much smaller than λ_c for the mesh convergence. Note that the band width (band size along Y direction) at $\Delta L/L_0 = 0.25$ (see fig. 5.11) is of the same order of $\lambda_c = 2\,\text{mm}$.

5.5 Application to ductile fracture of single crystals

Void growth and coalescence are known as the mechanisms controlling ductile fracture of metallic materials. In single crystals, lattice orientation has been shown to have an impact on void growth and coalescence (cf. Ling et al., 2016 and references therein). As void size decreases to micro-scale, size effects are expected in single crystals, which have been predicted by different approaches (e.g., see Shu,

1998, Borg and Kysar, 2007 and Borg et al., 2008 for FE unit cell simulations with strain gradient plasticity, see Hussein et al., 2008 and Chang et al., 2015 for DDD simulations and see Zhao et al., 2009 for MD). In this section, unit cell simulations are carried out with the micromorphic model for predicting size effects on void growth and coalescence in single crystals.

5.5.1 Unit cell simulation

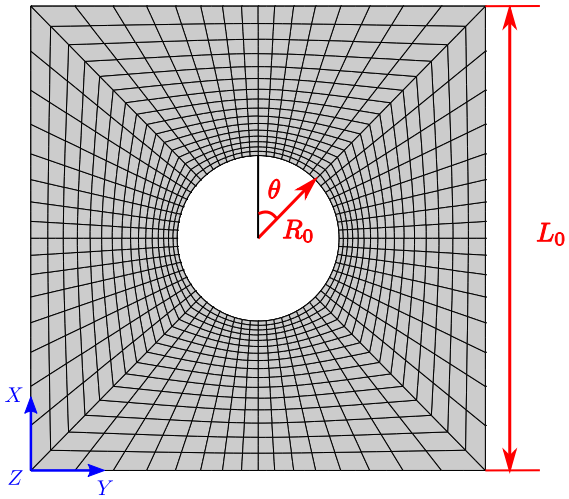

Figure 5.14: Typical FE mesh for the unit cell simulations.

A cylindrical void of radius R_0 in a square plate of side length L_0 is considered. A typical FE mesh with one element in thickness w_0 is shown in fig. 5.14 for an initial void volume fraction $f_0 = \pi R_0^2/L_0^2 = 0.1$. A biaxial tensile is imposed under plane strain conditions. The boundary conditions applied on the faces of the unit cell are

$$U_X(X=0)=0,\ U_X(X=L_0)=U_1(t), \tag{5.234}$$

$$U_Y(Y=0)=0,\ U_Y(Y=L_0)=U_2(t), \tag{5.235}$$

$$U_Z(Z=0)=0,\ U_Z(Z=w_0)=0. \tag{5.236}$$

Two external forces F_1 and F_2 are associated with $U_1(t)$ and $U_2(t)$. The prescribed U_2 is adjusted by one additional element for keeping a constant biaxiality ratio $a = \overline{\sigma}_{22}/\overline{\sigma}_{11}$ during the loading, where the overall stresses $\overline{\sigma}_{11}$ and $\overline{\sigma}_{22}$ are defined by

$$\overline{\sigma}_{11} = \frac{F_1}{w_0(L_0+U_2)},\ \overline{\sigma}_{22} = \frac{F_2}{w_0(L_0+U_1)}. \tag{5.237}$$

The FCC single crystal with 12 slip systems is considered. The slip systems are specified by the slip direction $\underline{\boldsymbol{l}}^s$ and the normal to the slip plane $\underline{\boldsymbol{n}}^s$ in the crystal

s	1	2	3	4	5	6	7	8	9	10	11	12
$\underline{\boldsymbol{n}}^s$	(111)			$(1\bar{1}1)$			$(\bar{1}11)$			$(\bar{1}\bar{1}1)$		
$\underline{\boldsymbol{l}}^s$	$[\bar{1}01]$	$[0\bar{1}1]$	$[\bar{1}10]$	$[\bar{1}01]$	$[011]$	$[110]$	$[0\bar{1}1]$	$[110]$	$[101]$	$[\bar{1}10]$	$[101]$	$[011]$

Table 5.1: Slip systems in FCC single crystals

coordinate system. They are listed in table 5.1. In the simulation, one crystal orientation is taken into account. The crystal orientation is specified with the lattice directions [100]–[010]–[001] along the coordinate axes X-Y-Z. A cubic elasticity is considered and thus $\underset{\approx}{\mathbf{\Lambda}}$ can be specified by three independent moduli C_{11}, C_{12} and C_{44}. The critical resolved shear stress τ_c^s of slip systems is determined by Eqs. (5.72) and (5.73). The material parameters used in the simulations are summarized in table 5.2. Note that a^{su} and b^{su} are 12×12 matrices and they can be specified by 6 independent parameters $a_1, a_2, \cdots, a_6$ and $b_1, b_2, \cdots, b_6$ (the structure of the matrices are presented in appendix A). The values of a^{su} are obtained by discrete dislocation dynamics (Kubin et al., 2008; Monnet, 2009), while no study is found in the literature for estimating the values of b_i $(i = 1, 2, \cdots, 6)$. It is presumed that $b_1 = 0$ and that $b_i = 0$ for $i \neq 1$. The initial values of adimensional dislocation densities r^s_{ini} ($s = 1, 2, \cdots, 12$) are assumed to be the same. Recall that $r^s = b^2\rho^s$, where ρ^s is the dislocation density and b is the norm of Burger's vector of the dislocation. $b = 2.54$ $\mathring{A}$ is considered for the FCC single crystal.

C_{11}	C_{12}	C_{44}	τ_0	n	K	μ	G_c	κ
199 GPa	136 GPa	105 GPa	88 MPa	15	1 MPa.s$^{1/\text{n}}$	65.6 GPa	10.4	42.8
a_1	a_2	a_3	a_4	a_5	a_6	b_1	b_i $(i \neq i)$	r^s_{ini}
0.124	0.124	0.07	0.625	0.137	0.122	0	1	5.38×10^{-11}

Table 5.2: Material parameters for the unit cell simulations (see Han, 2012)

To study size effects, we change the side length L_0 of the unit cell, while fix the moduli $H_\chi = 5 \times 10^4\,\text{MPa}$ and $A = 10\,\text{N}$. λ_c defined by Eq. (5.221) is taken as the material length scale, though H is positive in the present case. λ_c is obtained by performing uniaxial tensile simulation on one element with the same parameters. A positive H can thus be estimated according to the evolution of τ^s with respect to γ^s of one slip system at the beginning of its activation. In this way, λ_c is calculated to be $\lambda_c = 0.4\,\text{mm}$.

5.5.2 Void growth

Evolution of the void volume fraction is first investigated. The current void volume fraction is calculated by

$$f = 1 - \frac{V_{\text{mesh}}}{V_{\text{tot}}}, \tag{5.238}$$

where V_{mesh} is the volume of the mesh which can be evaluated by post-processing calculation and V_{tot} is the total volume of the unit cell which follows $V_{\text{tot}} = (L_0+U_1)(L_0+U_2)w_0$. The increase in the void volume fraction is equal to $\Delta f = f - f_0$.

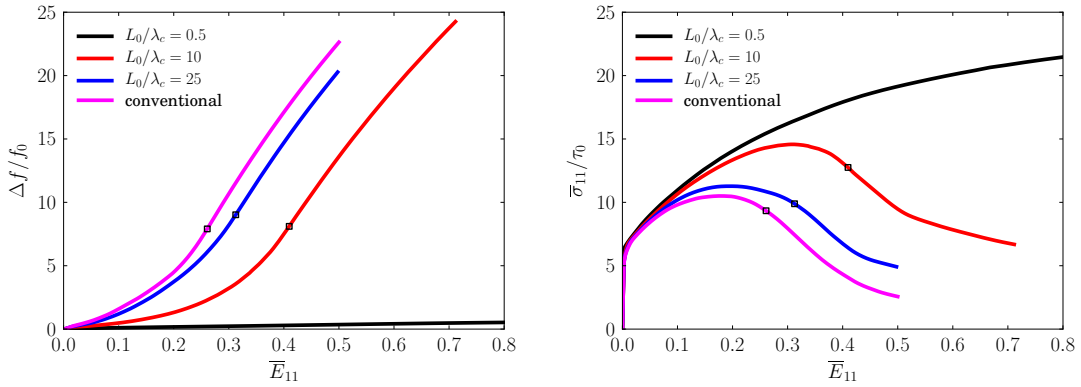

Figure 5.15: (a) Variation of the normalized void volume and (b) overall stress–strain curves for different sizes of the unit cell. $f_0 = 0.01$.

The variation of $\Delta f/f_0$ with respect to the overall strain $\overline{E}_{11} = U_1/L_0$ is shown in fig. 5.15a for the initial void volume fraction $f_0 = 0.01$. Note that the same computation has been performed with the conventional single crystal plasticity. Void evolution predicted by the conventional theory does not depend on the size of unit cell. In general, two stages of void evolution are observed: in the first stage, the void grows relatively slowly; in the second, void growth rate is accelerated. The two stages are termed respectively void growth and void coalescence in the literature. According to Koplik and Needleman, 1988, onset of the void coalescence is characterized by the transition from biaxial to uniaxial straining associated to the localization of the plastic flow in the intervoid ligament. Compared with the results by the conventional theory, the simulations with the micromorphic theory predict size dependent void evolution. Concerning the first stage of void evolution, i.e., void growth, void growth rate decreases with decreasing normalized unit cell size L_0/λ_c. The void growth rate is significantly reduced for the very small unit cell and an absence of void growth is predicted for $L_0/\lambda_c = 0.5$. In addition, the void evolution tends to converge to the result obtained by the conventional theory when L_0/λ_c is large enough.

The overall stress $\overline{\sigma}_{11}$ is plotted in fig. 5.15b as a function of the overall strain $\overline{E}_{11}$. For the simulation with the conventional theory, a hardening regime followed by a softening one is observed, which results from the competition between the strain hardening of the matrix, the softening due to void growth and the softening

due to void coalescence. The micromorphic theory predicts a higher stress level as a result of the reduced void growth. The hardening regime is enhanced with the decreasing unit cell size L_0/λ_c. In particular, no softening regime exhibits for the unit cell with $L_0/\lambda_c = 0.5$, which is due to extremely low void growth rate. In this case, the voided unit cell behaves like a void-free unit cell.

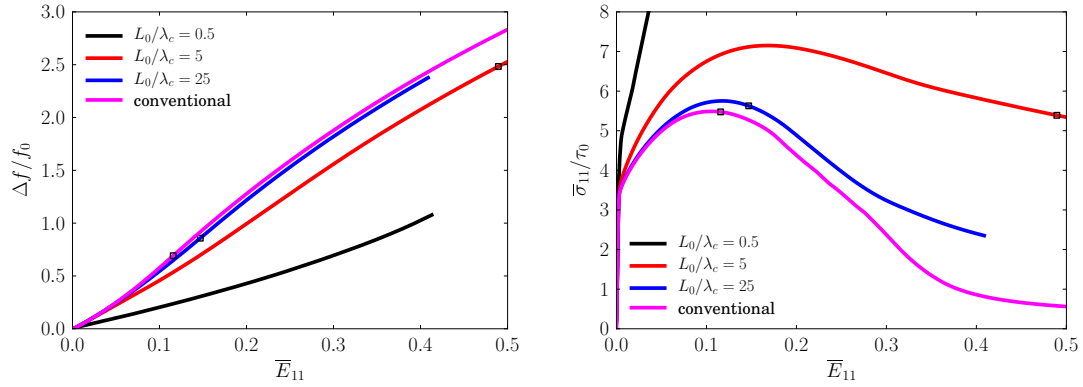

Figure 5.16: (a) Variation of void volume fraction and (b) overall stress–strain curves for different size of unit cell. $f_0 = 0.1$.

Results for $f_0 = 0.1$ are shown in fig. 5.16. Compared with the simulations for $f_0 = 0.01$, the evolution of $\Delta f/f_0$ does not exhibit an obvious transition to the accelerated void growth stage. However, the transition from the uniaxial to biaxial straining can be detected, i.e., the two stages (void growth and coalescence) exist for $f_0 = 0.1$. Size effect on void growth observed is similar to that for $f_0 = 0.01$: void growth rate is reduced for small L_0/λ_c. However, the void growth for $L_0/\lambda_c = 0.5$ cannot be neglected here, unlike in the case of $f_0 = 0.01$. In addition, similar size dependent overall stress–strain response is observed as that for $f_0 = 0.01$. It worth noticing that the unit cell with $L_0/\lambda_c = 0.5$ does not show softening regime even with a non-negligible void growth.

5.5.3 Void coalescence

The onset of void coalescence in the present study corresponds to a shift from biaxial to uniaxial straining, which is in good agreement with Koplik and Needleman, 1988. The onset is determined in the following way: calculate the ratio $a_0 = |U_1|/|U_2|$ at the beginning of the biaxial straining, choose a critical value as $a_c = 0.1a_0$ and find $\overline{E}_{11}$ for the onset as soon as a_0 decreases to a_c. The critical value of $\overline{E}_{11}$ for the onset of coalescence thus determined is denoted by $\overline{E}^c_{11}$.

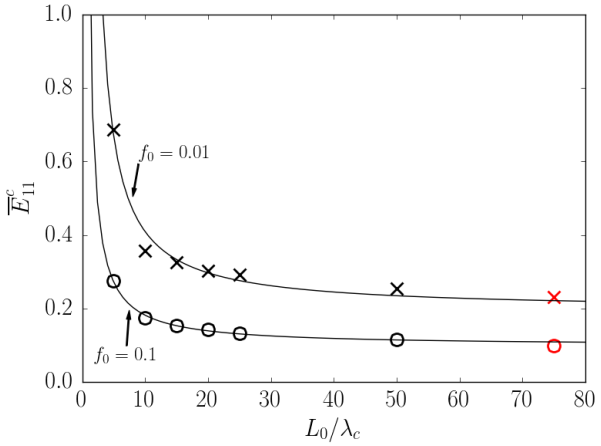

Figure 5.17: Critical strain $\overline{E}^c_{11}$ for onset of coalescence as a function of normalized size of unit cell. $f_0 = 0.01$ and 0.1.

The onset of coalescence is indicated by a hollow square in figs. 5.15 and 5.16. Compared with the result predicted by the conventional theory, the onset of coalescence is delayed for small unit cell size with micromorphic theory. $\overline{E}^c_{11}$ is plotted as a function of L_0/λ_c in fig. 5.17 for $f_0 = 0.01$ and 0.1, in which the red markers indicate $\overline{E}^c_{11}$ predicted by the conventional theory. Since the coalescence is not predicted for $L_0/\lambda_c = 0.5$, $\overline{E}^c_{11}$ does not exist and is not plotted in the figure. Qualitatively similar results are shown for the two levels of f_0. A rapid decrease in $\overline{E}^c_{11}$ is observed for $L_0/\lambda_c < 10$. It tends to stabilize with increasing L_0/λ_c and converge to the value predicted by the conventional theory.

5.5.4 Discussion

Size dependent overall behavior and void growth have been predicted by the micromorphic theory for voided single crystals. Qualitatively similar results have been shown for the unit cell with $f_0 = 0.01$ and $f_0 = 0.1$: unit cells of smaller size exhibit reduced void growth rate compared with larger ones; this results in higher hardening rate at the beginning of plastic regime and delays onset of void coalescence.

The impeded void growth in unit cells of small size is associated with the fact that the plastic deformation field is diffused in the micromorphic theory. The cumulative slip γ_{cum} is shown in section 5.5.4 for the unit cells with $f_0 = 0.1$ and different values of L_0/λ_c at the overall strain $\overline{E}_{11} = 0.1$. The conventional theory predicts the significant localization of γ_{cum} at four zones at the void, i.e., *A, B, C, D* shown in section 5.5.4. It is worth noticing that the maximum local γ_{cum} reaches 2.18 with the overall strain $E_{11} = 0.1$. By the micromorphic theory, the γ_{cum} field is diffused especially for the four zones and becomes more and more diffuse

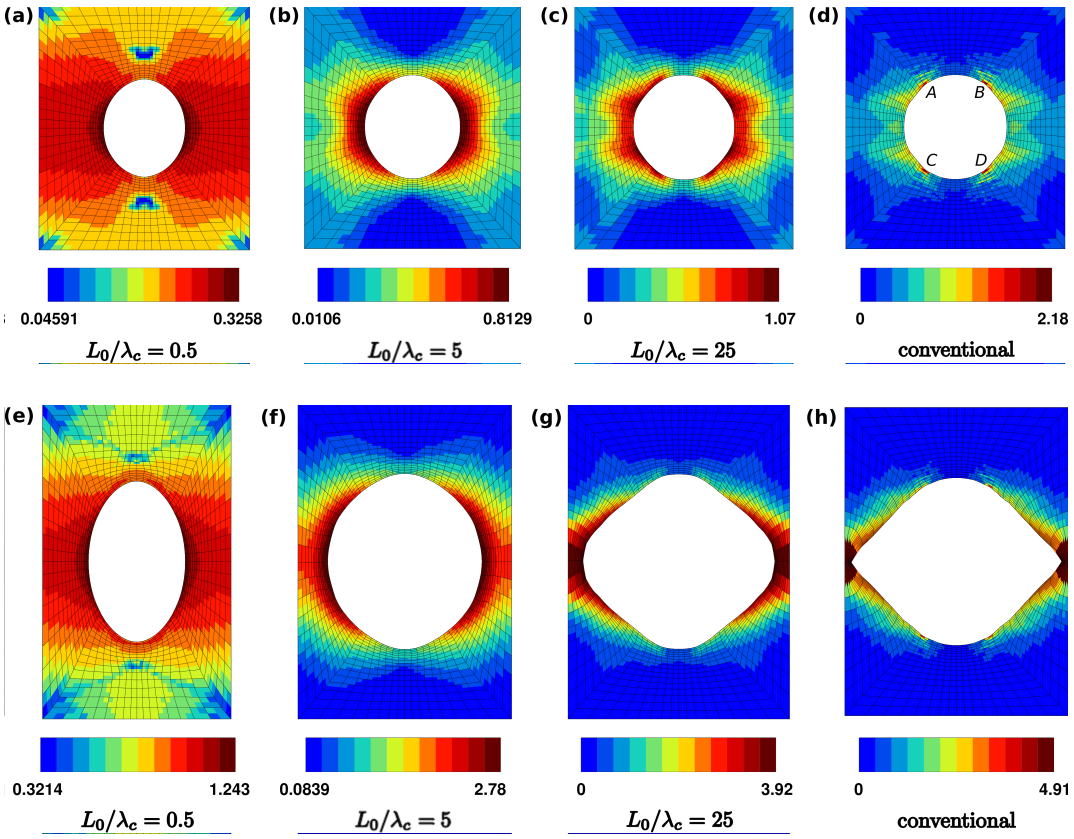

Figure 5.18: Void shape at $\overline{E}_{11} = 0.1$ ((a)–(d)) and $\overline{E}_{11} = 0.4$ ((e)–(h)) for different unit cell size: (a,e) $L/\lambda_c = 0.5$, (b,f) $L/\lambda_c = 5$, (c,g) $L/\lambda_c = 25$ and (d,h) conventional model. $f_0 = 0.1$. The field of γ_{cum} is shown.

as L_0/λ_c decreases from 25 to 0.5. As a result, void growth is slowed down and void coalescence is delayed. The diffused field of γ_{cum} also influences the evolution of void shape, as shown in section 5.5.4 for the unit cells of different sizes with $f_0 = 0.1$ at the overall strain $E_{11} = 0.4$. The void is shown to be ellipsoid for the small unit cell with $L_0/\lambda_c = 0.5$. In this case, since the void coalescence does not occur, the void is well elongated along the X–axis but the deformation of the void along the Y–axis is restricted. The void is also ellipsoid for $L_0/\lambda_c = 5$ at $E_{11} = 0.4$ (before the onset of void coalescence for this case). Compared with $L_0/\lambda_c = 0.5$, the void is more deformed along the Y–axis because of a less diffuse field of γ_{cum} in the region around the void. For the large unit cell with $L_0/\lambda_c = 25$, the lateral deformation of the void is significant at $E_{11} = 0.4$ as a result of void coalescence. The conventional theory predicts a similar void shape as the micromorphic theory with $L_0/\lambda_c = 25$, except that a sharp point shows. This is related to the highly localized plastic strain in the lateral regions.

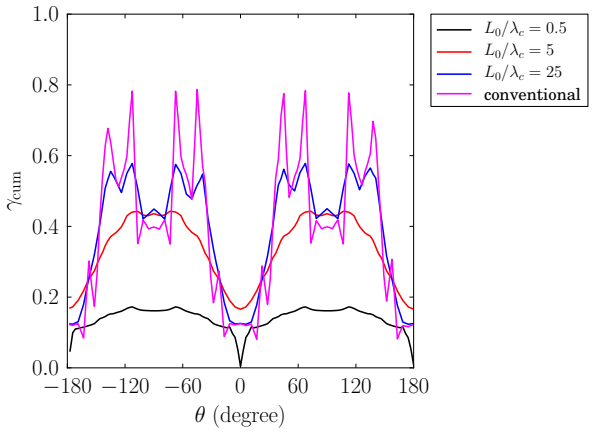

Figure 5.19: γ_{cum} at the void for $f_0 = 0.1$. $\overline{E}_{11} = 0.05$.

In addition, γ_{cum} at the void surface is investigated and plotted in fig. 5.19 as a function of the angle θ (cf. the definition of θ in fig. 5.14) at $E_{11} = 0.05$ (before significant void shape change). Angular sectors are observed as those by Borg and Kysar, 2007; Niordson and Kysar, 2014 and some similarities can be observed for different unit cell sizes. The distribution of γ_{cum} is shown to be smoother at the void surface for unit cells of smaller size than that of larger ones. This is directly related to the reduced void growth for unit cells of small size.

5.6 Conclusions

A micromorphic single crystal plasticity at finite deformation is derived by a thermodynamic approach in the present work. The model involves a single additional DOF, i.e., the microslip γ_χ. Two types of constitutive formulation are proposed without and with free energy potential depending on the microslip gradient variable $\underline{\boldsymbol{K}}^\sharp$ defined in the intermediate configuration. In the formulation involving $\underline{\boldsymbol{K}}^\sharp$, a gradient induced back-stress is found for each slip system. To the author's knowledge, the kinematic hardening is introduced for the first time in the enhanced single crystal plasticity model based on a single additional DOF. The formulation without back-stress in the constitutive equations is implemented in the FE code `Zset`.

The model is then applied to study analytically and numerically strain localization in single crystals. In shear banding with single slip, the width of shear band predicted analytically by the model is found to be proportional to $\sqrt{\frac{A}{|H|}}$ with the higher order modulus A and the strain softening modulus H, when a large value is adopted for the penalty parameter H_χ. FE simulations are performed for analyzing the influence of A and H_χ on the width of shear band. A good agreement

is observed between the analytical and numerical results. In simulations for studying strain localization in a crystal under tension, different strain localization modes are predicted by the conventional and the micromorphic model. Smooth stress-strain curves are obtained by the micromorphic model with fine meshes and a mesh convergence is found for the micromorphic model.

The model is then used to investigate growth of a cylindrical void in FCC single crystals by FE simulations. The void growth rate is found to be size dependent: smaller voids grow slower than bigger ones. The size effect on void growth is more pronounced for single crystals with 1% initial porosity than those with 10% initial porosity. In addition, the simulations also predict that onset of void coalescence is delayed for smaller voids. These results are related to a more diffuse field of plastic slip for single crystal with smaller voids. Moreover, a higher strain hardening rate is observed for crystals with bigger voids. The size effect on the overall strain hardening is more obvious for crystals with 10% initial porosity than those with 1% initial porosity.

The model will be coupled with the porous single crystal model presented in section 4.1 in a future work, resulting in a non-local model for single crystals. The coupled model can be applied, in the future, to simulate ductile fracture in single crystals and polycrystals.

6
Conclusions and outlook

Conclusions

In the present work, void growth and coalescence in single crystals have been investigated. These two mechanisms are involved in the ductile fracture of stainless steels. These steels are used as structural materials in the internal structure of the core of nuclear power plants. Ductility and fracture toughness are known to be strongly affected by irradiation in PWR environment. It has been shown that intragranular voids exist in irradiated austenitic stainless steels. The voids potentially have different origins and various sizes, at the nano and micro scale. This work aims to assess the mechanical behavior of voided single crystals.

For this purpose, FE unit cell simulations have been performed to investigate void growth and coalescence in FCC single crystals at finite strains. Effects of irradiation have been considered through a physically based crystal plasticity model which takes into account dislocations and irradiation-induced defects (Frank loops). Effects of crystal orientation and stress triaxiality have been investigated in a first step and some conclusions are drawn as follows:

- Void growth rate increases with stress triaxiality, which is consistent with the results for von Mises materials in the literature.
- Void growth rate exhibits a crystal orientation dependence, and voids grow at a higher rate with the [111] orientation than the other orientations considered in this work.
- Crystal orientation effect on void growth is more pronounced at lower stress triaxiality ($T = 1$).

- Critical void volume fraction for onset of void coalescence exhibits a crystal orientation dependence.
- Critical void volume fraction for onset of void coalescence is almost insensitive to stress triaxiality for a given crystal orientation (at least for the range of stress triaxialities considered $T = 1$ to 3).

The results are in good agreement with the results for BCC crystals in the literature. Note that those results hold for unirradiated crystals as well as for irradiated crystals. However, compared with unirradiated cases, it has been found that:

- voids grow at a higher rate in the irradiated single crystal;
- the onset of void coalescence occurs at a smaller value of the overall strain and at a smaller value of the void volume fraction in the irradiated crystals.

These results are consistent with experimental observations showing that fracture toughness decreases rapidly with dose, especially in the range of 0–10 dpa. Besides, more significant plastic strain localization in the region near the void is predicted in the irradiated crystal, correlated with the faster void growth and earlier onset of void coalescence. In addition, brittle-like overall behavior is predicted at high level of stress triaxiality, i.e. $T = 3$, in the voided irradiated crystal, while a large amount of plastic deformation is reached in the vicinity of the void. The enhanced plastic strain localization predicted for irradiated single crystals is in good agreement with the observations of Neustroev and Garner (2009) in AISI 321 stainless steels irradiated in BOR-60.

An elastoviscoplastic model at finite strains has been proposed for porous single crystals with a future objective to assess fracture toughness of polycrystalline materials. The model incorporates heuristically the influence of hardening behavior of single crystal matrix and is able to describe void growth up to coalescence. The assessment based on unit cell simulations has shown that the porous single crystal model satisfactorily describes the hierarchy of porous single crystal responses with respect to crystal orientation and void volume fraction. However, the model cannot predict the quasi-incompressible behaviour observed for strongly asymmetric orientations, e.g., $[\bar{1}25]$, with small initial void volume fraction at low stress triaxiality. In fact, the $[\bar{1}25]$ orientation corresponds to single slip orientation for a void-free FCC single crystal. For this type of orientation with small initial void volume fraction at low stress triaxiality, the void does not induce significant plastic slip heterogeneity in the single crystal matrix. As a result, the voided single crystal behaves like a void-free single crystal and exhibits a nearly single slip pattern with quasi-incompressible overall behaviour. No void growth is predicted by the unit cell simulation in this case. In contrast, the porous single crystal model predicts a weak

void growth for this case, due to the term $2q_1 f_i \cosh\left\{q_2\sqrt{\frac{3}{20}}\frac{M_m}{\tau_s^*}\right\}$ in Eq. (4.1), which is strictly positive even in the case of single slip and, by virtue of normality rule, induces void growth. Furthermore, the model underestimates the strain hardening for strongly asymmetric orientations with small initial void volume fraction at high stress triaxiality and with large f_0 at all levels of stress triaxiality considered. In fact, as the stress triaxiality and the initial void volume fraction increase, the plastic slip heterogeneity introduced by the void becomes significant. The porous single crystal deviates significantly from single slip and much more slip systems are activated around the void. As a result, in the unit cell simulation, the strain hardening rate is increased and the void growth is accelerated. As the porous single crystal model only considers a single slip situation for strongly asymmetric orientations, it underestimates the strain hardening and the void growth.

The model has then been applied to simulate the SENT test on a single crystal specimen of 316 stainless steels. The experimental results used in the present work were obtained in another work. The simulations predict that the slip systems of three slip planes are activated, which is in good agreement with the experimental observation. The prediction of a strong strain localization in the region near the notch tip is also in good agreement with the experimental result. However, compared with the experiment, the simulation predicts a force–notch-opening-displacement relation showing a higher yield stress and a lower strain hardening rate. Note that this work is not finished yet. In order to better simulate the test, the following works will be considered:

- Decrease the initial value of dislocation densities and investigate its influences on strain hardening rate;
- Introduce inclusions of ferrite by some particles with higher yield stress than the matrix in the FE mesh and study their influences on strain hardening rate;
- Investigate influences of boundary conditions prescribed in the simulations on the results.

With the objective to study size effects on void growth and coalescence, a micromorphic single crystal plasticity model at finite strains has been presented in the last part of the work. Two formulations have been proposed, one of which involves the free energy potential depending on the microslip gradient in the intermediate configuration and incorporates a size-dependent back-stress for each plastic slip system. The model has been applied to strain localization in single crystals with single slip. A material length has been found to be proportional to $\sqrt{\frac{A}{|H|}}$ with the higher order modulus A and the strain softening modulus H,

when a large value is adopted for the penalty parameter H_χ. Moreover, unit cell simulations have been performed to study size dependent void growth. Some important conclusions are drawn as follows:

- Smaller voids grow slower than bigger ones.
- Size effect on void growth is more pronounced for single crystals with 1% initial porosity than those with 10% initial porosity.
- Onset of void coalescence is delayed for smaller voids.
- A more diffuse field of plastic slip is predicted for single crystal with smaller voids.
- A higher strain hardening rate is observed for crystals with larger voids.
- Size effect on the overall strain hardening is more obvious for crystals with 10% initial porosity than those with 1% initial porosity.

Compared with existing models in the literature, the following advantages of the model are found:

- It is computationally more efficient;
- It regularizes slip shear and kinks bands.

Outlook

Some shortcomings of the elastoviscoplastic model for porous single crystals have been shown in this work. In future works, efforts can be devoted to improve the model, especially accounting for the quasi-incompressible behavior of porous single crystals loaded along single slip orientations. In addition, the elastoviscoplastic model for porous single crystals can also be enhanced using the micromorphic approach for incorporating plastic size effects.

Furthermore, in order to assess fracture toughness of polycrystalline materials, the elastoviscoplastic model for porous single crystals can be applied to simulations such as:

- a polycrystalline aggregate with a Voronoi-type mesh in 3D;
- a polycrystalline tensile specimen without or with a notch;
- a compact tension (CT) test of a polycrystalline materials.

These simulations allow to evaluate effects of post-irradiation hardening/softening behavior on fracture toughness of polycrystalline stainless steels. Eventually, the model can be applied to

- the prediction of fracture of irradiated internal structure components of nuclear power plants.

For the micromorphic crystal plasticity model, further works are needed for better understanding the model, including:

- Implementing the alternative formulation and comparing the two formulations;
- Comparing different free energy potentials and understanding differences between various regularization operators.

In order to perform unit cell simulations with the micromorphic model for any asymmetric crystal orientations, more numerical tools need to be developed, including:

- Periodic finite element for the micromorphic model;
- Numerical method for imposing constant stress triaxiality with periodic boundary conditions.

In addition, large scale simulations of experiments on polycrystalline specimen, such as SENT tests, CT tests, etc., can be performed for evaluating void size effects on fracture toughness.

In future work, localization of plasticity in channels of deformation which is a specific mode of deformation of irradiated FCC materials and its interaction with voids growth and coalescence, which was not considered in the present study, has to be evaluated.

Appendices

A

Form of the a^{su} and b^{su} matrices

In FCC single crystals, the matrices a^{su} and b^{su} $(s, u = 1, 2, \cdots, 12)$ have respectively $12 \times 12 = 144$ coefficients. For symmetry reasons, the number of coefficients is reduced to six, i.e., a_i and b_i with $i = 1, 2, \cdots, 6$ Franciosi, 1985. a^{su} is constructed as follows:

$$
[a^{su}] = \begin{array}{c}
\begin{array}{cccccccccccc} A2 & A3 & A6 & B2 & B4 & B5 & C1 & C3 & C5 & D1 & D4 & D6 \end{array} \\
\left[\begin{array}{cccccccccccc}
a_1 & a_2 & a_2 & a_4 & a_5 & a_5 & a_3 & a_5 & a_6 & a_3 & a_6 & a_5 \\
 & a_1 & a_2 & a_5 & a_3 & a_6 & a_5 & a_4 & a_5 & a_6 & a_3 & a_5 \\
 & & a_1 & a_5 & a_6 & a_3 & a_6 & a_5 & a_3 & a_5 & a_5 & a_4 \\
 & & & a_1 & a_2 & a_2 & a_3 & a_6 & a_5 & a_3 & a_5 & a_6 \\
 & & & & a_1 & a_2 & a_6 & a_3 & a_5 & a_5 & a_4 & a_5 \\
 & & & & & a_1 & a_5 & a_5 & a_4 & a_6 & a_5 & a_3 \\
 & & & & & & a_1 & a_2 & a_2 & a_4 & a_5 & a_5 \\
 & & & & \text{Symmetric} & & & a_1 & a_2 & a_5 & a_3 & a_6 \\
 & & & & & & & & a_1 & a_5 & a_6 & a_3 \\
 & & & & & & & & & a_1 & a_2 & a_2 \\
 & & & & & & & & & & a_1 & a_2 \\
 & & & & & & & & & & & a_1
\end{array}\right]
\end{array}
\begin{array}{c} A2 \\ A3 \\ A6 \\ B2 \\ B4 \\ B5 \\ C1 \\ C3 \\ C5 \\ D1 \\ D4 \\ D6 \end{array}
\quad . \tag{A.1}
$$

In the matrix, a_1 corresponds to self hardening, a_2 to coplanar interaction, a_3 to Hirth locks, a_4 to collinear interaction, a_5 to glissile junctions and a_6 to Lomer locks. The matrix b^{su} has the same structure as a^{su} and is not presented here for the sake of brevity.

B

Method used for imposing constant stress triaxiality

A special truss element has been developed for imposing constant macroscopic Cauchy stress triaxiality under periodic boundary conditions at finite strains.

This element is aligned with the main loading direction, i.e., x_1-axis. It has only one degree of freedom $\{\widehat{F}_{11} - 1\}$ for the node at the far end of the element and nine degrees of freedom $\{\overline{\overline{F}}_{ij},\ i,j = 1,2,3\}$ for the node at the near end of the element. It is connected to the unit cell in such a way that the nine degrees of freedom $\{\overline{\overline{F}}_{ij},\ i,j = 1,2,3\}$ of the node at the near end correspond to the nine components of the macroscopic deformation gradient of the unit cell, i.e., $\overline{\overline{F}}_{ij} = \overline{F}_{ij},\ i,j = 1,2,3$. Consequently, $\overline{F}_{ij}$ will be used instead of $\overline{\overline{F}}_{ij}$ in the following development for the nine degrees of freedom of the node at the near end of the element.

The element acts as a spring in the main loading direction as follows

$$\widehat{S}_{11} = K(\widehat{F}_{11} - \overline{F}_{11}), \tag{B.1}$$

with $\widehat{S}_{11}$ the first component of the first Piola-Kirchhoff stress tensor and K the element stiffness.

With the macroscopic Cauchy stress $\overline{\underset{\sim}{\boldsymbol{\sigma}}}$ taking the form of Eq. (3.32), the stress triaxiality T imposed over the unit cell follows Eq. (3.34).

Using Eq. (3.30), the corresponding macroscopic first Piola-Kirchhoff stress tensor $\overline{\underset{\sim}{\boldsymbol{S}}}$ can be written as

$$\overline{\underset{\sim}{\boldsymbol{S}}} = \overline{J}\overline{\underset{\sim}{\boldsymbol{\sigma}}}.\overline{\underset{\sim}{\boldsymbol{F}}}^{-T} = \overline{J}\overline{\sigma}_{11}\underset{\sim}{\boldsymbol{\eta}}\overline{\underset{\sim}{\boldsymbol{F}}}^{-T}, \tag{B.2}$$

If $\underset{\sim}{\boldsymbol{\eta}}$ and $\underset{\sim}{\overline{\boldsymbol{F}}}$ are re-written in the matrix form, one has

$$[\overline{S}_{ij}] = \overline{\sigma}_{11} \begin{bmatrix} F_{22}\overline{F}_{33} - \overline{F}_{23}\overline{F}_{32} & \overline{F}_{23}\overline{F}_{31} - \overline{F}_{21}\overline{F}_{33} & \overline{F}_{21}\overline{F}_{32} - \overline{F}_{22}\overline{F}_{31} \\ \eta_2(\overline{F}_{13}\overline{F}_{32} - \overline{F}_{12}\overline{F}_{33}) & \eta_2(\overline{F}_{11}\overline{F}_{33} - \overline{F}_{13}\overline{F}_{31}) & \eta_2(\overline{F}_{31}\overline{F}_{12} - \overline{F}_{11}\overline{F}_{32}) \\ \eta_3(\overline{F}_{12}\overline{F}_{23} - \overline{F}_{13}\overline{F}_{22}) & \eta_3(\overline{F}_{13}\overline{F}_{21} - \overline{F}_{11}\overline{F}_{23}) & \eta_3(\overline{F}_{11}\overline{F}_{22} - \overline{F}_{12}\overline{F}_{21}) \end{bmatrix}. \tag{B.3}$$

Because of the connection between the unit cell and the truss element at the near end of the element, one can use the equations (B.1) and (B.3) and obtain

$$\widehat{S}_{11} = \overline{S}_{11}. \tag{B.4}$$

Thus, one can get

$$\overline{\sigma}_{11} = \frac{K(\widehat{F}_{11} - \overline{F}_{11})}{\overline{F}_{22}\overline{F}_{33} - \overline{F}_{23}\overline{F}_{32}}. \tag{B.5}$$

As a result, the macroscopic first Piola-Kirchhoff stress applied over the unit cell via the truss element is equal to

$$[\overline{S}_{ij}] = \frac{K(\widehat{F}_{11} - \overline{F}_{11})}{\overline{F}_{22}\overline{F}_{33} - \overline{F}_{23}\overline{F}_{32}} \begin{bmatrix} \overline{F}_{22}\overline{F}_{33} - \overline{F}_{23}\overline{F}_{32} & \overline{F}_{23}\overline{F}_{31} - \overline{F}_{21}\overline{F}_{33} & \overline{F}_{21}\overline{F}_{32} - \overline{F}_{22}\overline{F}_{31} \\ \eta_2(\overline{F}_{13}\overline{F}_{32} - \overline{F}_{12}\overline{F}_{33}) & \eta_2(\overline{F}_{11}\overline{F}_{33} - \overline{F}_{13}\overline{F}_{31}) & \eta_2(\overline{F}_{31}\overline{F}_{12} - \overline{F}_{11}\overline{F}_{32}) \\ \eta_3(\overline{F}_{12}\overline{F}_{23} - \overline{F}_{13}\overline{F}_{22}) & \eta_3(\overline{F}_{13}\overline{F}_{21} - \overline{F}_{11}\overline{F}_{23}) & \eta_3(\overline{F}_{11}\overline{F}_{22} - \overline{F}_{12}\overline{F}_{21}) \end{bmatrix}, \tag{B.6}$$

such that constant macroscopic Cauchy stress triaxiality T is imposed as Eq. (3.34).

Finally, the boundary value problem, considered in unit cell simulations with prescribed stress triaxiality and periodic boundary conditions, is to search the periodic fluctuation vector $\underline{\boldsymbol{v}}$ when imposing $\widehat{F}_{11}$ such that

- the balance of momentum:

$$\operatorname{div} \underset{\sim}{\boldsymbol{\sigma}} = \underline{\mathbf{0}}\,,\ \forall \underline{\boldsymbol{x}} \in \Omega^{tot} \tag{B.7}$$

- and the boundary conditions:
  - Periodicity:

$$\underline{\boldsymbol{u}} = \underset{\sim}{\overline{\boldsymbol{F}}}.\underline{\boldsymbol{x}} + \underline{\boldsymbol{v}}\,,\ \forall \underline{\boldsymbol{x}} \in \Omega^{tot} \tag{B.8}$$

  - Rotation restriction:

$$\overline{F}_{12} = \overline{F}_{21},\ \overline{F}_{23} = \overline{F}_{32},\ \overline{F}_{31} = \overline{F}_{13} \tag{B.9}$$

  - Rigid translation restriction

$$\underline{\boldsymbol{u}}\,(\underline{\boldsymbol{X}}_n) = \underline{\mathbf{0}}\,,\ \underline{\boldsymbol{X}}_n \text{ is the coordinates of a chosen node of the unit cell} \tag{B.10}$$

– Loading via the truss element

$$\overline{S}_{11} = K(\widehat{F}_{11} - \overline{F}_{11}) \tag{B.11}$$

– Constant macroscopic Cauchy stress triaxiality

$$\overline{\sigma}_{12} = \overline{\sigma}_{23} = \overline{\sigma}_{31} = 0 \text{ and } \overline{\sigma}_{22} = \eta_2 \overline{\sigma}_{11},\ \overline{\sigma}_{33} = \eta_3 \overline{\sigma}_{11} \tag{B.12}$$

are fulfilled.

C

Implicit integration of the constitutive equations

Input variables v_I :

$$v_I := \{\underset{\sim}{\boldsymbol{F}},\ \gamma_\chi,\ \underline{\boldsymbol{K}}\} \tag{C.1}$$

Output variables v_O:

$$v_O := \{\underset{\sim}{\boldsymbol{S}},\ S,\ \underline{\boldsymbol{M}}\} \tag{C.2}$$

Variables to integrated v_{int}:

$$v_{int} := \{\underset{\sim}{\boldsymbol{E}},\ \gamma^s,\ r^s,\ \gamma_{cum}\} \tag{C.3}$$

Equations to be integrated

$$\dot{\underset{\sim}{\boldsymbol{E}}} = \dot{\underset{\sim}{\boldsymbol{F}}}.\underset{\sim}{\boldsymbol{F}}^{-1}.\underset{\sim}{\boldsymbol{E}} - \underset{\sim}{\boldsymbol{E}}.\left(\sum_{s=1}^{12}\dot{\gamma}^s\underset{\sim}{\boldsymbol{N}}^s\right) \tag{C.4}$$

$$\dot{\gamma}^s = \Phi\left(|\tau^s| - (\tau_c^s - S)\right)\mathrm{sign}\left(\tau^s\right) = \left\langle\frac{|\tau^s| - (\tau_c^s - S)}{K}\right\rangle^n \mathrm{sign}\left(\tau^s\right) \tag{C.5}$$

$$\dot{r}_D^s = |\dot{\gamma}^s|\left(\frac{\sqrt{b^{su}r_D^u}}{\kappa} - G_c r_D^s\right) \tag{C.6}$$

$$\dot{\gamma}_{cum} = \sum_{s=1}^{12}|\dot{\gamma}^s| \tag{C.7}$$

with

$$\begin{aligned} \tau^s &= \underset{\sim}{\boldsymbol{M}} : \underset{\sim}{\boldsymbol{N}}^s && \text{(C.8)} \\ \underset{\sim}{\boldsymbol{M}} &= \underset{\sim}{\boldsymbol{C}}^e . \underset{\sim}{\boldsymbol{\Pi}}^e && \text{(C.9)} \\ \underset{\sim}{\boldsymbol{C}}^e &= \underset{\sim}{\boldsymbol{E}}^T . \underset{\sim}{\boldsymbol{E}} && \text{(C.10)} \\ \underset{\sim}{\boldsymbol{\Pi}}^e &= \underset{\approx}{\boldsymbol{\Lambda}} : \underset{\sim}{\boldsymbol{E}}^e_{GL} && \text{(C.11)} \\ \underset{\sim}{\boldsymbol{E}}^e_{GL} &= \frac{1}{2}\left(\underset{\sim}{\boldsymbol{C}}^e - 1\right) && \text{(C.12)} \\ & && \text{(C.13)} \end{aligned}$$

and

$$\tau_c^s = \tau_0 + \mu \sqrt{\sum_{s=1}^{12} a^{su} r_D^u} \qquad \text{(C.14)}$$

and

$$\begin{aligned} S &= H_\chi(\gamma_\chi - \gamma_{cum}) && \text{(C.15)} \\ \underline{\boldsymbol{M}} &= A\underline{\boldsymbol{K}} && \text{(C.16)} \end{aligned}$$

Residual equations R_{int}

$$\begin{aligned} R_{\underset{\sim}{\boldsymbol{E}}} &= \Delta\underset{\sim}{\boldsymbol{E}} - \Delta\underset{\sim}{\boldsymbol{F}} . \underset{\sim}{\boldsymbol{F}}^{-1} . \underset{\sim}{\boldsymbol{E}} + \underset{\sim}{\boldsymbol{E}} . \left(\sum_{s=1}^{12} \Delta\gamma^s \underset{\sim}{\boldsymbol{N}}^s \right) && \text{(C.17)} \\ R_{\gamma^s} &= \Delta\gamma^s - \Phi\left(|\tau^s| - (\tau_c^s - S)\right) \operatorname{sign}(\tau^s)\, \Delta t && \text{(C.18)} \\ R_{r_D^s} &= \Delta r_D^s - |\Delta\gamma^s| \left(\frac{\sqrt{b^{su} r_D^u}}{\kappa} - G_c r_D^s \right) && \text{(C.19)} \\ R_{\gamma_{cum}} &= \Delta\gamma_{cum} - \sum_{s=1}^{12} |\Delta\gamma^s| && \text{(C.20)} \end{aligned}$$

Jacobian matrix $\dfrac{\partial R_{int}}{\partial v_{int}}$

The Jacobian matrix is organized as follows

$$\begin{pmatrix} \dfrac{\partial R_{\underset{\sim}{\boldsymbol{E}}}}{\partial \Delta \underset{\sim}{\boldsymbol{E}}} & \dfrac{\partial R_{\underset{\sim}{\boldsymbol{E}}}}{\partial \Delta\gamma^p} & \dfrac{\partial R_{\underset{\sim}{\boldsymbol{E}}}}{\partial \Delta r_D^q} & \dfrac{\partial R_{\underset{\sim}{\boldsymbol{E}}}}{\partial \Delta\gamma_{cum}} \\ \dfrac{\partial R_{\gamma^s}}{\partial \Delta \underset{\sim}{\boldsymbol{E}}} & \dfrac{\partial R_{\gamma^s}}{\partial \Delta\gamma^p} & \dfrac{\partial R_{\gamma^s}}{\partial \Delta r_D^q} & \dfrac{\partial R_{\gamma^s}}{\partial \Delta\gamma_{cum}} \\ \dfrac{\partial R_{r_D^s}}{\partial \Delta \underset{\sim}{\boldsymbol{E}}} & \dfrac{\partial R_{r_D^s}}{\partial \Delta\gamma^p} & \dfrac{\partial R_{r_D^s}}{\partial \Delta r_D^q} & \dfrac{\partial R_{r_D^s}}{\partial \Delta\gamma_{cum}} \\ \dfrac{\partial R_{\gamma_{cum}}}{\partial \Delta \underset{\sim}{\boldsymbol{E}}} & \dfrac{\partial R_{\gamma_{cum}}}{\partial \Delta\gamma^p} & \dfrac{\partial R_{\gamma_{cum}}}{\partial \Delta r_D^q} & \dfrac{\partial R_{\gamma_{cum}}}{\partial \Delta\gamma_{cum}} \end{pmatrix} \qquad \text{(C.21)}$$

- Derivatives of $R_{\underset{\sim}{\boldsymbol{E}}}$

$$R_{\underset{\sim}{\boldsymbol{E}}} = \Delta\underset{\sim}{\boldsymbol{E}} - \Delta\underset{\sim}{\boldsymbol{F}}.\underset{\sim}{\boldsymbol{F}}^{-1}.\underset{\sim}{\boldsymbol{E}} + \underset{\sim}{\boldsymbol{E}}.\left(\sum_{s=1}^{12}\Delta\gamma^s\underset{\sim}{\boldsymbol{N}}^s\right) \tag{C.22}$$

✓ $\dfrac{\partial R_{\underset{\sim}{\boldsymbol{E}}}}{\partial\Delta\underset{\sim}{\boldsymbol{E}}}$

$$\frac{\partial R_{\underset{\sim}{\boldsymbol{E}}}}{\partial\Delta\underset{\sim}{\boldsymbol{E}}} = \underset{\approx}{\mathbf{1}} - (\Delta\underset{\sim}{\boldsymbol{F}}.\underset{\sim}{\boldsymbol{F}}^{-1})\underline{\otimes}\underset{\approx}{\mathbf{1}} + \underset{\approx}{\mathbf{1}}\underline{\otimes}(\sum_{s=1}^{12}\Delta\gamma^s\underset{\sim}{\boldsymbol{N}}^s)^T \tag{C.23}$$

✓ $\dfrac{\partial R_{\underset{\sim}{\boldsymbol{E}}}}{\partial\Delta\gamma^p}$

$$\frac{\partial R_{\underset{\sim}{\boldsymbol{E}}}}{\partial\Delta\gamma^p} = \underset{\sim}{\boldsymbol{E}}.\underset{\sim}{\boldsymbol{N}}^p \tag{C.24}$$

✓ $\dfrac{\partial R_{\underset{\sim}{\boldsymbol{E}}}}{\partial\Delta r_D^q}$

$$\frac{\partial R_{\underset{\sim}{\boldsymbol{E}}}}{\partial\Delta r_D^q} = 0 \tag{C.25}$$

✓ $\dfrac{\partial R_{\underset{\sim}{\boldsymbol{E}}}}{\partial\Delta\gamma_{cum}}$

$$\frac{\partial R_{\underset{\sim}{\boldsymbol{E}}}}{\partial\Delta\gamma_{cum}} = 0 \tag{C.26}$$

- Derivatives of R_{γ^s}

$$R_{\gamma^s} = \Delta\gamma^s - \Phi\left(|\tau^s| - (\tau_c^s - S)\right)\mathrm{sign}\left(\tau^s\right)\Delta t \tag{C.27}$$

✓ $\dfrac{\partial R_{\gamma^s}}{\partial\Delta\underset{\sim}{\boldsymbol{E}}}$

$$\frac{\partial R_{\gamma^s}}{\partial\Delta\underset{\sim}{\boldsymbol{E}}} = -\frac{\partial\Phi}{\partial\tau^s}\frac{\partial\tau^s}{\partial\underset{\sim}{\boldsymbol{M}}} : \frac{\partial\underset{\sim}{\boldsymbol{M}}}{\partial\underset{\sim}{\boldsymbol{C}}^e} : \frac{\partial\underset{\sim}{\boldsymbol{C}}^e}{\partial\underset{\sim}{\boldsymbol{E}}} : \frac{\partial\underset{\sim}{\boldsymbol{E}}}{\partial\Delta\underset{\sim}{\boldsymbol{E}}}\mathrm{sign}\left(\tau^s\right)\Delta t \tag{C.28}$$

with

$$\frac{\partial\Phi}{\partial\tau^s} = \frac{\partial\Phi}{\partial|\tau^s|}\frac{\partial|\tau^s|}{\partial\tau^s} = \frac{n}{K}\left\langle\frac{|\tau^s| - (\tau_c^s - S)}{K}\right\rangle^{n-1}\mathrm{sign}\left(\tau^s\right) = \Phi'\mathrm{sign}\left(\tau^s\right) \tag{C.29}$$

$$\frac{\partial\tau^s}{\partial\underset{\sim}{\boldsymbol{M}}} = \underset{\sim}{\boldsymbol{N}}^s \tag{C.30}$$

$$\frac{\partial\underset{\sim}{\boldsymbol{M}}}{\partial\underset{\sim}{\boldsymbol{C}}^e} = \frac{\partial\left[\underset{\sim}{\boldsymbol{C}}^e.\left(\underset{\approx}{\boldsymbol{\Lambda}} : \frac{1}{2}(\underset{\sim}{\boldsymbol{C}}^e - 1)\right)\right]}{\partial\underset{\sim}{\boldsymbol{C}}^e} = (\underset{\sim}{\mathbf{1}}\underline{\otimes}\underset{\sim}{\boldsymbol{\Pi}}^{eT}) + \frac{1}{2}(\underset{\sim}{\boldsymbol{C}}^e\underline{\otimes}\underset{\sim}{\mathbf{1}}) : \underset{\approx}{\boldsymbol{\Lambda}} \tag{C.31}$$

$$\frac{\partial\underset{\sim}{\boldsymbol{C}}^e}{\partial\underset{\sim}{\boldsymbol{E}}} = \underset{\sim}{\mathbf{1}}\overline{\otimes}\underset{\sim}{\boldsymbol{E}}^T + \underset{\sim}{\boldsymbol{E}}^T\underline{\otimes}\underset{\sim}{\mathbf{1}} \tag{C.32}$$

$$\frac{\partial\underset{\sim}{\boldsymbol{E}}}{\partial\Delta\underset{\sim}{\boldsymbol{E}}} = \underset{\approx}{\mathbf{1}} \tag{C.33}$$

Finally,

$$\boxed{\frac{\partial R_{\gamma^s}}{\partial \Delta \underset{\sim}{\boldsymbol{E}}} = -\Delta t \Phi' \underset{\sim}{\boldsymbol{N}}^s : \left[(\underset{\sim}{\mathbf{1}} \underline{\otimes} \underset{\sim}{\boldsymbol{\Pi}}^e) + \frac{1}{2} (\underset{\sim}{\boldsymbol{C}}^e \underline{\otimes} \underset{\sim}{\mathbf{1}}) : \underset{\approx}{\boldsymbol{\Lambda}} \right] : (\underset{\sim}{\mathbf{1}} \overline{\otimes} \underset{\sim}{\boldsymbol{E}}^T + \underset{\sim}{\boldsymbol{E}}^T \underline{\otimes} \underset{\sim}{\mathbf{1}})} \tag{C.34}$$

with

$$\Phi' = \frac{n}{K} \left\langle \frac{|\tau^s| - (\tau_c^s - S)}{K} \right\rangle^{n-1} \tag{C.35}$$

✓ $\dfrac{\partial R_{\gamma^s}}{\partial \Delta \gamma^p}$

$$\boxed{\frac{\partial R_{\gamma^s}}{\partial \Delta \gamma^p} = \delta_{sp}} \tag{C.36}$$

✓ $\dfrac{\partial R_{\gamma^s}}{\partial \Delta r_D^q}$

$$\frac{\partial R_{\gamma^s}}{\partial \Delta r_D^q} = -\frac{\partial \Phi}{\partial \tau_c^s} \frac{\partial \tau_c^s}{\partial r_D^q} \frac{\partial r_D^q}{\partial \Delta r_D^q} \text{sign}\,(\tau^s)\, \Delta t \tag{C.37}$$

with

$$\frac{\partial \Phi}{\partial \tau_c^s} = = -\Phi' = -\frac{n}{K} \left\langle \frac{|\tau^s| - (\tau_c^s - S)}{K} \right\rangle^{n-1} \tag{C.38}$$

$$\frac{\partial \tau_c^s}{\partial r_D^q} = \frac{1}{2} \mu \left(\sum_{u=1}^{12} a^{su} r_D^u \right)^{-\frac{1}{2}} a^{sq} \tag{C.39}$$

$$\frac{\partial r_D^q}{\partial \Delta r_D^q} = 1 \tag{C.40}$$

Finally

$$\boxed{\frac{\partial R_{\gamma^s}}{\partial \Delta r_D^q} = \frac{1}{2} \text{sign}\,(\tau^s)\, \Delta t \Phi' \mu a^{sq} \left(\sum_{u=1}^{12} a^{su} r_D^u \right)^{-\frac{1}{2}}} \tag{C.41}$$

✓ $\dfrac{\partial R_{\gamma^s}}{\partial \Delta \gamma_{cum}}$

$$\frac{\partial R_{\gamma^s}}{\partial \Delta \gamma_{cum}} = -\frac{\partial \Phi}{\partial S} \frac{\partial S}{\partial \gamma_{cum}} \frac{\partial \gamma_{cum}}{\partial \Delta \gamma_{cum}} \text{sign}\,(\tau^s)\, \Delta t \tag{C.42}$$

with

$$\frac{\partial \Phi}{\partial S} = \Phi' = \frac{n}{K} \left\langle \frac{|\tau^s| - (\tau_c^s - S)}{K} \right\rangle^{n-1} \tag{C.43}$$

$$\frac{\partial S}{\partial \gamma_{cum}} = -H_\chi \tag{C.44}$$

$$\frac{\partial \gamma_{cum}}{\partial \Delta \gamma_{cum}} = 1 \tag{C.45}$$

Finally

$$\boxed{\frac{\partial R_{\gamma^s}}{\partial \Delta\gamma_{cum}} = \text{sign}\left(\tau^s\right) \Delta t H_\chi \Phi'} \tag{C.46}$$

- Derivatives of $R_{r_D^s}$

$$R_{r_D^s} = \Delta r_D^s - |\Delta\gamma^s| \left(\frac{\sqrt{b^{su} r_D^u}}{\kappa} - G_c r_D^s \right) \tag{C.47}$$

✓ $\dfrac{\partial R_{r_D^s}}{\partial \Delta \underset{\sim}{\boldsymbol{E}}}$

$$\frac{\partial R_{r_D^s}}{\partial \Delta \underset{\sim}{\boldsymbol{E}}} = 0 \tag{C.48}$$

✓ $\dfrac{\partial R_{r_D^s}}{\partial \Delta\gamma^p}$

$$\frac{\partial R_{r_D^s}}{\partial \Delta\gamma^p} = -\text{sign}\left(\Delta\gamma^s\right) \delta_{sp} \left(\frac{\sqrt{b^{su} r_D^u}}{\kappa} - G_c r_D^s \right) \tag{C.49}$$

✓ $\dfrac{\partial R_{r_D^s}}{\partial \Delta r_D^q}$

$$\frac{\partial R_{r_D^s}}{\partial \Delta r_D^q} = \delta_{sq} - |\Delta\gamma^s| \left(\frac{1}{2} \frac{\left(\sqrt{b^{su} r_D^u}\right)^{-\frac{1}{2}} b^{sq}}{\kappa} - G_c \delta_{sq} \right) \tag{C.50}$$

✓ $\dfrac{\partial R_{r_D^s}}{\partial \Delta\gamma_{cum}}$

$$\frac{\partial R_{r_D^s}}{\partial \Delta\gamma_{cum}} = 0 \tag{C.51}$$

- Derivatives of $R_{\gamma_{cum}}$

$$R_{\gamma_{cum}} = \Delta\gamma_{cum} - \sum_{s=1}^{12} |\Delta\gamma^s| \tag{C.52}$$

✓ $\dfrac{\partial R_{\gamma_{cum}}}{\partial \Delta \underset{\sim}{\boldsymbol{E}}}$

$$\frac{\partial R_{\gamma_{cum}}}{\partial \Delta \underset{\sim}{\boldsymbol{E}}} = 0 \tag{C.53}$$

✓ $\dfrac{\partial R_{\gamma_{cum}}}{\partial \Delta\gamma^p}$

$$\frac{\partial R_{\gamma_{cum}}}{\partial \Delta\gamma^p} = -\text{sign}\left(\Delta\gamma^p\right) \tag{C.54}$$

✓ $\dfrac{\partial R_{\gamma_{cum}}}{\partial \Delta r_D^q}$

$$\frac{\partial R_{\gamma_{cum}}}{\partial \Delta r_D^q} = 0 \tag{C.55}$$

✓ $\dfrac{\partial R_{\gamma_{cum}}}{\partial \Delta\gamma_{cum}}$

$$\frac{\partial R_{\gamma_{cum}}}{\partial \Delta\gamma_{cum}} = 1 \tag{C.56}$$

D

Details on the consistent tangent matrix

The matrix $\dfrac{\partial \Delta v_O}{\partial \Delta v_I}$ is written as

$$\frac{\partial \Delta v_O}{\partial \Delta v_I} = \begin{pmatrix} \frac{\partial \Delta \underset{\sim}{\boldsymbol{S}}}{\partial \Delta \underset{\sim}{\boldsymbol{F}}} & \frac{\partial \Delta \underset{\sim}{\boldsymbol{S}}}{\partial \Delta \gamma_\chi} & \frac{\partial \Delta \underset{\sim}{\boldsymbol{S}}}{\partial \Delta \underline{\underline{\boldsymbol{K}}}} \\ \frac{\partial \Delta \widetilde{S}}{\partial \Delta \underset{\sim}{\boldsymbol{F}}} & \frac{\partial \Delta S}{\partial \Delta \gamma_\chi} & \frac{\partial \Delta S}{\partial \Delta \underline{\underline{\boldsymbol{K}}}} \\ \frac{\partial \Delta \underline{\underline{\boldsymbol{M}}}}{\partial \Delta \underset{\sim}{\boldsymbol{F}}} & \frac{\partial \Delta \underline{\underline{\boldsymbol{M}}}}{\partial \Delta \gamma_\chi} & \frac{\partial \Delta \underline{\underline{\boldsymbol{M}}}}{\partial \Delta \underline{\underline{\boldsymbol{K}}}} \end{pmatrix} \tag{D.1}$$

The matrix $\dfrac{\partial R}{\partial \Delta v_I}$ is organized as

$$\frac{\partial R}{\partial \Delta v_I} = \begin{pmatrix} \frac{\partial R_{\underset{\sim}{\boldsymbol{E}}}}{\partial \Delta \underset{\sim}{\boldsymbol{F}}} & \frac{\partial R_{\underset{\sim}{\boldsymbol{E}}}}{\partial \Delta \gamma_\chi} & \frac{\partial R_{\underset{\sim}{\boldsymbol{E}}}}{\partial \Delta \underline{\underline{\boldsymbol{K}}}} \\ \frac{\partial R_{\gamma^s}}{\partial \Delta \underset{\sim}{\boldsymbol{F}}} & \frac{\partial R_{\gamma^s}}{\partial \Delta \gamma_\chi} & \frac{\partial R_{\gamma^s}}{\partial \Delta \underline{\underline{\boldsymbol{K}}}} \\ \frac{\partial R_{r^s}}{\partial \Delta \underset{\sim}{\boldsymbol{F}}} & \frac{\partial R_{r^s}}{\partial \Delta \gamma_\chi} & \frac{\partial R_{r^s}}{\partial \Delta \underline{\underline{\boldsymbol{K}}}} \\ \frac{\partial R_{\gamma_{cum}}}{\partial \Delta \underset{\sim}{\boldsymbol{F}}} & \frac{\partial R_{\gamma_{cum}}}{\partial \Delta \gamma_\chi} & \frac{\partial R_{\gamma_{cum}}}{\partial \Delta \underline{\underline{\boldsymbol{K}}}} \end{pmatrix} \tag{D.2}$$

Each block of the matrix $\dfrac{\partial R}{\partial \Delta v_I}$ is calculated respectively in the following.

- Derivatives of $R_{\underset{\sim}{\boldsymbol{E}}}$

$$R_{\underset{\sim}{\boldsymbol{E}}} = \Delta \underset{\sim}{\boldsymbol{E}} - \Delta \underset{\sim}{\boldsymbol{F}} . \underset{\sim}{\boldsymbol{F}}^{-1} . \underset{\sim}{\boldsymbol{E}} + \underset{\sim}{\boldsymbol{E}} . \left(\sum_{s=1}^{12} \Delta \gamma^s \underset{\sim}{\boldsymbol{N}}^s \right) \tag{D.3}$$

✓ $\dfrac{\partial R_{\underset{\sim}{\boldsymbol{E}}}}{\partial \Delta \underset{\sim}{\boldsymbol{F}}}$

$$\frac{\partial R_{\underset{\sim}{\boldsymbol{E}}}}{\partial \Delta \underset{\sim}{\boldsymbol{F}}} = -\frac{\partial (\Delta \underset{\sim}{\boldsymbol{F}}.\underset{\sim}{\boldsymbol{F}}^{-1}.\underset{\sim}{\boldsymbol{E}})}{\partial \Delta \underset{\sim}{\boldsymbol{F}}} \tag{D.4}$$

$$= -\underset{\sim}{\mathbf{1}} \underline{\otimes} \left(\underset{\sim}{\boldsymbol{F}}^{-1}.\underset{\sim}{\boldsymbol{E}}\right)^T - (\Delta \underset{\sim}{\boldsymbol{F}} \underline{\otimes} \underset{\sim}{\boldsymbol{E}}^T) : \frac{\partial \underset{\sim}{\boldsymbol{F}}^{-1}}{\partial \underset{\sim}{\boldsymbol{F}}} : \frac{\partial \underset{\sim}{\boldsymbol{F}}}{\partial \Delta \underset{\sim}{\boldsymbol{F}}} \tag{D.5}$$

$$= -\underset{\sim}{\mathbf{1}} \underline{\otimes} \left(\underset{\sim}{\boldsymbol{E}}^T.\underset{\sim}{\boldsymbol{F}}^{-T}\right)^T - (\Delta \underset{\sim}{\boldsymbol{F}} \underline{\otimes} \underset{\sim}{\boldsymbol{E}}^T) : (-\underset{\sim}{\boldsymbol{F}}^{-1} \underline{\otimes} \underset{\sim}{\boldsymbol{F}}^{-T}) : \underset{\approx}{\mathbf{1}} \tag{D.6}$$

$$= -\underset{\sim}{\mathbf{1}} \underline{\otimes} \left(\underset{\sim}{\boldsymbol{E}}^T.\underset{\sim}{\boldsymbol{F}}^{-T}\right) + (\Delta \underset{\sim}{\boldsymbol{F}} \underline{\otimes} \underset{\sim}{\boldsymbol{E}}^T) : (\underset{\sim}{\boldsymbol{F}}^{-1} \underline{\otimes} \underset{\sim}{\boldsymbol{F}}^{-T}) \tag{D.7}$$

Finally,

$$\boxed{\frac{\partial R_{\underset{\sim}{\boldsymbol{E}}}}{\partial \Delta \underset{\sim}{\boldsymbol{F}}} = -\underset{\sim}{\mathbf{1}} \underline{\otimes} \left(\underset{\sim}{\boldsymbol{E}}^T.\underset{\sim}{\boldsymbol{F}}^{-T}\right) + (\Delta \underset{\sim}{\boldsymbol{F}} \underline{\otimes} \underset{\sim}{\boldsymbol{E}}^T) : (\underset{\sim}{\boldsymbol{F}}^{-1} \underline{\otimes} \underset{\sim}{\boldsymbol{F}}^{-T})} \tag{D.8}$$

✓ $\dfrac{\partial R_{\underset{\sim}{\boldsymbol{E}}}}{\partial \Delta \gamma_\chi}$

$$\boxed{\frac{\partial R_{\underset{\sim}{\boldsymbol{E}}}}{\partial \Delta \gamma_\chi} = 0} \tag{D.9}$$

✓ $\dfrac{\partial R_{\underset{\sim}{\boldsymbol{E}}}}{\partial \Delta \underline{\boldsymbol{K}}}$

$$\boxed{\frac{\partial R_{\underset{\sim}{\boldsymbol{E}}}}{\partial \Delta \underline{\boldsymbol{K}}} = 0} \tag{D.10}$$

- Derivatives of R_{γ^s}

$$\underline{R_{\gamma^s} = \Delta\gamma^s - \Phi\left(|\tau^s| - (\tau_c^s - S)\right) \operatorname{sign}(\tau^s)\, \Delta t} \tag{D.11}$$

✓ $\dfrac{\partial R_{\gamma^s}}{\partial \Delta \underset{\sim}{\boldsymbol{F}}}$

$$\boxed{\frac{\partial R_{\gamma^s}}{\partial \Delta \underset{\sim}{\boldsymbol{F}}} = 0} \tag{D.12}$$

✓ $\dfrac{\partial R_{\gamma^s}}{\partial \Delta \gamma_\chi}$

$$\frac{\partial R_{\gamma^s}}{\partial \Delta \gamma_\chi} = -\frac{\partial \Phi}{\partial S}\frac{\partial S}{\partial \gamma_\chi}\frac{\partial \gamma_\chi}{\partial \Delta \gamma_\chi} \operatorname{sign}(\tau^s)\, \Delta t \tag{D.13}$$

$$= -\Phi' H_\chi \operatorname{sign}(\tau^s)\, \Delta t \tag{D.14}$$

Finally,

$$\boxed{\frac{\partial R_{\gamma^s}}{\partial \Delta \gamma_\chi} = -\Phi' H_\chi \operatorname{sign}(\tau^s)\, \Delta t} \tag{D.15}$$

✓ $\dfrac{\partial R_{\gamma^s}}{\partial \Delta \underline{\underline{\boldsymbol{K}}}}$

$$\boxed{\frac{\partial R_{\gamma^s}}{\partial \Delta \underline{\underline{\boldsymbol{K}}}} = 0} \tag{D.16}$$

- Derivatives of $R_{r_D^s}$

$$R_{r_D^s} = \Delta r_D^s - |\Delta \gamma^s| \left(\frac{\sqrt{b^{su} r_D^u}}{\kappa} - G_c r_D^s \right) \tag{D.17}$$

✓ $\dfrac{\partial R_{r^s}}{\partial \Delta \underset{\sim}{\boldsymbol{F}}}$

$$\boxed{\frac{\partial R_{r^s}}{\partial \Delta \underset{\sim}{\boldsymbol{F}}} = 0} \tag{D.18}$$

✓ $\dfrac{\partial R_{r^s}}{\partial \Delta \gamma_\chi}$

$$\boxed{\frac{\partial R_{r^s}}{\partial \Delta \gamma_\chi} = 0} \tag{D.19}$$

✓ $\dfrac{\partial R_{r^s}}{\partial \Delta \underline{\underline{\boldsymbol{K}}}}$

$$\boxed{\frac{\partial R_{r^s}}{\partial \Delta \underline{\underline{\boldsymbol{K}}}} = 0} \tag{D.20}$$

- Derivatives of $R_{\gamma_{cum}}$

$$R_{\gamma_{cum}} = \Delta \gamma_{cum} - \sum_{s=1}^{12} |\Delta \gamma^s| \tag{D.21}$$

✓ $\dfrac{\partial R_{\gamma_{cum}}}{\partial \Delta \underset{\sim}{\boldsymbol{F}}}$

$$\boxed{\frac{\partial R_{\gamma_{cum}}}{\partial \Delta \underset{\sim}{\boldsymbol{F}}} = 0} \tag{D.22}$$

✓ $\dfrac{\partial R_{\gamma_{cum}}}{\partial \Delta \gamma_\chi}$

$$\boxed{\frac{\partial R_{\gamma_{cum}}}{\partial \Delta \gamma_\chi} = 0} \tag{D.23}$$

✓ $\dfrac{\partial R_{\gamma_{cum}}}{\partial \Delta \underline{\underline{\boldsymbol{K}}}}$

$$\boxed{\frac{\partial R_{\gamma_{cum}}}{\partial \Delta \underline{\underline{\boldsymbol{K}}}} = 0} \tag{D.24}$$

The matrix $\dfrac{\partial v_O}{\partial v_I}$ is organized as

$$\frac{\partial v_O}{\partial v_I} = \begin{pmatrix} \dfrac{\partial \underset{\sim}{\boldsymbol{S}}}{\partial \underset{\sim}{\boldsymbol{F}}} & \dfrac{\partial \underset{\sim}{\boldsymbol{S}}}{\partial \gamma_\chi} & \dfrac{\partial \underset{\sim}{\boldsymbol{S}}}{\partial \underline{\underline{\boldsymbol{K}}}} \\ \dfrac{\partial S}{\partial \underset{\sim}{\boldsymbol{F}}} & \dfrac{\partial S}{\partial \gamma_\chi} & \dfrac{\partial S}{\partial \underline{\underline{\boldsymbol{K}}}} \\ \dfrac{\partial \underline{\underline{\boldsymbol{M}}}}{\partial \underset{\sim}{\boldsymbol{F}}} & \dfrac{\partial \underline{\underline{\boldsymbol{M}}}}{\partial \gamma_\chi} & \dfrac{\partial \underline{\underline{\boldsymbol{M}}}}{\partial \underline{\underline{\boldsymbol{K}}}} \end{pmatrix} \tag{D.25}$$

The blocks are calculated in the following

- Derivatives of $\underset{\sim}{\boldsymbol{S}}$

$$\underline{\underset{\sim}{\boldsymbol{S}} = \frac{J}{J_e} \underset{\sim}{\boldsymbol{E}}. \left(\frac{\underset{\approx}{\boldsymbol{\Lambda}}}{2} (\underset{\sim}{\boldsymbol{E}}^T . \underset{\sim}{\boldsymbol{E}} - \underset{\sim}{\boldsymbol{1}}) \right) . \underset{\sim}{\boldsymbol{E}}^T . \underset{\sim}{\boldsymbol{F}}^{-T}} \tag{D.26}$$

✓ $\dfrac{\partial \underset{\sim}{\boldsymbol{S}}}{\partial \underset{\sim}{\boldsymbol{F}}}$

$$\begin{aligned} \frac{\partial \underset{\sim}{\boldsymbol{S}}}{\partial \underset{\sim}{\boldsymbol{F}}} &= (\underset{\sim}{\boldsymbol{\sigma}} . \underset{\sim}{\boldsymbol{F}}^{-T}) \otimes \frac{\partial J}{\partial \underset{\sim}{\boldsymbol{F}}} + J \frac{\partial \underset{\sim}{\boldsymbol{\sigma}} . \underset{\sim}{\boldsymbol{F}}^{-T}}{\partial \underset{\sim}{\boldsymbol{F}}^{-T}} : \frac{\partial \underset{\sim}{\boldsymbol{F}}^{-T}}{\partial \underset{\sim}{\boldsymbol{F}}} && \text{(D.27)} \\ &= J(\underset{\sim}{\boldsymbol{\sigma}} . \underset{\sim}{\boldsymbol{F}}^{-T}) \otimes \underset{\sim}{\boldsymbol{F}}^{-T} + J(\underset{\sim}{\boldsymbol{\sigma}} \underline{\otimes} \underset{\sim}{\boldsymbol{1}}) : (-\underset{\sim}{\boldsymbol{F}}^{-T} \overline{\otimes} \underset{\sim}{\boldsymbol{F}}^{-1}) && \text{(D.28)} \end{aligned}$$

Finally,

$$\boxed{\frac{\partial \underset{\sim}{\boldsymbol{S}}}{\partial \underset{\sim}{\boldsymbol{F}}} = J(\underset{\sim}{\boldsymbol{\sigma}} . \underset{\sim}{\boldsymbol{F}}^{-T}) \otimes \underset{\sim}{\boldsymbol{F}}^{-T} + J(\underset{\sim}{\boldsymbol{\sigma}} \underline{\otimes} \underset{\sim}{\boldsymbol{1}}) : (-\underset{\sim}{\boldsymbol{F}}^{-T} \overline{\otimes} \underset{\sim}{\boldsymbol{F}}^{-1})} \tag{D.29}$$

✓ $\dfrac{\partial \underset{\sim}{\boldsymbol{S}}}{\partial \gamma_\chi}$

$$\boxed{\frac{\partial \underset{\sim}{\boldsymbol{S}}}{\partial \gamma_\chi} = 0} \tag{D.30}$$

✓ $\dfrac{\partial \underset{\sim}{\boldsymbol{S}}}{\partial \underline{\underline{\boldsymbol{K}}}}$

$$\boxed{\frac{\partial \underset{\sim}{\boldsymbol{S}}}{\partial \underline{\underline{\boldsymbol{K}}}} = 0} \tag{D.31}$$

- Derivatives of S

$$\underline{S = H_\chi (\gamma_\chi - \gamma_{cum})} \tag{D.32}$$

✓ $\dfrac{\partial S}{\partial \underset{\sim}{\boldsymbol{F}}}$

$$\boxed{\frac{\partial S}{\partial \underset{\sim}{\boldsymbol{F}}} = 0} \tag{D.33}$$

✓ $\dfrac{\partial S}{\partial \gamma_\chi}$

$$\boxed{\frac{\partial S}{\partial \gamma_\chi} = H_\chi} \tag{D.34}$$

✓ $\dfrac{\partial S}{\partial \underline{\underline{\boldsymbol{K}}}}$

$$\boxed{\frac{\partial S}{\partial \underline{\underline{\boldsymbol{K}}}} = 0} \tag{D.35}$$

- Derivatives of $\underline{\underline{\boldsymbol{M}}}$

$$\underline{\underline{\boldsymbol{M}}} = A\underline{\underline{\boldsymbol{K}}} \tag{D.36}$$

✓ $\dfrac{\partial \underline{\underline{\boldsymbol{M}}}}{\partial \underset{\sim}{\boldsymbol{F}}}$

$$\boxed{\frac{\partial \underline{\underline{\boldsymbol{M}}}}{\partial \underset{\sim}{\boldsymbol{F}}} = 0} \tag{D.37}$$

✓ $\dfrac{\partial \underline{\underline{\boldsymbol{M}}}}{\partial \gamma_\chi}$

$$\boxed{\frac{\partial \underline{\underline{\boldsymbol{M}}}}{\partial \gamma_\chi} = 0} \tag{D.38}$$

✓ $\dfrac{\partial \underline{\underline{\boldsymbol{M}}}}{\partial \underline{\underline{\boldsymbol{K}}}}$

$$\boxed{\frac{\partial \underline{\underline{\boldsymbol{M}}}}{\partial \underline{\underline{\boldsymbol{K}}}} = A} \tag{D.39}$$

The matrix $\dfrac{\partial v_O}{\partial v_{int}}$ is organized as

$$\frac{\partial v_O}{\partial v_{int}} = \begin{pmatrix} \dfrac{\partial \underset{\sim}{\boldsymbol{S}}}{\partial \underset{\sim}{\boldsymbol{E}}} & \dfrac{\partial \underset{\sim}{\boldsymbol{S}}}{\partial \gamma^s} & \dfrac{\partial \underset{\sim}{\boldsymbol{S}}}{\partial r^s} & \dfrac{\partial \underset{\sim}{\boldsymbol{S}}}{\partial \gamma_{cum}} \\ \dfrac{\partial \widetilde{S}}{\partial \underset{\sim}{\boldsymbol{E}}} & \dfrac{\partial S}{\partial \gamma^s} & \dfrac{\partial S}{\partial r^s} & \dfrac{\partial S}{\partial \gamma_{cum}} \\ \dfrac{\partial \underline{\underline{\widetilde{\boldsymbol{M}}}}}{\partial \underset{\sim}{\boldsymbol{E}}} & \dfrac{\partial \underline{\underline{\boldsymbol{M}}}}{\partial \gamma^s} & \dfrac{\partial \underline{\underline{\boldsymbol{M}}}}{\partial r^s} & \dfrac{\partial \underline{\underline{\boldsymbol{M}}}}{\partial \gamma_{cum}} \end{pmatrix} \tag{D.40}$$

The blocks are calculated in the following.

- Derivatives of $\underset{\sim}{\boldsymbol{S}}$

$$\underset{\sim}{\boldsymbol{S}} = J\underset{\sim}{\boldsymbol{\sigma}}.\underset{\sim}{\boldsymbol{F}}^{-T} = \frac{J}{J_e}\underset{\sim}{\boldsymbol{E}}.\left(\frac{\underset{\approx}{\boldsymbol{\Lambda}}}{2}(\underset{\sim}{\boldsymbol{E}}^T.\underset{\sim}{\boldsymbol{E}} - \underset{\sim}{\mathbf{1}})\right).\underset{\sim}{\boldsymbol{E}}^T.\underset{\sim}{\boldsymbol{F}}^{-T} \tag{D.41}$$

✓ $\dfrac{\partial \underset{\sim}{\boldsymbol{S}}}{\partial \underset{\sim}{\boldsymbol{E}}}$

$$\frac{\partial \underset{\sim}{\boldsymbol{S}}}{\partial \underset{\sim}{\boldsymbol{E}}} = \frac{\partial \underset{\sim}{\boldsymbol{S}}}{\partial \underset{\sim}{\boldsymbol{\sigma}}} : \frac{\partial \underset{\sim}{\boldsymbol{\sigma}}}{\partial \underset{\sim}{\boldsymbol{E}}} \tag{D.42}$$

$$\frac{\partial \underset{\sim}{\boldsymbol{S}}}{\partial \underset{\sim}{\boldsymbol{\sigma}}} = J \underset{\sim}{\mathbf{1}} \underline{\otimes} \underset{\sim}{\boldsymbol{F}}^{-1} \tag{D.43}$$

$$\begin{aligned} \frac{\partial \underset{\sim}{\boldsymbol{\sigma}}}{\partial \underset{\sim}{\boldsymbol{E}}} = & -\frac{1}{J_e}(\underset{\sim}{\boldsymbol{E}}.\underset{\sim}{\boldsymbol{\Pi}}^e.\underset{\sim}{\boldsymbol{E}}^T) \otimes \underset{\sim}{\boldsymbol{E}}^{-T} + \frac{1}{J_e}\underset{\sim}{\mathbf{1}} \underline{\otimes} (\underset{\sim}{\boldsymbol{\Pi}}^e.\underset{\sim}{\boldsymbol{E}}^T)^T \\ & + \frac{1}{J_e}(\underset{\sim}{\boldsymbol{E}} \underline{\otimes} \underset{\sim}{\boldsymbol{E}}) : \frac{\partial \underset{\sim}{\boldsymbol{\Pi}}^e}{\partial \underset{\sim}{\boldsymbol{E}}} + \frac{1}{J_e}\left[(\underset{\sim}{\boldsymbol{E}}.\underset{\sim}{\boldsymbol{\Pi}}^e) \underline{\otimes} \underset{\sim}{\mathbf{1}}\right] : (\underset{\sim}{\mathbf{1}} \overline{\otimes} \underset{\sim}{\mathbf{1}}) \end{aligned} \tag{D.44}$$

$$\frac{\partial \underset{\sim}{\boldsymbol{\Pi}}^e}{\partial \underset{\sim}{\boldsymbol{E}}} = \frac{\partial \underset{\sim}{\boldsymbol{\Pi}}^e}{\partial \underset{\sim}{\boldsymbol{E}}^e_G L} : \frac{\partial \underset{\sim}{\boldsymbol{E}}^e_G L}{\partial \underset{\sim}{\boldsymbol{E}}} \tag{D.45}$$

$$\frac{\partial \underset{\sim}{\boldsymbol{\Pi}}^e}{\partial \underset{\sim}{\boldsymbol{E}}^e_G L} = \underset{\approx}{\boldsymbol{\Lambda}} \tag{D.46}$$

$$\frac{\partial \underset{\sim}{\boldsymbol{E}}^e_G L}{\partial \underset{\sim}{\boldsymbol{E}}} = \frac{1}{2}(\underset{\sim}{\mathbf{1}} \overline{\otimes} \underset{\sim}{\boldsymbol{E}}^T + \underset{\sim}{\boldsymbol{E}}^T \underline{\otimes} \underset{\sim}{\mathbf{1}}) \tag{D.47}$$

✓ $\dfrac{\partial \underset{\sim}{\boldsymbol{S}}}{\partial \gamma^s}$

$$\boxed{\frac{\partial \underset{\sim}{\boldsymbol{S}}}{\partial \gamma^s} = 0} \tag{D.48}$$

✓ $\dfrac{\partial \underset{\sim}{\boldsymbol{S}}}{\partial r^s}$

$$\boxed{\frac{\partial \underset{\sim}{\boldsymbol{S}}}{\partial r^s} = 0} \tag{D.49}$$

✓ $\dfrac{\partial \underset{\sim}{\boldsymbol{S}}}{\partial \gamma_{cum}}$

$$\boxed{\frac{\partial \underset{\sim}{\boldsymbol{S}}}{\partial \gamma_{cum}} = 0} \tag{D.50}$$

- Derivatives of S

$$\underline{S = H_\chi(\gamma_\chi - \gamma_{cum})} \tag{D.51}$$

✓ $\dfrac{\partial S}{\partial \underset{\sim}{\boldsymbol{E}}}$

$$\boxed{\frac{\partial S}{\partial \underset{\sim}{\boldsymbol{E}}} = 0} \tag{D.52}$$

✓ $\dfrac{\partial S}{\partial \gamma^s}$

$$\boxed{\frac{\partial S}{\partial \gamma^s} = 0} \tag{D.53}$$

✓ $\dfrac{\partial S}{\partial r^s}$

$$\boxed{\frac{\partial S}{\partial r^s} = 0} \tag{D.54}$$

✓ $\dfrac{\partial S}{\partial \gamma_{cum}}$

$$\boxed{\frac{\partial S}{\partial \gamma_{cum}} = -H_\chi} \tag{D.55}$$

- Derivatives of $\underline{\underline{\boldsymbol{M}}}$

$$\underline{\underline{\boldsymbol{M}}} = A\underline{\underline{\boldsymbol{K}}} \tag{D.56}$$

✓ $\dfrac{\partial \underline{\underline{\boldsymbol{M}}}}{\partial \underset{\sim}{\boldsymbol{E}}}$

$$\boxed{\frac{\partial \underline{\underline{\boldsymbol{M}}}}{\partial \underset{\sim}{\boldsymbol{E}}} = 0} \tag{D.57}$$

✓ $\dfrac{\partial \underline{\underline{\boldsymbol{M}}}}{\partial \gamma^s}$

$$\boxed{\frac{\partial \underline{\underline{\boldsymbol{M}}}}{\partial \gamma^s} = 0} \tag{D.58}$$

✓ $\dfrac{\partial \underline{\underline{\boldsymbol{M}}}}{\partial r^s}$

$$\boxed{\frac{\partial \underline{\underline{\boldsymbol{M}}}}{\partial r^s} = 0} \tag{D.59}$$

✓ $\dfrac{\partial \underline{\underline{\boldsymbol{M}}}}{\partial \gamma_{cum}}$

$$\boxed{\frac{\partial \underline{\underline{\boldsymbol{M}}}}{\partial \gamma_{cum}} = 0} \tag{D.60}$$

E

Convergence improvement of the micromorphic model

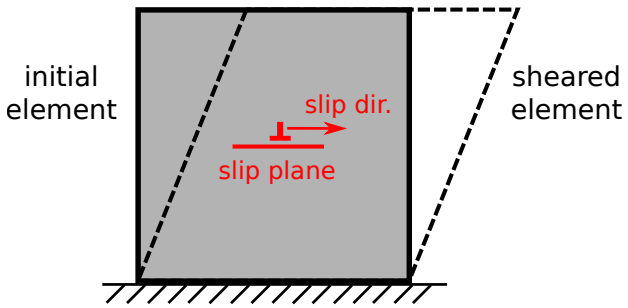

Figure E.1: Simple glide test on one volume element.

For showing the convergence improvement by the algorithm, simulations of simple shearing on one element are carried out by imposing displacement on all the nodes the element. Only one slip system is defined as shown in fig. E.1. We drop the subscript s of γ^s and refer to γ as the plastic slip. A linear hardening law is considered:

$$\tau_c = \tau_0 + H\gamma, \tag{E.1}$$

with $H > 0$. As only one slip system is defined, $\gamma_{cum} = \gamma$. Simulations with the micromorphic theory are compared with those with the conventional single crystal plasticity theory. For the problem considered, the plastic slip field is homogeneous. As a result, the result predicted by the micromorphic model should be in agreement with that by the conventional model.

Small time steps are prescribed for passing the elastic-plastic transition and then large time steps of the same length are prescribed for steady plastic regime. A

critical time step in the plastic regime over which convergence cannot be reached is looked for.

Case 1: $H_\chi = 0$ and $A = 0$

$H_\chi = 0$ and $A = 0$ are first considered with $\gamma_\chi = 0$ imposed on the nodes. As result, the micromorphic model is reduced to the conventional model. Notice that, since all the degrees of freedom are imposed, no iteration is needed for integrating the FE equations. Hence, the consistent tangent matrix is not involved in the solution process.

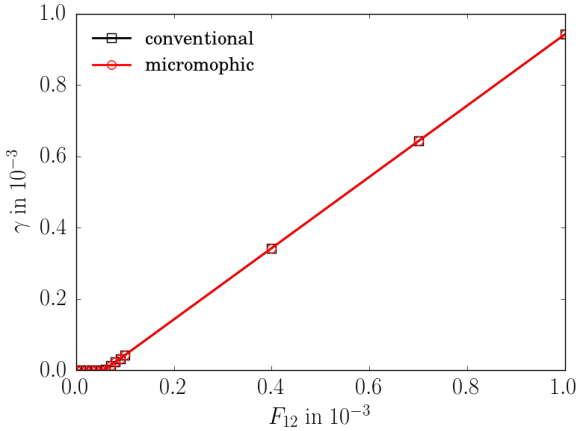

Figure E.2: Comparison: conventional model and strain gradient model with $H_\chi = 0$ and $A = 0$

The results obtained by the two models are in good agreement as shown in fig. E.2 for the evolution of γ. The same convergence is observed for the two calculations.

Case 2: $H_\chi = 10^5$ and $A = 10$ with the analytical Jacobian matrix

The value of A does not influence the result in this case, since the slip field is homogeneous. $H_\chi = 10^5$ which is large enough to ensure $\gamma_\chi = \gamma$. As in the previous case, we want to imposing all the degrees of freedom in the simulation with the micromorphic model, i.e., $\{u_i, \gamma_\chi\}$, and to exclude influence of consistent tangent matrix on the convergence. However, γ_χ is *a priori* unknown. To this end, the evolution of γ in the simulation with the conventional model is used to prescribe γ_χ in the micromorphic model.

As shown in fig. E.3, very small time steps are needed for the simulation with the micromorphic model, while the calculation with the conventional model can even converge with larger time step than that in fig. E.3. Possible explanations are: 1) the Jacobian matrix for integration of the constitutive equations is not correctly

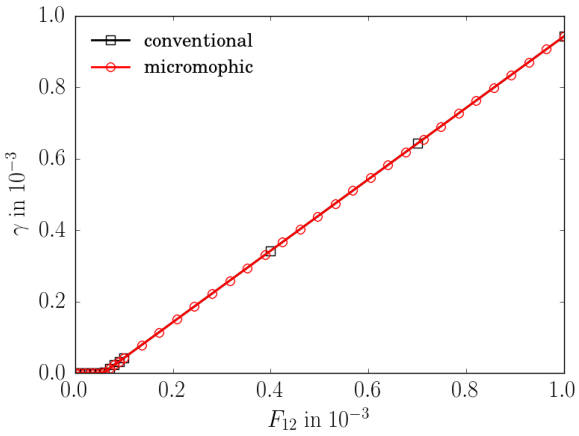

Figure E.3: Comparison: conventional model and strain gradient model with $H_\chi = 10^5$ and $A = 10$

derived or implemented in the code; 2) the convergence of the integration of the power law is not good, because a large value of H_χ is chosen.

To make sure that the problem is not caused by possible errors in the analytical Jacobian matrix, a perturbation method is used for calculating it.

Case 3: $H_\chi = 10^5$ and $A = 10$ with the numerical Jacobian matrix

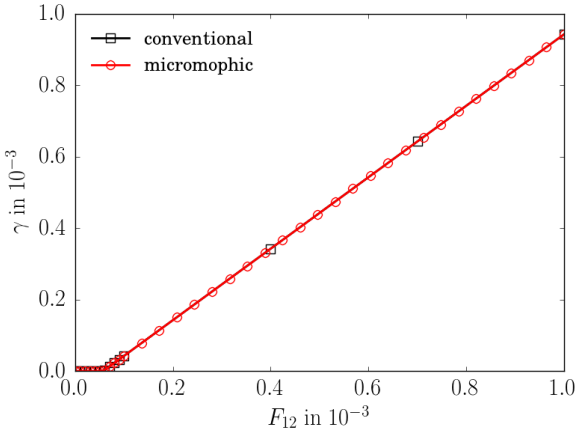

Figure E.4: Comparison: conventional model and micromorphic model with $H_\chi = 10^5$ and $A = 10$ using perturbation method

As can been seen in fig. E.4, the critical time step for the micromorphic model is the same as that obtain with the analytical Jacobian matrix. Thus, the convergence problem is not due to the implementation of the analytical Jacobian matrix.

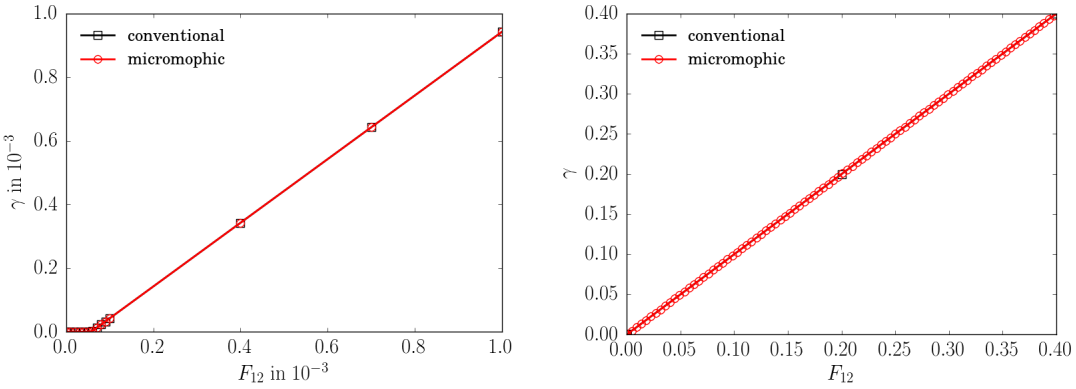

(a) **(b)**

Figure E.5: Comparison: conventional model and micromorphic model with $H_\chi = 10^5$ and $A = 10$ with improved algorithm

Case 4: $H_\chi = 10^5$ and $A = 10$ with the improved algorithm

With the improved algorithm for the power law, the time step for the micromorphic model is highly increased (see fig. E.5a with the same time step in a small range of deformation). We try to find the critical time step over which the simulation does not converge for the two models, as shown in fig. E.5b. Even though the convergence for the micromorphic model is improved, it cannot be as good as that for the conventional theory.

References

[1] Ahn, D. C., Sofronis, P., Kumar, M., Belak, J., and Minich, R. "Void growth by dislocation-loop emission". In: *Journal of Applied Physics* 101.6, 063514 (2007).

[2] Aifantis, E. C. "The physics of plastic deformation". In: *International Journal of Plasticity* 3.3 (1987), pp. 211–247.

[3] Anoukou, K., Pastor, F., Dufrenoy, P., and Kondo, D. "Limit analysis and homogenization of porous materials with Mohr–Coulomb matrix. Part I: Theoretical formulation". In: *Journal of the Mechanics and Physics of Solids* 91 (2016), pp. 145–171.

[4] Arminjon, M. "A regular form of the Schmid law. Application to the ambiguity problem". In: *Textures and Microstructures* 14.18 (1991), pp. 1121–1128.

[5] Asaro, R. and Rice, J. "Strain localization in ductile single crystals". In: *Journal of the Mechanics and Physics of Solids* 25.5 (1977), pp. 309–338.

[6] Ashby, M. F. "The deformation of plastically non-homogeneous materials". In: *Philosophical Magazine* 21.170 (1970), pp. 399–424.

[7] Aslan, O., Cordero, N., Gaubert, A., and Forest, S. "Micromorphic approach to single crystal plasticity and damage". In: *International Journal of Engineering Science* 49.12 (2011). Advances in generalized continuum mechanicsA collection of studies in Engineering Sciences in memory of the late A.C. Eringen (1921-2009), pp. 1311–1325.

[8] Bailat, C., Almazouzi, A., Baluc, N., Schäublin, R., Grapschel, F., and Victoria, M. "The effects of irradiation and testing temperature on tensile behaviour of stainless steels". In: *Journal of Nuclear Materials* 283–287, Part 1 (2000). 9th Int. Conf. on Fusion Reactor Materials, pp. 446–450.

[9] Bargmann, S., Ekh, M., Runesson, K., and Svendsen, B. "Modeling of polycrystals with gradient crystal plasticity: A comparison of strategies". In: *Philosophical Magazine* 90.10 (2010), pp. 1263–1288.

[10] Bayley, C. J., Brekelmans, W. A. M., and Geers, M. G. D. "A three-dimensional dislocation field crystal plasticity approach applied to miniaturized structures". In: *Philosophical Magazine* 87.8-9 (2007), pp. 1361–1378.

[11] Bayley, C., Brekelmans, W., and Geers, M. "A comparison of dislocation induced back stress formulations in strain gradient crystal plasticity". In: *International Journal of Solids and Structures* 43.24 (2006). Size-dependent Mechanics of Materials, pp. 7268–7286.

[12] Benzerga, A., Besson, J., and Pineau, A. "Anisotropic ductile fracture: Part I: experiments". In: *Acta Materialia* 52.15 (2004), pp. 4623–4638.

[13] Benzerga, A. and Leblond, J.-B. “Ductile fracture by void growth to coalescence”. In: *Advances in Applied Mechanics* 44 (2010), pp. 169–305.

[14] Benzerga, A. A. “Rupture ductile des tôles anisotropes. Simulation de la propagation longitudinale dans un tube pressurisé”. PhD thesis. Ecole Nationale Supérieure des Mines de Paris, 2000.

[15] Benzerga, A. A. and Besson, J. “Plastic potentials for anisotropic porous solids”. In: *European Journal of Mechanics - A/Solids* 20.3 (2001), pp. 397–434.

[16] Benzerga, A. A., Leblond, J.-B., Needleman, A., and Tvergaard, V. “Ductile failure modeling”. In: *International Journal of Fracture* 201.1 (2016), pp. 29–80.

[17] Besson, J. “Damage of ductile materials deforming under multiple plastic or viscoplastic mechanisms”. In: *International Journal of Plasticity* 25.11 (2009), pp. 2204–2221.

[18] Besson, J. “Continuum Models of Ductile Fracture: A Review”. In: *International Journal of Damage Mechanics* 19.1 (2010), pp. 3–52.

[19] Besson, J., Cailletaud, G., Chaboche, J.-L., and Forest, S. *Non-linear mechanics of materials*. Vol. 167. Springer Science & Business Media, 2009.

[20] Besson, J. and Foerch, R. “Object-Oriented Programming Applied to the Finite Element Method Part I. General Concepts”. In: *Revue Européenne des Éléments Finis* 7.5 (1998), pp. 535–566.

[21] Blewitt, T., Coltman, R., Jamison, R., and Redman, J. “Radiation hardening of copper single crystals”. In: *Journal of Nuclear Materials* 2.4 (1960), pp. 277–298.

[22] Borg, U. “Strain gradient crystal plasticity effects on flow localization”. In: *International Journal of Plasticity* 23.8 (2007), pp. 1400–1416.

[23] Borg, U. and Kysar, J. W. “Strain gradient crystal plasticity analysis of a single crystal containing a cylindrical void”. In: *International Journal of Solids and Structures* 44.20 (2007), pp. 6382–6397.

[24] Borg, U., Niordson, C. F., and Kysar, J. W. “Size effects on void growth in single crystals with distributed voids”. In: *International Journal of Plasticity* 24.4 (2008), pp. 688–701.

[25] Bringa, E. M., Traiviratana, S., and Meyers, M. A. “Void initiation in fcc metals: Effect of loading orientation and nanocrystalline effects”. In: *Acta Materialia* 58.13 (2010), pp. 4458–4477.

[26] Bruemmer, S., Cole, J., Carter, R., and Was, G. “Defect microstructures and deformation mechanisms in irradiated austenitic stainless steels”. In: *Materials Research Society Symposium - Proceedings*. Vol. 439. France, 1997, pp. 437–444.

[27] Bulatov, V. V., Wolfer, W. G., and Kumar, M. “Shear impossibility: Comments on “Void growth by dislocation emission” and “Void growth in metals: Atomistic calculations””. In: *Scripta Materialia* 63.1 (2010), pp. 144–147.

[28] Busso, E. P. and Cailletaud, G. “On the selection of active slip systems in crystal plasticity”. In: *International Journal of Plasticity* 21.11 (2005). Plasticity of Heterogeneous Materials, pp. 2212–2231.

[29] Byun, T., Hashimoto, N., and Farrell, K. "Deformation mode map of irradiated 316 stainless steel in true stress–dose space". In: *Journal of Nuclear Materials* 351.13 (2006). Proceedings of the Symposium on Microstructural Processes in Irradiated Materials, pp. 303–315.

[30] Cazacu, O., Revil-Baudard, B., Chandola, N., and Kondo, D. "New analytical criterion for porous solids with Tresca matrix under axisymmetric loadings". In: *International Journal of Solids and Structures* 51.34 (2014), pp. 861–874.

[31] Chang, H.-J., Segurado, J., de la Fuente, O. R., Pabón, B. M., and LLorca, J. "Molecular dynamics modeling and simulation of void growth in two dimensions". In: *Modelling and Simulation in Materials Science and Engineering* 21.7 (2013), p. 075010.

[32] Chang, H.-J., Segurado, J., and LLorca, J. "Three-dimensional dislocation dynamics analysis of size effects on void growth". In: *Scripta Materialia* 95 (2015), pp. 11–14.

[33] Chang, Y. and Asaro, R. "An experimental study of shear localization in aluminum-copper single crystals". In: *Acta Metallurgica* 29.1 (1981), pp. 241–257.

[34] Cheong, K.-S. and Busso, E. P. "Discrete dislocation density modelling of single phase {FCC} polycrystal aggregates". In: *Acta Materialia* 52.19 (2004), pp. 5665–5675.

[35] Cole, J. I. and Bruemmer, S. M. "Post-irradiation deformation characteristics of heavy-ion irradiated 304L SS". In: *Journal of Nuclear Materials* 225 (1995), pp. 53–58.

[36] Cordero, N., Gaubert, A., Forest, S., Busso, E., Gallerneau, F., and Kruch, S. "Size effects in generalised continuum crystal plasticity for two-phase laminates". In: *Journal of the Mechanics and Physics of Solids* 58.11 (2010), pp. 1963–1994.

[37] Dai, Y., Gavillet, D., Paschoud, F., and Victoria, M. "Mechanical properties and microstructure of 600 MeV proton irradiated copper single crystals". In: *Journal of Nuclear Materials* 212 (1994), pp. 393–398.

[38] Dai, Y. "Mechanical properties and microstructures of copper gold and palladium single crystals irradiated with 600 MeV protons". eng. PhD thesis. Lausanne, 1995.

[39] Danas, K. and Aravas, N. "Numerical modeling of elasto-plastic porous materials with void shape effects at finite deformations". In: *Composites Part B: Engineering* 43.6 (2012). Homogenization and Micromechanics of Smart and Multifunctional Materials, pp. 2544–2559.

[40] Das, A. and Tarafder, S. "Experimental investigation on martensitic transformation and fracture morphologies of austenitic stainless steel". In: *International Journal of Plasticity* 25.11 (2009), pp. 2222–2247.

[41] DeBotton, G. and Castaneda, P. P. "Variational Estimates for the Creep Behaviour of Polycrystals". In: *Proceedings of the Royal Society of London A: Mathematical, Physical and Engineering Sciences* 448.1932 (1995), pp. 121–142.

[42] Dimiduk, D., Uchic, M., and Parthasarathy, T. "Size-affected single-slip behavior of pure nickel microcrystals". In: *Acta Materialia* 53.15 (2005), pp. 4065–4077.

[43] Dormieux, L. and Kondo, D. "An extension of Gurson model incorporating interface stresses effects". In: *International Journal of Engineering Science* 48.6 (2010), pp. 575–581.

[44] Edwards, D., Simonen, E., Garner, F., Greenwood, L., Oliver, B., and Bruemmer, S. "Influence of irradiation temperature and dose gradients on the microstructural evolution in neutron-irradiated 316SS". In: *Journal of Nuclear Materials* 317.1 (2003), pp. 32–45.

[45] Edwards, D., Singh, B., and Bilderensen, J. "Initiation and propagation of cleared channels in neutron-irradiated pure copper and a precipitation hardened CuCrZr alloy". In: *Journal of Nuclear Materials* 342.13 (2005), pp. 164–178.

[46] Ekh, M., Grymer, M., Runesson, K., and Svedberg, T. "Gradient crystal plasticity as part of the computational modelling of polycrystals". In: *International Journal for Numerical Methods in Engineering* 72.2 (2007), pp. 197–220.

[47] Ertürk, A., van Dommelen, J., and Geers, M. "Energetic dislocation interactions and thermodynamical aspects of strain gradient crystal plasticity theories". In: *Journal of the Mechanics and Physics of Solids* 57.11 (2009), pp. 1801–1814.

[48] Essmann, U. and Rapp, M. "Slip in copper crystals following weak neutron bombardment". In: *Acta Metallurgica* 21.9 (1973), pp. 1305–1317.

[49] Evers, L., Brekelmans, W., and Geers, M. "Non-local crystal plasticity model with intrinsic {SSD} and {GND} effects". In: *Journal of the Mechanics and Physics of Solids* 52.10 (2004), pp. 2379–2401.

[50] Faleskog, J., Gao, X., and Shih, C. F. "Cell model for nonlinear fracture analysis – I. Micromechanics calibration". In: *International Journal of Fracture* 89.4 (1998).

[51] Fish, R., Straalsund, J., Hunter, C., and Holmes, J. "Swelling and tensile property evaluations of high-fluence EBR-II thimbles". In: *Effects of Radiation on Substructure and Mechanical Properties of Metals and Alloys*. ASTM International, 1973.

[52] Fleck, N. and Hutchinson, J. "A phenomenological theory for strain gradient effects in plasticity". In: *Journal of the Mechanics and Physics of Solids* 41.12 (1993), pp. 1825–1857.

[53] Fleck, N. and Hutchinson, J. "Strain gradient plasticity". In: *Advances in applied mechanics* 33 (1997), pp. 296–361.

[54] Fleck, N. and Hutchinson, J. "A reformulation of strain gradient plasticity". In: *Journal of the Mechanics and Physics of Solids* 49.10 (2001), pp. 2245–2271.

[55] Fleck, N., Muller, G., Ashby, M., and Hutchinson, J. "Strain gradient plasticity: Theory and experiment". In: *Acta Metallurgica et Materialia* 42.2 (1994), pp. 475–487.

[56] Flouriot, S., Forest, S., Cailletaud, G., Köster, A., Rémy, L., Burgardt, B., Gros, V., Mosset, S., and Delautre, J. "Strain localization at the crack tip in single crystal CT specimens under monotonous loading: 3D Finite Element analyses and application to nickel-base superalloys". In: *International Journal of Fracture* 124.1 (2003), pp. 43–77.

[57] Forest, S. "Modeling slip, kink and shear banding in classical and generalized single crystal plasticity". In: *Acta Materialia* 46.9 (1998), pp. 3265–3281.

[58] Forest, S., Blazy, J.-S., Chastel, Y., and Moussy, F. "Continuum modeling of strain localization phenomena in metallic foams". In: *Journal of Materials Science* 40.22 (2005), pp. 5903–5910.

[59] Forest, S. and Sievert, R. "Elastoviscoplastic constitutive frameworks for generalized continua". In: *Acta Mechanica* 160.1 (2003), pp. 71–111.

[60] Forest, S. "Micromorphic Approach for Gradient Elasticity, Viscoplasticity, and Damage". In: *Journal of Engineering Mechanics* 135.3 (2009), pp. 117–131.

[61] Franciosi, P. "The concepts of latent hardening and strain hardening in metallic single crystals". In: *Acta Metallurgica* 33.9 (1985), pp. 1601–1612.

[62] Franciosi, P. and Zaoui, A. "Multislip in f.c.c. crystals a theoretical approach compared with experimental data". In: *Acta Metallurgica* 30.8 (1982), pp. 1627–1637.

[63] Fukuya, K., Nishioka, H., Fujii, K., Kamaya, M., Miura, T., and Torimaru, T. "Fracture behavior of austenitic stainless steels irradiated in PWR". In: *Journal of Nuclear Materials* 378.2 (2008), pp. 211–219.

[64] Gambin, W. "Refined analysis of elastic-plastic crystals". In: *International Journal of Solids and Structures* 29.16 (1992), pp. 2013–2021.

[65] Gan, Y. X., Kysar, J. W., and Morse, T. L. "Cylindrical void in a rigid-ideally plastic single crystal II: Experiments and simulations". In: *International Journal of Plasticity* 22.1 (2006), pp. 39–72.

[66] Gao, H., Huang, Y., Nix, W., and Hutchinson, J. "Mechanism-based strain gradient plasticity— I. Theory". In: *Journal of the Mechanics and Physics of Solids* 47.6 (1999), pp. 1239–1263.

[67] Gao, X., Faleskog, J., and Shih, C. F. "Cell model for nonlinear fracture analysis – II. Fracture- process calibration and verification". In: *International Journal of Fracture* 89.4 (1998), pp. 375–398.

[68] Garner, F., Porollo, S., Konobeev, Y. V., and Maksimkin, O. "Void swelling of austenitic steels irradiated with neutrons at low temperatures and very low dpa rates". In: *Proceedings of the 12th International Conference on Environmental Degradation of Materials in Nuclear Power System: Water Reactors*. Ed. by T.R. Allen, P. K. and Nelson, L. 2005.

[69] Germain, P. "The Method of Virtual Power in Continuum Mechanics. Part 2: Microstructure". In: *SIAM Journal on Applied Mathematics* 25.3 (1973), pp. 556–575.

[70] Gologanu, M., Leblond, J.-B., and Devaux, J. "Approximate models for ductile metals containing non-spherical voids: Case of axisymmetric prolate ellipsoidal cavities". In: *Journal of the Mechanics and Physics of Solids* 41.11 (1993), pp. 1723–1754.

[71] Gologanu, M., Leblond, J.-B., and Devaux, J. "Approximate models for ductile metals containing nonspherical voids: case of axisymmetric oblate ellipsoidal cavities". In: *Journal of Engineering Materials and Technology* 116.3 (1994), pp. 290–297.

[72] Greenfield, I. G. and Wilsdorf, H. G. F. “Effect of Neutron Irradiation on the Plastic Deformation of Copper Single Crystals”. In: *Journal of Applied Physics* 32.5 (1961), pp. 827–839.

[73] Greer, J. R., Oliver, W. C., and Nix, W. D. “Size dependence of mechanical properties of gold at the micron scale in the absence of strain gradients”. In: *Acta Materialia* 53.6 (2005), pp. 1821–1830.

[74] Gudmundson, P. “A unified treatment of strain gradient plasticity”. In: *Journal of the Mechanics and Physics of Solids* 52.6 (2004), pp. 1379–1406.

[75] Gurson, A. L. “Continuum theory of ductile rupture by void nucleation and growth: Part I–Yield criteria and flow rules for porous ductile media”. In: *Journal of Engineering Materials and Technology* 99.1 (1977), pp. 2–15.

[76] Gurtin, M. E. “On the plasticity of single crystals: free energy, microforces, plastic-strain gradients”. In: *Journal of the Mechanics and Physics of Solids* 48.5 (2000), pp. 989–1036.

[77] Gurtin, M. E. “A gradient theory of single-crystal viscoplasticity that accounts for geometrically necessary dislocations”. In: *Journal of the Mechanics and Physics of Solids* 50.1 (2002), pp. 5–32.

[78] Gurtin, M. E. and Anand, L. “Thermodynamics applied to gradient theories involving the accumulated plastic strain: The theories of Aifantis and Fleck and Hutchinson and their generalization”. In: *Journal of the Mechanics and Physics of Solids* 57.3 (2009), pp. 405–421.

[79] Gururaj, K., Robertson, C., and Fivel, M. “Channel formation and multiplication in irradiated FCC metals: a 3D dislocation dynamics investigation”. In: *Philosophical Magazine* 95.12 (2015), pp. 1368–1389.

[80] Ha, S. and Kim, K. “Void growth and coalescence in F.C.C. single crystals”. In: *International Journal of Mechanical Sciences* 52.7 (2010), pp. 863–873.

[81] Han, X. “Modélisation de la fragilisation due au gonflement dans les aciers inoxydables austénitiques irradiés”. PhD thesis. Mines ParisTech, 2012.

[82] Han, X., Besson, J., Forest, S., Tanguy, B., and Bugat, S. “A yield function for single crystals containing voids”. In: *International Journal of Solids and Structures* 50.14-15 (2013), pp. 2115–2131.

[83] Hashimoto, N., Byun, T., and Farrell, K. “Microstructural analysis of deformation in neutron-irradiated fcc materials”. In: *Journal of Nuclear Materials* 351.13 (2006). Proceedings of the Symposium on Microstructural Processes in Irradiated MaterialsProceedings of the Symposium on Microstructural Processes in Irradiated Materials, pp. 295–302.

[84] Hashimoto, N., Byun, T., Farrell, K., and Zinkle, S. “Deformation microstructure of neutron-irradiated pure polycrystalline vanadium”. In: *Journal of Nuclear Materials* 336.23 (2005), pp. 225–232.

[85] Horton, J., Ohr, S., and Jesser, W. “TEM observations of crack tip – cavity interactions”. In: *Journal of Nuclear Materials* 104 (1981), pp. 865–869.

[86] Huang, M., Li, Z., and Wang, C. “Discrete dislocation dynamics modelling of microvoid growth and its intrinsic mechanism in single crystals”. In: *Acta Materialia* 55.4 (2007), pp. 1387–1396.

[87] Huang, Y., Gao, H., Nix, W., and Hutchinson, J. "Mechanism-based strain gradient plasticity—II. Analysis". In: *Journal of the Mechanics and Physics of Solids* 48.1 (2000), pp. 99–128.

[88] Huang, Z. and Wang, J. "Nonlinear mechanics of solids containing isolated voids". In: *Applied Mechanics Reviews* 59.4 (2006), pp. 210–229.

[89] Huo, B., Zheng, Q.-S., and Huang, Y. "A note on the effect of surface energy and void size to void growth". In: *European Journal of Mechanics - A/Solids* 18.6 (1999), pp. 987–994.

[90] Hussein, M., Borg, U., Niordson, C., and Deshpande, V. "Plasticity size effects in voided crystals". In: *Journal of the Mechanics and Physics of Solids* 56.1 (2008), pp. 114–131.

[91] Khraishi, T. A., Khaleel, M. A., and Zbib, H. M. "A parametric-experimental study of void growth in superplastic deformation". In: *International Journal of Plasticity* 17.3 (2001), pp. 297–315.

[92] Koplik, J. and Needleman, A. "Void growth and coalescence in porous plastic solids". In: *International Journal of Solids and Structures* 24.8 (1988), pp. 835–853.

[93] Krasnikov, V. and Mayer, A. "Plasticity driven growth of nanovoids and strength of aluminum at high rate tension: Molecular dynamics simulations and continuum modeling". In: *International Journal of Plasticity* 74 (2015), pp. 75–91.

[94] Krishna, S. and De, S. "A temperature and rate-dependent micromechanical model of molybdenum under neutron irradiation". In: *Mechanics of Materials* 43.2 (2011), pp. 99–110.

[95] Krishna, S., Zamiri, A., and De, S. "Dislocation and defect density-based micromechanical modeling of the mechanical behavior of fcc metals under neutron irradiation". In: *Philosophical magazine* 90.30 (2010), pp. 4013–4025.

[96] Kubin, L., Devincre, B., and Hoc, T. "Modeling dislocation storage rates and mean free paths in face-centered cubic crystals". In: *Acta Materialia* 56.20 (2008), pp. 6040–6049.

[97] Kuroda, M. and Tvergaard, V. "A finite deformation theory of higher-order gradient crystal plasticity". In: *Journal of the Mechanics and Physics of Solids* 56.8 (2008), pp. 2573–2584.

[98] Kysar, J. W. and Briant, C. L. "Crack tip deformation fields in ductile single crystals". In: *Acta Materialia* 50.9 (2002). Computational Thermodynamics and Materials Design, pp. 2367–2380.

[99] Kysar, J. W., Gan, Y. X., and Mendez-Arzuza, G. "Cylindrical void in a rigid-ideally plastic single crystal. Part I: Anisotropic slip line theory solution for face-centered cubic crystals". In: *International Journal of Plasticity* 21.8 (2005), pp. 1481–1520.

[100] Lee, E., Byun, T., Hunn, J., Yoo, M., Farrell, K., and Mansur, L. "On the origin of deformation microstructures in austenitic stainless steel: part I. microstructures". In: *Acta Materialia* 49.16 (2001), pp. 3269–3276.

[101] Lee, E. H. "Elastic-plastic deformation at finite strains". In: *Journal of Applied Mechanics* 36.1 (1969), pp. 1–6.

[102] Ling, C., Besson, J., Forest, S., Tanguy, B., Latourte, F., and Bosso, E. "An elastoviscoplastic model for porous single crystals at finite strains and its assessment based on unit cell simulations". In: *International Journal of Plasticity* 84 (2016), pp. 58–87.

[103] Little, E. "Fracture mechanics evaluations of neutron irradiated Type 321 austenitic steel". In: *Journal of Nuclear Materials* 139.3 (1986), pp. 261–276.

[104] Lucas, G. "The evolution of mechanical property change in irradiated austenitic stainless steels". In: *Journal of Nuclear Materials* 206.2 (1993), pp. 287–305.

[105] Luu, T. T. "Déchirure ductile des aciers à haute résistance pour gazoducs (X100)". PhD thesis. École Nationale Supérieure des Mines de Paris, 2006.

[106] Mandel, J. "Equations constitutives et directeurs dans les milieux plastiques et viscoplastiques". In: *International Journal of Solids and Structures* 9.6 (1973), pp. 725–740.

[107] Margolin, B., Sorokin, A., Shvetsova, V., Minkin, A., Potapova, V., and Smirnov, V. "The radiation swelling effect on fracture properties and fracture mechanisms of irradiated austenitic steels. Part I. Ductility and fracture toughness". In: *Journal of Nuclear Materials* 480 (2016), pp. 52–68.

[108] Mbiakop, A., Constantinescu, A., and Danas, K. "A model for porous single crystals with cylindrical voids of elliptical cross-section". In: *International Journal of Solids and Structures* 64 (2015), pp. 100–119.

[109] Mbiakop, A., Constantinescu, A., and Danas, K. "An analytical model for porous single crystals with ellipsoidal voids". In: *Journal of the Mechanics and Physics of Solids* 84 (2015), pp. 436–467.

[110] McClintock, F. A. "A criterion for ductile fracture by the growth of holes". In: *Journal of applied mechanics* 35.2 (1968), pp. 363–371.

[111] McElhaney, K. W., Vlassak, J. J., and Nix, W. D. "Determination of indenter tip geometry and indentation contact area for depth-sensing indentation experiments". In: *Journal of Materials Research* 13.5 (1998), pp. 1300–1306.

[112] Mecking, H. and Lücke, K. "A new aspect of the theory of flow stress of metals". In: *Scripta Metallurgica* 4.6 (1970), pp. 427–432.

[113] Miehe, C., Mauthe, S., and Hildebrand, F. "Variational gradient plasticity at finite strains. Part III: Local-global updates and regularization techniques in multiplicative plasticity for single crystals". In: *Computer Methods in Applied Mechanics and Engineering* 268 (2014), pp. 735–762.

[114] Miehe, C. "Variational gradient plasticity at finite strains. Part I: Mixed potentials for the evolution and update problems of gradient-extended dissipative solids". In: *Computer Methods in Applied Mechanics and Engineering* 268 (2014), pp. 677–703.

[115] Miehe, C., Welschinger, F., and Aldakheel, F. "Variational gradient plasticity at finite strains. Part II: Local-global updates and mixed finite elements for additive plasticity in the logarithmic strain space". In: *Computer Methods in Applied Mechanics and Engineering* 268 (2014), pp. 704–734.

[116] Mindlin, R. D. "Micro-structure in linear elasticity". In: *Archive for Rational Mechanics and Analysis* 16.1 (1964), pp. 51–78.

[117] Monchiet, V. and Bonnet, G. "A Gurson-type model accounting for void size effects". In: *International Journal of Solids and Structures* 50.2 (2013), pp. 320–327.

[118] Monchiet, V. and Kondo, D. "Combined voids size and shape effects on the macroscopic criterion of ductile nanoporous materials". In: *International Journal of Plasticity* 43 (2013), pp. 20–41.

[119] Monnet, G. "A crystalline plasticity law for austenitic stainless steel". EDF R&D internal report, PERFORM Projet, H-B60-2008-04690-EN. 2009.

[120] Morin, L., Kondo, D., and Leblond, J.-B. "Numerical assessment, implementation and application of an extended Gurson model accounting for void size effects". In: *European Journal of Mechanics - A/Solids* 51 (2015), pp. 183–192.

[121] Mughrabi, H. *Materials Science and Technology, Plastic Deformation and Fracture of Materials*. Materials Science and Technology. Wiley, 1996.

[122] Neustroev, V. and Garner, F. "Very high swelling and embrittlement observed in a Fe–18Cr–10Ni–Ti hexagonal fuel wrapper irradiated in the BOR-60 fast reactor". In: *Journal of Nuclear Materials* 378.3 (2008), pp. 327–332.

[123] Neustroev, V. and Garner, F. "Severe embrittlement of neutron irradiated austenitic steels arising from high void swelling". In: *Journal of Nuclear Materials* 388 (2009). Fusion Reactor Materials Proceedings of the Thirteenth International Conference on Fusion Reactor Materials, pp. 157–160.

[124] Niordson, C. F. "Void growth to coalescence in a non-local material". In: *European Journal of Mechanics - A/Solids* 27.2 (2008), pp. 222–233.

[125] Niordson, C. F. and Kysar, J. W. "Computational strain gradient crystal plasticity". In: *Journal of the Mechanics and Physics of Solids* 62 (2014). Sixtieth anniversary issue in honor of Professor Rodney Hill, pp. 31–47.

[126] Niordson, C. F. and Redanz, P. "Size-effects in plane strain sheet-necking". In: *Journal of the Mechanics and Physics of Solids* 52.11 (2004), pp. 2431–2454.

[127] Nix, W. D. and Gao, H. "Indentation size effects in crystalline materials: A law for strain gradient plasticity". In: *Journal of the Mechanics and Physics of Solids* 46.3 (1998), pp. 411–425.

[128] Nye, J. "Some geometrical relations in dislocated crystals". In: *Acta Metallurgica* 1.2 (1953), pp. 153–162.

[129] Parthasarathy, T. A., Rao, S. I., Dimiduk, D. M., Uchic, M. D., and Trinkle, D. R. "Contribution to size effect of yield strength from the stochastics of dislocation source lengths in finite samples". In: *Scripta Materialia* 56.4 (2007), pp. 313–316.

[130] Paux, J., Morin, L., Brenner, R., and Kondo, D. "An approximate yield criterion for porous single crystals". In: *European Journal of Mechanics - A/Solids* 51 (2015), pp. 1–10.

[131] Pawel, J., Rowcliffe, A., Alexander, D., Grossbeck, M., and Shiba, K. "Effects of low temperature neutron irradiation on deformation behavior of austenitic stainless steels". In: *Journal of Nuclear Materials* 233 (1996), pp. 202–206.

[132] Peirce, D., Asaro, R., and Needleman, A. "An analysis of nonuniform and localized deformation in ductile single crystals". In: *Acta Metallurgica* 30.6 (1982), pp. 1087–1119.

[133] Pineau, A., Benzerga, A., and Pardoen, T. “Failure of metals I: Brittle and ductile fracture”. In: *Acta Materialia* 107 (2016), pp. 424–483.

[134] Pineau, A. and Pardoen, T. “Failure of Metals”. In: *Comprehensive Structural Integrity*. Ed. by Milne, I., Ritchie, R., and Karihaloo, B. Oxford: Pergamon, 2007, pp. 684–797.

[135] Pokor, C., Averty, X., Bréchet, Y., Dubuisson, P., and Massoud, J. “Effect of irradiation defects on the work hardening behavior”. In: *Scripta Materialia* 50.5 (2004), pp. 597–600.

[136] Pokor, C., Bréchet, Y., Dubuisson, P., Massoud, J.-P., and Averty, X. “Irradiation damage in 304 and 316 stainless steels: experimental investigation and modeling. Part II: Irradiation induced hardening”. In: *Journal of Nuclear Materials* 326.1 (2004), pp. 30–37.

[137] Pokor, C., Bréchet, Y., Dubuisson, P., Massoud, J.-P., and Barbu, A. “Irradiation damage in 304 and 316 stainless steels: experimental investigation and modeling. Part I: Evolution of the microstructure”. In: *Journal of Nuclear Materials* 326.1 (2004), pp. 19–29.

[138] Poole, W., Ashby, M., and Fleck, N. “Micro-hardness of annealed and work-hardened copper polycrystals”. In: *Scripta Materialia* 34.4 (1996), pp. 559–564.

[139] Potirniche, G., Horstemeyer, M., Wagner, G., and Gullett, P. “A molecular dynamics study of void growth and coalescence in single crystal nickel”. In: *International Journal of Plasticity* 22.2 (2006), pp. 257–278.

[140] Renault, A., Malaplate, J., Pokor, C., Gavoille, P., Massoud, J.-P., and Garnier, J. “Effects of chemical composition, metallurgical state and stress during irradiation on microstructure of neutron-irradiated austenitic stainless steels: comparison of PWR and BOR-60 irradiations”. In: *Fontevraud 7 - Contribution of materials investigations to improve the safety and performance of LWRs*. France, 2010.

[141] Rice, J. and Tracey, D. “On the ductile enlargement of voids in triaxial stress fields”. In: *Journal of the Mechanics and Physics of Solids* 17.3 (1969), pp. 201–217.

[142] Rodney, D. and Martin, G. “Dislocation Pinning by Small Interstitial Loops: A Molecular Dynamics Study”. In: *Phys. Rev. Lett.* 82 (16 Apr. 1999), pp. 3272–3275.

[143] Rudd, R. E. “Void growth in bcc metals simulated with molecular dynamics using the Finnis–Sinclair potential”. In: *Philosophical Magazine* 89.34-36 (2009), pp. 3133–3161.

[144] Sabnis, P. A., Forest, S., Arakere, N. K., and Yastrebov, V. “Crystal plasticity analysis of cylindrical indentation on a Ni-base single crystal superalloy”. In: *International Journal of Plasticity* 51 (2013), pp. 200–213.

[145] Sabnis, P., Mazière, M., Forest, S., Arakere, N. K., and Ebrahimi, F. “Effect of secondary orientation on notch-tip plasticity in superalloy single crystals”. In: *International Journal of Plasticity* 28 (2012), pp. 102–123.

[146] Sauzay, M., Bavard, K., and Karlsen, W. "TEM observations and finite element modelling of channel deformation in pre-irradiated austenitic stainless steels: Interactions with free surfaces and grain boundaries". In: *Journal of Nuclear Materials* 406.1 (2010). FP6 IP PERFECT Project: Prediction of Irradiation Damage Effects in Reactor Components, pp. 152–165.

[147] Schmid, V. E. and Boas, W. *Kristallplastizität*. Berlin: Verlag Julius Springer, 1935.

[148] Segurado, J. and Llorca, J. "An analysis of the size effect on void growth in single crystals using discrete dislocation dynamics". In: *Acta Materialia* 57.5 (2009), pp. 1427–1436.

[149] Seppälä, E. T., Belak, J., and Rudd, R. E. "Effect of stress triaxiality on void growth in dynamic fracture of metals: A molecular dynamics study". In: *Phys. Rev. B* 69 (13 Apr. 2004), p. 134101.

[150] Sharp, J. V. "Deformation of neutron-irradiated copper single crystals". In: *Philosophical Magazine* 16.139 (1967), pp. 77–96.

[151] Sharp, J. "Deformation of neutron irradiated copper alloys". In: *Acta Metallurgica* 22.4 (1974), pp. 449–457.

[152] Shu, J. Y. "Scale-dependent deformation of porous single crystals". In: *International Journal of Plasticity* 14.10-11 (1998), pp. 1085–1107.

[153] Shu, J. Y. and Fleck, N. A. "Strain gradient crystal plasticity: size-dependentdeformation of bicrystals". In: *Journal of the Mechanics and Physics of Solids* 47.2 (1999), pp. 297–324.

[154] Singh, B., Foreman, A., and Trinkaus, H. "Radiation hardening revisited: role of intracascade clustering". In: *Journal of Nuclear Materials* 249.2 (1997), pp. 103–115.

[155] Singh, B., Horsewell, A., and Toft, P. "Effects of neutron irradiation on microstructure and mechanical properties of pure iron". In: *Journal of Nuclear Materials* 272 (1999), pp. 97–101.

[156] Smyshlyaev, V. and Fleck, N. "The role of strain gradients in the grain size effect for polycrystals". In: *Journal of the Mechanics and Physics of Solids* 44.4 (1996), pp. 465–495.

[157] Stelmashenko, N., Walls, M., Brown, L., and Milman, Y. "Microindentations on W and Mo oriented single crystals: An STM study". In: *Acta Metallurgica et Materialia* 41.10 (1993), pp. 2855–2865.

[158] Stölken, J. and Evans, A. "A microbend test method for measuring the plasticity length scale". In: *Acta Materialia* 46.14 (1998), pp. 5109–5115.

[159] Stoller, R. E. "Modeling dislocation evolution in irradiated alloys". In: *Metallurgical Transactions A* 21.7 (1990), pp. 1829–1837.

[160] Suresh, S., Nieh, T.-G., and Choi, B. "Nano-indentation of copper thin films on silicon substrates". In: *Scripta Materialia* 41.9 (1999), pp. 951–957.

[161] Svendsen, B. and Bargmann, S. "On the continuum thermodynamic rate variational formulation of models for extended crystal plasticity at large deformation". In: *Journal of the Mechanics and Physics of Solids* 58.9 (2010), pp. 1253–1271.

[162] Tabourot, L., Fivel, M., and Rauch, E. "Generalised constitutive laws for f.c.c. single crystals". In: *Materials Science and Engineering: A* 234 (1997), pp. 639–642.

[163] Tang, F.-L., Cai, H.-M., Bao, H.-W., Xue, H.-T., Lu, W.-J., Zhu, L., and Rui, Z.-Y. "Molecular dynamics simulations of void growth in γ-TiAl single crystal". In: *Computational Materials Science* 84 (2014), pp. 232–237.

[164] Tang, T., Kim, S., and Horstemeyer, M. "Molecular dynamics simulations of void growth and coalescence in single crystal magnesium". In: *Acta Materialia* 58.14 (2010), pp. 4742–4759.

[165] Tang, Y., Bringa, E. M., and Meyers, M. A. "Ductile tensile failure in metals through initiation and growth of nanosized voids". In: *Acta Materialia* 60.12 (2012), pp. 4856–4865.

[166] Tang, Y., Bringa, E. M., Remington, B. A., and Meyers, M. A. "Growth and collapse of nanovoids in tantalum monocrystals". In: *Acta Materialia* 59.4 (2011), pp. 1354–1372.

[167] Tanguy, B., Han, X., Besson, J., Forest, S., Robertson, C., and Rupin, N. "Dislocations and irradiation defects-based micromechanical modelling for neutron irradiated austenitic stainless steels". International Symposium on Plasticity and its Current Applications. 2013.

[168] Taylor, G. I. "The Mechanism of Plastic Deformation of Crystals. Part I. Theoretical". In: *Proceedings of the Royal Society of London. Series A, Containing Papers of a Mathematical and Physical Character* 145.855 (1934), pp. 362–387.

[169] Teodosiu, C. and Sidoroff, P. "A finite theory of the elastoviscoplasticity of single crystals". In: *International Journal of Engineering Science* 14.8 (1976), pp. 713–723.

[170] Traiviratana, S., Bringa, E. M., Benson, D. J., and Meyers, M. A. "Void growth in metals: Atomistic calculations". In: *Acta Materialia* 56.15 (2008), pp. 3874–3886.

[171] Trinkaus, H., Singh, B., and Foreman, A. "Mechanisms for decoration of dislocations by small dislocation loops under cascade damage conditions". In: *Journal of Nuclear Materials* 249.2 (1997), pp. 91–102.

[172] Trinkaus, H., Singh, B., and Foreman, A. "Segregation of cascade induced interstitial loops at dislocations: possible effect on initiation of plastic deformation". In: *Journal of Nuclear Materials* 251 (1997). Proceedings of the International Workshop on Defect Production, Accumulation and Materials Performance in an Irradiation Environment, pp. 172–187.

[173] Tucker, R., Wechsler, M., and Ohr, S. "Dislocation channeling in neutron-irradiated niobium". In: *Journal of Applied Physics* 40.1 (1969). cited By 46, pp. 400–408.

[174] Tvergaard, V. and Needleman, A. "Analysis of the cup-cone fracture in a round tensile bar". In: *Acta Metallurgica* 32.1 (1984), pp. 157–169.

[175] Tvergaard, V. "On localization in ductile materials containing spherical voids". In: *International Journal of Fracture* 18.4 (1982), pp. 237–252.

[176] Tvergaard, V. "Material Failure by Void Growth to Coalescence". In: ed. by Hutchinson, J. W. and Wu, T. Y. Vol. 27. Advances in Applied Mechanics. Elsevier, 1989, pp. 83–151.

[177] Uchic, M. D., Dimiduk, D. M., Florando, J. N., and Nix, W. D. "Sample Dimensions Influence Strength and Crystal Plasticity". In: *Science* 305.5686 (2004), pp. 986–989.

[178] Was, G. S. "Fundamentals of radiation materials science: metals and alloys". In: Springer Science & Business Media, 2007, p. 296.

[179] Weck, A., Wilkinson, D., Maire, E., and Toda, H. "Visualization by X-ray tomography of void growth and coalescence leading to fracture in model materials". In: *Acta Materialia* 56.12 (2008), pp. 2919–2928.

[180] Wei, Y. and Hutchinson, J. W. "Steady-state crack growth and work of fracture for solids characterized by strain gradient plasticity". In: *Journal of the Mechanics and Physics of Solids* 45.8 (1997), pp. 1253–1273.

[181] Wen, J., Huang, Y., Hwang, K., Liu, C., and Li, M. "The modified Gurson model accounting for the void size effect". In: *International Journal of Plasticity* 21.2 (2005), pp. 381–395.

[182] Wolfer, W. and Glasgow, B. "Dislocation evolution in metals during irradiation". In: *Acta Metallurgica* 33.11 (1985), pp. 1997–2004.

[183] Wulfinghoff, S. and Böhlke, T. "Equivalent plastic strain gradient enhancement of single crystal plasticity: theory and numerics". In: *Proceedings of the Royal Society of London A: Mathematical, Physical and Engineering Sciences* 468.2145 (2012), pp. 2682–2703.

[184] Wulfinghoff, S. and Böhlke, T. "Equivalent plastic strain gradient crystal plasticity – Enhanced power law subroutine". In: *GAMM-Mitteilungen* 36.2 (2013), pp. 134–148.

[185] Xu, S., Hao, Z., Su, Y., Yu, Y., Wan, Q., and Hu, W. "An analysis on nanovoid growth in body-centered cubic single crystalline vanadium". In: *Computational Materials Science* 50.8 (2011), pp. 2411–2421.

[186] Yang, Y., Abe, H., and Sekimura, N. "Behavior of Frank-loops under stress environment". In: *Physics Letters A* 315.34 (2003), pp. 293–300.

[187] Yerra, S., Tekoglu, C., Scheyvaerts, F., Delannay, L., Houtte, P. V., and Pardoen, T. "Void growth and coalescence in single crystals". In: *International Journal of Solids and Structures* 47.7-8 (2010), pp. 1016–1029.

[188] Zhao, K., Chen, C., Shen, Y., and Lu, T. "Molecular dynamics study on the nano-void growth in face-centered cubic single crystal copper". In: *Computational Materials Science* 46.3 (2009). Proceedings of the 18th International Workshop on Computational Mechanics of Materials IWCMM-18, pp. 749–754.

[189] Zhu, W., Song, Z., Deng, X., He, H., and Cheng, X. "Lattice orientation effect on the nanovoid growth in copper under shock loading". In: *Phys. Rev. B* 75 (2 Jan. 2007), p. 024104.

[190] Zinkle, S., Maziasz, P., and Stoller, R. "Dose dependence of the microstructural evolution in neutron-irradiated austenitic stainless steel". In: *Journal of Nuclear Materials* 206.2 (1993), pp. 266–286.

[191] Zinkle, S. and Was, G. "Materials challenges in nuclear energy". In: *Acta Materialia* 61.3 (2013). The Diamond Jubilee IssueMaterials Challenges in Tomorrow: World Selected Topics in Materials Science and Engineering, pp. 735–758.

[192] Zouari, M., Fournier, L., Barbu, A., and Bréchet, Y. "Cluster Dynamics Prediction of the Microstructure Evolution of 300-Series Austenitic Stainless Steel under Irradiation: Influence of Helium". In: *15th International Conference on Environmental Degradation of Materials in Nuclear Power Systems-Water Reactors*. John Wiley & Sons, Inc., 2012, pp. 1371–1382.

Résumé

L'irradiation peut modifier les propriétés mécaniques des aciers inoxydables austénitiques. Une diminution de la ténacité à la rupture des aciers en fonction de la dose est observée. La rupture ductile due à la croissance et la coalescence des cavités est toujours un mécanisme dominant dans les aciers irradiés jusqu'à 10 dpa. Des cavités peuvent être créées de manière différente: nucléées à partir des inclusions ou des précipités d'irradiation, ou créées directement par irradiation. Cette thèse a pour objectif d'étudier la rupture ductile des aciers irradiés due à la croissance et la coalescence des cavités intragranulaires. Basées sur la plasticité cristalline, des simulations en éléments finis sont effectuées sur les cellules unitaires pour étudier l'effet de l'orientation cristallographique et de la triaxialité de contraintes sur la croissance et la coalescence des cavités. L'effet de l'écrouissage post-irradiation sur la croissance et la coalescence des cavités est étudié avec un modèle de la plasticité cristalline prenant compte des défauts d'irradiation. En outre, un modèle élasto-visco-plastique en grandes transformations est proposé pour décrire la croissance des cavités dans le monocristal. Le modèle est appliqué à la simulation de l'endommagement ductile dans le monocristal et le polycristal. Des cavités peuvent avoir des tailles différentes et la taille peut avoir une influence sur la ténacité à la rupture des aciers. Afin d'étudier cet effet, un modèle micromorphe de plasticité cristalline est proposé et appliqué à la simulation de la croissance et la coalescence des cavités intragranulaires de différentes tailles ainsi qu'aux phénomènes de localisation dans les monocristaux.

Mots Clés

rupture ductile, acier CFC, irradiation, cavités intragranulaires, plasticité cristalline, plasticité à gradient

Abstract

Irradiation causes drastic modifications of mechanical properties of austenitic stainless steels and a decrease in the fracture toughness with irradiation has been observed. Ductile fracture due to void growth and coalescence remains one dominant fracture mechanism for doses in the range of 0–10 dpa. Voids may have different origins: nucleated at inclusions or irradiation-induced precipitates during mechanical loading, or produced directly by irradiation. The present work is to investigate ductile fracture of irradiated steels due to growth and coalescence of intragranulaire voids. Based on continuum crystal plasticity theory, FE simulations are performed on unit cells for studying effects of lattice orientation and stress triaxiality on void growth and coalescence. The influence of post-irradiation hardening/softening on void growth and coalescence is evaluated with a physically based crystal plasticity model. Besides, an elastoviscoplastic model at finite strains is proposed to describe void growth up to coalescence in single crystals, and is assessed based unit cell simulations. The model is then applied to simulate ductile damage in single crystals and polycrystals. As voids in irradiated steels may have different origins, they may have different sizes, which potentially have an influence on ductile fracture process and fracture toughness of irradiated steels. In order to assess the size effect, a micromorphic crystal plasticity model is proposed and applied to simulate growth and coalescence of intragranular voids of different sizes.

Keywords

ductile fracture, FCC steels, irradiation, intragranular voids, crystal plasticity, strain gradient plasticity